Aspects of Magnetic fields in the Late Stages of Stellar Evolution

by

Anand Thirumalai

B.Tech., The Indian Institute of Technology - Roorkee, 2002
M.A.Sc., The University of British Columbia, 2005
M.Sc., The University of British Columbia, 2007

A THESIS SUBMITTED IN PARTIAL FULFILLMENT OF
THE REQUIREMENTS FOR THE DEGREE OF

DOCTOR OF PHILOSOPHY

in

The Faculty of Graduate Studies

(Physics)

THE UNIVERSITY OF BRITISH COLUMBIA

(Vancouver)

October 2012

Abstract

We investigate the implications of a magnetic field in the late stages of stellar evolution, in relation to the process of mass-loss via a stellar wind. We develop the very first hybrid magnetohydrodynamic-dust-driven wind model for intermediate-mass Asymptotic Giant Branch (AGB) stars. This model consists of incorporating a canonical Weber-Davis magneto-centrifugal scenario with the effects of radiation pressure on dust grains in the envelope of an AGB star. This results in a dual-fluid description, the solution of which is seen to possess traits of both types of winds. In this context, we additionally investigate the implications of spots on the photosphere that alter the location of dust formation and hence the wind solutions.

This model is adapted to tackle the case of the red supergiant Betelgeuse. The underlying motivation is to delineate a new mechanism for solving the problem of transport of stellar material from the photosphere out to the dust formation radius, many stellar radii away. Various dust formation scenarios are investigated and it is concluded that the simplest of such scenarios, with silicate dust forming at a large distance, is the most viable one as well.

This theory is also applied to the low-mass end of AGB stars; the star Mira. By applying a modified wind model we solve for a hybrid MHD-dust-driven wind solution and find that the magnetic field required to model the observed wind is about 4 G, well within the range of current estimates for AGB stars. We also formulate a hot-spot model to rationalise dust shells at a distance of several stellar radii.

Finally, we study the effects of a strong magnetic field in post-AGB compact objects; magnetised white dwarfs and neutron stars. We develop a fast and efficient solution for Hartree-Fock atoms in strong magnetic fields using pseudospectral methods. The atomic structure package developed for this purpose is seen to be many orders of magnitude faster than finite-element based methods. We also obtain for the first time, estimates for the binding energies of certain low-lying states of the lithium atom, that have not been reported thus far in the literature.

Preface

The content of the research work presented in this thesis represents original work entirely due to the author of this thesis. All the content presented here was written by the author. The principal investigator, Dr. Jeremy S. Heyl, acted in a supervisory capacity steering the direction of research and offering advice as the PhD thesis advisor.

The majority of the content of this thesis is published in journals, or is currently in the process of review, prior to publication. These details are provided below.

- A version of Chapter 3 has been published in *Monthly Notices of the Royal Astronomical Society*, Vol. 409 (4), pp. 1669−81, 2010. © Anand Thirumalai & Jeremy S. Heyl. © Royal Astronomical Society.

- A version of Chapter 4 has been published in *Monthly Notices of the Royal Astronomical Society*, Vol. 422 (2), pp. 1272−82, 2012. © Anand Thirumalai & Jeremy S. Heyl. © Royal Astronomical Society.

- A version of Chapter 5 has been submitted to a journal. This work is currently in review.

- A version of Chapter 6 has been submitted to a journal and is currently in review. Some aspects of the work are based upon previously published work by the author and as such the material borrows from Anand Thirumalai & Jeremy S. Heyl, *Physical Review A*, 79, 012514 (2009), © The American Physical Society as well as from Jeremy S. Heyl & Anand Thirumalai, *Monthly Notices of the Royal Astronomical Society*, Vol. 407(1), pp. 590−98, 2010. © Jeremy S. Heyl & Anand Thirumalai. © Royal Astronomical Society.

Table of Contents

List of Tables

List of Figures

Acknowledgements

Dedication

To my parents.

Chapter 1

Introduction

The late stages of stellar evolution are perhaps one of the most intriguing of the outstanding questions in the field of stellar astrophysics. Much of our knowledge regarding the penultimate stages of stellar life cycles has come from multi-wavelength observations of evolved stars, viz., red giant and asymptotic giant branch (AGB) stars. The latter class of stars represent the final stages in the lives of low- and intermediate-mass stars. The fate of our own Sun can, in essence, be surmised using observations of different AGB stars in various stages of evolution.

1.1   Historical Overview

The history of the discovery of AGB stars [e.g. 1] is a potpourri of serendipitous discoveries and insights coupled with advances in quantum mechanics and latterly, observational techniques and computing capacity. Perhaps the very first discoveries can be traced back to Ptolemy finding and characterising a certain star as being "ruddy" in colour and later Arabic astronomers naming this red star, *Betelgeuse*, which although technically is not an AGB star, the fact that it appears red to the naked eye, sparked much debate in the scientific community all the way up to the early 1900's. At the time, with Planck's theory coming into light, it became known that the redder stars are cooler. It was around the same time that Hertzsprung [see 2] and Russell [see 3] were independently working towards classifying stellar spectral types correlated with luminosity. Their classifications however, further deepened the mysteries surrounding these stars when it was realised that they were also *giants*, which is about the time when the term was coined [e.g. 1].

Linked with these mysteries is the history relating the discovery of the long period variables, or as they are popularly known, Mira-variables or Mira-type stars. In ca. 1596 the German theologian and astronomer David Fabricius from Frisia, discovered that a particular star in the constellation of the Whale, *Cetus*, known today as the star Mira, "disappeared" from the sky.

At the time, he dubbed it another "Stella Nova", as the one that was seen earlier in 1572 by Tycho Brahe. It was only a few decades later in ca. 1638 that another Dutch Frisian astronomer Holwarda, was able to unambiguously determine that the star changed in brightness from low to high with an approximate period of one year. He estimated it to be about 330 days which is remarkably accurate considering current estimates put the number to be at 331.9 days. Being perplexed by this behaviour he termed it "Stella Mira" or "miraculous" or "amazing" star. In the following decades, several variable stars like Mira were discovered by various astronomers. Incidentally, in ca. 1611 when David Fabricius' son (Johannes) returned from university in the Netherlands with telescopes, the pair started observing the stars including the sun. At the crack of dawn Johannes was able to see spots on the surface of the sun and during the day they would both observe the sun with the telescope. Soon they adopted the "*camera obscura*" method to form inverted images of the sun. They, along with the English astronomer Thomas Harriot, were the first to observe sun spots with a telescope.

A deeper understanding of the variability of Miras had to wait until 1963, when Feast [see 4] surmised from observations that Mira variables with shorter periods were older. However, it was only relatively recently in 1981, that Glass and Evans [see 5] established an empirical linear relationship between the K-magnitude and the log of the period in Mira variables (see Figure 1.1).

Somewhat parallel to the discovery of Mira variables and red giants, in ca. 1868, Father Secchi, a Vatican Observatory astronomer [e.g. 1, 6], classified around 4000 stars using stellar spectrograms, and discovered that some of the "red" stars were very different than the others. He remarked that they showed similarities to the the light seen in carbon arcs, at the time. This discovery led to the classification of "red" stars into eventually two broad categories, as those having predominantly carbon lines and those without. These are now understood (partly due to Russell in 1934 [see 7]) to be two distinct types of AGB stars, namely carbon-rich and oxygen-rich giants. The relative abundances of carbon and oxygen in these stars ultimately determine the type of AGB star. The complicated physical nature of the interior of these stars came to full light in 1975 when Iben [see 8] and Sugimoto & Nomoto [see 9] showed that a combination of not only the s-process but also the triple-alpha process nucleosynthesis, with convective dredge-up of material in these stars, leads to a sufficient increase in carbon, turning them into carbon-rich stars. The evidence of this dredge-up, common to most Miras, comes chiefly
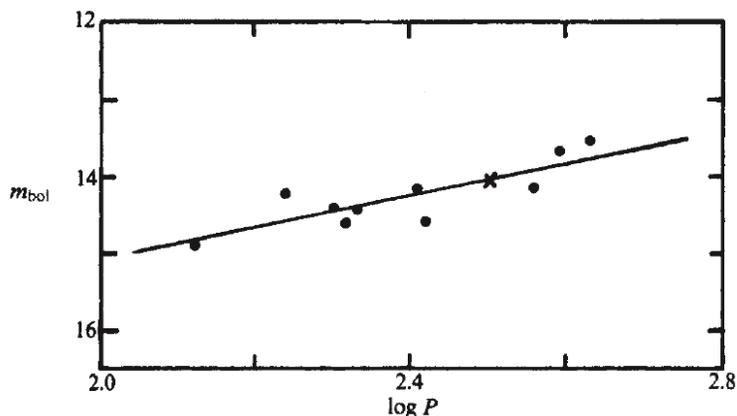
Figure 1.1: Empirical linear relationship between K-band magnitude and log of the period (in days) of Mira variables in the Large Magellanic Cloud. From [5]. *Nature*, 291:303, ©1981 Macmillan Journals Ltd., by permission.

from the lines of the s-process element technetium (Tc), which have been seen in Mira stars [e.g. 10–12, see Figure 1.2].

However, on the theoretical side, understanding of the true nature of these red giants did not start to emerge until the 1920's and 1930's. Eddington in 1926 proposed that probably hydrogen is converted to helium in the interiors of stars but it was only in 1939 that Bethe [see 13] and von Weizsäcker in 1938 [see 14], using advances in nuclear physics, were able to propose the pp-reaction and the CNO cycle, as the workhorses for energy production in stars. However, even at the time, it was not known how the red giants in the Hertzsprung-Russell (HR) diagrams came about. It was even surmised by von Weizsäcker, that perhaps red giants were young stars that were still contracting. This was not an unreasonable deduction, since young stars that are still contracting do indeed lie close to the giant stars on the HR diagram [e.g. 15]. The upshot of all this cumulative research was that red giant stars were peculiar and as yet unexplained and that there seemed to be two distinct categories of them.

It was only after the second World War, with the advent of more accurate photometry, that Arp, Baum and Sandage in 1953 [see 16] discovered that in a Hertzsprung-Russell diagram of a globular cluster that there appeared to be a "bifurcation of the red giant branch" (see Figure 1.3). It was shortly

3
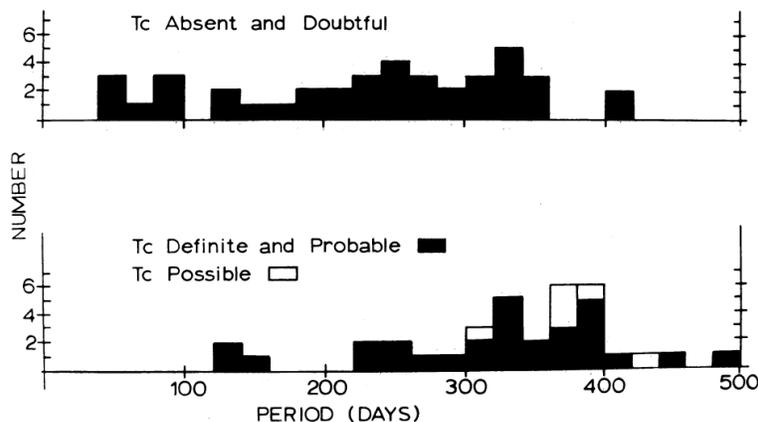
Figure 1.2: The first detection of Technetium in Mira variables confirming the occurrence of the s-process in AGB stars. From [11]. *The Astronomical Journal*, 84:13741383, September 1979. ©1979 American Astronomical Society (AAS). Reproduced by permission of the AAS.

thereafter that these objects were termed "asymptotic giant branch stars". In 1952, inspired by the fact that the red giant branch in the Hertzsprung-Russell diagram seemed to connect with the main sequence, Sandage and Schwarzschild [see 17] did an extraordinary thing. They analysed these stars not as young stars still contracting but rather as old stars that have exhausted their hydrogen supply in their cores and completely converted the cores to helium (see Figure 1.4). They were able to show with a set of hybrid models, representing different time epochs in the late evolution of an old main sequence star, that as the core contracted, the surrounding hydrogen envelope expanded by a large factor accompanied by an increase in luminosity. This was the first explanation of a red giant star that was close to the actual picture. This heralded a slew of papers and thereafter Hoyle and Schwarzschild in 1955 [see 18] showed that these stars evolved through the red giant branch to a maximum luminosity and then down to the horizontal branch. These discoveries were also among the first numerical models of the early part of post-main-sequence stellar evolution. Understanding of the next part of the evolution, after the horizontal branch, came about around a decade later.

Schwarzschild & Härm in 1965 [see 19] and Weigert independently in 1966 [see 20] saw what at first appeared to be numerical glitches in the models for
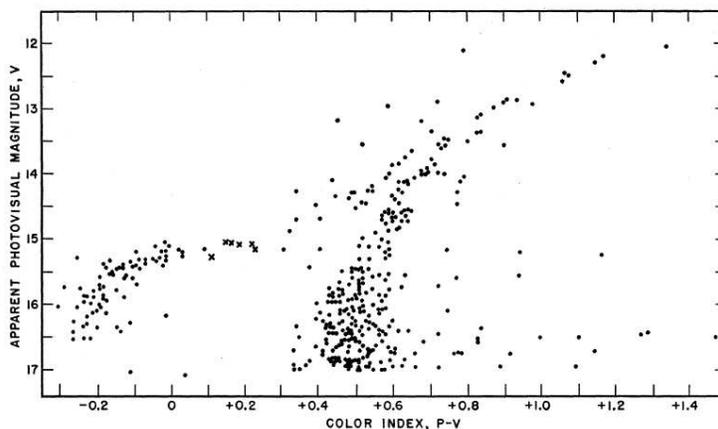
Figure 1.3: "Bifurcation in the Red Giant Branch". From [16]. *The Astronomical Journal*, 58:4, February 1953. ©American Astronomical Society (AAS). Reproduced by permission of the AAS.

red giant stars. It turned out that what they had discovered were the He-shell flashes that occur when the He-burning shell around the carbon-oxygen core approaches the inner edge of the hydrogen envelope. At this stage an instability develops and He-shell flash occurs, which was later termed a "thermal pulse". In a few years time, Schwarzschild & Härm [see 21] were able to show that after a number of such thermal pulses, a convective zone extending from the He-burning shell makes contact with the convective H-envelope sitting atop it. At this stage a greater amount of mixing ensues, ensuring that conditions become favourable for nucleosynthesis, as new elements may be brought upwards. Shortly thereafter, Sanders [see 22] argued that the s-process might work well under the conditions for He-shell burning.

The s-process, was first proposed by Burbidge, Burbidge, Fowler and Hoyle in 1957 [see 23] in their seminal study of nuclear reactions under astrophysical conditions. They labelled one particular chain of reactions the *s-process*, which involves a sequence of slow neutron capture events followed by β-decay. After Sanders' paper it was determined in a slew of papers that the short but repeating high-energy conditions in the He-burning layer in thermally pulsing (TP) AGB stars, appear to be efficient for nucleosynthesis via the s-process. However a significant amount of modelling was needed to delineate self-consistently, the conditions during a thermal pulse when the
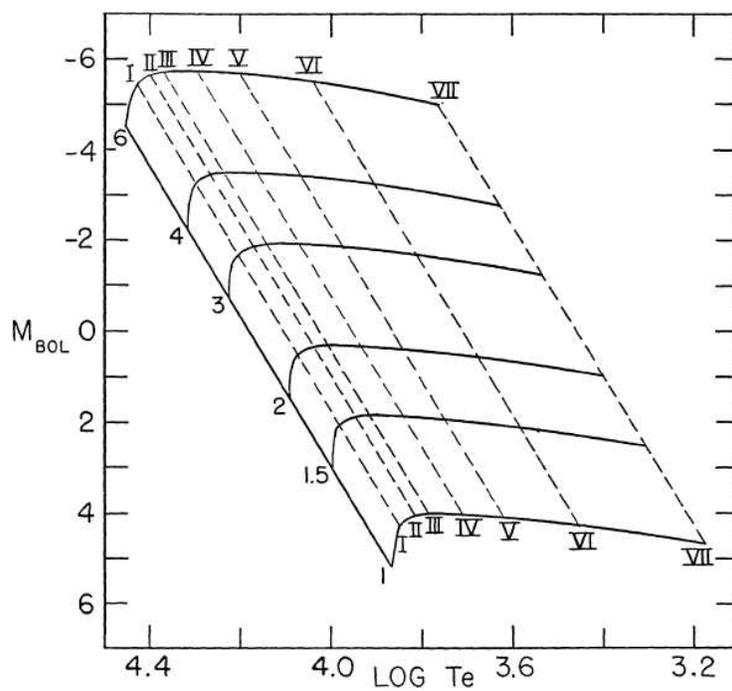
Figure 1.4: The first correct evolutionary models showing migration from the main sequence after core contraction. From [17]. *The Astrophysical Journal*, 116:463, November 1952. ©American Astronomical Society (AAS). Reproduced by permission of the AAS.

critical parts of the stellar structure were varying quite rapidly. These various models were in a large part made feasible primarily due the advent of greater and greater computing power. It was with such models that eventually in 1975, the seminal work of Iben [see 8] and Sugimoto and Nomoto [see 9] came about showing the importance of not only the s-process but also the 3α-process during the dredge-up events from the He-burning layer.

During the 1960's infrared astronomy really took-off in a big way, particularly in the United States, partly spurred by military interest. Gradually, observations were made possible at longer and longer wavelengths. There came a deluge of discoveries of strange objects with the landmark survey at 2.2μm; the IRC-survey by Neugebauer and Leighton in 1969 [see 24], where they found about 5000 objects, many of which were red giants that were "strangely" enshrouded in huge circumstellar envelopes (CSE) of dust. In some of these discovered objects the surrounding dust has such a large optical depth that the majority of the stellar radiation is emitted at wavelengths longer than 2.2μm. Thus it was seen that AGB stars came with CSE's many of which were carbon-rich. A little later in 1976, Price and Walker's catalogue of more that 2400 point sources detected between 4 and 28μm found even more fascinating, unique objects. These have been subsequently studied with a variety of instruments and wavelengths, and are now established to be post-AGB stars in various stages of evolution. Later the IRAS catalogue found a few hundred thousand such sources, thus providing a window into the future of perhaps the fate of our own sun, using observations of several AGB and post-AGB objects.

Around the same time in the mid- and late 1960's, radio astronomy was also coming into the forefront of observational science. Wilson and Barrett in 1968 [see 25] found a circumstellar line of the OH molecule, when observing the supergiant star NML Cyg at radio wavelengths. What was even more perplexing was that the line was so strong that it could only be attributed to maser emission. Contemporaneous observations found variability in such line emissions from similar objects that showed a variability of 300 to 1000 days, thus establishing maser emission from long-period variables.

The push to study these objects at even longer wavelengths using submillimetre and millimetre astronomy was made possible with the development of cryogenically cooled receivers and new high-precision antennae. The primary trouble being that at these wavelengths, the noise from thermal photons of the instruments were quite significant, thus advances needed to wait for reliable cryogenic technology to catch up. Using such instruments in the

1970's and 1980's several observations were carried out and many different molecules were detected. However, instrumental in furthering the knowledge regarding AGB stars, was the first detection by Solomon et al. in 1971 [see 26], of vibrational-rotational thermal transitions of the CO molecule, at 2.6 mm from the carbon star IRC +10216. Further observations using greater precision enabled estimates of the properties of the circumstellar envelopes, in particular the expansion velocities. Since then analysis of the CO line brightness maps from such stars, has become a very important tool in the study of CSE's of AGB stars and their mass-loss process.

The mass-loss process of stars was first proposed by Biermann in 1951 [see 27]. Later in 1967 Weber & Davis [see 28] and Mestel in 1967 [see 29] arrived at similar magnetohydrodynamic (MHD) models explaining the mass loss from our sun. The following chapter gives a brief chronological review of the state of MHD models. However in evolved stars, the evidence of circumstellar lines seen in M-type giants seemed to suggest that there must occur some form of mass-loss, but the exact mechanism that could lead to escape of material was not proven. The first evidence came as early as 1956, when Deutsch [see 30] observed the binary system $\alpha-$Her. His observations led him to conclude that the gas extended as far out as $2 \times 10^5 R_\odot$ from the MII spectral type giant, many orders of magnitude greater than the then suspected stellar radius of the object. He also found that the expansion velocity of the gas was about 10 km/s, enabling him to arrive at an estimate of the mass-loss rate of about $3 \times 10^{-8} M_\odot$ yr^{-1}, approximately a million times greater than the mass-loss rate of our sun.

In the early and mid-1960's, there were several observations giving indirect indications of mass-loss in stars, one such study was due to Auer and Woolf in 1965 [see 31] who found that in the Hyades cluster there are many white dwarfs below the Chandrashekhar limit of $1.4 M_\odot$ and many main sequence stars that were about $2 M_\odot$. Thus, presumably many such stars had lost at least about $0.6 M_\odot$, and Auer and Woolf's argument was that they should have been seen somewhere losing mass, but such stars had been missed somehow in observations up to that point. The question they asked was, what do stars look like when they are losing mass at a prodigious rate?

Following their observations in 1968, Gillett et al [see 32] and Woolf & Ney [see 33] in 1969, unveiled perhaps one of the most significant milestones in our understanding of AGB stars. They discovered for the first time an emission band around 10μm in the spectra of M-type giants, as due to emission from small particles of silicates (see Figure 1.5). After this seminal paper, came a
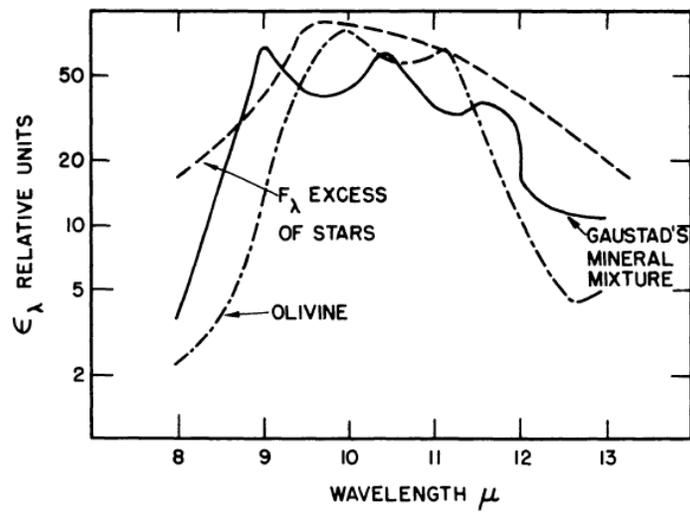
Figure 1.5: Fitting the excess radiation from AGB stars with emission from terrestrial mineral grains. The dashed line is the stellar spectrum. From [33]. *The Astrophysical Journal, Letters*, 155:L181, March 1969. ©American Astronomical Society (AAS). Reproduced by permission of the AAS.

great many investigations revealing observations of dust around several giant stars. From this cumulative evidence there began to emerge a picture that there were largely two types of dust grains; one produced by M-type giants and the other produced in carbon stars. These findings were instrumental in inspiring and cultivating an entire industry devoted to dust formation and dynamics in evolved stars. Nearly a decade after Auer and Woolf's initial findings, Reimers in 1975 [see 34] collected data on many giant systems and arrived at an empirical relationship relating the mass-loss rate ($\dot{M}$) to the stellar luminosity (L), mass (M) and radius (R); $\dot{M} \propto LR/M$, which would later come to be known as "Reimers' relation". Contemporary to these discoveries, Wickramasinghe et al showed convincingly in 1966 [see 35] that radiation pressure on graphite dust grains could not only drive dust grains outwards due to radiation pressure, but also that the dust grains would drag the surrounding gas along with them as they ploughed through stellar atmosphere. Later in 1976, Elitzur, Goldreich and Scoville [see 36, 37] developed the first spherical models for the CSE of an AGB star with matter flowing through it. They also explained the existence of the OH masers as due to infrared pumping of OH molecules that form from H_2O photodissociation in a thin molecular layer in the atmosphere of the star.

In 1981 Renzini and Voli [see 38] suggested that red giant stars experience a mild wind that gets more prodigious as they evolve further. Finally in the last TP-AGB phase a very dense "superwind" occurs, wherein they lose the majority of their mass. Evidence for the latter also came from maser emission revealing very high mass loss rates of about $10^{-4} M_\odot$ yr^{-1} [e.g. 39, 40].

This represents the cumulative data and understanding of AGB stars up to about thirty years ago. An excellent and oft quoted review of AGB stars was carried out by Iben and Renzini in 1983 [see 41] and the reader is referred to the same for further details. The following section relates the current-state-of-the-art with regard to our understanding of AGB stars and thus the work presented in the current thesis is motivated.

1.2 The Current State-of-the-Art in AGB Star Physics

AGB stars are presently understood to be a complex laboratory where the interplay of many kinds of physics governs the evolution of the star towards

its ultimate end. These objects are now thought to have a degenerate carbon-oxygen (C/O) core, surrounded by thin shells of nuclear burning of helium and hydrogen. The more massive AGB stars are thought to have oxygen-neon-magnesium cores [see 42]. AGB stars are now known to be efficient factories for nucleosynthesis producing elements via the s-process and thus play a crucial role in governing the metal enrichment of stellar systems and the interstellar medium.

Modern day understanding of the evolution of these stars is shown in Figure 1.6, which shows the evolutionary track of a $2M_\odot$ star that turns off from the main sequence as the supply of hydrogen in the core has been exhausted and converted to helium. Next the core begins to contract and hydrogen burning ignites in shells surrounding the He core. The star then evolves to the base of the red giant branch in the HR Diagram shown in Figure 1.6. While the core continues to collapse gravitationally, the energy released is deposited in the layers surrounding it, further heating the surroundings of the core. This results in an expansion of the giant on the whole and the luminosity of the H-burning shell increases greatly with energy input from the core and nuclear burning. Thereafter, the star proceeds upwards along the red giant branch (RGB) and during this time the envelope is convectively unstable. As the core contracts, at some stage the temperature is high enough to ignite He nuclear burning. Exactly when this occurs depends upon the initial mass of the star; see Figure 1.7. It appears from simulations of stellar evolution and structure that if the initial mass is less than approximately $1.8M_\odot$ then the He core has become electron-degenerate when the star evolves to the tip of the RGB. These stars experience a degenerate core He flash and settle afterwards in quiescent He-core burning on the zero-age horizontal branch (ZAHB). Initially more massive stars on the other hand, ignite He burning in the core in a nonviolent mode and thereafter their evolution proceeds along the horizontal branch [see 42].

Nuclear burning of He in the core leaves behind a C/O core that is surrounded by layers in which He- and H-burning occurs. Once the C/O core is formed, further evolution once more depends upon the mass of the star. It turns out that if the initial mass of the star is less than about $8M_\odot$ then carbon burning does not ignite, meaning that the temperature increase in the contracting C/O core is not enough to initiate C-burning. The C/O core then further contracts and becomes increasingly electron-degenerate, ultimately a nascent white dwarf. On the other hand, for the more massive stars, numerical simulations seem to indicate the C-burning is possible leading to further
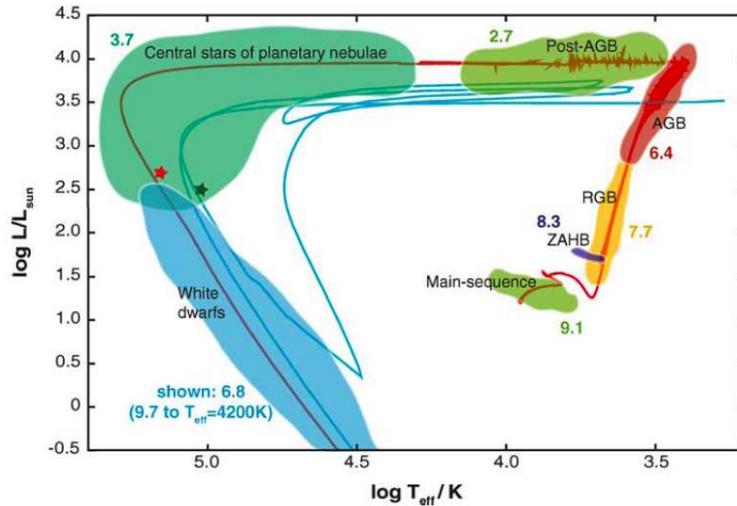
Figure 1.6: Stellar evolutionary track of at $2M_\odot$ star. The red and green stars are the locations of the central stars of the planetary nebulae of the different sub-tracks, red and blue respectively. These other tracks involve extra thermally pulsing phases during the post-AGB phase. The evolution proceeds upwards along the base of the RGB and then to the ZAHB. Afterwards the star proceeds upwards on the RGB and then the AGB phase. Later it enters the TP-AGB phase and after post-AGB evolution it finally forms a planetary nebula. The central compact object, the white dwarf then continues cooling downwards along the HR diagram. From [42]. *Annual Reviews of Astronomy and Astrophysics*, 43:435-479, September 2005, ©Annual Reviews, by permission.
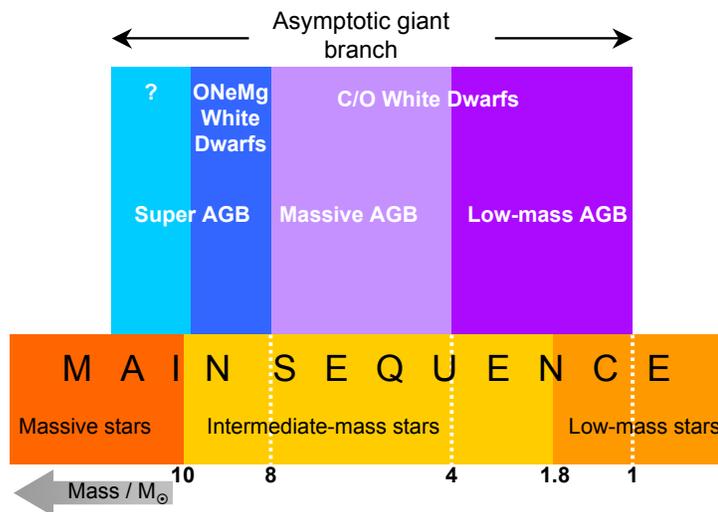
Figure 1.7: Classification of stars by initial main sequence mass (lower part) and AGB mass (upper part). Adapted from [42]. *Annual Reviews of Astronomy and Astrophysics*, 43:435-479, September 2005, ©Annual Reviews, by permission.

nucleosynthesis in the core.

At this stage the stellar evolution enters what is termed the early AGB phase which is characterised by the He shell which dominates nuclear production. This stage lasts a significant period of time ($10^4 - 10^5$ yrs) before the star enters the so-called thermally pulsing phase.

The He-burning shell is convective and burning occurs outwards until it it reaches the H shell surrounding it. Most of the inner He has been burned and there remains a layer of He burning just underneath the H-burning layer. Thus, nuclear energy release is dominated by the H shell. Since both the He-burning and the H-burning regions are convective, and in contact, this is a perfect breeding ground for instabilities. Thus, the predominant H-burning is interrupted periodically by thermonuclear runaway He-shell flash events that initiate a complex series of further convection and other mixing events (see Figure 1.8) that lead to greater dredge-up. The reader is referred to an article by Woosley, Heger and Weaver [see 43] for further details regarding the modelling that has been able to establish the nature of these explosions in relation to stellar evolution.

Finally as the star proceeds to evolve along the TP-AGB there occur greater and greater thermal pulses that render the star more and more convectively unstable. At some stage beyond the TP-AGB there ensues a "superwind" which is responsible for prodigious mass-loss leading to the star losing its envelope and it begins its post-AGB evolution. There exist many debates regarding the nature, cause and influence of the superwind in the final stages of AGB evolution. The reader is referred to the introduction of Chapter 3 for a brief discussion of possible superwind mechanisms with the relevant literature mentioned therein.

The brief description given above by no means does justice to the past three decades of research that has gone into formulating self-consistent models for AGB evolution. The reader is referred to a review by Willson [see 44] on the current understanding of the mass-loss process in AGB stars. Similarly for a review detailing post-AGB evolution see van Winckel [see 45]. Finally for a review of the current state-of-the-art that is presently emerging regarding the interior of AGB stars particularly in relation to the myriad nucleosynthesis reactions, the reader is referred to a review by Herwig (2005) [see 42]. The common thread tying all these different facets of an AGB star is the underlying mass-loss that it is undergoing. Indeed it is also one of the most important observable aspects, that gives us hints regarding the evolution of the AGB star itself. The mass loss process itself is tied to the wind
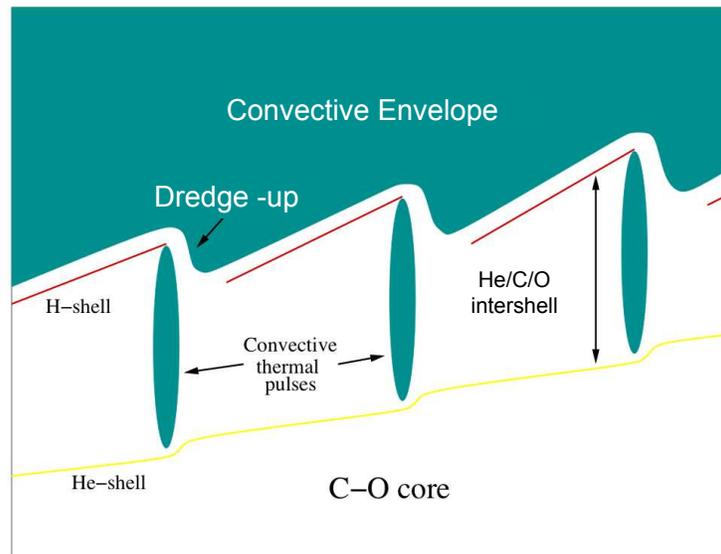
Figure 1.8: Thermal pulses causing dredge-up events. The evolution proceeds towards the right. The red solid line indicates the H-shell, while the yellow solid line represents the He-shell, below which is the C/O core. The solid green regions between the two shells are the zones of convection extending from the He-shell to the convective envelope atop the H-shell. These convective events cause dredge-up of material. Adapted from [42]. *Annual Reviews of Astronomy and Astrophysics*, 43:435-479, September 2005, ©Annual Reviews, by permission.

mechanism, which is closely related to the physics of the CSE and the inner atmosphere and indeed, the interior processes that modulate the physical conditions at the photosphere. For a brief chronological review of AGB star winds, the reader is referred to Chapter 3. The picture that has emerged from decades of simulations is that dust formation in the atmosphere is central to driving a stellar wind which is what is needed for mass-loss, without which an AGB star cannot evolve into a post-AGB planetary nebula and thence a white dwarf.

1.3 Justification and Scope

Somewhat parallel to the development of stellar evolution models that have succeeded in providing a detailed description of processes that govern the RGB and AGB phases, has been the modelling of stellar winds of regular main sequence, hydrogen burning stars. In recent years, many of the stellar wind models have incorporated magnetic fields, and MHD modelling of winds has made it possible to capture much of the non-linear dynamics at work in stellar effluxes [e.g. 46–48]. Many of the stellar wind models pertain to hot luminous stars, in which radiation pressure on the gas drives the wind [see 49, 50, for reviews]. The conditions for these winds require a hot plasma and recent efforts have been in the direction of multi-dimensional modelling with the effects of stellar magnetism incorporated self-consistently into the governing equations for fluid flow [e.g. 51]. The majority of these studies can trace their motivation back to numerical simulations of the complicated physics of the solar interior and adaptation of such modelling to rationalise observations of other stellar types has become an outstanding goal.

On the other hand, modelling the wind of cool evolved stars has focused for the most part on the microphysics of the dust grains [e.g. 52, 53]. A wealth of understanding has emerged not only from terrestrial experiments with dust grain nucleation and growth [see 54, 55, for reviews], but also from the immense efforts in both the theoretical and observational fronts for discerning the astrophysical conditions for dust grain growth in stellar atmospheres [see 56, 57, and references therein]. In tandem, the modelling of dust-driven winds has steadily progressed from simple spherically symmetric models to the current-state-of-the-art 2D hydrodynamic axisymmetric simulations that calculate radiative transfer on-the-fly through dusty shells [e.g. 58, 59]. These latter models incorporate the effects of stochastic dust

formation although grain growth is assumed to occur by a much simpler mathematical prescription. There have also been efforts directed at simulating non-spherical dust-driven winds that have complemented these efforts significantly [e.g. 60]. The reader is referred to a summary of the literature provided in Chapter 3 for details regarding the current state-of-affairs in this field of study.

Furthermore, the study of stellar magnetism, a field unto itself, whose history can be traced back to the study of sunspots and geo-magnetism [see 61, for a review], has played a key role in spurring observations of magnetic fields in stars. These studies further inspired modelling the role that the solar magnetic field may play in various aspects of solar phenomena such as granulation of the solar surface, sunspot cycles and flares [see 61]. The unequivocal and resounding inference that emerged from this cumulative effort was that an understanding of magnetohydrodynamic processes was key to unlocking several aspects of solar physics.

The search for solar-type activity in other stars yielded dividends with the first discovered stellar magnetic fields in a late-type star other than the sun by Robinson et al in 1980 [see 62]. Shortly thereafter came discoveries of a magnetic field in a cool giant [see 63] and in a T Tauri star [see 64]. In later years several objects were discovered to have magnetic fields based on similar Zeeman observations. These discoveries were quite remarkable because they established a much sought after link. As early as 1969, Richards and Comella [65] measured the rotation period of the pulsar NP 0532, and this object was used to theorise the slow-down of rotating magnetised neutron stars by Gold [66]. In that year, independently Pacini [67] had also published a paper theorising similarly that the magnetic fields in neutron stars were probably decaying with time, thus motivating the slow-down of rotating pulsars. Within a year, strong magnetic fields were then found in compact objects; circular polarization studies of magnetised white dwarfs by Kemp et al in 1970 [see 68], revealing that some of these objects have rather high magnetic fields ranging from 10^6 to a few 10^8 G, or more. Then a few years later came conclusive evidence for even stronger fields in compact objects which were found in neutron stars [see 69, 70]. Thus an important part of the puzzle was then revealed, that the remnants of stellar evolution can contain significantly high magnetic fields, and this naturally provoked the question, *do their progenitors, cool giant stars, then have dynamically important magnetic fields as well?*

An important step in this direction came in 1975 (incidentally, a year

before OH masers were explained by Goldreich and Scoville [see 36]) when Johnson and Clark [see 71] made the first complete SiO linear polarisation observations of some evolved stars. This study gave hints that it is possible to ascertain the existence of magnetic fields by studying polarised emission from evolved stars. However, the breakthrough came only recently, when Diamond and Kemball in 1997 [see 72] obtained the very first image of the magnetic field of a star using circular polarisation arising from SiO masing regions within a few stellar radii of the Mira-variable TX Cam. This study unambiguously revealed that significantly strong magnetic fields may exist in cool giants, with the detection of a $5 - 10$ G field in inner atmosphere of TX Cam, at a distance of about $5 - 10$ AU from the stellar photosphere.

Since then several maser polarisation studies have been carried out that find a large variety of magnetic field strengths at the distances of all three kinds of cool giant masers; OH, H_2O, and SiO. The range of magnetic fields inferred in these stars then ranges from a few milligauss to a hundred gauss or so [e.g. 73–79, also see reviews in Chapters 3, 4 and 5]. Moreover, in a recent study, Auriere et al [see 80, 81] have found unambiguous evidence for a 1 G field in the red supergiant Betelgeuse and there exist hints of a magnetic field in the star Mira from SiO maser polarisation observations [e.g. see 82].

These findings show that magnetic fields are present in AGB stars. However, to the best of the author's knowledge, there exist no investigations in the literature that combine the effects of a magnetic field with the well understood dust-driving mechanism for modelling the wind of an AGB star, i.e., a hybrid MHD-dust-driven wind scenario. This represents a shortcoming in the understanding of AGB star physics that this thesis hopes to address. Here we investigate the implications of a stellar magnetic field on the dust-driven stellar wind in not only low- and intermediate-mass AGB stars but also at the high mass end; cool evolved supergiants. This covers the entire spectrum of cool giants shown in Figure 1.6. The aim of the work is to ascertain *whether it is possible to have a hybrid wind scenario in which both MHD effects and dust-driving can produce a combined outflow?*

As discussed earlier, towards the end of the AGB phase the star is convectively unstable and goes through a phase of frequent thermal pulsations, just prior to the onset of the superwind. This stage of the AGB phase is quite poorly understood, however, the aim of the current work is to provide a hybrid mechanism at the *early stages of the AGB*, long before the onset of the thermally pulsing phase. The hope is to lay the groundwork upon which more complicated dynamical hybrid models may be constructed to

ultimately enable the tackling of the TP-AGB phase.

To this end we develop, as a first approximation, the simplest possible hybrid-MHD-dust-driven wind model (Chapter 3), by combining a classical Weber-Davis type magneto-rotational wind with the standard dust-driving picture, modelling a steady-state outflow. This general model is then applied to particular stars. We chose to model the two stars that were in a large part responsible for human interest in evolved stars; Betelgeuse (Chapter 4) and Mira (Chapter 5), both of which come with their own accoutrements of mysteries.

The final end product of the evolution of these two particular stars will likely be a neutron star for Betelgeuse and a white dwarf star for Mira. The run-of-the-mill neutron stars can have magnetic fields on the order of about 10^{11} G or more [e.g. 83], while white dwarf stars can have fields ranging from $10^6 - 10^9$ G or so [e.g. 83] such as in white dwarfs like PG 1031+234 and SDSS J234605+385337 where fields around 10^9G have been observed [see 84–86, and references therein]. Figure 1.9 shows observations of the object PG1015+014 by Euchner et al [see 87] and Figure 1.10 shows a greater resolution spectrum of the same object obtained by Jeremy S. Heyl. This white dwarf has a field of about 10^8G, which was inferred from the Zeeman shift in the spectral lines [see 87].

In order to facilitate a proper examination of the spectra of such highly magnetised objects it is necessary to have data for the structure of atoms in strong magnetic fields. There exist only a few investigations in the literature for atoms in strong magnetic fields, and only for the low-Z elements such as H, He, Li etc. Even then, this data is limited to only a few states. For example, there exist only a handful of studies in the literature for the Li atom, and many of the tightly bound states in strong magnetic fields have not been investigated, in particular the so-called negative parity states (see review in Chapter 6). Moreover, in many cases the computational overhead is quite high, particularly in terms of computing time, such as when using a finite-element based approach for 2D atoms in strong fields [e.g. 88] or the method of solution is burdened with many layers of computational complexity [e.g. 89, 90]. Therefore, a secondary goal of this thesis is to formulate a straight-forward computationally fast and efficient method of solution for determining the atomic structure of 2D atoms in the strong magnetic fields. The ultimate aim is to facilitate spectral analysis of magnetised white dwarf stars and neutron stars.

To this end a pseudospectral method based approach (see Chapter 6)
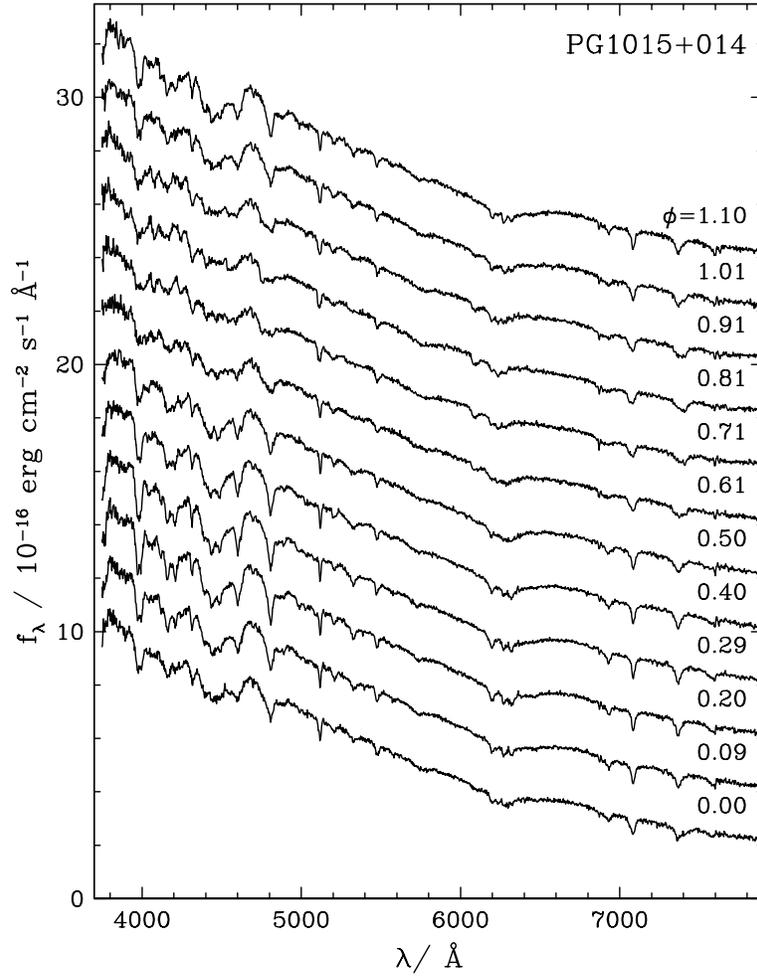
Figure 1.9: The spectrum of magnetised white dwarf PG1015+014. The quantity ϕ represents rotational phase of the object. Credit: Fabian Euchner [87], *Astronomy and Astrophysics*, 451, pp 671-681, 2006, reproduced with permission ©ESO.
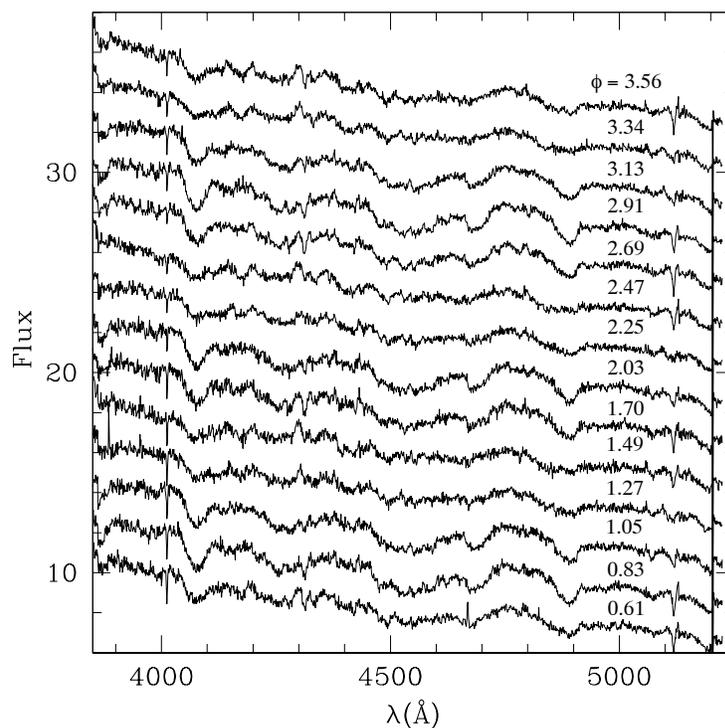
Figure 1.10: A greater resolution spectrum of the magnetised white dwarf star PG1015+014. Courtesy Jeremy S. Heyl. The ordinate axis values are scaled in units of 10^{-16} erg cm^{-2} s^{-1} $\AA^{-1}$. The quantity ϕ represents rotational phase of the object.

for solving the Hartree-Fock equations [e.g. 91] is formulated. This study represents an extension of two earlier studies carried out by the author, Refs. [88, 92] and investigates the atoms He and Li in strong magnetic fields.

Thus overall, this thesis aims to study the implications of a magnetic field in the late stages of stellar evolution.

1.4 Thesis Outline

The work carried out as a part of this thesis is organised as follows. Chapter 2 very briefly introduces the concepts of stellar winds in a rudimentary manner. An isothermal stellar wind is considered and the chapter also provides the a short description of the topology of solutions, in particular the critical point in the model. Thereafter chapter 3 describes a general hybrid MHD-dust-driven wind model that is developed for intermediate-mass AGB stars. As mentioned earlier, our aim is to ascertain whether it is feasible to formulate such a hybrid picture. For this purpose the modelling adopts a rather simplified prescription and we restrict our attention to an axisymmetric wind in the equatorial plane. The formulation of the model is described in detail in Section 3.2. The dust is treated in a simple manner, by assuming that it forms at a certain distance from the photosphere where the temperature falls below the dust condensation temperature. The details of forming the dust and inclusion of a coupled dust momentum equation are again given in Section 3.2. The numerical procedure that is developed for solving this coupled system of gas and dust outflow alongside magneto-rotational effects are described in detail in Section 3.3.

Thereafter in Section 3.4 we present the results of the hybrid-MHD-dust-driven wind model and the key features of the modelling are discussed. The entire topology of the family of solutions are discussed and compared with standard dust-driven stellar winds as well as with magneto-rotational winds. A discussion regarding the question of photospheric spots can also be found therein. The contribution to the energy carried by the efflux by its different components are also shown and discussed in length. Finally in Section 3.5 the findings of the study are summarised and a brief discussion is provided with regard to the avenues for future work. The primary conclusions drawn are that there are two types of hybrid models that are physically viable, the first in which dust forms within a few stellar radii, and the second in which dust forms at a great distance, a few tens of stellar radii away from

the photosphere. We also discuss the possibility of forming dust in a more realistic way (in-situ) and motivate the need for time-dependent modelling. We also comment on the importance of pulsation and motivate the need for including such effects in future models.

After having formulated a steady-state dual-fluid MHD-dust-driven wind theory, we test the feasibility of the theory by applying it to particular stars; we model the wind of the red supergiant star Betelgeuse in Chapter 4. In doing so, we extend the framework of the theory to encompass high-mass red giants; these have cool outer atmospheres with dust condensation. The primary reason that makes Betelgeuse an interesting candidate is that observations indicate very little dust interior to about $30R_0$, where R_0 is the photospheric radius. Thus, our objective was to test the second type of hybrid model derived in Chapter 3, in which dust forms a great distance from the photosphere. A review of the literature focussing on the wind and the atmospheric properties of Betelgeuse is provided in Section 4.1. The salient features of the model that pertain to Betelgeuse, are then provided in Section 4.2, with direct comparisons to intermediate-mass AGB stars. The numerical optimisation method developed for modelling the wind of Betelgeuse is provided in Section 4.3. Then in Section 4.4, different dust formation scenarios are discussed for Betelgeuse, largely motivated by recent findings that indicate the possibility of forming alumina close to the photosphere. We additionally consider scenarios in which alumina both forms and later, undergoes spallation in the wind. Finally in Section 4.5 the findings of the study are summarised.

The hybrid MHD-dust-driven wind theory developed in Chapter 3 is then applied to the star Mira in Chapter 5. Mira is a star in the early stages of the AGB. It is a low-mass AGB star, thus modelling the wind of Mira, enables us to extend the theory to the low-mass end of the spectrum of AGB stars. Thus with this investigation we cover all three mass ranges shown in Figure 1.7. Mira is a very different star in comparison to Betelgeuse, it is about 10 times less massive, it is also thought to be spinning a little slower in comparison and there are recent hints of magnetic activity in the atmosphere of the star. In contrast to Betelgeuse, dust formation occurs within a few stellar radii of the photosphere in Mira. Thus, one of our aims was to apply a hybrid wind model of the first kind, described in Chapter 3, with dust forming in the inner reaches of the atmosphere, close to the photosphere. A short review of the relevant literature on the nature of the wind of Mira and its atmosphere, is provided in Section 5.1. The details of the model for Mira's wind alongside

a brief description of the numerical methodology are described in Section 5.2. The results of the modelling are discussed in Section 5.3. Since neither the surface magnetic field strength nor the rotation rate are exactly known for Mira, these were treated as variable parameters. Estimates are provided for these variables that yield modelling results consistent with observations. Thereafter the findings are concluded in Section 5.4.

Thus overall, Chapter 3 describes a novel hybrid stellar wind model, and the findings indicate that two types of hybrid MHD-dust-driven winds are possible. Each of these models are then tested by applying them to particular stars; Betelgeuse and Mira, in Chapters 4 and 5 respectively. Thus the feasibility of combining a dust-driven wind picture with magneto-rotational effects is fully explored for different types of cool evolved red giant stars.

Chapter 6 then explores an altogether different question. As mentioned earlier, the fate of Betelgeuse is likely a neutron star and that of Mira, is a white dwarf. It is also known that these objects can be highly magnetised. The lowest magnetic fields in neutron stars are seen in the so-called recycled millisecond pulsars, and these objects can have fields upwards of about 10^8 G or so. While the most magnetised white dwarfs that are presently being discovered, have fields well in excess of 10^9 G or so. As a result, observations of these objects that rely upon an analysis of their spectra, require accurate estimates of the energy levels of various atoms in intense magnetic fields. This would enable a correct interpretation of the different features seen in the spectra of these objects. However, there are very few studies in the literature for atoms with more than two electrons in intense magnetic fields, namely Lithium, Beryllium, Boron etc. The studies that have been carried out so far, merely restrict themselves to the so-called positive parity states. In addition, many of these studies are computationally intensive and burdened with approximations that add to the computational complexity of the problem. Thus the aim of the study described in Chapter 6 is two-fold. First, we formulate a fast and efficient method of solution of the problem of low-Z atoms in intense magnetic fields employing pseudospectral methods. The key enabling advantage of this method is that is computationally straight-forward and drastically reduces computational time without sacrificing accuracy. Second, the prototype atomic structure code developed as a part of this study, is compact and thus can be directly employed in atmosphere models of white dwarf stars and neutron stars. This would enable computation of the energy levels of different atoms on-the-fly with little computational overhead; the calculations would yield accurate results within a

matter of a thousand seconds or so.

Section 6.1 details the relevant literature in the field of atomic structure in intense magnetic fields and motivates the study described in Chapter 6. Thereafter, the particular 2-dimensional cylindrical form of the Hartree-Fock equations are provided in Section 6.2 with definitions of different parameters. The pseudospectral method is described in great detail in Section 6.3 with explicit examples delineating the method of implementing boundary conditions for both the one- and two-electron problem. The numerical details for solving the resulting coupled algebraic eigenvalue problem is described briefly in Section 6.4. The results obtained in the study are presented alongside a discussion in Section 6.5. There we provide data for two states of the lithium atom, that have not been studied thus far in the literature. Finally, in Section 6.6 the findings are summarised and the avenues for improving the prototype software are discussed in detail, with particular emphasis on adopting a parallel implementation of the algorithm.

Finally, the entire body of work described in this thesis is summarised in Chapter 7 and a brief version of all the different avenues for future work can be found therein.

Chapter 2

The Parker Wind

In this chapter a very brief introduction is provided to the topic of stellar winds. Please note that the discussion that follows is in several textbooks and is therefore intended as a description at a very rudimentary level. The reader is referred to Ref. [93] for further details and references.

We shall restrict our discussion to a wind from a hypothetical star in which the gas is assumed to be isothermal and is subjected to only two forces, the gravity of the star that pulls the gas in towards the centre, and the gas pressure that has a negative radial gradient, such that it opposes gravity. When these two forces are equally balanced, then the situation resembles a hydrostatic atmosphere. Concordantly, when there is an imbalance, there occurs a situation of either gravitational collapse, or one of an outflow of material from the star − a stellar wind. We shall be interested in the latter. Furthermore, we shall, for the sake of conveying a rudimentary picture, restrict ourselves to a spherically symmetric one-dimensional model.

There are three basis conservation laws that can be imposed on the fluid flow. Namely, conservation of mass, momentum and energy. Each of these results in an equation that describes the relevant physical quantities in the motion of the gas. For the case of a time-independent stellar wind with a constant mass loss rate, we can write,

$$\frac{dM}{dt} = 4\pi r^2 \rho(r) v(r).$$ (2.1)

This equation conveys that the amount of gas passing through a spherical shell at any given distance r is constant. The motion of the gas in a stellar wind is given by Newton's second law and can be written as,

$$f = \rho \frac{dv}{dt},$$ (2.2)

where f is the force per unit volume and therefore, f/ρ is the force per unit mass residing in a unit volume. We can write a velocity gradient for the fluid

element that is accelerated in a stellar wind as,

$$\frac{dv(r,t)}{dt} = \frac{\partial v(r,t)}{\partial t} + \frac{\partial v(r,t)}{\partial r}\frac{dr}{dt} = v(r)\frac{dv}{dr}. \tag{2.3}$$

The last equality in Eq. (2.3) comes about because in a stationary time-independent stellar outflow, the wind velocity at any given distance does not change with time. Therefore the quantity $\partial v(r,t)/\partial t = 0$ and, since we are dealing with a spherically symmetric picture, we can replace $\partial v(r,t)/\partial r = dv/dr$ and $dr/dt = v(r)$. As mentioned earlier, the only forces at work in this hypothetical star are those of gravity and the pressure gradient of the gas itself; these two forces oppose each other. The imbalance of these two forces is essentially the force on the gas accelerating it outwards. Therefore we can write,

$$v\frac{dv}{dr} + \frac{1}{\rho}\frac{dp}{dr} + \frac{GM_*}{r^2} = 0. \tag{2.4}$$

This equation describes momentum conservation in the flow and is therefore simply known as the *momentum equation*. The difference between the pressure gradient (second term) and the gravity (third term) produces acceleration in the wind (first term).

Finally, the third basic concept, conservation of energy is embodied in the simple equation,

$$T(r) = T = \text{constant}, \tag{2.5}$$

since the thermal structure in the wind is assumed to be somehow maintained. If we assume that the gas is also ideal, then we can employ an ideal gas equation of state for closing the equations.

$$p = R\rho T/\mu, \tag{2.6}$$

where R is the gas constant and μ is the mean atomic weight of the gas expressed in units of hydrogen mass. Using Eq. (2.6) the pressure gradient can be expressed as,

$$\frac{1}{\rho}\frac{dp}{dr} = R\mu\frac{dT}{dr} + \frac{RT}{\mu\rho}\frac{d\rho}{dr} = \left(\frac{RT}{\mu}\right)\frac{1}{\rho}\frac{d\rho}{dr}, \tag{2.7}$$

where we have employed the conservation of energy equation (2.5) to eliminate the gradient of the temperature in Eq. (2.7). The unknown quantity

$d\rho/dr$ can be expressed using the mass continuity equation in the form of a derivative as,

$$\frac{1}{\rho}\frac{d\rho}{dr} = -\frac{1}{v}\frac{dv}{dr} - \frac{2}{r}. \tag{2.8}$$

Substituting Eqs. (2.7) and (2.8) into (2.4) then yields,

$$v\frac{dv}{dr} + \frac{RT}{\mu}\left\{-\frac{1}{v} - \frac{2}{r}\right\} + \frac{GM_*}{r^2} = 0, \tag{2.9}$$

which can be rearranged to give the velocity gradient as,

$$\frac{dv}{dr} = v\left\{\frac{2a^2}{r} - \frac{GM_*}{r^2}\right\}\Big/\left\{v^2 - a^2\right\}, \tag{2.10}$$

where a is the speed of sound given by,

$$a = (RT/\mu)^{1/2}. \tag{2.11}$$

Equation (2.10) above is the celebrated Parker stellar wind model. The topology of the family of solutions of this differential equation are discussed at length in several textbooks, here we shall provide a short description of the salient features. There is a critical point in the phase-space of the differential equation in Eq. (2.10), namely the sonic point. Upon examining the equation it is evident that at a certain critical radius, $r = r_c$, the velocity of the wind becomes equal to the speed of sound, $v_c = a$. This point is unique in the phase-space as at this location (r_c, v_c), both the numerator and the denominator of Eq. (2.10) identically vanish. The critical distance from the photosphere at which this occurs is obtained by setting the numerator equal to zero. We thus obtain $r_c = GM_*/2a^2$.

The topology of solutions is shown in Figure 2.1. Of key interest is the critical solution which starts off at the base of the wind, the photosphere, sub-sonic. The wind then gets accelerated through the sonic point and then emerges super-sonic at large distances from the star. The other solution that passes through the sonic point is a Bondi-type solution, in which material is in-falling; it starts off sub-sonic at large distances, gets slowly accelerated until it passes through the sonic point. Thereafter it becomes super-sonic rapidly and plunges into the photosphere at super-sonic speeds. The Bondi solution cannot be interpreted as a wind solution, as a wind cannot be super-sonic at the photosphere. The family of solutions just below the critical point
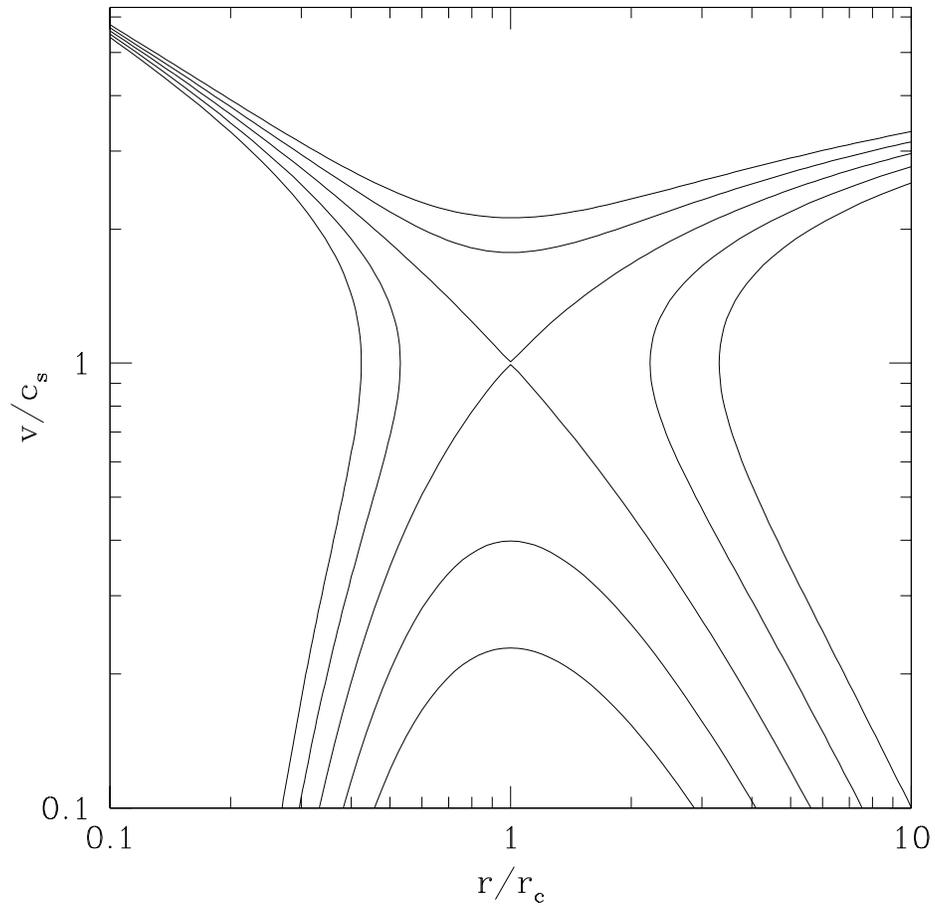
Figure 2.1: Isothermal Parker wind model. The critical point is located at the sonic point. $c_s = v_c = a$ is the speed of sound in this model. The critical point is an X-type singularity. Courtesy: Jeremy S. Heyl.

that form inverted-U's are the so-called failed wind solutions. These solutions start off at the photosphere with speeds just slightly lower than that of the critical solution. As a results they are unable to pass through the X-type singularity. At the critical radius, they therefore have sub-sonic speeds and are not able to escape the star. As a result the velocities of these wind solutions diminish to zero in the limit of large radial distances.

The family of solutions above the critical point that form broadened-U's belong to a different set of unphysical solutions. These are generally interpreted as either unphysical wind solutions that start off super-sonic at the photosphere, get mildly decelerated but still leave the star super-sonic. Once again such an interpretation is an unphysical wind, as a physically viable wind cannot be super-sonic at the photosphere. The other possible interpretation of these solutions is that it is an accreting solution, one in which material is heading towards the star at super-sonic velocities, gets mildly decelerated as it has to negotiate its way through the region in the vicinity of the singular point, and thereafter gets accelerated to higher and higher Mach numbers, before plunging into the photosphere.

The family of solutions in the region to the left of the critical points are unphysical double-valued solutions. These solutions start off at the photosphere sub-sonic, but still with velocities slightly greater than the critical solution. As a result, they overshoot the critical solution, becoming super-sonic inside the critical radius. However, since these are double-valued, they cannot be interpreted as physical solutions. The same applies to the family of solutions in the region to the right of the critical point.

Thus, we see that the topology of the solutions of the differential equation for the gas velocity profile, in an isothermal stellar wind, is quite interesting. The critical point is important because if a wind must leave the star then it must become super-sonic at exactly the right distance from the star, the critical radius r_c. As a result, there is only one unique physical wind solution and that is called the critical solution. The reader is asked to keep this discussion regarding the topology of solutions in mind, since the following chapter that details a hybrid AGB wind, is not only a generalisation of the Parker stellar wind, but also incorporates magneto-rotational effects. As a result, the topology of solutions has other critical points, in addition to the sonic point that has been discussed here.

This concludes our brief introduction to the Parker stellar wind model. In the following chapter, we shall provide a literature review of the topic of stellar winds of AGB stars as well as magnetohydrodynamic wind models

that incorporate magneto-centrifugal effects. Motivation is provided for the need for combining magneto-rotational effects with that of radiation pressure on the dust grains of an AGB star and thereafter a hybrid AGB wind model is developed and the solutions and implications are discussed at length.

Chapter 3

A Hybrid Steady-State Magnetohydrodynamic Dust-Driven Stellar Wind Model for AGB Stars [†]

3.1 Introduction

In recent years several observations of evolved stars and planetary nebulae have indicated that magnetic fields may exist in these objects [see for e.g. 73, 94–98]. The inferred magnetic fields in such objects, at the distances of the masers, indicate a variety of field strengths ranging from a few milligauss to a hundred gauss or so [see 74]. This in turn, may indicate a variety of field strengths at the surfaces of such objects. The idea of studying the effects of a magnetic field on the nature of the AGB wind has been carried out mainly with regard to explaining the diversity of the observed shapes of planetary nebulae [e.g. 99, 100, and references therein]. As a result, the modelling of magnetic fields in these stars has focussed on the final stages of the AGB phase, at the very tip of the AGB, or on the post-AGB phase itself, employing the so called interacting wind scenario [see 101–103, for outlines of the key points of interacting wind models].

It has therefore been argued that magnetic fields play a vital role in shaping planetary nebulae by several researchers. Pascoli [104] investigated a spherically symmetric time-independent model for the gas outflow, with randomly generated frozen-in magnetic fields that obeyed a power-law distribution in the outflow. He found that it was possible to generate gas ejection using such a mechanism. Later, the implications of having a magnetic field in

---

an AGB star were investigated at the very end of the AGB phase by Pascoli [105], thereby affecting the morphology of the planetary nebula formed. The origin of magnetic fields in circumstellar envelopes has also been investigated employing a magnetic dynamo in the degenerate cores of AGB stars at the very tip of the AGB [e.g. 106]. Additionally, three-dimensional steady-state ideal MHD models have also been constructed to investigate production of the superwind at the very end of the AGB phase [see 107]. Elsewhere, it has been argued that magnetic fields may play a dominant role in shaping planetary nebulae through magnetised wind bubbles [e.g. 108–110], where they explore, within the framework of the interacting wind model, at the end of the AGB phase, the idea that a shocked portion of the wind (a bubble) in the envelope has an enhanced magnetic field and is responsible for shaping the planetary nebula. Gardiner and Frank [103] and García-Segura et al. [111] have studied magnetic collimation in the outflows of TP-AGB and post-AGB stars using the magnetic wind blown bubble model. Meanwhile, full MHD simulations for post-AGB stars have been carried out in two and three dimensions to include the effects stellar rotation and photo-ionisation of the gas in an effort to produce collimated outflows [e.g. 112–117] for rationalising the shapes of planetary nebulae with jets or ansae. Garcia-Segura et al. [118] have also studied the effect of solar-like magnetic cycles on the slow wind of an AGB star with the aim of producing concentric rings in the spherically symmetric outflow, as have been observed around a few planetary nebulae [e.g. 119]. Their simulations were able to qualitatively reproduce such features. Matt et al. [120] have been able to show that, in AGB stars with dipolar magnetic fields, it is possible to have disk formation, wherein the plasma is deflected preferentially towards the equator. They find in their MHD simulations, that dense equatorial disks are formed for dipole fields of only a few gauss at the stellar surface. They argue that this may be relevant for shaping planetary nebulae.

All of the above mentioned models advocate a more or less global dynamical role to the magnetic field, in shaping the outflow towards the end of the AGB phase. Soker and co-workers, on the other hand, advocate a locally enhanced magnetic field, such as in the magnetic-cool spots of the sun, to play a key role in shaping asymmetric outflow [e.g. 121–126]. They find that dust formation is enhanced locally above magnetic-cool spots and thus, mass loss is facilitated due to radiation pressure on the dust, which in turn, has formed closer to the stellar surface. Thus asymmetries arise in the mass loss from an AGB star at the end of the AGB phase. It has also been shown

33

that the presence of a binary companion to an AGB star can be crucial for shaping planetary nebulae [see for e.g. 127–130].

Mastrodemos and Morris [131, 132] performed a quantitative study using smooth particle hydrodynamics, exploring the question of the effect of a binary companion on the winds of an AGB star. They found that they were able to qualitatively reproduce many of the elliptical, bipolar and quasi-spherical morphologies of planetary nebulae; however, the effects of magnetic fields on the outflows were not included. Soker [133] examined the question of whether accompanying planets can help form elliptical planetary nebulae. He found that if the planet is large enough then it can deposit a significant amount of angular momentum in the AGB star and spin it up, triggering magnetic activity that will lead to the formation of magnetic-cool spots, thus resulting in axisymmetrical mass loss. Additionally, Soker [134, 135] investigated the effect of having solar-like cycles in an AGB star and the results show that such magnetic activity will enhance spot formation, leading to asymmetric mass loss and thus he is also able to rationalise the multiple arcs and rings that are seen in some planetary nebulae. Soker [136] has also studied the effect of density inhomogeneities, with regard to its effects on radiative transfer in the later stages of the AGB phase. These effects result in instabilities in the flow giving rise to inhomogeneities in the mass loss process itself.

From the brief review presented above, it is clear that magnetic activity in AGB stars is quite important, whether it plays a global or a local role is not completely certain; however, both types of studies are able to reproduce or rationalise many of the key features observed in the shapes of planetary nebulae. However, none of the full 2- and 3-D MHD models described above take into account the effect of radiation pressure on the dust grains in the envelope of an AGB star. It is generally thought that the mass loss in AGB stars is largely governed by this mechanism coupled with strong stellar pulsations [e.g. 93, 137–142]. However, to the best of our knowledge, there have not been any investigations combining a standard dust-driven wind scenario with MHD effects, in the literature. Such a study, given the importance of magnetic activity in AGB stars, would help bring together two different sub-classes of stellar winds. This is the aim of the current study; to investigate the implications of combining magneto-rotational effects with a dust-driven wind in AGB stars. It is to be mentioned that this would be applicable at the early stages of the AGB phase, long before the interacting wind scenario becomes important, wherein the models described above would be more likely

candidates for describing the outflows.

At this juncture, we conduct a brief survey of the available literature with regard to both dust-driven winds and magneto-rotational equatorial winds. However, the reader is referred to a review by Tsinganos [143, and references therein] for MHD outflows and likewise, reviews by Dorschner [144] and Habing and Olofsson [145] for historical reviews of AGB stars and dust-driven winds. Thereafter, the model developed in the current study, is elucidated.

With regard to magneto-rotational equatorial winds, seminal work was carried out by Weber and Davis [28, hereafter WD]. They formulated a steady state description for the radial and azimuthal components of the solar wind's momentum. Essentially the same results were also arrived at independently, by Mestel [29]. These studies formed the groundwork upon which further studies were conducted. Thereafter, magnetic braking by a stellar wind was also investigated by Mestel [146] and later in greater detail by Okamoto [147, 148], wherein the theory was extended to cover a variety of field configurations with poloidal fields. The Weber and Davis equatorial wind theory was extended by Goldreich and Julian [149] towards a relativistic treatment of the wind, including the effects of pressure and gravitation. Michel [150] carried out a similar analysis of the WD model but neglected pressure and gravity and thus, relativistic magnetosonic critical points do not appear in his model. The first effort to investigate the importance of the interactions between the gas and the magnetic field, with regard to determining properties of the structure and dynamics of the solar corona, was carried out by Pneuman and Kopp [151]. They found that the assumed dipolar field configuration had a profound effect on the solar wind in creating streamers. Yeh [152] conducted a parametric study of the mass and angular momentum effluxes of magneto-rotational stellar winds and found that the mass efflux would be large, if the mass of the star was small, with a large radius, provided the stellar corona was dense and hot. Simultaneously, he found that the angular momentum efflux became greater when the magnetic field and stellar rotation parameters were increased. Belcher and MacGregor [153] revisited the Weber and Davis theory and identified two regimes; the so-called slow and fast magnetic rotators, which are defined by the ratios of the Michel and Parker velocities of the wind. The former is related to the ratio of the magneto-rotational flux to the mass flux and the latter is related to the squares of the sound speed, escape velocity and radial bulk gas velocity at the surface. Presently, the reader is referred to Belcher and MacGregor [153]

for mathematical expressions for these quantities. Belcher and MacGregor were able to delineate the angular momentum evolution of the two types of rotators on the main sequence. Barker and Marlborough [154] extended the Weber-Davis theory for the case of non-zero photospheric mass loss, showing that including a dimensionless constant corrected the original theory. The original WD theory was also re-analysed elsewhere, with an effort to study standing MHD shocks by Chakrabarti [155]. Various solutions of the WD solution topology were studied and he found that many of them allowed for MHD shock formation in both accretion and winds of a compact magnetised object. With the advent of increased computational capabilities of computers in the 1980's, Sakurai [156] successfully generalised the original Weber and Davis theory to two dimensions. There appear the usual slow and fast modes in his solution, as in the original Weber and Davis theory; however, in this case, the momentum equation was found to be singular on an Alfvén surface and regularising the solution on this surface alongside the boundary condition at the photosphere uniquely determined the solution of the two-dimensional problem. Keppens and Goedbloed [46, 47] have over the past few years, developed two- and three-dimensional MHD models for investigating magento-rotational stellar winds. Their models have clearly shown that the dipolar nature of the magnetic field structure is important for stellar winds. At the same time they have shown that the poloidal component leads to density enhancement along the equatorial region. They also find that their trans-sonic wind solutions have been found to have dead zones which have a latitudinal dependence, which can be traced back to the configuration of the magnetic field. They have also investigated shock formation in magneto-rotational outflows [see 48] and the nature and formation of Kelvin-Helmholtz instabilities [e.g. 157]. These studies indicate that the mass efflux from magneto-rotational outflows can be asymmetric in nature. Their models also have been used to study the evolution of rotational velocity distribution in late-type stars while on the main sequence. The stellar winds in these stars were assumed to be WD-like steady-state winds [see 158].

Concomitant to the development of MHD winds, the field of dust-driven winds in evolved stars has flourished as a separate research focus altogether. The early models of dust-driven outflows from AGB stars were 1D models and did not include radiative transfer through the dust-laden envelope and dynamical dust formation [see 93, for a brief review]. Later one-dimensional models involved dynamics of dust formation and growth in a time-dependent manner building upon initial studies of C-type AGB stars [e.g. 159–161].

36

These models revealed, that due to the dynamical interaction between dust and gas and the radiation field, dust-laden shells were formed in the envelopes of AGB stars [e.g 140] and dynamical instabilities in the flow also manifested themselves leading to aspherical mass loss [see 60, 162, 163]. Models have also been constructed that investigate dust grain drift through the gas which modifies dust growth rates and the efficiency of the wind acceleration process [see 164]. There have also been further improvements in treating the radiative transfer in a frequency dependent way alongside detailed micro-physics of molecular and grain opacities [e.g. 165, 166]. The reader is presently referred to a recent review by Höfner [167] on the status of modern-day radiation-hydrodynamical modelling of dust-driven winds of AGB stars. One of the first models to capture the onset of instabilities in the outflow as arising from effects of dust formation, albeit in spherically symmetric isothermal outflow was due to Woodrow and Auman [168]. Following that, in recent years, the modelling of dust-driven winds has been extended to more than one dimension, capturing the aspherical nature of the outflow in a very clear way [see 58, 59, 169–171]. These models incorporate hydrodynamics with radiation pressure on the dust, equilibrium chemistry for the nucleation of dust in a time-dependent way, and they take into account radiative transfer in a frequency dependent manner. They were able to capture in their simulations, many of the highly dynamical aspects of the outflow, including turbulent and inhomogeneous dust formation and Rayleigh-Taylor flow instabilities that result in cloud-like structure formations in the efflux. With the help of such models it has become clear that the winds in these stars are far more complicated than simple one-dimensional (spherically symmetric) pictures and may have an impact on shaping planetary nebulae due to their asphericity [e.g. 172] or by having an impact on the superwind at the end of the AGB, as is suggested by Lagadec and Zijlstra [173], with regard to the abundance of carbon in the envelopes of some AGB stars. The latter suggests that the effort to include complicated micro-chemistry of the dust grains, as is done in modern AGB wind models, may prove to be a key factor in resolving issues regarding the superwind in the late stages of the AGB phase. For a more thorough description of AGB envelopes and the stochastic nature of dust formation process itself, the reader is referred to Habing and Olofsson [145] and to Dirks et al. [174] as well as references therein.

It has also been argued that asymmetric mass loss on the AGB may result in kicks and spin being delivered to the nascent white dwarf within [see 175]. More recently, the effect of kicks to white dwarfs has been investigated

with regard to their impact on the dynamics of globular clusters and binaries [see 176–181]. These studies indicate that the study of AGB winds in relation to asphericity is rather important. In the literature, hybrid equatorial winds have only been considered for rotating hot stars [see 182–186]. MHD stellar winds for AGB stars have been simulated for a coupled disk and star system, clearly showing that magnetocentrifugal winds can occur in planetary nebulae and AGB stars, at the tip of the AGB [see 187, and references therein]. Other researchers have considered a hybrid wind for AGB stars by coupling Alfvén waves with radiation pressure [see 188, 189], showing that it is possible to obtain low-velocity mass efflux in supergiant cool stars through such a mechanism. A similar study has also been carried out for Wolf-Rayet stars [e.g 190], of course obtaining much faster winds. From the brief survey of the literature conducted above, it is evident that winds from AGB stars whether during the initial or final phases of the AGB can have asymmetries that result in aspherical mass loss either due to purely MHD effects, or due to the dynamics between the dust and gas and the radiation field. However, present day dust-driven models still do not include magneto-rotational effects, particularly when more and more observations indicate the presence of magnetic fields in these objects, and the pure MHD wind models do not include the effect of dust condensation and radiation pressure in the envelopes of these stars. The aim of the current work is to investigate the implications of including magneto-rotational effects with a simplified dust-driven model in 1.5 dimensions; the azimuthal terms are determined entirely from their dependence on the radial terms (the standard WD-picture). We shall however, for the sake of simplicity, be considering a steady-state case. It is to be mentioned at the very outset, that the current model may only be valid at the early phases of the AGB, long before the onset of the superwind at the end of the AGB.

We present the underlying assumptions of the model in Section 3.2. In Section 3.3 we present the numerical details, thereafter in Section 3.4 the results are presented and discussed. Finally, in Section 3.5 the current study is summarised and future avenues for development of the current model are briefly discussed.

3.2 The Hybrid Wind Model

We begin with the standard picture of a *Weber-Davis (WD) equatorial wind*; we shall be following their definitions and general derivation closely. However, we shall be including the dust as a second fluid. As in the WD model we shall assume complete axial symmetry and the customary explicit form for the magnetic field within the equatorial plane,

$$\vec{B} = B_r(r)\hat{r} + B_\phi(r)\hat{\phi}, \tag{3.1}$$

while the velocity of the gas and the dust can respectively, be written as,

$$\vec{u} = u_r(r)\hat{r} + u_\phi(r)\hat{\phi} \tag{3.2}$$

and

$$\vec{v} = v_r(r)\hat{r} + v_\phi(r)\hat{\phi}. \tag{3.3}$$

As can be seen, the velocity fields are functions of the radial distance alone. In addition, there is no time dependence, explicit or implicit, thus conforming with the steady-state assumption. Accordingly, the continuity equation for the gas and dust combined can be written as,

$$\rho u r^2 + n_d m_d v r^2 \Theta(r - r_d) = \text{constant}, \tag{3.4}$$

where, ρ is the gas density in cgs units, n_d is the number density of the dust grains and m_d is the mass of a single dust grain. $\Theta(r - r_d)$ is the standard Heaviside function which is equal to unity for $r \geq r_d$. Prior to the dust formation radius, there is only one fluid, namely the gas. Please note that we have dropped the subscript r from the radial velocities for brevity and future convenience. We are explicitly assuming, for the sake of simplicity, that all dust formation occurs at a certain distance (r_d) from the centre of the star. Beyond this, there is no further condensation of dust. We shall also assume that all the dust grains are identical and perfectly spherical with a radius of $a = 0.05\mu$m and a mass density of $\rho_d \approx 2.25\text{g/cm}^3$ [e.g. 93]. This yields the mass for an individual dust grain as, $m_d = \frac{4}{3}\pi a^3 \rho_d$.

In addition, we shall assume that the dust-to-gas ratio in the stellar wind is given by,

$$\frac{n_d m_d}{\rho} = \delta \leq \frac{1}{200}, \tag{3.5}$$

following Lamers and Cassinelli [93], in other words, $n_d m_d \ll \rho$. The maximum value for this ratio is at the dust formation radius and it decreases

monotonically thereafter. For deriving the momentum equations for the gas and the dust, our starting point is the Euler equation, one for each of the fluids. These equations essentially convey conservation of momentum for the two fluids. For the gas we can write,

$$(\vec{u} \cdot \vec{\nabla})\vec{u} + \frac{1}{\rho}\vec{\nabla}p + \frac{GM_*}{r^2}\hat{r} - \frac{1}{\rho c}\vec{J} \times \vec{B} - \frac{n_d}{\rho}\vec{f}_D = 0, \qquad (3.6)$$

where p is the gas pressure and $\vec{J}$ is the current density. It is assumed here implicitly that there is no relative motion of the ions with respect to the neutrals. The first and second terms are related to the velocity and pressure gradients respectively, the third term is the gravitational acceleration on the gas, the fourth term is the Lorentz force divided by the gas density and the final term is proportional to the drag force that is experienced by the gas, due to the dust grains moving through it. The current density must satisfy Ohm's law in the form,

$$\vec{J} = \sigma\left(\vec{E} + \frac{1}{c}\vec{u} \times \vec{B}\right), \qquad (3.7)$$

where σ is the conductivity of the fluid. Assuming that the plasma is a perfect conductor requires that σ be infinite, therefore, in order to keep the current density finite, the Lorentz force term in Eq. (3.7) must vanish; i.e., force-free MHD. This yields,

$$\vec{E} = -\frac{1}{c}\vec{u} \times \vec{B}. \qquad (3.8)$$

Taking the curl of both sides of Eq. (3.8) and using Faraday's law in steady-state, that $\vec{\nabla} \times \vec{E} = -\frac{1}{c}\frac{\partial \vec{B}}{\partial t} = 0$, we obtain,

$$\vec{\nabla} \times (\vec{u} \times \vec{B}) = 0. \qquad (3.9)$$

Noting that the azimuthal component of Eq. (3.9) vanishes, we obtain the usual relation,

$$r(uB_\phi - u_\phi B_r) = \text{constant} = -R_0^2\Omega B_{r,0}, \qquad (3.10)$$

where, R_0 is the stellar radius (radius of the photosphere), Ω is the rotation rate of the star and $B_{r,0}$ is the radial component of the magnetic field at the stellar surface. Requiring that $\vec{\nabla} \cdot \vec{B} = 0$, yields the familiar relation

$$r^2 B_r = R_0^2 B_{r,0}. \qquad (3.11)$$

Presently, let us turn our attention to the Euler equation for the second fluid, viz., the dust grains. The rationale is that obtaining expressions for the drag force components will allow us to re-write Eq. (3.6), the Euler equation for the gas. The Euler equation for the dust grains can be written as,

$$(\vec{v} \cdot \vec{\nabla})\vec{v} + \frac{GM_*}{r^2}\hat{r} - \frac{\pi a^2 Q_{rp} L_*}{4\pi r^2 c m_d}\hat{r} + \frac{1}{m_d}\vec{f_D} = 0. \tag{3.12}$$

In the above equation, Q_{rp} is the radiation pressure mean efficiency [e.g. 93]. In the current study, since our aim is to present a simplistic picture we shall not be calculating this term. L_* is the luminosity of the star and c is the speed of light. The first term in Eq. (3.12) is related to the velocity gradient of the dust grains, the second term is the gravitational acceleration experienced by the dust grain, the third term is the radiation pressure that the dust grain experiences, that drives it outward and the final term is the drag force per unit mass of the dust grain, as it moves through the surrounding gas. At this stage, we can make the usual simplifying assumption that for a single dust grain, the radiation pressure and the drag force terms in Eq. (3.12) dominate completely over the other terms [e.g. 93] and balance each other. We can then write,

$$\frac{\pi a^2 Q_{rp} L_*}{4\pi r^2 c m_d}\hat{r} - \frac{1}{m_d}\vec{f_D} = 0. \tag{3.13}$$

We can now write the radial and azimuthal components of Eq. (3.13) separately. Each of these components must identically vanish. Thus we get for the radial component,

$$\frac{\pi a^2 Q_{rp} L_*}{4\pi r^2 c} = f_D^r, \tag{3.14}$$

where f_D^r is the radial component of the drag force, defined as,

$$f_D^r = \pi a^2 \rho (v - u)\sqrt{(v - u)^2 + a_{th}^2} \, , \tag{3.15}$$

where a_{th} is the thermal speed given by $a_{th} = \sqrt{2kT/\mu m_u}$ and μm_u is the mean molecular mass of the gas. Typically for AGB stars with nearly solar abundance with pulsational shocks that extend the density structure we can use $\mu \approx 1.3$ [e.g. 138]. From Eq. (3.13) we can immediately write the azimuthal momentum equation for the dust grains as,

$$\frac{f_D^\phi}{m_d} = 0, \tag{3.16}$$

41

where f_D^ϕ, the azimuthal component of the drag force, implying that there is no drag in the azimuthal direction. That is, the dust is co-rotating with the gas. Having obtained expressions for the radial and azimuthal components for the dust grains we can now re-visit the Euler equation for the gas. The radial momentum equation for the gas can be re-cast in the form,

$$u\frac{du}{dr} - \frac{u_\phi^2}{r} + \frac{1}{\rho}\frac{dp}{dr} + \frac{GM_*}{r^2} - \frac{1}{\rho c}(\vec{J}\times\vec{B})_r - \frac{n_d}{\rho}\frac{\pi a^2 Q_{rp}L_*}{4\pi r^2 c} = 0, \qquad (3.17)$$

where we have used the definition in Eq. (3.14). We can combine the fourth and sixth terms of Eq. (3.17) into a single term and re-write Eq. (3.17) as,

$$u\frac{du}{dr} - \frac{u_\phi^2}{r} + \frac{1}{\rho}\frac{dp}{dr} + \frac{GM_*(1-\Gamma_d)}{r^2} - \frac{1}{\rho c}(\vec{J}\times\vec{B})_r = 0, \qquad (3.18)$$

wherein, we have the usual definition that,

$$\Gamma_d = \frac{n_d}{\rho}\frac{\pi a^2 Q_{rp}L_*}{4\pi c G M_*}. \qquad (3.19)$$

Presently, the azimuthal momentum equation for the gas can be written as,

$$\frac{u}{r}\frac{d}{dr}(ru_\phi) - \frac{1}{\rho c}(\vec{J}\times\vec{B})_\phi = 0. \qquad (3.20)$$

It is to be noted that the azimuthal component of the drag force does not appear in Eq. (3.20) as it vanishes (see Eq. (3.16)). As is customary, we can at this stage use Maxwell's relation for the curl of the magnetic field to make further progress and write,

$$\frac{1}{\rho c}(\vec{J}\times\vec{B})_r = -\frac{1}{4\pi\rho}\left(\frac{B_\phi}{r}\frac{d}{dr}(rB_\phi)\right)\hat{r} \qquad (3.21)$$

and

$$\frac{1}{\rho c}(\vec{J}\times\vec{B})_\phi = \frac{1}{4\pi\rho}\left(\frac{B_r}{r}\frac{d}{dr}(rB_\phi)\right)\hat{\phi}. \qquad (3.22)$$

Substituting Eq. (3.22) into Eq. (3.20) we obtain after re-arranging terms,

$$\rho u r^2 \frac{d}{dr}(ru_\phi) - r^2 B_r \frac{d}{dr}(rB_\phi) = 0. \qquad (3.23)$$

However, since the dust-to-gas ratio is small, i.e., $n_d m_d \ll \rho$ and since the dust and gas velocities are expected to be on the same order with the dust velocity exceeding the gas velocity by a small fraction of the gas velocity, it is reasonable to make the approximation that $\rho u r^2 \gg n_d m_d v r^2$. This allows us to further make the approximation that $\rho u r^2 = $ constant in Eq. (3.4). Therefore, we can immediately simplify Eq. (3.23) and recover the usual expression for the total specific angular momentum of the wind as,

$$r u_\phi - \frac{B_r}{4\pi\rho u} r B_\phi = L. \tag{3.24}$$

Using Eqs. (3.4) and (3.11) it can be easily verfied that,

$$\frac{B_r}{4\pi\rho u} = \frac{B_r r^2}{4\pi\rho u r^2} = \text{constant.} \tag{3.25}$$

Employing the definition that,

$$M_A^2 = \frac{4\pi\rho u^2}{B_r^2}, \tag{3.26}$$

for the radial Alfvénic Mach number and using Eq. (3.10), we can obtain an expression for the azimuthal velocity of the gas in terms of the angular momentum of the wind and the Mach number, from Eq. (3.24) as,

$$u_\phi = \Omega r \frac{M_A^2 L r^{-2} \Omega^{-1} - 1}{M_A^2 - 1}. \tag{3.27}$$

Requiring that the azimuthal gas velocity remain finite as the Mach number approaches unity, immediately yields the conventional result that,

$$L = \Omega r_A^2, \tag{3.28}$$

where r_A is the Alfvén radius, defined as the distance from the centre of the star at which the radial magnetic energy density is equal to the kinetic energy density, i.e., $\frac{1}{2}\rho u^2 = \frac{B_r^2}{8\pi}$. Using Eqs. (3.4), (3.11), (3.25) and (3.26) and the approximation that $\rho u r^2 \gg n_d m_d v r^2$, we can re-express the Mach number as,

$$M_A^2 = \frac{u r^2}{u_A r_A^2} = \frac{\rho_A}{\rho}, \tag{3.29}$$

where the subscript A refers to quantities at the Alfvén radius. This result immediately enables us to re-write Eq. (3.27) as,

$$u_\phi = \frac{\Omega r}{u_A} \frac{u_A - u}{1 - M_A^2}.$$ (3.30)

In addition we obtain an expression for the azimuthal magnetic field as,

$$B_\phi = -B_r \frac{\Omega r}{u_A} \frac{r_A^2 - r^2}{r_A^2(1 - M_A^2)}.$$ (3.31)

We shall also assume that the gas is an ideal gas and employ a polytropic equation of state;

$$p = p_0 \left(\frac{\rho}{\rho_0}\right)^\gamma,$$ (3.32)

where, p_0 and ρ_0 are the pressure and density, respectively, at the surface of the star and γ is the polytropic index. After substituting Eq. (3.21) into Eq. (3.18) and expressing ρ, u_ϕ and B_ϕ in terms of u and r with the help of Eqs. (3.29-3.31), we can easily obtain the expression for the gas velocity gradient as,

$$\frac{dw}{dx} = \frac{w}{x} \frac{N(w, x)}{D(w, x)},$$ (3.33)

where, $w = u/u_A$ is the gas speed normalised using the Alfvén speed and $x = r/r_A$ is the radial distance expressed in units of the Alfvén radius. The quantities $N(w, x)$ and $D(w, x)$ are the numerator and denominator respectively and are given by,

$$N(w, x) = \left(2\gamma S_T(wx^2)^{1-\gamma} - \frac{S_G}{x}(1 - \Gamma_d \cdot \Theta(x - x_d))\right)$$
$$\times (wx^2 - 1)^3 + S_\Omega x^2(w - 1)\left(1 - 3wx^2 + (wx^2 + 1)w\right)$$ (3.34)

and

$$D(w, x) = \left(w^2 - \gamma S_T(wx^2)^{1-\gamma}\right)(wx^2 - 1)^3 - S_\Omega x^2 \times$$
$$(wx^2)^2 \left(\frac{1}{x^2} - 1\right)^2.$$ (3.35)

In the above equations, the parameters $S_T = \frac{2kT_A}{m_p u_A^2}$, $S_G = \frac{GM_*}{r_A u_A^2}$ and $S_\Omega = \frac{\Omega^2 r_A^2}{u_A^2}$ along with γ uniquely determine the locations of the critical points, and hence

the morphology of the family of solutions of Eq. (3.33). The critical points are, as usual, defined as the locations at which the both the numerator and denominator vanish, thereby keeping the right-hand side of Eq. (3.33) finite; the ratio of the numerator and denominator would approach some constant value in the limit of the radius and the gas velocity, each approaching critical values. The presence of the Heaviside function in Eq. (3.34) represents the formation of dust at the location $x = x_d$, the dust condensation radius in units of the Alfvén radius. The critical wind solution of Eq. (3.33) will yield the gas velocity profile and thereby enable determination of other dependent variables, such as the dust velocity profile (to be discussed below), the Mach number as a function of distance from the star, the azimuthal velocity of the gas, the azimuthal component of the magnetic field, the temperature profile and the density structure of the gas in the envelope of the AGB star.

As mentioned above, we can determine the dust velocity profile after having determined u, the gas velocity as a function of radius, with the help of Eqs. (3.14) and (3.15). This allows us to express the drift speed as (e.g. [e.g. 93]),

$$(v - u)^4 + (v - u)^2 a_{th}^2 - \left(\frac{Q_{rp} L_*}{4\pi r^2 \rho c} \right)^2 = 0. \qquad (3.36)$$

This yields the solution (after employing Eq. (3.19)),

$$v(r) = u(r) + \left(\frac{\sqrt{a_{th}^4 + 4 \left(\frac{\Gamma_d G M_*}{\pi a^2 n_d r^2} \right)^2} - a_{th}^2}{2} \right)^{1/2} \qquad (3.37)$$

The dust grain number density n_d, can be obtained from Eq. (3.5). In the current study we are not solving for the dust velocity simultaneously with Eq. (3.33). However, since the dust-to-gas ratio is already a small number and decreases monotonically in the wind away from the star to become even smaller, we shall therefore make the simplifying assumption that $n_d m_d / \rho \approx \langle \delta \rangle$, the average dust-to-gas ratio in the wind and evaluate n_d for different values of $\langle \delta \rangle$. This essentially implies that $n_d m_d \ll \rho$, in the wind. This is a consequence of the dust-to-gas ration being a small fraction.

Finally the energy flux per second per steradian can be determined by

expressing Eq. (3.33) as a total derivative. This yields,

$$
\frac{F}{\rho u r^2} = \left(\frac{u^2}{2} + \frac{u_\phi^2}{2} + \frac{\gamma}{\gamma - 1} \frac{p_A}{\rho_A} \left(\frac{\rho}{\rho_A} \right)^{\gamma - 1} \right.
$$
$$
\left. - \frac{GM_*(1 - \Gamma_d\Theta(r - r_d))}{r} - \frac{B_\phi B_r}{4\pi\rho} \frac{\Omega r}{u} \right). \tag{3.38}
$$

It is immediately evident upon inspecting Eq. (3.38) that the Heaviside function will present a discontinuity in the flux at the dust formation radius, therefore, in order to preserve the constancy of energy flux across the dust formation interface at $r = r_d$, it becomes necessary to subtract a constant term to the energy flux outside the dust formation interface, such that,

$$
\frac{F(r)|_{r=r_d^-}}{\rho u r^2} = \frac{F(r)|_{r=r_d^+}}{\rho u r^2} - \text{constant}. \tag{3.39}
$$

This constant is essentially the difference between the energy fluxes on either side of the dust formation radius ($r = r_d$) and is given by $const = GM_*\Gamma_d/r_d$. Such a constant term effectively redefines the gravitational potential, without altering the dynamics; i.e., its derivative vanishes, since it is a constant and thus, it does not change the solution topology of Eq. (3.33). Therefore we can write,

$$
\frac{F(r \leq r_d)}{\rho u r^2} = \left(\frac{u^2}{2} + \frac{u_\phi^2}{2} + \frac{\gamma}{\gamma - 1} \frac{p_A}{\rho_A} \left(\frac{\rho}{\rho_A} \right)^{\gamma - 1} \right.
$$
$$
\left. - \frac{GM_*}{r} - \frac{B_\phi B_r}{4\pi\rho} \frac{\Omega r}{u} + \frac{GM_*\Gamma_d}{r_d} \right). \tag{3.40}
$$

Similarly, for $r \geq r_d$ we obtain Eq. (3.38), thus we ensure that flux is constant across the dust formation interface.

This completes our derivation of the governing equations for the hybrid wind model. We see that once a solution of Eq. (3.33) is determined, i.e., the gas velocity profile, it in turn determines all the other relevant variables including the dust grain velocity as given by Eq. (3.37) and the energy fluxes given by Eqs. (3.38-3.40). In the following section we shall describe the numerical treatment breifly and the results are presented and discussed in Section 3.4.

Table 3.1: Summary of the different parameters for modelling an AGB star hybrid wind

Parameter	Symbol	Value and/or Comment
Mass	M	$\sim 5 M_\odot$
Radius	R_0	$\sim 500 R_\odot$
Mass loss rate	$\dot{M}$	$\sim 1.6 \times 10^{-6} M_\odot \ \mathrm{yr}^{-1}$
Surface magnetic field strength	B_0	~ 1 G
Bulk radial gas velocity at the surface	u_0	$\sim 2 \times 10^{-8} v_{esc,0}$ (vanishingly small)
Surface temperature (effective)	T_0	~ 3000K
Stellar rotation rate	Ω	$\sim 2 \times 10^{-10}$ rad/s
Surface escape velocity	$v_{esc,0}$	6.19×10^6 cm/s
Polytropic exponent	γ	1.06

3.3   Numerical Details

The ordinary differential equation (ODE) for the gas velocity gradient, given in Eq. (3.33) was integrated as an initial value problem for a range of initial conditions in the $w - x$ phase space. The domain of integration was $x_0 \leq x \leq 5$, where x_0 represents the stellar surface. Table 3.1 summarises all the physical parameters employed for a typical AGB star. The first step in the numerical procedure is the determination of the critical points, this is described below. It is to be mentioned in this regard, that we chose the value of the polytropic exponent to be approximately mid-way between unity and the values employed in current 2D-axisymmetric MHD codes, ≈ 1.13 [e.g. 46]. A value of unity represents an isothermal equation of state and since the envelopes of AGB stars may be well-mixed due to convection, we chose

a value slightly more than unity to resemble a sort of effective cooling.

3.3.1 Determination of critical points

The critical points are the locations in the $w - x$ phase space at which both the numerator ($N(w, x)$) and the denominator ($D(w, x)$) in Eqs. (3.34) and (3.35), identically vanish. Once the values of the parameters S_T, S_G, S_Ω and γ are established, we then proceed to solve the system of non-linear algebraic equations given by,

$$N(w_s, x_s) = 0 \qquad (3.41)$$
$$N(w_f, x_f) = 0 \qquad (3.42)$$
$$D(w_s, x_s) = 0 \qquad (3.43)$$
$$D(w_f, x_f) = 0, \qquad (3.44)$$

where, x_s represents the distance from the photosphere (in units of r_A) at which the gas velocity is equal to the local sound speed, w_s (in units of u_A). Similarly, the point (w_f, x_f) represents the location in the phase space at which the kinetic energy density of the gas is equal to the local total magnetic energy density, i.e., $\frac{1}{2}\rho u^2 = \frac{B_r^2 + B_\phi^2}{8\pi}$; the so-called fast point. The root finding is accomplished using a Levenberg-Marquardt medium-scale root finding algorithm [e.g. 191]. Typical tolerances employed were about 10^{-15} in order to ascertain the zeros of the system of equations (3.41 - 3.44). This procedure is carried out for parameters S_T, S_G and S_Ω on both sides of the dust formation interface. Across the interface the only change is that,

$$S_G^+ = S_G^-(1 - \Gamma_d), \qquad (3.45)$$

where S_G^+ represents the value of the parameter outside of the dust formation interface, while S_G^- represents the value inside the dust formation interface. The remaining two parameters S_T and S_Ω are unchanged across the interface. Presently, we describe the procedure employed for determining the location of the radial Alfvén point and the dust parameter Γ_d.

3.3.2 Determination of the radial Alfvén point and dust parameter Γ_d

We begin with a set of parameters S_T, S_G and S_Ω that are chosen arbitrarily; however, with the constraint that, for the given set of parameters, a critical

solution is not physically possible. The rationale being that a purely Weber-Davis wind is not possible for an AGB star. This will be explained in detail later, when the results are discussed. Once the above mentioned parameters are chosen, the remaining parameters u_A and r_A are continuously varied for different values of Γ_d until we are able to achieve a physical critical solution. The chief criterion for the latter being that the solution is continuous through the radial Alfvén point and does not have a kink and is required to originate at the base of the wind sub-sonic, pass through all three critical points, viz., the sonic point, the radial Alfvén point and the fast point and subsequently leave the star super-Alfvénic. The reader at this stage is referred to the sub-section on determination of the critical solution for details (see sub-section 3.3.3.2). Following an initial guess for the parameters $(u_A,\ r_A)$ with Γ_d fixed to a certain value, they are varied with typical step sizes of 10^{-6} until suitable values are obtained. Once u_A and r_A are determined, the temperature at the radial Alfvén point is determined according to,

$$T_A = T_0 \left(\frac{u_0 R_0^2}{u_A r_A^2} \right)^{1-\gamma} , \qquad (3.46)$$

wherein, the parameters at the base of the wind (subscripted with 0) are given in Table 3.1. We now turn our attention to the matter of integrating the ODE in Eq. (3.33) after having determined the above mentioned parameters.

3.3.3 Integration of the ODE and determination of the critical solution

3.3.3.1 ODE integration

Integration of the ODE was accomplished with the software package ODE-PACK employing the subroutine DLSODE using backward difference formulae and chord iteration with the Jacobian supplied [192, 193]. Initial conditions were supplied at the beginning of the integration. Typical error tolerances for convergence testing that were employed were on the order of 10^{-12} for both the absolute and relative errors [see 192]. For a typical integration over the domain $x_0 \leq x \leq 5$, a step size of 10^{-8} was employed, resulting in typically 10^8-10^9 function evaluations. A hybrid stellar wind software package was specifically developed for the current study and this was constructed to be capable of reproducing self-consistently the entire family of solutions beginning with an arbitrary choice of wind parameters. The

entire code takes approximately an hour to execute on an AMD Opteron® 844 1.8 GHz processor.

3.3.3.2 The critical solution

The critical solution is rather unique; it passes through all three critical points. In the current study the critical solution was determined using a tail procedure. For a given set of parameters γ, S_T, S_G and S_Ω, forward and backward integrations were carried out from the points (w_s, x_s) and (w_f, x_f). The backward integration from (w_s, x_s) was carried out all the way to the photosphere of the star and similarly, the forward integration from (w_f, x_f) was carried out all the way to the outer boundary of the domain at $x = 5$. In between the backward integration from (w_f, x_f) was matched with the forward integration from (w_s, x_s). An initial guess was made for the matching point to be half way between x_s and x_f defined by x_m. The tails of the forward and backward integrations were terminated at this location and the values of the gas velocity w and the velocity gradient $\frac{dw}{dx}$ were compared for the two tails to ensure that the conditions

$$\left| \left(\Delta w = w(x_m) \big|_{x=x_m^-} - w(x_m) \big|_{x=x_m^+} \right) \right| \leq 10^{-7} \qquad (3.47)$$

$$\left| \left(\frac{dw}{dx} \bigg|_{x=x_m^-} - \frac{dw}{dx} \bigg|_{x=x_m^+} \right) \right| \leq 10^{-7}, \qquad (3.48)$$

were both met. If the conditions in Eqs.(3.47) and (3.48) were not met, then depending upon the sign of Δw, the matching point x_m was appropriately shifted either forward or backward by a small amount, typically by $\Delta x_m = 10^{-6}$ and the tail procedure was re-iterated. Once the tail procedure was successful the critical solution was considered to be determined. This ensured that the critical solution was continuous through the radial Alfvén point. The tolerance employed in Eqs. (3.47) and (3.48) was considered to be sufficient given the fact that the integration step size was $\Delta x = 10^{-8}$. For achieving a higher tolerance, a further reduction in the step size was found to be necessary, rendering the the procedure needlessly lengthy and increasingly cumbersome in a computational sense.

This completes our discussion of the numerical details regarding determining the complete family of solutions of Eq. (3.33). The results are presented in the following section and are discussed therein.

3.4 Results and Discussion

We present the results obtained by integrating the ODE in Eq. (3.33) to obtain the family of solutions. In the current study, the following methodology was employed for calculating the hybrid wind. First, for a certain set of arbitrary parameters $\{S_T, S_G, S_\Omega$ and $\gamma\}$, Eqs. (3.41-3.44) were solved to obtain the location of the slow and fast points, with the radial Alfvén point located at $(1, 1)$ in the $w - x$ phase space. At this stage, the dust parameter Γ_d was set equal to zero, meaning that there hasn't been any dust formation in the gas. The parameters are chosen such that a pure WD wind is not a physical one, i.e., it is not continuous through the radial Alfvén point (see Figure 3.3 and discussion thereof). The rationale being that for AGB stars, it is not possible to have a mass efflux without dust formation in the envelope, therefore a pure WD wind is explicitly required to not be a physical solution. Second, the dust parameter was set equal to a fraction such that $0 \leq \Gamma_d \leq 1$ and the procedure described in sub-section 3.3.2 for determing the Alfvén velocity and radius is carried out in tandem with solving Eqs. (3.41-3.44) to obtain the sonic point and the fast point. Each time this yields a set of parameters $\{u_A, r_A, (w_s, x_s), (w_f, x_f)\}$. With these parameters, Eq. (3.33) is integrated to obtain the critical solution according to the procedure described in sub-section 3.3.3.2. If success is achieved in finding the critical solution then the iterations are ceased and the resulting parameters are fixed for the given value of Γ_d.

We then determine the temperature profile using the velocity profile of the critical solution. This is achieved using the prescription,

$$T(r) = T_A \left(\frac{u_A r_A^2}{u r^2} \right)^{\gamma-1}, \tag{3.49}$$

where, T_A is the Alfvén temperature and is given by Eq. (3.46). Once the temperature profile is known, it is possible to invert Eq. (3.49) to yield the radius r_d, at which the temperature falls below the dust condensation temperature T_d. The dust condensation radius r_d is a derived quantity that is determined based upon the temperature profile of the wind. Once the dust condensation radius (r_d) is determined, we then proceed to determine the family of solutions to Eq. (3.33) such that integration from the photosphere at $r = R_0$ to $r = r_d$ is carried out with $\Gamma_d = 0$ and integration from $r = r_d$ to the outer boundary at $r = 5r_A$ is done with $\Gamma_d \neq 0$. The same is then done for the critical solution as well.

51
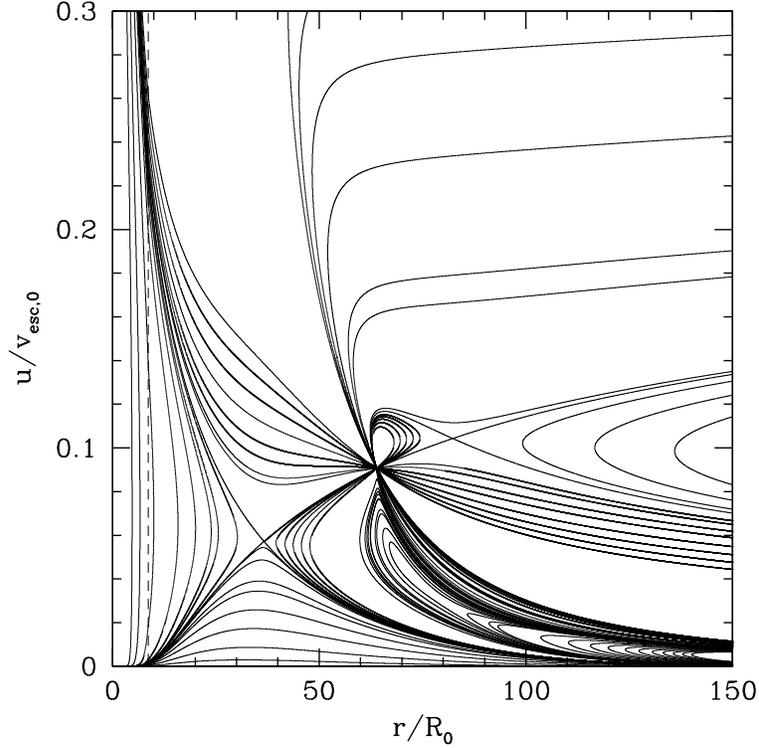
Figure 3.1: Family of solutions of Eq. (3.33) with parameters $u_A \approx 0.09 v_{esc,0}$, $r_A \approx 63.93 R_0$, $\Gamma_d = 0.3$ and remaining parameters as given in Table 3.1. The dashed line at $r \approx 8.65 R_0$ represents the dust formation radius.

As mentioned before, it is implicitly assumed, for the sake of analysing a patently simple model, that beyond the dust condensation radius the value of Γ_d is constant. Concordantly, all the dust forms at the condensation radius and the dust-to-gas ratio is small and given by Eq. (3.5). The family of solutions determined using the procedures described above are shown in Figure 3.1. For the solutions shown therein, the dust parameter was fixed at $\Gamma_d = 0.3$. It can be seen that the dust condensation radius is located at $r_d \approx 8.65 R_0$. The temperature at this location was determined using Eq. (3.49), to be approximately 1200K. The dust condensation temperature was chosen somewhat arbitrarily to lie between $1000 - 1500$K. Within the dust condensation radius x_d, the wind solution to Eq. (3.33) is a purely Weber-Davis-type of wind, and thereafter it is a hybrid wind with dust grains

52
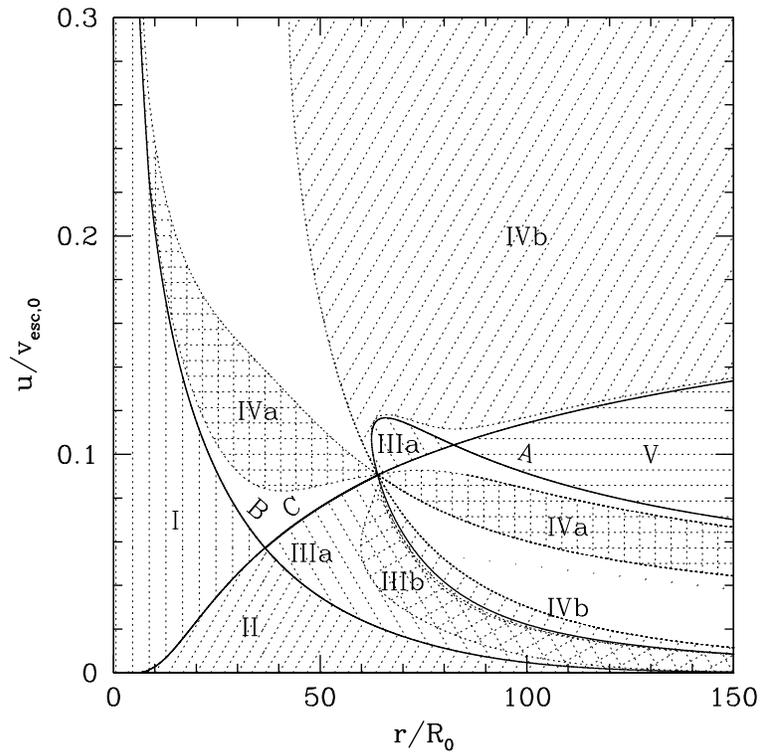
Figure 3.2: Illustration showing the locations of the different types of solutions of Eq. (3.33)

included. The topology of solutions in Figure 3.1 looks typically like a WD-solution, with the three critical points clearly visible, viz., the sonic point, the radial Alfvén point and the fast point. The critical solution emerges from the surface of the star sub-sonic, gets accelerated through to the dust condensation radius, subsequently passes through the three critical points and finally emerges super-Alfvénic at large distances.

At this stage it is convenient to classify the different types of solutions in Figure 3.1. The different types of solutions and their respective locations in the phase space are illustrated qualitatively in Figure 3.2. Therein, it can be seen that the unphysical double-valued solutions to the left of the sonic point are referred to, in the current study, as Type I solutions. The failed wind solutions, directly below the sonic point, are called Type II. The unphysical multi-valued solutions that make loops, between the radial Alfvén point and the fast point, are designated as Type IIIa. The unphysical double-valued solutions adjacent to the loop solutions are called Type IIIb.

The solitary unphysical solution that passes through the sonic X-type singularity, is called the *Bondi solution*, this is labelled as B, in Figure 3.2. While the unphysical double-valued solution that intersects the critical solution, at exactly the two Alfvén points, is designated the *Alfvénic solution*; labelled A. Similarly, the critical solution is labelled as C.

The unphysical wind solutions that start at the photophere with super-sonic velocities, just to the right of the Bondi solution and subsequently pass through the radial Alfvén point and get decelerated to sub-sonic velocities at large distances from the star, are designated as Type IVa. Meanwhile, the unphysical double-valued solutions that pass through the radial Alfvén point alone, are designated as Type IVb. Finally, the unphysical double-valued solutions, in the region between the critical solution and the Alfvénic solution, immediately to the right of the fast point, are referred to as Type V.

As mentioned earlier, the dust grains condense from the gas beyond r_d, where the temperature falls below the condensation temperature. Beyond r_d, we therefore solve the hybrid ODE with a fixed value of Γ_d. Thus at the dust condensation radius, the two types of solutions, dust-free and hybrid, must match, in terms of velocity of the gas. This is illustrated in Figure 3.3, where we have expressed the coordinates using a logarithmic scale to facilitate examination. In Figure 3.3, the red solid line represents a hybrid wind solution for a dust parameter of $\Gamma_d = 0.3$, while the black long-dash-dotted line that passes through the radial Alfvén point with a kink at (u_A, r_A), is a
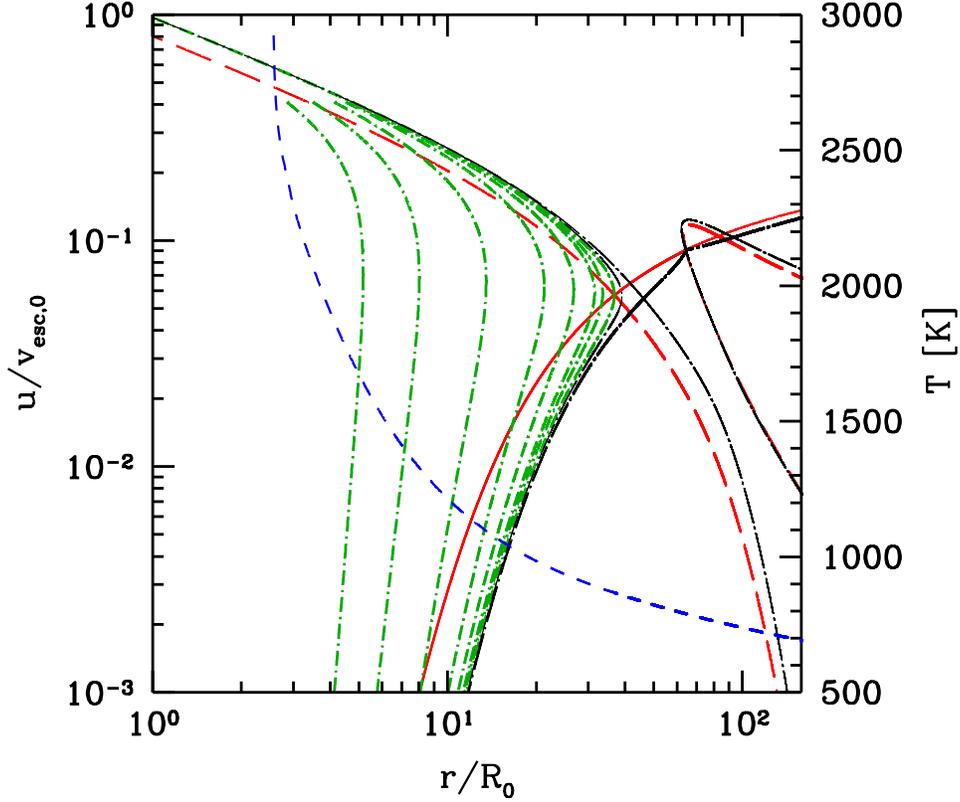
Figure 3.3: Plausible hybrid wind solutions with parameters $u_A \approx 0.09 v_{esc,0}$, $r_A \approx 63.93 R_0$, $\Gamma_d = 0.3$ and remaining parameters as given in Table 3.1. The red solid line and black long-dash-dotted line intersecting at the radial Alfvén point, are the critical solutions of the hybrid wind model and pure WD wind model, respectively. The green-short-dash-dotted lines are possible Type I wind solutions of a pure WD wind that can leave the star via the hybrid critical solution after dust condensation at the intersection points of the green-short-dash-dotted lines and the red solid line. The blue dashed line is the temperature profile calculated for the hybrid wind critical solution. It should be interpreted using the secondary axis.

pure WD solution with $\Gamma_d = 0$. As can be clearly seen, the kink at the radial Alfvén point indicates that this solution is not physical. This indicates that it is not possible to have a pure WD wind for AGB stars; only with dust formation is it possible to achieve an outflow. The Bondi type solutions for both the hybrid wind (long-dashed red line) and the pure WD solution (black long-dash-dotted line), can also be seen to pass through the respective sonic points. Similarly the two fast points can also be distinguished clearly for the two types of solutions; the Alfvénic solutions pass through them. It is to be mentioned at this juncture, that inclusion of an outward force in the wind due to radiation pressure has the effect of suppressing both the sonic point and the fast point towards the photosphere; the sonic and the fast points for the hybrid wind (in red) can clearly be seen to lie inside their respective counterparts of the pure WD wind, in terms of distance from the star's photosphere. The green short-dash-dotted lines are solutions of Type I, for a pure WD wind. The points of intersection of the red solid line representing the critical solution of the hybrid model and the green short-dash-dotted lines, represent different dust formation radii. The temperatures corresponding to these can be inferred using the blue line, which represents the temperature profile, determined using the critical solution of the hybrid wind, via Eq. (3.49). Thus, if a wind solution starts off at the base of the wind sub-sonic and travels through the envelope of the AGB star according to (say) the fourth green short-dash-dotted line from the left, then it can pass through the dust formation radius at approximately 1000K, just ahead of about $10R_0$ and leave the star via the red solid line, the critical solution of the hybrid wind. We therefore see that the unphysical Type I solutions that start off dust-free, can intersect the hybrid critical solution and leave the star as a hybrid critical wind. However, there is a constraint. The last Type I solution that can leave the star as a hybrid wind intersects the critical solution in red, at the sonic point. Any solution of Type I that intersects the red solid line, after it has turned and become double-valued, does not represent a physical hybrid wind. This is illustrated in the black long-dash-dotted Type I solution that turns and then intersects the red solid line, just ahead of the hybrid sonic point in Figure 3.3. Therefore, all the green short-dash-dotted lines are allowed possible solutions of different hybrid winds.

Figure 3.3 also shows that if a hybrid wind is to be achieved, there are two possibile scenarios. First, the dust formation radius can lie within or at most upon the sonic point of the hybrid wind solution. Second, it can lie beyond or upon the fast point of the hybrid solution, or exactly at the radial Alfvén

point. Only the first possibility places the dust formation temperature in the acceptable range for typical AGB parameters so we will focus mainly on this class of solutions (however, c.f. Figure 3.9 and discussion thereof). While the latter scenarios do represent legitimate mathematical solutions, it is however unlikely that the dust formation temperature be significantly lower than about 1000K and concomitantly, that the dust formation radius in AGB stars, should lie as far out as nearly $70R_0$. Since it is expected that the dust formation must occur within a few stellar radii in AGB stars, the only plausible solutions are therefore the Type I green short-dash-dotted lines, that intersect the hybrid critical line in red.

For the hybrid critical solution shown in Figures 3.1 and 3.3, it is possible to calculate the azimuthal velocity profile of the gas according to Eq. (3.27). This calculation is carried out and the results are shown in Figure 3.4. As can be seen the gas velocity profile rises sharply to a maximum value close to the sonic point and then falls off less steeply than the rise; this is consistent with the usual WD-picture. The locations of the dust formation radius and the three critical points are also indicated therein.

In Figure 3.5 we have plotted the energy flux per second per steradian leaving the star, in the equatorial plane, for the critical solution, alongside the various components of the energy flux. The solid line shows the total energy flux in the gas as function of radius; it is constant for the critical solution. It is the sum of all the other lines on the plot. This is calculated via Eqs. (3.38-3.40). The short-dash-dotted line is the magneto-rotational energy flux, which is the sum of the second and the last term in Eq. (3.38). As the distance from the photosphere increases, the radial magnetic field falls of as $\sim 1/r^2$, however the rotational energy is expected to peak close to the sonic point, as can be inferred from Figure 3.4, where the azimuthal velocity peaks. The two competing terms collectively yield a large positive sum closer to the star, and the contribution diminishes quite rapidly, beyond approximately the dust formation radius, as can be seen in Figure 3.5. The long-dashed line represents the gravitational potential energy of the wind, the fourth term in Eq. (3.38) and it is therefore negative. The short-dashed line is the kinetic energy of the wind (the first term in Eq. (3.38)) which gradually increases away from the star as the wind is accelerated. On the other hand, the long-dash-dotted line is the enthalpy (the third term in Eq. (3.38)) which gradually decreases from a maximum value at the stellar surface where the density of the gas is expected to be the highest and follows a power law, of the form $\sim \rho^{\gamma-1}$. The decrease is quite gradual as the exponent is 0.06 since
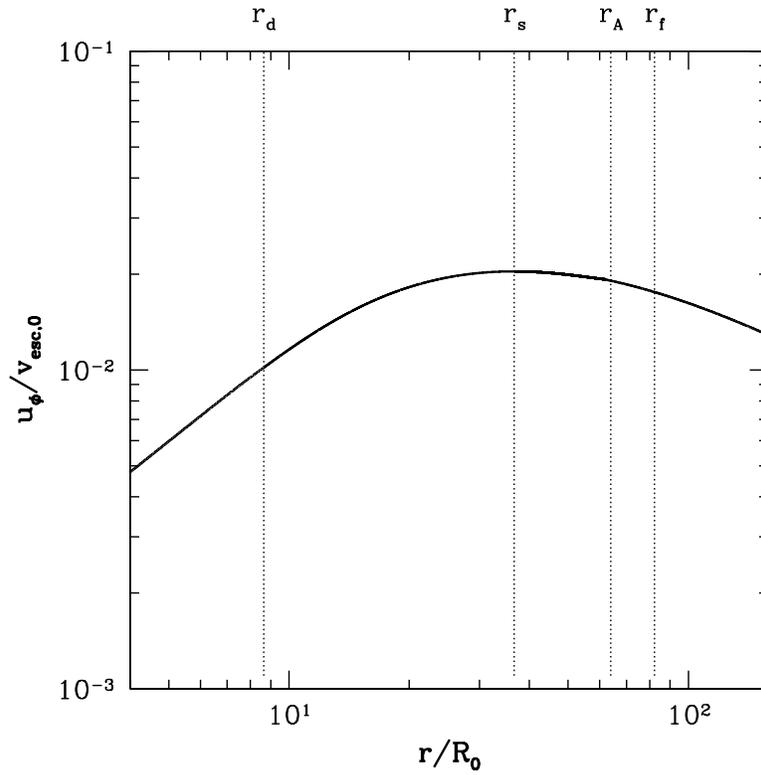
Figure 3.4: Critical azimuthal gas velocity as a function of radius. The vertical dotted lines indicate the locations of the dust formation radius and the three critical points.
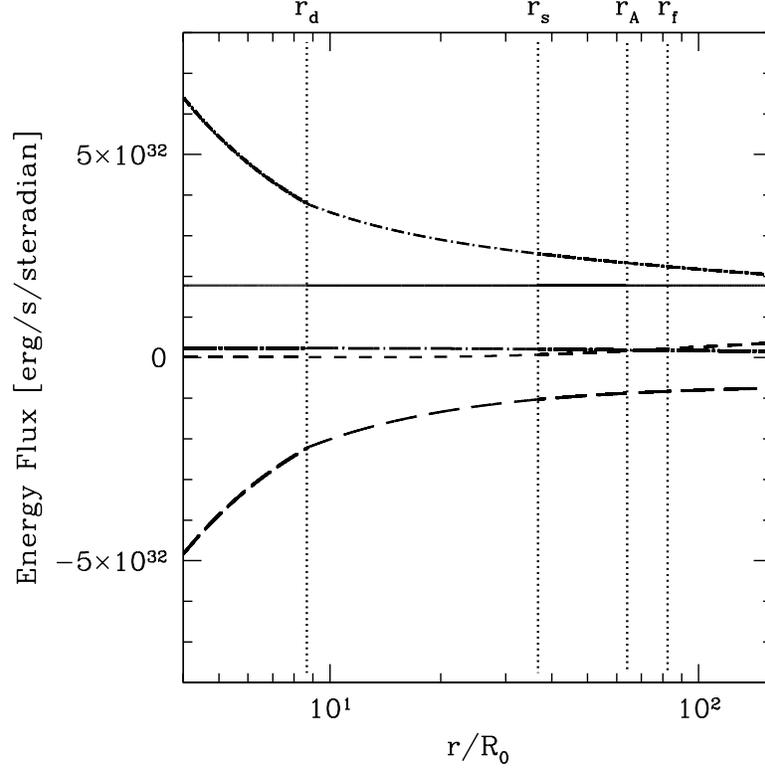
Figure 3.5: Plot showing the energy fluxes calculated using Eqs. (3.38-3.40) for the critical hybrid wind solution with parameters $u_A \approx 0.09 v_{esc,0}$, $r_A \approx 63.93 R_0$, $\Gamma_d = 0.3$ and remaining parameters as given in Table 3.1. The vertical dotted lines indicate the dust formation radius and the the three critical points. The solid horizontal line represents the total constant energy flux. From the top short-dash-dotted curve shows the magneto-rotational energy, the long-dash-dotted curve represents the enthalpy, the short-dashed curve shows the variation in kinetic energy and finally at the bottom the long-dashed line represents the gravitational potential energy of the gas.

we used $\gamma = 1.06$. The contribution of the kinetic energy and the enthalpy are quite small in comparison to the magneto-rotational energy. However, when the magneto-rotational energy is added to the gravitational potential energy, then the sum is comparable to the kinetic energy. Again, the dust formation radius and the three critical points are indicated in the figure. It is also to be mentioned that, since it is possible to recover the momentum terms of Eq. (3.18) by differentiating Eq. (3.38), therefore the slopes of the different lines shown in Figure 3.5 would indicate the contributions of these terms. In particular, it can be clearly seen that the slopes of the magneto-rotational energy and the gravitational energy (which includes radiation pressure) are the most prominent features in Figure 3.5. This indicates that the the most significant contributions to accelerating the wind are indeed due to the Lorentz force term plus rotational term in Eq. (3.18) and the gravitational potential which includes the effect of radiation pressure on the dust grains. In this regard, it is evident upon inspecting Figure 3.5, that beyond approximately the radial Alfvén point, the gravitational energy flux becomes flat, indicating that the acceleration due to the gravitational potential modified by radiation pressure, becomes negligible in the wind. However, beyond $r = r_A$, the magneto-rotational energy still has a small contribution and continues to accelerate the wind. In summary, at small distances, ($r <\approx r_s$), both the magneto-rotational terms and the modified gravitational potential terms of Eq. (3.18) have a combined and pronounced effect in accelerating the wind; however, at large distances ($r >\approx r_A$) the effect of the gravitational potential becomes negligible while there still persists a small contribution from the magneto-rotational term, that mildly accelerates the wind outward.

Figure 3.6 shows the velocity profiles of the dust and the gas plotted as a function of distance from the centre of the star. The velocity of the dust grains exceeds that of the gas bulk, as is required by the hybrid wind model, in order to produce an outward drag force on the gas, to accelerate it outward. The velocity of the dust grains is determined according to Eq. (3.37), once the velocity profile of the gas is ascertained, with an assumed average value for the dust-to-gas ratio $\langle \delta \rangle$. Figure 3.6 shows the gas and dust velocity profiles for two different sets of model parameters. The solid black line represents the gas velocity while the dotted black line represents the corresponding dust velocity. This model had parameters $\Gamma_d = 0.3$ and $\langle \delta \rangle = 1/1000$. In order to investigate the effect of changing the average dust-to-gas ratio, we kept all other parameters of the model fixed, in particular, the radiation pressure mean efficiency and the stellar luminosity, were
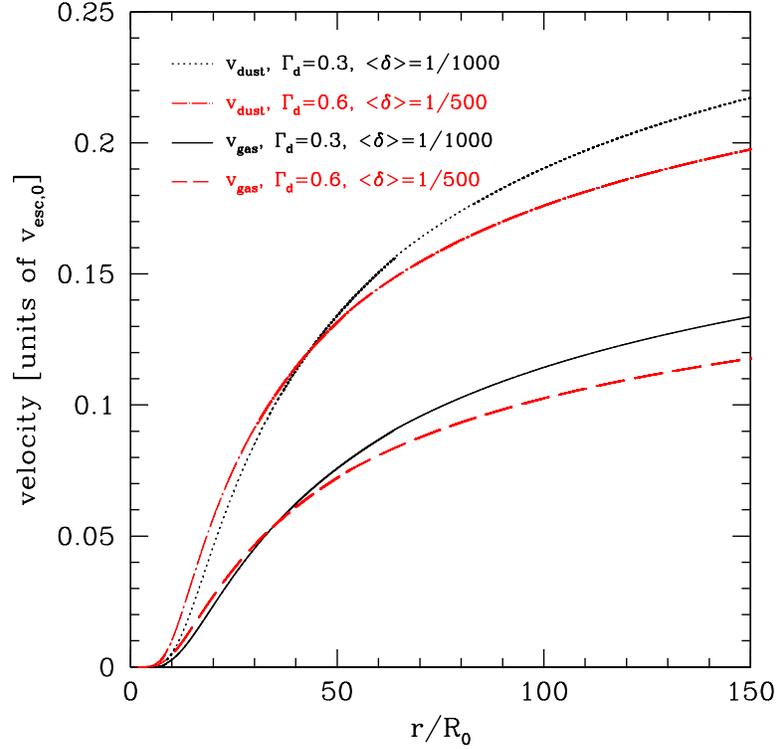
Figure 3.6: Dust and gas velocity profiles for two hybrid winds with parameters $u_A \approx 0.09 v_{esc,0}$, $r_A \approx 63.93 R_0$, $\Gamma_d = 0.3$ (in black) and with parameters $u_A \approx 0.07 v_{esc,0}$, $r_A \approx 53.05 R_0$, $\Gamma_d = 0.6$ (in red). In the former case, the dust-to-gas ratio was $\langle \delta \rangle = 1/1000$ and in the latter case it was double this value, i.e. $\langle \delta \rangle = 1/500$. The remaining wind parameters are given in Table 3.1. The dust velocity profile in each case is determined using Eq. (3.37).

kept constant. Then, according to Eq. (3.19), if the average dust-to-gas ratio is doubled then, then accordingly, the dust parameter Γ_d must also double. Thus, for the second model's results shown in Figure 3.6, we took $\Gamma_d = 0.6$ and $\langle \delta \rangle = 1/500$. Thus, the red-dashed line represents the gas velocity profile, while the red-long-dash-dotted line represents the corresponding dust velocity profile. However, changing the dust parameter also changes the locations of the the three critical points. With $\Gamma_d = 0.3$ the Alfvén velocity and Alfvén radius were found to be $u_A \approx 0.09v_{esc,0}$, $r_A \approx 63.93R_0$, while for $\Gamma_d = 0.6$, the corresponding values were found to be $u_A \approx 0.08v_{esc,0}$, $r_A \approx 53.05R_0$ respectively. It can clearly be seen that within about $50R_0$ (which is approximately the location of the radial Alfvén point for the second model), the dust in the second model (red-long-dash-dotted line) has a steeper rise, indicating a larger acceleration in the wind. Beyond about $50R_0$, the acceleration of the wind in the second model ($\Gamma_d = 0.6$) starts to decline (see Figure 3.5 and discussion thereof). However, the wind in the first model ($\Gamma_d = 0.3$) at this distance, is still getting accelerated, therefore its velocity increases. Thus, when Γ_d is smaller, acceleration due to radiation pressure continues to have an effect, out to larger distances from the star. In addition, at a distance of about $50R_0$, the temperature in the wind is about $\approx 800K$ for the model with $\Gamma_d = 0.3$ and about $\approx 550K$ for the model with $\Gamma_d = 0.6$. Thus, the bulk of the gas is much cooler in the latter case. As a result, it is natural that the velocities in the second model are slightly lower than the first. That being said, it is to be acknowledged that by increasing the dust parameter by increasing the average dust-to-gas ratio, the wind gets accelerated much faster closer to the star. This is expected; however, the terminal velocity in this case is lower, as the acceleration due to radiation pressure does not have a pronounced effect out to large distances ($r > \approx r_A$).

At this stage we turn our attention to the question of changing the temperature at the base of the wind. In AGB stars, it is likely that due to density pulsations within the star, the temperature and density at the stellar photosphere are likely to undergo change [e.g. 93]. It has also been suggested by Soker and Clayton [124] that magnetic-cool spots probably exist in the region around the equator of an AGB star, much like our sun. If such is the case, then the temperature at the base of the hybrid wind will change locally, and this will have an effect on the stellar wind beyond the photosphere in the AGB envelope. In order to investigate this, we constructed a hybrid model with an altogether different base temperature. Following Soker and Clayton [124], we set the base temperature in a magnetic-cool spot to be sig-

nificantly less than the prescribed average 3000K, of the stellar photosphere. Accordingly, in order to achieve a hybrid stellar wind, that starts with negligible velocity at the stellar surface and gets accelerated to super-Alfvénic velocities having passed through the dust formation radius and the the three critical points, we treated Γ_d, u_A and r_A as free parameters. As described in sub-section 3.3.2 we varied the values of these parameters until a successful critical solution was achieved. When the base temperature is changed to 2000K, we found that in order to achieve a hybrid stellar wind, the three free parameters required to take on values; $\Gamma_d \approx 0.62$, $u_A \approx 0.07 v_{esc,0}$ and $r_A \approx 52.19 R_0$. Figure 3.7 shows how the morphology of the solution changes when the base temperature is changed. We have merely shown the key solutions, namely, the critical solutions, the Bondi and the Alfvénic solutions. The solid black lines are the hybrid wind solutions when the base temperature is $T_0 = 3000$K and the dust parameter is $\Gamma_d = 0.3$. The lighter red lines are for $T_0 = 2000$K and $\Gamma_d \approx 0.62$. The dashed lines at the far left indicate the locations of the respective dust formation radii for the two models; in both cases the dust formation temperature was taken to be $T_d \approx 1200$K. It can be clearly seen in Figure 3.7, that when the base temperature is decreased to 2000K, all the critical points as well as the dust formation radius, are suppressed towards the photosphere. The formation of dust closer to the stellar surface is directly related to the steep drop in the temperature profile ahead of the photosphere in the AGB envelope. This finding is consistent with the results of Soker and Clayton [124], who found that dust formation occurred closer to the stellar surface ahead of magnetic-cool spots on the equator of an AGB star. Additionally, the stellar wind critical solution for $T_0 = 2000$K has a lower terminal velocity than its counterpart for $T_0 = 3000$K. This is directly related to the fact that the bulk of the gas is much cooler when the base temperature is lower. If there exist magnetic-cool spots on the surface of an AGB star, then the stellar wind properties, namely the wind speed and momentum of the outflow will change, ahead of the cool spot in the envelope of the star. This will result in asymmetric flows between different parts of the star, in addition to the fact, that dust formation will occur closer to the star. These will directly lead to MHD instabilities, that can grow and become unstable and result in asymmetric mass loss. However, it is to be noted, that investigating such effects is beyond the scope of the current study. In order to investigate instabilities it will be necessary to carry out MHD calculation in at least two, if not three dimensions. By definition, the current steady-state model cannot incorporate dynamic effects such as instabilities.
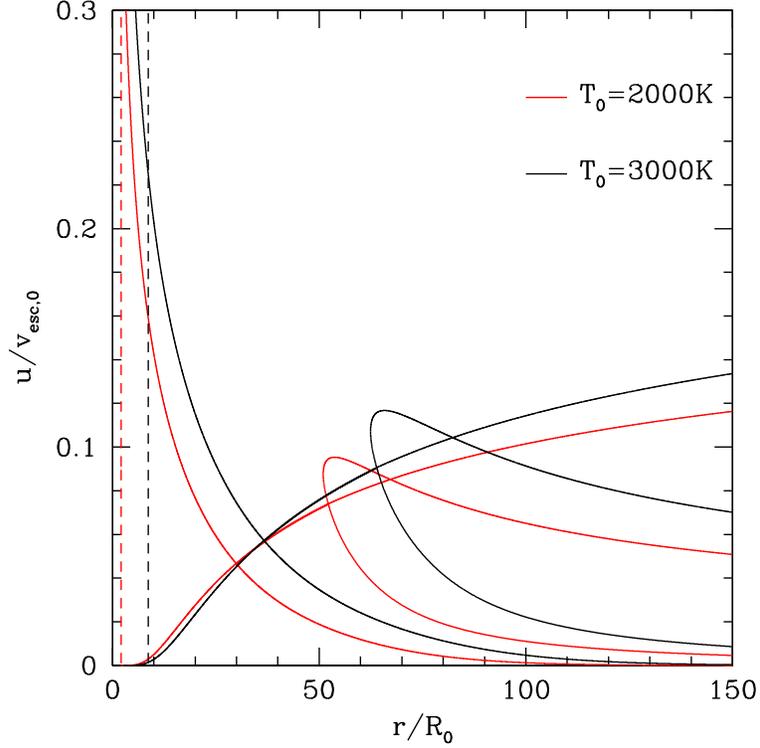
Figure 3.7: Plot showing the effect of changing the temperature at the base of the stellar wind. The black lines are for a hybrid wind with parameters $T_0 = 3000$K, $u_A \approx 0.09v_{esc,0}$, $r_A \approx 63.93R_0$ and $\Gamma_d = 0.3$ while the red lines are for a hybrid wind with parameters $T_0 = 2000$K, $u_A \approx 0.07v_{esc,0}$, $r_A \approx 52.19R_0$ and $\Gamma_d \approx 0.62$. Both winds have identical remaining wind parameters, as given in Table 3.1. The dashed lines represent the locations of the respective dust formation radii for the two hybrid winds with $T_d \approx 1200$K, in both cases. Dust formation occurs closer to the stellar surface when the base temperature is lowered.

Addition of effects of radiative transfer, along with internal chemistry, that affects dust grain formation, with relaxation of the assumption of spherical grains, would be the ultimate goal of such an endeavour. It has already been shown by Woitke and Niccolini [58] using 2-D hydrodynamic codes with radiative transfer, that it is possible to capture hydrodynamic instabilities. The addition of magneto-rotational effects to these models would result in richer gas (and dust) dynamics and quite different instabilities in the flow altogether, due to the presence of MHD effects. The presence of instabilities in the outflow are the precursors for asymmetric mass loss, which has been theorised to be responsible for white dwarf kicks [see 175–181]. In this context, the current work is relevant, as it presents a steady-state solution that 2- and 3-D MHD-dust-driven wind models can reproduce by eliminating the time dependence, i.e., setting the $\partial/\partial t$ terms to zero. It also presents an additional avenue for the formation of instabilities, in AGB stellar winds.

It is also to be noted that, when the dust parameter was increased to values closer to unity, it resulted in the critical points being suppressed towards the photosphere; this can clearly be seen in Figure 3.7. Concordantly, as the dust parameter is increased, it results in dust condensation closer to the stellar surface. In Figure 3.8 we have plotted the location of the three critical points as a function of the dust parameter Γ_d. The short-dash-dotted line represents the location of the sonic point (r_s) as Γ_d is varied, the solid line shows the variation in the radial Alfvén point (r_A), while the long-dash-dotted line shows the change in the fast point (r_f). Also plotted therein, is the temperature at the radial Alfvén point; the short-dashed line. As can be clearly seen, in the limit of $\Gamma_d \to 1$, the three critical points converge and their locations approach the stellar surface. The sharp decline in the radial Alfvén temperature beyond $\Gamma_d \approx 0.7$ indicates that the temperature profile in the AGB envelope falls off in an extremely steep manner, making the solutions of the gas momentum equation implausible and indeed unphysical.

To determine the dependence of the critical points on the dust parameter, we continuously changed the value of Γ_d with a step size of 10^{-4}, within the limits shown in Figure 3.7 and for each given value of Γ_d, we determined the appropriate set of parameters $\{u_A, r_A, (w_s, x_s) \text{ and } (w_f, x_f)\}$, that yielded a continuous monotonically increasing critical solution through the critical points. Following which, the temperature at the radial Alfvén point was determined according to Eq. (3.46).

However in Figure 3.8 we have only shown the effect of changing a single
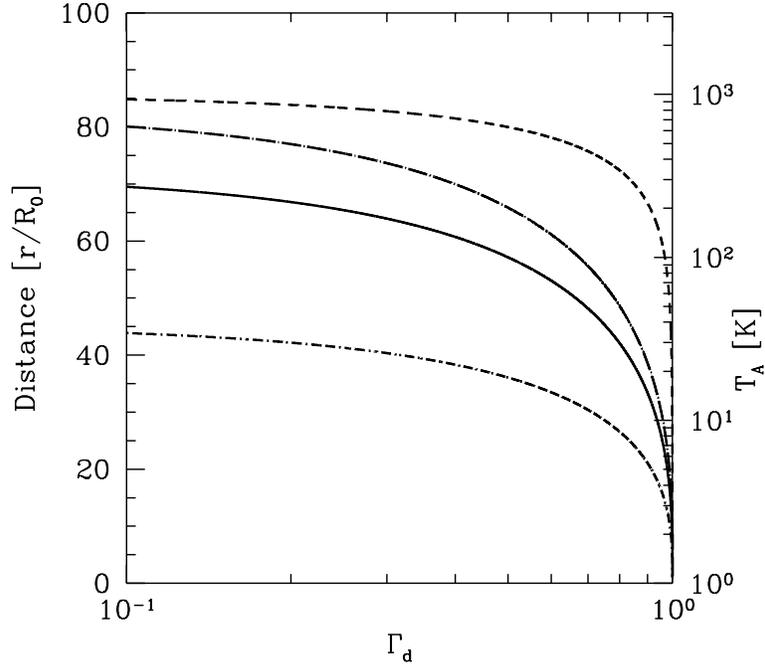
Figure 3.8: Plot showing the effect of changing the dust parameter Γ_d on the morphology of the family of solutions to Eq. (3.33). In all calculations the common parameters for the models are shown in Table 3.1. The short-dash-dotted line shows variation in the sonic point (r_s) as a function of Γ_d, the solid line shows the change in the radial Alfvén point (r_A) with changing Γ_d, while the long-dash-dotted line represents the change in the fast point (r_f) for the same case. The short-dashed line traces the dependence of the temperature at the radial Alfvén point on Γ_d, this should be interpreted using the secondary axis.

parameter. The determination of the location of the critical points also depends on other parameters, such as the polytropic index, the photospheric temperature, the mass-loss rate, etc. While the wind solutions are stable for the locations of the critical points shown in Figure 3.8, a full-stability analysis would be required to establish how the solutions change as a result of changing the other parameters mentioned above. Such a detailed analysis was considered to be outside the scope of the current study and we present in Figure 3.8 merely the stable solutions that arise after changing a single parameter while all the others are kept fixed.

In simple isothermal dust-driven wind models, a stellar outflow is achieved by setting $\Gamma_d > 1$ (e.g. [e.g. 93]). This is done to counteract the force of gravity and to drive the gas outward. However, in the current study we found that setting the dust parameter to be greater than unity, did not yield a set of critical points; i.e., they were found not to exist in the domain $R_0 \leq r \leq 150R_0$, for which Eqs. (3.41-3.44) were satisfied simultaneously. Hybrid winds were successfully achieved for $0 < \Gamma_d < 1$. Indeed, as is shown in Figure 3.7, $\Gamma_d \approx 0.7$ is a reasonable physical upper limit, where $T_A(\Gamma_d \approx 0.7) \approx 450$K and after which point the decline in the temperature proceeds very rapidly. It is to be mentioned that for all of the calculations carried out to produce Figure 3.7, the temperature at the base of the wind was $T_0 = 3000$K and all the remaining parameters were identical to those given in Table 3.1.

Finally, for the sake of completeness, we have shown in Figure 3.9, the plausible hybrid wind solutions, should the dust formation radius exist outside the fast point. Again the parameters of the hybrid wind are identical to those shown in Table 3.1. It is to be mentioned that it is likely that dust formation lies within a few stellar radii [e.g. 93]; however, since the parameters of Table 3.1 may all be scalable to suit an altogether different type of star, we have therefore included Figure 3.9, to complete the scenario of dust forming in the envelope or indeed the outer atmosphere of the star.

In Figure 3.9, the solid black line represents the critical solution of a pure Weber-Davis stellar wind, without any dust. While the long-dash-dotted red line represents the hybrid wind critical solution with $\Gamma_d = 0.3$ and $u_A \approx 0.07v_{esc,0}$ and $r_A \approx 48.20R_0$, the pure WD wind has the same values for u_A and r_A. As can be seen in this case, the hybrid wind is not a physical possibility as it is not continuous through the radial Alfvén point. On the other hand the pure WD-equatorial wind is continuous. The Bondi and Alfvénic solutions for the two types of solutions, with and without dust, are
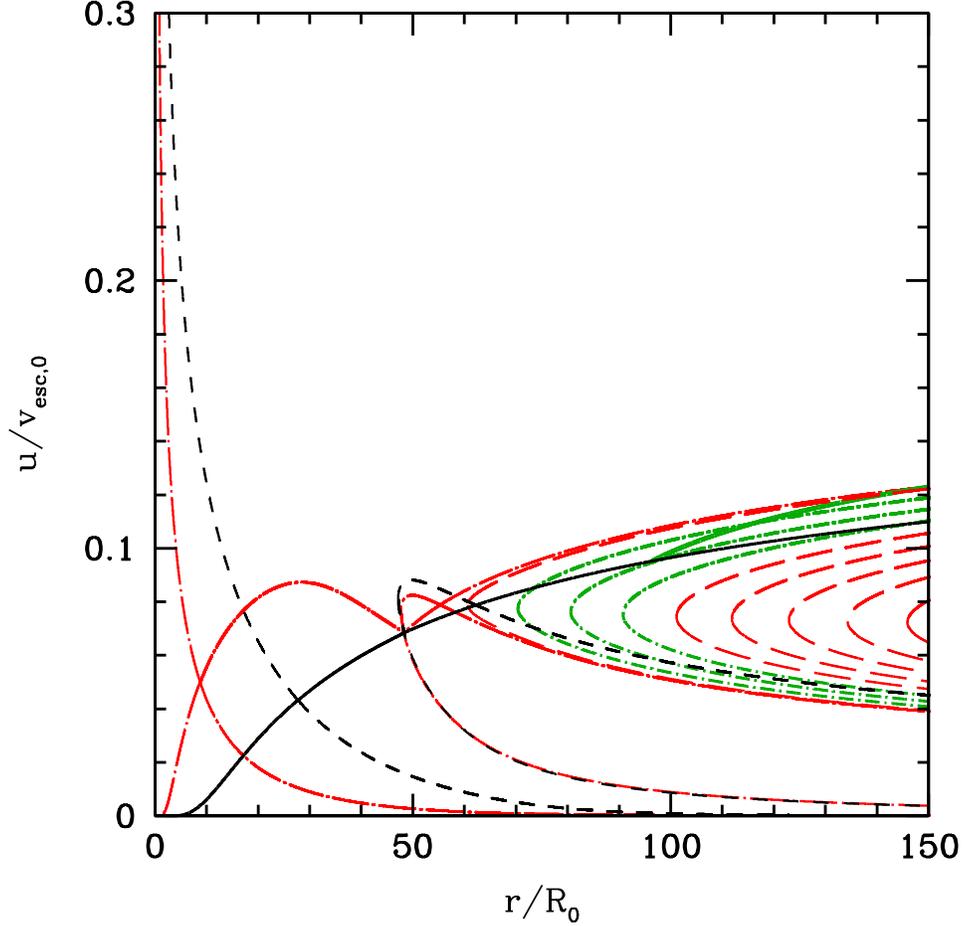
Figure 3.9: Plausible hybrid wind solutions with dust formation occurring beyond the fast point. The red-long-dash-dotted line and the black solid line intersecting at the radial Alfvén point, are the critical solutions of the hybrid wind model and pure WD wind model, respectively. The green-short-dash-dotted lines are possible Type V wind solutions of a hybrid wind ($\Gamma_d = 0.3$) that can leave the star as a dust laden wind after dust formation occurs at the intersections with the solid black WD critical solution. The thick green solid line represents a possible hybrid wind solution with $\Gamma_d = 2$.

also plotted in long-dash-dotted-red and black-dashed lines respectively. The long-dashed lines in red represent the hybrid unphysical solutions of Type V. The intersections of the pure WD critical solution in black, with the Type V hybrid green-short-dash-dotted lines, represent possible locations for the dust formation radius. Thus a wind may start off as a pure WD wind at the surface of the star, pass through all three critical points and then undergo dust formation beyond the fast point. At this stage the critical solution may leave the star by following a hybrid solution represented by the short-dash-dotted lines in green, after dust condensation. The red-long-dashed lines are not plausible as they have either turned and become double-valued (the left most long-dashed-red dashed line) or they do not intersect the solid black line (the long-dashed-red lines to the right of the green-short-dash-dotted lines), at least within the domain indicated. The thick solid green line that intersects the solid black line at about $r \approx 95R_0$, is a hybrid wind solution of Type V. This solution has the dust parameter set to a value greater than unity ($\Gamma_d = 2$). Thus it can be seen that it is possible to have a hybrid wind with $\Gamma_d > 1$ if $r_d > r_f$. In this case, the critical points for the hybrid wind parameters are unphysical and do not lie within the domain $R_0 \leq r \leq 150R_0$ (see earlier discussion relating to Figure 3.8). However in this case, the critical wind solution has already been accelerated through the physically possible pure-WD critical points before dust condensation occurs in the wind. Thus, the hybrid picture can still work with the dust parameter greater than unity as long as dust condensation occurs beyond the fast point. As mentioned before, Figure 3.9 does not apply to AGB stars (since dust condensation likely occurs within a few stellar radii), it is included here for the sake of completeness and understanding the full nature of the hybrid wind solutions.

This completes our discussion of the results of the study. In the following section we present our summary and conclusions along side a short discussion of directions for further investigation.

3.5   Conclusion

We present below a brief summary of the current study and thereafter a short discussion of possible avenues for further work.

3.5.1   Summary

In the preceding discussion we presented a hybrid wind model for AGB stars. The model consists of incorporating a dust-driven wind with a Weber-Davis MHD equatorial wind. The resulting wind momentum equations yielded expressions for the radial and azimuthal velocities of the gas and the dust. After eliminating the azimuthal equations, two radial equations remained in the model that described the velocity profiles of both the gas and the dust. In the model described in this study, we explicitly assumed a steady-state for the wind dynamics.

A WD wind was assumed to begin at the surface of the star, one that would eventually fail if not for the formation of dust grains at a given radius, which allows the hybrid wind to leave the star at super-Alfvénic velocities. The dust formation was assumed to occur abruptly, at a pre-determined radius. All the dust grains were assumed to be perfectly spherical with identical size. It was implicitly assumed that radiation pressure was purely in the radial direction without scattering. The opacity of the grains was implicitly assumed to be such that all of the radiation impinging on the grains was absorbed and imparted momentum to the grains. The resulting drag force was assumed to be purely radial as well. The rationale was to develop a simple model to delineate the key points of the theory.

The hybrid wind ODE was subsequently solved using finite difference methods, for different values of the dust parameter Γ_d. It was found that, in order to achieve a successful hybrid wind, it was necessary for the dust parameter to take values such that $0 < \Gamma_d < 1$, when dust formation occurs within the slow point, i.e., $r_d < r_s$. The effect of changing the dust parameter revealed that $\Gamma_d > 1$, did not yield plausible stellar wind parameters. It was found that when $\Gamma_d \to 1$, all three critical points converged to the the stellar surface.

Finally, the effect of changing the temperature at the base of wind was also investigated. The temperature was changed from $T_0 = 3000\text{K}$ to $T_0 = 2000\text{K}$ to represent a magnetic-cold spot on the equator of an AGB star. It was found that lowering the temperature not only changed the morphology of the family of solutions by suppressing the critical points towards the stellar surface, but also required a greater value of the dust parameter in order to achieve a successful hybrid wind. This additionally resulted in suppressing the dust formation radius as well, towards the photosphere of the star, consistent with the findings of Soker and Clayton [124]. Since the velocity of the

wind, ahead of the magnetic-cool spot in the AGB envelope, was found to be appreciably lesser, than the case when the temperature was the average equatorial temperature, it was accordingly conjectured, that such an effect, would likely produce asymmetric outflows, owing to the formation of MHD instabilities in the wind.

3.5.2 Avenues for further investigation

The question of MHD instabilities is an intriguing one. It presents a direct route for the onset of asymmetric outflows, that have been theorised to cause kicks to the nascent white dwarf within an AGB star [see 175–181]. Hydrodynamic instabilities have already been captured in 2-D simulations of AGB winds [see 58, 59, 169–171]. Therefore the next logical step would be to incorporate magnetic fields; a complicated step, but one that is necessary in order to get a more complete picture of these stars. In such models the dust would form in the envelope in-situ and add to the outflow. In order to realise the onset of MHD instabilities in the flow, a starting point would be a 2-D axisymmetric model with magneto-rotational effects coupled with dust formation in the envelope. The results of the current study could be used as a check for the steady-state solution of such a model. Such an endeavour would undoubtedly yield interesting results and would shed new light upon the formation of instabilities in the outflows from these stars and answer the question of whether such instabilities can lead to appreciably asymmetric mass loss and momentum transfer.

A second avenue, would be to relax one, or indeed several, of the assumptions that were made in deriving the current model. As a first experiment, it may be possible to assume that there also exists drag in the azimuthal direction. Such a drag term would result if there is scattering of radiation in the azimuthal direction, or even if the assumption of spherical dust grains were to be relaxed. This would result in a modification of Eqs. (3.16) and (3.23), to include an azimuthal drag term. Concomitantly, the assumption that the dust-to-gas ratio is small can be relaxed so that Eq. (3.4) cannot be approximated. This would ultimately result in four coupled ODE's (one each for the radial and azimuthal momenta of both the gas and the dust) that can be solved simultaneously to yield the dust and gas velocity profiles in both the radial and azimuthal directions. Third, the dust parameter can be assumed to vary with radius rather than be kept fixed, this may be the easiest to implement. Depending upon the nature of the dependence $\Gamma_d(r)$,

it will change the topology of the solution to Eq. (3.33), since the solutions of Eqs. (3.41-3.44) will change appreciably. Fourth, the dust grain sizes can be assumed to have a distribution, rendering the determination of the drag force more tedious, but definitely closer to reality. Additionally, there can even be assumed to exist a certain degree of scattering, which will effectively change the radiation pressure term in Eq. (3.12). Finally, the effect of pulsations can also be incorporated in the modelling, by including at first a simple radial prescription for pulsation and later incorporating non-radial modes. The effect of pulsation would be two-fold. First, the location of the critical points of the solution will change, thereby altering the morphology of the family of solutions in the $u - r$ phase-space. Secondly, the inclusion of pulsation will alter the density profile, thus altering the continuity equation as well. Therefore the inclusion o pulsation would definitely change the nature of solutions of the hybrid model, but more than that, the problem would then be more tractable within a time-dependent framework in order to capture the complication variations over the timescale of a radial (or non-radial) pulsation. All these changes will necessarily make the computation more intensive, but will all ultimately yield good dividends and further the understanding of AGB winds, complementing the current state-of-the-art models.

Chapter 4

The Magnetised Bellows of Betelgeuse [†]

4.1 Introduction

Betelgeuse ($\alpha-$Orionis), one of the closest cool-evolved supergiant stars to Earth, has been the focus of research for many decades now. However, despite the considerable amount of attention it has received, our understanding of the wind of the star and the nature of its mass efflux remain as yet, mysterious in more ways than one. Even though modern understanding of the stellar wind of this M-type supergiant star, despite formidable challenges on both the observational and theoretical fronts, has progressed well beyond the rudimentary stages [see 194–203], still however, significant gaps in our understanding remain quite entrenched. For example, observations in neither the ultra-violet (UV) nor the infra-red (IR), reveal blue-shifted emission lines; a requisite signature of gas outflow [see 204], should the wind get sufficiently accelerated close to the star. It is also still not known how the stellar wind is supported. We do however understand that dust forms at small and large distances from the photosphere, at radii $r \gtrsim 1.33R_0$ [e.g. 205] and $r \gtrsim 25 - 30R_0$ [e.g. 196, 204, 206–208] respectively where R_0 is the optical photospheric radius. While there is now evidence of dust forming species such as alumina being present in small quantities, in the lower reaches of Betelgeuse's atmosphere ($\sim 1.3 - 1.5R_0$) [see 205, 209], there is no evidence that this results in a dust-driven wind at these distances [e.g. 204]. It has been conjectured that alumina may form close to the star and then, once transported to large distances ($r \gtrsim 30R_0$), may provide nucleation sites for silicate dust to form [see 209]. However, this scenario still requires transport of stellar material to these larger distances in the atmosphere and presently,

it is not known how this is achieved [see 204, 210, 211]. It is believed that a combination of MHD effects, pulsation and convection may be responsible, but there are presently no models that demonstrate this unequivocally [see 204]. On the other hand, efforts at modelling the stellar wind of Betelgeuse (and red supergiants and AGB stars) remain almost as disparate factions, modelling either solely magnetohydrodynamic (MHD) or acoustic waves [e.g. 188, 189, 212, 213] or relying upon a combination of dust- [see 58, 214, 215] and pulsation-driven mechanisms [see 137–142, 159]. Each of these models achieves a modicum of success, while ignoring stellar rotation altogether. Though it is widely acknowledged, that both magneto-centrifugal effects and the presence of dust grains in the gas, may be part of a greater coupled picture [see 188, 189, 210, 216, 217], there have however been no efforts, thus far, at combining the two for a red supergiant like Betelgeuse.

In addition to these concerns, it is also clearly seen that the atmosphere around Betelgeuse is not spherically symmetric. Indeed, there are some inhomogeneities that are seen, attributable to clumps in the outflow [see 200]. These concerns are compounded by the fact that observations reveal that the temperature structure has a complicated form. Differences are seen at the same radius in different parts of the atmosphere [see 218], revealing a slight departure from a spherically symmetric picture. With regard to seeing a clear signature of a stellar wind in the form of blue shifted emission lines, the observations have had severe difficulties in being able to resolve the spectra at close distances from the photosphere [see 204]. Indeed, observations have revealed that in parts of Betelgeuse's atmosphere there is redshifted emission indicating that there may be infall of matter back onto the star [see 219].

The rotation rate of Betelgeuse has also been reported in the literature [e.g. 220, see Table 4.1]. More recently, Zeeman observations also reveal unambiguously, that there exists a magnetic field on the surface of Betelgeuse [see 80, 81]. These observations naturally raise several questions regarding the role that magneto-rotational effects might play in the star's wind. Thus overall, we see that there are several unanswered questions regarding the nature of the outflow from Betelgeuse. Here, we present the very first model integrating MHD and rotational effects with a dust-driven wind scenario for Betelgeuse. The aim of the current study is to shed a new light on these issues and attempt to answer, at least some of these concerns. In this study, we find that the presence of a small magnetic field, on the order of what was recently discovered; of about 1 G [see 80], is sufficient to drive material from close to the stellar surface up and out of its gravity well, by

means of a magneto-rotational wind. Dust condensation later occurs at large distances from the star ($\sim 30R_0$) which finally results in a hybrid-MHD-dust-driven outflow. This model provides a possible alternative resolution of this issue [see 204, 210, 211]. It is to be mentioned at the very outset, that this model is merely suggested as an *additional* mechanism that can play a role in transport of stellar material and is not intended to supplant the altogether feasible models involving MHD or acoustic waves as likely candidates.

The theoretical model that we developed for intermediate mass asymptotic-giant-branch (AGB) stars [see 216] has been extended to tackle the case of a supergiant like Betelgeuse. The reader is referred to our earlier work [see 216, and also Chapter 3] for details of the model. Here we shall present only the salient features of the theory. We also find that the wind velocities that are obtained from the model are in good agreement with current estimates [e.g. 188, 200, 204].

4.2 Betelgeuse's Hybrid Wind Model

For the purposes of modelling, there are some marked differences that Betelgeuse exhibits from a run-of-the-mill AGB star. For example, Betelgeuse is much more massive ($\sim 15M_\odot$, e.g. Smith et al. [197]) than an intermediate mass AGB star. It also has a far more extended and cooler atmosphere. More importantly, the dust condensation radius is much farther out, in terms of stellar radii, from the photosphere in comparison to a canonical AGB star. In the former, the primary process governing mass-loss is the radiation pressure on dust grains that form at close distances from the photosphere, typically no greater than $10R_0$, coupled with strong stellar pulsation. The presence of a magnetic field then has the effect of playing a secondary role governing the gas dynamics. In an AGB star, the hybrid-MHD-dust-driven mechanism is such, that without the onset of dust formation, it is not possible to achieve an outflow and thereafter, the predominant energy exchange in the wind is between the magneto-rotational and gravitational components; see Figure 3.5. In such a scenario, it was seen quite crucially, that dust formation must occur prior to the hybrid model's sonic point and concomitantly, it was seen that the dust parameter, Γ_d was required to be less than unity for achieving a hybrid wind. Such is not the case for Betelgeuse where observations find only a small amount of dust inside $r \lesssim 25 - 30 \; R_0$.

In our earlier study, we had additionally investigated the possibility of

locating the dust condensation radius outside the fast Alfvén point. It was shown that such a hybrid wind is entirely theoretically possible, given typical parameters of an AGB star [see Fig. 9 of 216]. It was concluded therein that while such a scenario is unlikely for a typical AGB star it may well apply to an altogether different type of stellar wind. It is this second type of hybrid-MHD-dust-driven model that is adapted herein to formulate a stellar efflux scenario for Betelgeuse, with dust formation occurring at a large distance $\sim 30~R_0$, from the star.

Our theoretical model can be summed up as follows (the interested reader is referred to Thirumalai and Heyl [216] for the steps involved in the derivation). We imagine that we are looking down upon the two-dimensional equatorial plane of Betelgeuse. Therein, we assume that the magnetic field and the gas (and dust) velocity are functions of purely the radial distance from the centre of the star. The poloidal (co-latitudinal) components of these vectors vanish; this is the fundamental assumption behind the canonical Weber-Davis [see 28, hereafter WD] model for our sun. The gas forms the first fluid and carries the magnetic field. However, unlike the sun, in the atmosphere of Betelgeuse, embedded within the gas is a second fluid; the dust. The two fluids co-exist and are coupled to each other through drag. In an evolved supergiant like Betelgeuse, the circumstellar atmosphere is cool enough ($\lesssim 1000$K) that dust grains can condense out of the surrounding gas [e.g. 196, 204, 206–208]. In fact, direct imaging has enabled estimates for the inner dust shell temperature to be ~ 700 K at around $\sim 30R_0$ [e.g. 221]. Stellar radiation from the interior impinging upon the dust grains, can impart enough momentum to power these exiguous solar sails and propel them outward through the surrounding gaseous matter. However, whilst moving through the gas, the dust *drags* the gas along with it, resulting in a prodigious and combined mass efflux of both dust and gas, from the star; the so-called dust-driven wind. It is to be kept in mind, that the dust-to-gas mass-ratio is small; for Betelgeuse, it is expected to be on the order of $\approx 6 \times 10^{-4} - 5 \times 10^{-3}$ or so [see 222]. Additionally, the dust grains in our model are assumed to be spherical in shape, thus presenting a circular cross-section for radiation pressure to act upon. The surface temperature of Betelgeuse (T_0) plays a key role in determining the hybrid wind parameters, such as the bulk gas velocity at the base of the wind and the location of the critical points (see below). We also assume that the gas has the thermodynamic equation of state of a polytrope, with a polytropic index $\gamma > 1$, where a value of unity represents the isothermal limit. We model the fluid flow as an inviscid one and the elec-

trodynamic properties of the fluid are taken to obey ideal MHD, i.e., there is no Lorentz force acting on the fluid and the electric and magnetic forces balance each other completely. Additionally, the model requires as input, a number of observed quantities, such as the mass of the star, its rotation rate, the surface magnetic field strength and the mass-loss rate. These and other parameters for Betelgeuse are listed in Table 4.1. With these ingredients, upon examining the Euler equations for fluid flow for both the dust and the gas that are coupled with each other and invoking mass and energy flux continuity and ensuring that the divergence of the magnetic field explicitly vanishes within the governing equations, we can arrive at a steady-state description of the hybrid dual-fluid wind in the equatorial plane of Betelgeuse [see 216]. The radial equation for the gas velocity profile is then given by,

$$\frac{dw}{dx} = \frac{w}{x}\frac{N(w,x)}{D(w,x)} \ , \tag{4.1}$$

where, $w = u/u_A$ is the gas speed normalised using the Alfvén speed and $x = r/r_A$, is the radial distance expressed in units of the Alfvén radius. Hereafter, the subscript 'A' refers to values of the different variables at the Alfvén radius. The quantities $N(w,x)$ and $D(w,x)$ are the numerator and denominator respectively and are given by,

$$N(w,x) = \left(2\gamma S_T(wx^2)^{1-\gamma} - \frac{S_G}{x}(1 - \Gamma_d \cdot \Theta(x - x_d))\right)$$
$$\times (wx^2 - 1)^3 + \ S_\Omega x^2(w - 1)\left(1 - 3wx^2 + (wx^2 + 1)w\right) \tag{4.2}$$

and

$$D(w,x) = \left(w^2 - \gamma S_T(wx^2)^{1-\gamma}\right)(wx^2 - 1)^3 - S_\Omega x^2 \times$$
$$(wx^2)^2\left(\frac{1}{x^2} - 1\right)^2. \tag{4.3}$$

In the above equations, the parameters $S_T = \frac{2kT_A}{m_p u_A^2}$, $S_G = \frac{GM_*}{r_A u_A^2}$ and $S_\Omega = \frac{\Omega^2 r_A^2}{u_A^2}$ along with γ uniquely determine the locations of the critical points, and hence the morphology of the family of solutions of Eq. (4.1). Here T_A is the gas temperature at the Alfvén radius, k is the Boltzmann constant and m_p is the mass of a proton. The critical points are, as usual, defined as the locations at which both the numerator and the denominator vanish, thereby keeping the

right-hand side of Eq. (4.1) finite, these are the sonic point, the radial Alfvén point and the fast point [e.g. 28]. The presence of the Heaviside function in Eq. (4.2) represents the formation of dust at the location $x = x_d$, the dust condensation radius in units of the Alfvén radius. The critical wind solution of Eq. (4.1) will yield the gas velocity profile, thereby enabling the determination of all other dependent variables, such as the dust velocity profile (to be discussed below), the Mach number as a function of distance from the star, the azimuthal velocity of the gas, the azimuthal component of the magnetic field, the temperature profile and the density structure of the gas in the envelope of the Betelgeuse. The critical solution of Eq. (4.1) is defined as one that starts off at the base of the wind sub-sonic, passes through the three critical points in a continuous manner and emerges super-Alfvénic at large distances from the star. The dust velocity profile is then given by [see 216],

$$v(r) = u(r) + \left(\frac{\sqrt{a_{th}^4 + 4\left(\frac{\Gamma_d GM_*}{\pi a^2 n_d r^2}\right)^2} - a_{th}^2}{2} \right)^{1/2} , \qquad (4.4)$$

where a_{th} is the thermal speed given by $a_{th} = \sqrt{2kT/\mu m_u}$ and μm_u is the mean molecular mass of the gas and n_d is the dust grain number density, which is assumed to be given by, $n_d m_d/\rho \approx \langle\delta\rangle$ where $\langle\delta\rangle$ is the average dust-to-gas ratio in the wind [see 216]. The dust in the current theory is treated in a simplistic and idealised manner, without rigorously considering the effects of dust radiative properties or including the effects of scattering and absorption on the radiation pressure mean efficiency. While such an analysis would no doubt portray a more complete picture, the current rudimentary treatment nevertheless captures the salient features of the coupled outflow from the star. As our purpose here is to illustrate the feasibility of a hybrid-MHD-dust-driven wind model for Betelgeuse, the current simplistic treatment of dust was considered sufficient.

Eq. (4.1) is solved numerically, and the reader is referred to our earlier work [see 216] for complete details on the numerical methodology. The pertinent points of the method are conveyed below, in brief.

Table 4.1: Various parameters for modelling Betelgeuse.

Parameter	Symbol	Value / Comment
Mass	M_*	$\sim 15 M_\odot$
Radius	R_0	$\sim 650 R_\odot$
Mass loss rate	$\dot{M}$	$\sim 3 \times 10^{-6} M_\odot/\text{yr}$
Surface magnetic field strength	B_0	~ 1 G
Bulk surface gas velocity (radial)	u_0	$\sim 10^{-12} v_{\text{esc},0}$ (vanishingly small)
Surface temperature (effective)	T_0	~ 3650K
Stellar rotation rate	Ω	$\sim 1.2 \times 10^{-8}$ rad/s
Surface escape velocity	$v_{\text{esc},0}$	9.39×10^6 cm/s
Polytropic exponent	γ	> 1
Alfvén Radius	r_A	$\sim 25 R_0$
Alfvén speed	u_A	$\sim 0.15 v_{\text{esc},0}$
Dust Parameter	Γ_d	varied
Dust grain radius	a	spherical grains
Dust grain mass	m_d	$\sim 4/3 \pi a^3 \rho_d$
Dust grain density	ρ_d	4 g/cm^3

4.3 Numerical Method

Eq. (4.1) is solved using the package ODEPACK employing a finite difference method with chord iteration with the Jacobian supplied [see 192, 193]. Initial conditions were supplied at the beginning of the integration. Typical error tolerances for convergence testing that were employed were on the order of 10^{-12} for both the absolute and relative errors [see 192]. For a typical integration, step sizes of 10^{-9} or 10^{-10}, in units of the Alfvén radius, were employed depending upon the region of integration being near the critical points or sufficiently away from them. This resulted in typically $10^9 - 10^{10}$ function evaluations. In the current study, in contrast to [e.g. 216], we located the radial Alfvén point at around $25R_0$ with an Alfvénic temperature of $T_A \approx 720$ K, and Alfvénic velocity $u_A \approx 0.15 v_{\text{esc},0} \approx 14$ km/s, because we wanted to have a dust formation temperature of ~ 700 K with dust condensation occurring at $\sim 30R_0$. The polytropic exponent γ was varied and the locations of the sonic point and the fast point were found according to the method described in [e.g. 216]. Once a particular value for γ is chosen, the bulk radial gas velocity at the photosphere is found using the relation,

$$u_0 = u_A \left(\frac{r_A}{R_0} \right)^2 \left(\frac{T_A}{T_0} \right)^{1/(\gamma - 1)} \tag{4.5}$$

Thus, with these parameters now identified, a solution of Eq. (4.1) is obtained that is continuous through the critical points with a tolerance for testing continuity of about 10^{-8}, about an order of magnitude greater than the integration step size. The polytropic exponent is varied until a suitable set of values for the parameters $\{r_s, u_s, r_f, u_f, u_0\}$, are obtained so that the solution would be first continuous through all the critical points and second, result in a temperature of about 700 K in the vicinity of $30R_0$.

4.4 Results and Discussion

Observations of the circumstellar atmosphere of Betelgeuse indicate that dust primarily exists in the form of a shell at a distance of about $\sim 30R_0$ [e.g. 221]. However, recent observations as discussed above, seem to indicate that there may be small amounts of alumina (Al_2O_3) present rather close to the photosphere [see 205, 209], within $1.5R_0$. However, it is thought that this alumina may be either transient, perhaps even destroyed at around $1.5R_0$ or

even further out in the chromosphere [see 209], or is present in such small quantities as to be unable to support a dust-driven wind at these distances. There is a third possibility, however remote, that the small amount of alumina present does result in a mild dust-driven wind, but the alumina is transparent until it accumulates silicates on its surface [see 223], which occurs in the dust shell at around $30R_0$.

Regardless, observations do not indicate a significant presence of dust in the region $1.5R_0 \lesssim r \lesssim 30R_0$. In this study, we address each of these possibilities, within the framework of the hybrid-dust-driven wind model. Physically, there are four distinct scenarios that emerge and these are listed in Table 4.2. Each of these scenarios are explored in the following discussion.

4.4.1 Scenario 1: Silicate dust forms at $30R_0$

This is the simplest and perhaps the most likely scenario to fit the observations of Betelgeuse's atmosphere. Herein, there is no dust formation at close distances and silicate dust condenses at a distance of about $30R_0$ where the temperature drops to about 700 K. Stellar material is transported from the photosphere to this distance of $30R_0$ by means of a Weber-Davis magneto-rotational wind. This is shown in Figure 5.1, with two cases corresponding to silicate dust formation in reasonable and large amounts at a distance of about $30R_0$. The gas velocities of the critical hybrid-wind solutions of Eq. (4.1) are shown in Figure 5.1 as the red and green long-dashed lines. These solutions start at the base of the wind subsonic and accelerate first through the sonic point at about $5.27R_0$; after this the wind is supersonic. It can be readily seen that the Mach numbers are small for the critical solution close to the photosphere ($r \lesssim 5R_0$). Beyond the sonic point, the wind mildly accelerates through the radial and fast Alfvén points, that are nearly coincident upon one another, and emerges super-Alfvénic at large distances ($r > 25R_0$). A little further out, dust condenses out from the gas at a radial distance of $r_d = 30R_0$, shown by the vertical dashed line marked "r_d". At this distance from the surface of Betelgeuse, the temperature has dropped below the dust condensation temperature for silicates of about ≈ 700 K; the temperature is given by the blue solid line and should be interpreted using the right-hand axis. The temperature profile shown in Figure 5.1, corresponds to Scenario 1a, wherein silicate dust forms in reasonable amounts at around $30R_0$. Thereafter the wind is a coupled MHD-dust-driven wind and the gas outflow rapidly approaches the terminal velocity. Thus, the solution is purely

81

Table 4.2: Different dust formation scenarios in Betelgeuse

Scenario 1a	Silicate dust forms at $r = 30R_0$ in reasonable quantities ($\Gamma_d = 0.5$, $\langle \delta \rangle \sim 1/2000$)
Scenario 1b	Silicate dust forms at $r = 30R_0$ in large quantities ($\Gamma_d = 5$, $\langle \delta \rangle \sim 1/200$)
Scenario 2a	Alumina dust forms at $r < 1.5R_0$ in small quantities ($\Gamma_d = 0.05$, $\langle \delta \rangle \sim 1/20000$) and provides nucleation sites for silicate dust around $r = 30R_0$
Scenario 2b	Alumina dust forms at $r < 1.5R_0$ in large quantities ($\Gamma_d = 0.5$, $\langle \delta \rangle \sim 1/2000$) and provides nucleation sites for silicate dust around $r = 30R_0$
Scenario 3a	Alumina dust forms at $r < 1.5R_0$ in small quantities ($\Gamma_d = 0.05$, $\langle \delta \rangle \sim 1/20000$) and is subsequently destroyed at $r \approx 7.53R_0$ due to a chromospheric component in the atmosphere and silicate dust later forms at $r = 30R_0$
Scenario 3b	Alumina dust forms at $r < 1.5R_0$ in large quantities ($\Gamma_d = 0.5$, $\langle \delta \rangle \sim 1/2000$) and is subsequently destroyed at $r \approx 7.53R_0$ due to a chromospheric component in the atmosphere and silicate dust later forms at $r = 30R_0$
Scenario 4a	Alumina dust forms at $r < 1.5R_0$ in small quantities ($\Gamma_d = 0.05$, $\langle \delta \rangle \sim 1/20000$) and is subsequently destroyed at $r \approx 1.5R_0$ and silicate dust forms at $r = 30R_0$
Scenario 4b	Alumina dust forms at $r < 1.5R_0$ in large quantities ($\Gamma_d = 0.5$, $\langle \delta \rangle \sim 1/2000$) and is subsequently destroyed at $r \approx 1.5R_0$ and silicate dust forms at $r = 30R_0$

WD from the phototsphere ($r = R_0$) to the dust condensation radius ($r = r_d$) and thereafter it is hybrid. This is the primary salient feature of the hybrid wind model developed for Betelgeuse.

Also shown in Figure 5.1 are the corresponding dust velocities for these two models in this scenario, shown by the solid lines that lie above the long-dashed ones. It can be seen that the dust grains are moving radially faster than the gas and dragging the gas along with them. The solid red line represents the dust velocity profile for a model with parameters $\Gamma_d = 0.5$ and $\langle \delta \rangle = 1/2000$; Scenario 1a. In order to investigate the effect of changing the average dust-to-gas ratio and therefore the dust parameter Γ_d, we kept all other parameters of the model fixed, in particular, the radiation pressure mean efficiency and the stellar luminosity, were kept constant. Now, if the average dust-to-gas ratio is increased by an order of magnitude then accordingly, the dust parameter Γ_d must also correspondingly increase by an order of magnitude. Thus, for the second model's results shown in Figure 5.1, we took $\Gamma_d = 5$ and $\langle \delta \rangle = 1/200$; Scenario 1b. For this latter model, the dust velocity profile is shown with the green solid line that lies below the red solid line. This range of the dust-to-gas ratio of $1/2000 \le \langle \delta \rangle \le 1/200$, represents a reasonable bound for the amount of dust in the atmosphere of Betelgeuse [e.g. 222]. It was seen in our earlier work [c.f. Figure 6 of 216] that changing the dust parameter shifted the location of the critical points. In general, increasing the value of the dust parameter Γ_d results in moving the location of the sonic point and fast point towards the surface of the star; this is the case should dust formation occur inside the sonic point in the hybrid wind model. However, it was shown earlier [see Figure 9 of 216, and discussion thereof] that formation of dust beyond the fast point does not influence the location of the critical points. Then, Eq. (4.1) can simply be integrated with the presence of the Heaviside function from $r = r_d$ to $r = \infty$ for a given value of Γ_d. Thus in this case, the wind has already successfully passed through the critical points and emerged super-Alfvénic prior to dust condensation.

Beyond about $r \approx r_A = 25R_0$, the acceleration of the gas in the wind due to dust drag in the second model ($\Gamma_d = 5$, Scenario 1b) starts to decline more steeply than in the case of a hybrid model with a smaller value of $\Gamma_d = 0.5$ (Scenario 1a). Thus, the gas in the wind in the first model ($\Gamma_d = 0.5$, Scenario 1a) at this distance, is still getting accelerated, therefore its terminal velocity is slightly larger and the red long-dashed line lies above the green long-dashed line. Thus, when Γ_d is smaller, acceleration due to radiation pressure continues to have an effect, out to larger distances from the star.
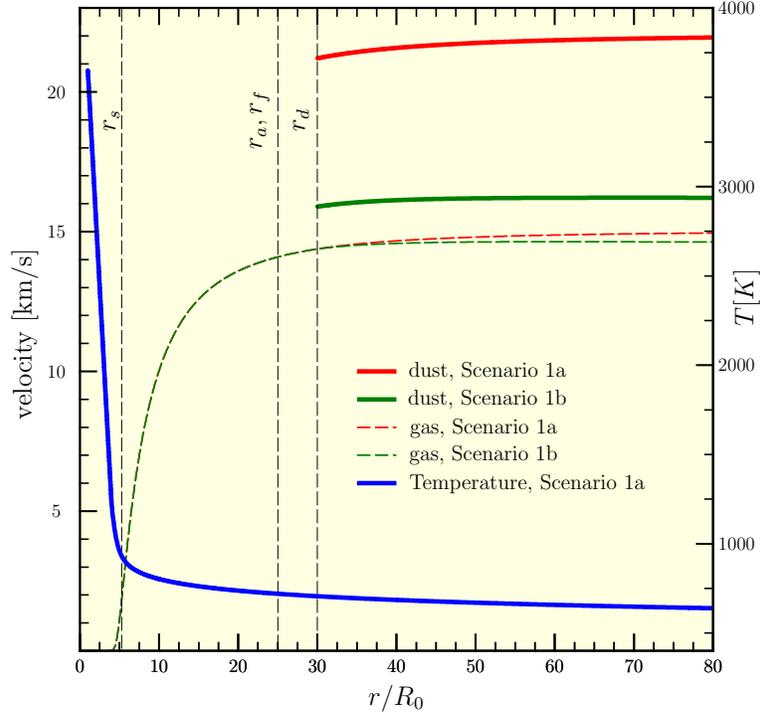
Figure 4.1: A hybrid wind solutions are shown for Scenario 1 with parameters $u_A = 0.15 v_{esc,0}$, $r_A = 25 R_0$, for different Γ_d and remaining parameters as given in Table 4.1. The red and green solid lines trace the dust velocity profiles for Scenarios 1a and 1b respectively, corresponding gas velocity profiles are shown by the red and green long-dashed lines. The decreasing blue solid line traces the temperature and should be interpreted using the right hand y-axis.

The effect on the dust grains is a little counter-intuitive and can be understood by examining Eq. (4.4). We can re-write Eq. (4.4) by replacing the dust grain number density with an expression employing the dust-to-gas ratio as,

$$v(r) = u(r) + \left(\frac{\sqrt{a_{th}^4 + 4 \left(\frac{\Gamma_d G M_* m_d}{\pi a^2 \rho \langle \delta \rangle r^2} \right)^2} - a_{th}^2}{2} \right)^{1/2} . \qquad (4.6)$$

Upon examining the second term under the square-root; the radiation pressure term, we can see that the smaller the value of the average dust-to-gas ratio, the larger this term will be and therefore the larger the value of the dust grain velocity, $v(r)$. Thus, when the radiation pressure mean efficiency and the stellar luminosity are kept constant, then naturally, the dust grain velocity is larger for smaller dust-to-gas ratios; this is the effect seen in Figure 5.1. For the calculations carried out above, we assumed that the dust grains were spherical and were assumed to be on average [see 205] about 0.005μm in size with a density of about 4 g/cm^3.

With regard to scattering of radiation by the dust grains, in the current study this was assumed to be absent, thus precluding the complications that arise upon including this effect. Briefly, the inclusion of isotropic scattering would have the effect, for the simple theory described here, of altering the radiation pressure mean efficiency as, $Q_{rp} \mapsto Q^A + Q^S$, where Q^A and Q^S represent the efficiencies of absorption and isotropic scattering, respectively. In a more rigorous model, these could be calculated for a particular type of dust grain and used in the equations, thus incorporating scattering of photons by dust grains.

Moreover, in the framework of the current theory, the dust grains do not possess azimuthal velocity with respect to the gas. That being said, Poynting-Robertson drag due to scattering of radiation by dust grains would inevitably decelerate the grains in the azimuthal direction, thereby altering the momentum equations further. In reality however, it is to be acknowledged that scattering is probably anisotropic since the dust grains may well align themselves along field lines. Such a detailed analysis involving the complex phenomena touched upon above, while being extremely pertinent and closer to a realistic picture, was considered to be outside the scope of the current study, where the aim is to portray a simple picture.

It is implicitly assumed in our model that dust condensation occurs

abruptly at a distance where the gas temperature (T_{gas}) falls below the dust condensation temperature T_{dust}^c. In addition, we assume that that the conditions are conducive for grain growth. In the current, rather idealised treatment of the dust, we are not concerned with the radiative properties of the dust. We are therefore content with the assumption that the temperature of the outflow is governed by the gas. This was considered to be reasonable considering that the dust-to-gas ratio employed was small $\langle\delta\rangle = 1/2000$. It has also been shown that the temperature profile in the circumstellar environment of Betelgeuse is rather complicated [e.g. 224], with effects such as dust-grain drag contributing to heating. Such an analysis as well as inclusion of rigorous dust radiative properties was considered to be outside the scope of the current study. We simply assume for determining the dust-grain temperature, that the dust grains must be in radiative equilibrium with the stellar luminosity field and that it is optically thin. Therefore, we can assume a relationship for the temperature profile for the dust, outside the dust condensation radius as [e.g. 93, 223],

$$T_d(r) = C\ T_0 \left(\frac{R_0}{2r}\right)^{2/5}, \forall\ r \geq 30R_0, \tag{4.7}$$

where, the coefficient C, depends upon the radiation pressure mean efficiency. In the current study we are treating the dust in a rather simplistic manner, therefore instead of calculating the radiation pressure mean efficiency we can assume that the coefficient C lies in a range between zero and unity, i.e., $0 < C \leq 1$. This then allows us to calculate a range of values for the dust temperature at the condensation radius, $T_d(30R_0)$. The mean of these calculated values, for the given range in C and the adopted values of R_0 and T_0 given in Table 4.1, is found to be $\langle T_d\rangle|_{30R_0} \approx 390$ K. This rather rudimentary estimate is in reasonably good agreement with the value obtained by Harper et al. [222], of 360 K at around $33R_0$. The dust in the current model may therefore be able to mimic, in a qualitative sense, the radio and IR behaviour of the dust model of Harper et al. [222]. Given the idealistic nature of the current hybrid-MHD-dust-driven wind theory, the formulation of a detailed model, such as that described by Harper et al. [222], was considered to be outside the scope of the current investigation. We shall end with a cautionary note, that a detailed analysis would nevertheless be required, before conclusions can be drawn about the dust related physics and we acknowledge this as a limitation of the current theory.

In summary, the result in Figure 5.1 demonstrates that it is possible to obtain a coupling between magneto-centrifugal effects and the usual dust-driving mechanism. There are however a few pertinent observations with respect to the hybrid wind model in specific, that warrant mentioning. First, it can be clearly seen, that magneto-centrifugal effects, with a small magnetic field (~ 1 G) and slow rotation, $\Omega \approx 1.2 \times 10^{-8}$rad/s, [see 220] can quite clearly lift material from the photosphere of Betelgeuse up into the circumstellar atmosphere. In the latter region, dust condenses in the gas to result in a hybrid wind at large distances. This reveals that magneto-centrifugal driving can be an additional mechanism for solving the mystery of how to lift stellar material out into the circumstellar envelope in not only Betelgeuse, but potentially in all cool, evolved supergiant stars. Second, the temperature profile obtained in the solution, is reasonably consistent with observations [see 200, 204, 218]. For example, the profile indicates that around $2R_0$, the gas temperature drops to about 2840 K, lying well within the measured range [see 218].

In addition, the temperature range in the region $R_0 \leq r \leq 4.1R_0$ can be inferred from Figure 5.1 to be $1200 \lesssim T \leq 3650$ K and it can be seen that lower limit for the observed [Fe II] emission of 2110 K [see 204] lies in this region. It can also be seen that the gas velocities are small in this region, consistent with the lack of observations for Doppler blue-shifted wind signatures.

Third, the resulting terminal velocity is about $14-15$ km/s; this is consistent with present estimates [e.g. 188, 211] and in reasonably good agreement with the adopted value of about ~ 10 km/s for modelling by Harper et al. [204]. It is to be remembered that measured or inferred values for the outflow velocity would indicate a somewhat averaged value for gas velocity at a given distance from the star; however, within the framework of the current model, outflow velocity is calculated in the equatorial plane alone. Simulations of large-scale MHD convection in Betelgeuse have suggested that it is possible to have variation in the radial velocities on the order of $1-10$ km/s in both up- and down-flowing regions [e.g. 225]. In addition, it is also to be mentioned that the stellar efflux is thought to be variable in Betelgeuse, observations seem to suggest variability over a 40 year period or so [see 196], however the current framework assumes a steady-state case, thus the interpretation of the calculated values of outflow obtained in this study, need to be tempered by these observations. In light of all this, we considered the agreement of velocities to be good.

In addition, once the radial velocity profile has been determined, it is possible to determine the azimuthal component of the magnetic field. With this it becomes possible to estimate, *á posteriori*, the importance of the Lorentz force and any ion-neutral drag. The rationale being to check the validity of the ideal-MHD assumption. In the current framework, it is assumed implicitly that the ions and neutrals are well coupled in the equatorial plane and non-ideal MHD effects such as ambipolar diffusion are negligible and thus ignored. A way to assess this is to calculate the ratio of the gyrofrequency and the momentum exchange rate [e.g. 226] as,

$$\beta_j(r) = \frac{Z_j e B(r)}{m_j c} \frac{(m + m_j)}{\rho(r) \langle \sigma v \rangle_j}. \tag{4.8}$$

Where β_j is the ratio for the jth ionic species, Z_j is the atomic number, m_j is particle mass of the given ionic species, B is the magnitude of the magnetic field, e is the electronic charge, c is the speed of light and m is the averaged particle mass of the neutrals. Here ρ is the gas density, determined once the solution to Eq. (4.1) is calculated. Finally, $\langle \sigma v \rangle_j$ is the ion-neutral collision momentum transfer rate coefficient [see Table 2.1 and Equation 2.34 of 53] and is given by

$$\langle \sigma v \rangle_j = 2.0 \times 10^{-9} \left(\frac{m_H}{\mu} \right)^{1/2} \text{ cm}^3 \text{ s}^{-1}, \tag{4.9}$$

where, $\mu = m_j \mu_n / (m_j + \mu_n)$ is the reduced mass in a typical ion-neutral collision, with μ_n the mean molecular mass of neutrals. Similarly, the electron-neutral collision momentum transfer rate can be determined as [e.g. 52, 226],

$$\langle \sigma v \rangle_e |_r = 8.3 \times 10^{-9} \times \max \left[1, \left(\frac{T(r)}{100 \text{ } K} \right)^{1/2} \right] \text{ cm}^3 \text{ s}^{-1} \tag{4.10}$$

Assuming that the largest single ionic species is Si, we can then calculate the ratio of the gyrofrequency to the momentum exchange rate, for both the ions (β_{Si}) and the electrons (β_e).

We find that $\beta_{Si}^{max} \approx 7.9 \times 10^{-7}$, while $\beta_e^{max} = 2.7 \times 10^{-4}$. In general, we find over the entire domain for r in the equatorial plane, that $\beta_{Si}(r) \ll \beta_e(r) \ll 1$. As mentioned earlier, one of the central assumptions in the model is that the Lorentz force vanishes in the fluid, i.e., we have force-free MHD, therefore it is to be expected that the ratios β of the gyrofrequencies to the

momentum transfer rate, would also accordingly be small. This then implies, that for the radial range considered in this study, i.e. $0 \leq r \leq 80R_0$, the Hall and ambipolar diffusion terms arising from electron-ion drift and ion-neutral drift respectively, are negligible. Additionally, the conductivity of the plasma can be estimated using the usual relation, $\sigma = 10^7 T_e^{3/2} \mathrm{K}^{-3/2} \Omega^{-1} \mathrm{cm}^{-1}$ [e.g. 227], where T_e is the electron temperature, such that $T_e(r) > T_{\mathrm{gas}}(r)$. Figure 5.1 shows that the minimum temperature for the gas far away from the photosphere is about $T_{\mathrm{gas}}^{\mathrm{min}} \approx 640$ K. We can therefore find an estimate for the lower limit of the conductivity using this temperature and estimate a value of $\sigma_{\mathrm{min}} \approx 1.6 \times 10^{11}$ Ω^{-1} cm^{-1}, yielding a magnetic Reynolds number [e.g. 228] of $\mathrm{Re}_m = U L \mu_0 \sigma_{min} \sim 10^{23}$, so Ohmic diffusion is unimportant ($U \sim 10$ km/s and $L \approx R_0$ are typical velocity and length scales for Betelgeuse and μ_0 is the permeability of the vacuum, $4\pi \times 10^{-7} \Omega \mathrm{s/m}$). The assumption of effectively infinite plasma conductance, is then a reasonable assumption. Thus, we see that the central assumption of ideal-MHD in the equatorial plane of Betelgeuse is a reasonable first approximation to make, for the purpose of conveying a simple picture.

Finally, the Alfvénic Mach numbers in the inner region of the circumstellar envelope are small and actually, do not exceed unity before the sonic point, located at around $5.27R_0$. Therefore our model does not suffer from the same drawbacks as many Alfvén wave models that have the artifact of having large Mach numbers close to the surface of the star. Indeed, in our model the wind only becomes super-Alfvénic beyond the Alfvén point at around $25R_0$ and even then, only mildly so.

In Figure 5.2 we have shown the azimuthal velocity, $u_\phi(r)$ of the gas (red solid line). The dust is assumed to co-rotate with the gas, thus the azimuthal velocity profile shown in the figure is also true for the dust (for $r \geq r_d$), since there is no drag between the dust and the gas in the azimuthal direction. The azimuthal velocity profile is obtained once the radial velocity profile is known [see 216]. The velocity profile obtained is typical for a magneto-rotational wind. The dotted lines in the figure and in its inset represent the rotation of the star [see 220]. It is readily seen that the azimuthal wind velocity closely traces the observed rotation of the star and only begins to depart markedly after $r \approx 4.5R_0$. This decoupling from stellar rotation occurs in the inner wind region of the magneto-rotational wind, at a physical distance corresponding to $\approx 2.03 \times 10^{14}$cm, for Betelgeuse. It is also interesting to note that at large distances the azimuthal velocity of the gas is strongly de-coupled from the stellar rotation rate. Therefore, the chromospheric component in
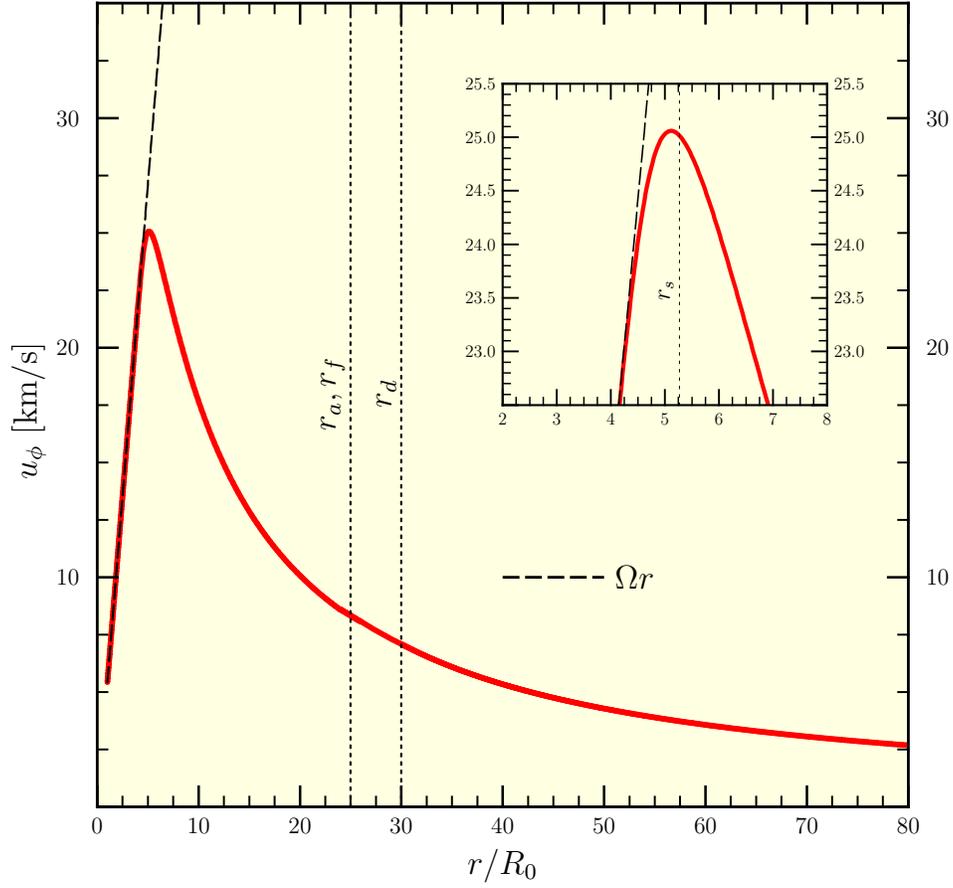
Figure 4.2: The azimuthal velocity of the gas is shown as a function of the radial distance (red solid line) for Scenario 1a. The inset shows a magnified region around the peak of the profile around the sonic point.

the atmosphere at a few stellar radii may also appear to be de-coupled from stellar rotation as was observed by Harper and Brown [198]. However, it is to be remembered that the hybrid-MHD-dust-driven theory presented in this study, concerns itself with the equatorial plane alone, while the observations of Harper and Brown [198] are spatially resolved in the cross-dispersion direction; this may have an averaging effect along the dispersion direction. Thus, the theoretically obtained rotational decoupling that occurs in the equatorial plane, in the current study, may well be quite a bit different from the observations of Harper and Brown [198]. Therefore any inferences drawn in this regard must be tempered by the observation that the current model is a rather simple picture, with concomitant limitations.

We now turn our attention to the question of spots on the surface of Betelgeuse and the related question of temperature inhomogeneities. Recent observations [see 229–232] suggest that there may be a few (on the order of 2 or 3) large spots on the surface of Betelgeuse, indicating that there are temperature inhomogeneities on the surface of Betelgeuse. We therefore chose to model Betelguese with two different photospheric temperatures in order to examine the effect of spots on its equator [see 124].

In the current study however, these spots were taken to be colder than the effective temperature so that the temperature profile close to the photosphere $1.0 \leq r \leq 3.5R_0$ may be investigated so as place constraints on the alumina formation region, if at all, close to the star. The spots were considered to have temperatures of 2600 K and 3000 K respectively, well within fluctuations of about 1000 K or so, about the effective temperature [see 233]. The magnetic field was left unchanged so that the effect of changing a single parameter could be patently established. The solitary requisite constraint that was placed however, was that regardless of the photospheric spot temperature, the temperature at a distance of about $30R_0$ should be in the vicinity of 700 K, for silicate dust formation in the circumstellar shell at this distance. Thus, the radial Alfvén point was left unchanged. Therefore the other free parameter that was varied in order to achieve an efflux was the bulk gas radial velocity at the surface, u_0. The gas velocity profiles were then solved for by integrating Eq. (4.1), above the spots located at the photosphere. Figure 4.3 shows the temperature profiles obtained in the wind ahead of the spots in the close circumstellar environment of Betelgeuse. The temperature profile obtained using the effective temperature of 3650 K is also shown for comparison as the top most blue solid line. It can be seen that the lower the photospheric temperature, the flatter the temperature profile is, in the inner
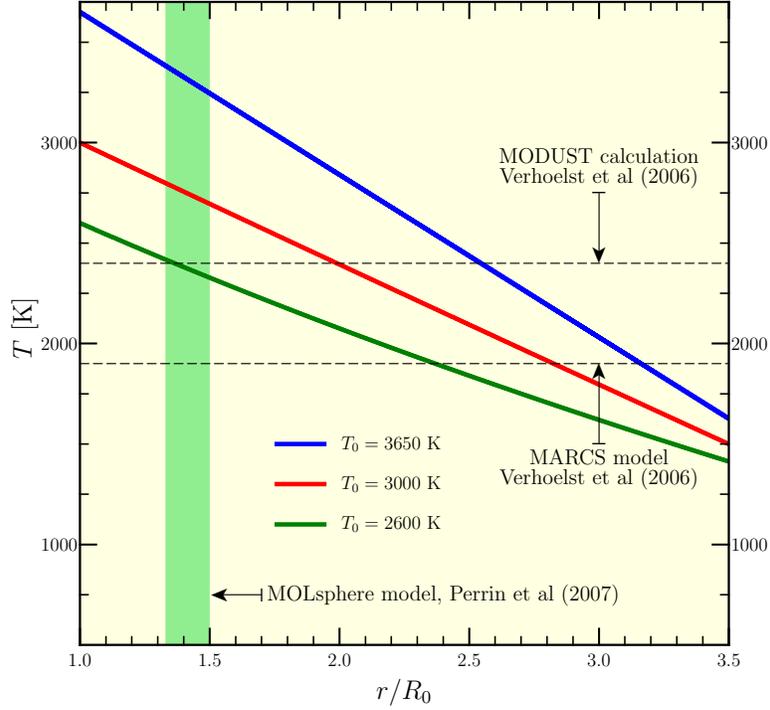
Figure 4.3: Temperature profile in the close circumstellar environment with two photospheric spots of temperatures 2600 K and 3000 K. The two dashed horizontal lines show calculated alumina condenstation temperatures from two different models. The vertical green shaded region shows the MOLsphere region predicted by Perrin et al (2007). Only the model with photospheric spot temperature of $T_0 = 2600$ K has an overlap with the MOLsphere region for the alumina condensation temperature range.

wind region. Thus the red solid line ($T_0 = 3000$ K) lies below the blue solid line ($T_0 = 3650$ K) and above the green solid line ($T_0 = 2600$ K).

Also shown in Figure 4.3 are two temperature bounds calculated by Verhoelst et al. [209] for alumina dust condensation. The upper bound of 2400 K is the value that they arrived at by demanding radiative equilibrium of dust grains using the radiative transfer code MODUST, for alumina condensation. The lower bound of 1900 K on the other hand, is the temperature that their MARCS model predicts in the region about $0.5R_0$ above the photosphere. It is to be kept in mind however, that at such short distances, the MARCS model may have limitations due to acoustic wave heating and the breakdown of the assumption of local thermal equilibrium. With this caveat in place, it can be seen that this range of temperature only occurs in the region $2.55R_0 \leq r \leq 3.16R_0$ for the model with $T_0 = 3650$ K, indicating the possible alumina dust condensation region. Similarly, the corresponding range for the model with the spot of temperature $T_0 = 3000K$ places this region to be $1.99R_0 \leq r \leq 2.83R_0$. Both these regions lie well outside the observed thin shell for the MOLsphere of $1.33R_0 \leq r \lesssim 1.5R_0$ [e.g. 205, 209]; shown as the green band in Figure 4.3.

It is however interesting to note, that the model for the photospheric spot temperature of 2600 K, predicts a possible alumina condensation region of $1.37R_0 \leq r \leq 2.37R_0$. This region quite interestingly, overlaps slightly with the MOLsphere model of Perrin et al. [205]. However, it is to be remembered that current observations do not reveal any dust in the region $1.5R_0 \leq r \leq 20 - 30R_0$ [e.g. 209]. Thus, we see that within the framework of the hybrid-MHD-dust-driven model presented in this study for Betelgeuse, it is possible to form alumina dust very close to the photosphere in the region of interest; $1.33R_0 \leq r \lesssim 1.5R_0$, by lowering the photospheric temperature to about 2600 K. For temperatures above this, our model predicts the possible alumina condensation region to lie further out from the photosphere and there is no overlap between our model and the MOLsphere model of Perrin et al. [205].

Additionally, it can be seen in Figure 4.3, that temperatures predicted by the models with photospheric spots are different at the same height above the photosphere, in the close circumstellar environment of Betelgeuse. Thus, the observed variability in temperature [see 218] at the same radial distance from the photosphere can, at least in part, be attributed to the presence of spots. The temperature profile in the wind above the spots is different from that above normal regions. Thus, our model with equatorial spots, can reproduce these differences in temperature, at least qualitatively, indicating

an asymmetric temperature distribution.

Presently, we discuss the other possible scenarios for dust formation listed in Table 4.2. The motivation for these scenarios is the observation that alumina dust may be present in small quantities close to the photosphere of Betelgeuse. Therefore, one can naturally ask the question whether alumina first forms in sufficient amounts to facilitate a slow dust-driven wind and second, what would happen if alumina dust is subsequently destroyed at some distance from the star? In this regard there are a few possibilities. It is to be kept in mind that there are no observations that support the presence of dust between $\approx 1.5R_0$ and about $20 - 30R_0$ [e.g. 209]. Therefore, the first possibility is we can assume that alumina forms in both small and sufficient quantities close to the star (*Scenarios 2a and 2b* respectively), to facilitate a slow wind, but the alumina dust is transparent until it accumulates silicates on its surface beyond $30R_0$. In both these models, the assumption is that alumina dust provides nucleation sites for silicates to form upon.

The second possibility is that alumina dust forms close to the star (in small and large quantities; explored in *Scenarios 3a and 3b* respectively). This results in a slow MHD-dust-driven hybrid wind. The dust is then destroyed at around $\approx 7.53R_0$ due to a chromospheric component in the atmosphere where the temperatures are high [e.g. 219]. Note that Lobel and Dupree [219] adopted a value for the radius of the photosphere as $700R_\odot$, whereas we have adopted $650R_\odot$, hence we obtain the outer limit for the chromosphere as $\approx 7.53R_0$ rather than $7R_0$. Silicate dust later condenses at large distances $\sim 30R_0$. It is implicitly assumed in this model that alumina dust is transparent so as not to reveal any dust signature between $1.5R_0$ and $30R_0$.

The third possibility is we can assume formation of alumina in the region $r \leq 1.5R_0$ (in small and large quantities; explored in *Scenarios 4a and 4b* respectively). This dust then gets destroyed at a distance of $1.5R_0$ due to perhaps convective turbulence in regions closer to the photosphere and changes in pressure or perhaps due to temperature variability in the chromosphere. Whatever the reason may be, dust is not seen between $1.5R_0$ and about $20 - 30R_0$. Silicate dust later condenses at large distances.

The purpose of these scenarios is not to elaborate on the details of dust spallation, but rather to ask the pertinent question that, within the framework of the hybrid-MHD-dust-driven wind theory, is it possible to achieve an efflux, should alumina first form and perhaps even be destroyed in the wind, at some distance? In addition, it is to be kept in mind that for the models

94

presented in Scenarios $2 - 4$ the photospheric temperature was considered to be $T_0 = 2600$ K.

4.4.2 Scenarios 2 and 3: Alumina forms and has an influence on the wind

Figure 4.4 shows both Scenarios 2 and 3 each containing two hybrid wind models. Scenario 2 is shown in the upper panel of Figure 4.4 while Scenario 3 is shown in the lower panel. The red and green solid lines represent the dust velocity profiles in these scenarios for small and large amounts of alumina condensation, respectively. Similarly, the long-dashed green and red lines represent the corresponding gas velocity profiles. Quite importantly, in Scenarios 2a and 2b, the numerator in Eq. (4.2) was modified to accommodate for the two different dust species; alumina and silicates as,

$$N(w, x) = \left(2\gamma S_T (wx^2)^{1-\gamma} - \frac{S_G}{x} \times (1 - \Gamma_d^{\text{alumina}} \cdot \Theta(x - x_d^{(1)}) - \right.$$

$$\left. \Gamma_d^{\text{silicate}} \cdot \Theta(x - x_d^{(2)})) \right)$$

$$\times (wx^2 - 1)^3 + S_\Omega x^2 (w - 1) \left(1 - 3wx^2 + (wx^2 + 1)w \right), \quad (4.11)$$

where, $x_d^{(1)} = 1.38$ for alumina dust condensation and $x_d^{(2)} = 30$ for silicate dust condensation. Thus, Eq. (4.1) is integrated as a pure WD wind in the region $R_0 \leq r \leq 1.38R_0$, then with alumina dust in the region $1.38R_0 \leq r \leq 30R_0$ and finally with both alumina and silicate dust in the region $30R_0 \leq r \leq 40R_0$. In Scenario 2 (upper panel of Fig. 4.4) the portion of the hybrid solution in the region $1.38R_0 \leq r \leq 30R_0$ is a critical solution as it navigates through the critical points. The portions of the solutions outside this interval are not part of the critical solution, but rather lie elsewhere in the $u - r$ phase space of each of the models, respectively.

The alumina condensation radius of $1.38R_0$ lies in the range suggested by Perrin et al. [205], for the thin molecular shell that contains alumina in the close circumstellar environment of Betelgeuse. This value also lies inside the green shaded region of Figure 4.3. The lower red solid lines in Figure 4.4, in both the upper and lower panels, represent the dust velocity profiles for models with formation of alumina dust in small quantities ($\langle \delta \rangle = 1/20000$). This is an order of magnitude less than what is expected for silicate dust in the dust shell at around $30R_0$. Accordingly, we assumed an order
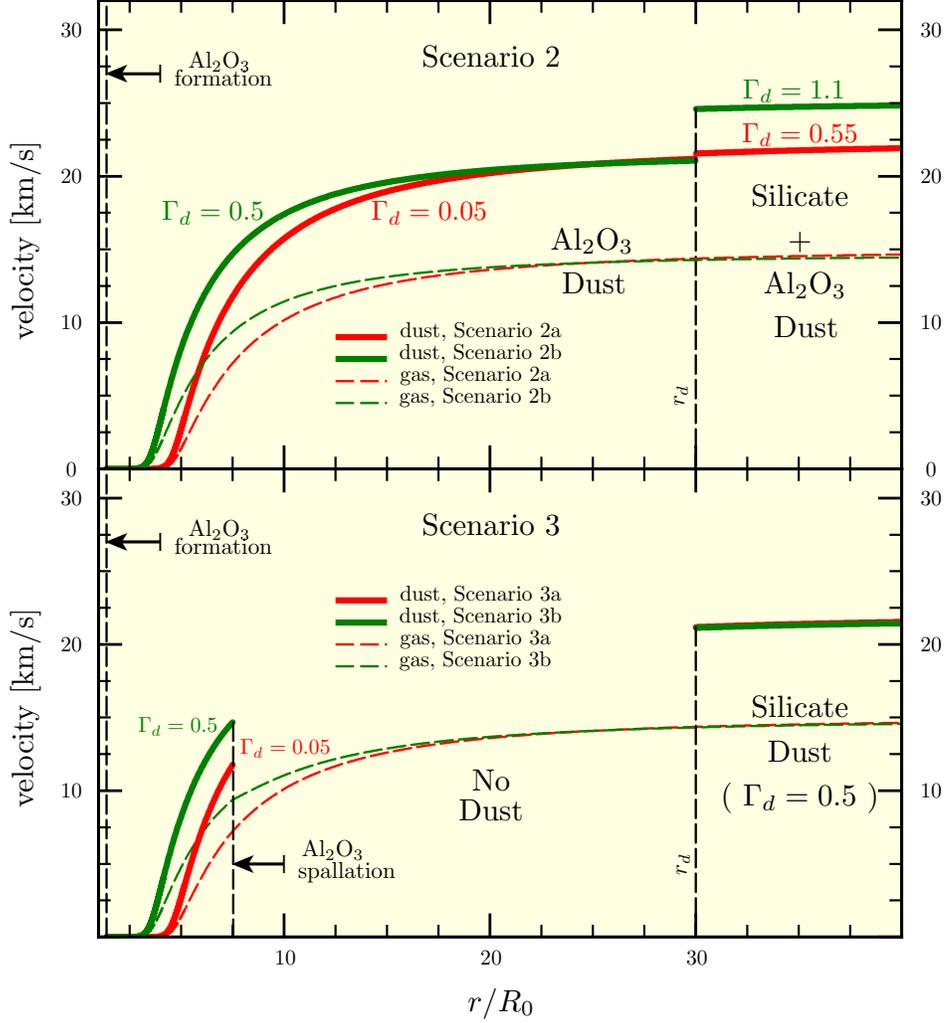
Figure 4.4: Dust and gas velocity profiles for Scenarios 2 (upper panel) and 3 (lower panel). The dust velocities are shown using solid lines and the gas velocities with long-dashes lines. The dust and gas velocity profiles for the models with greater dust formation, i.e. larger Γ_d, lie above those with lesser amount of alumina dust formation in the inner wind region. Scenario 2 shows influence of the presence of both alumina and silicate dust species in the wind, whereas, Scenario 3 shows the effect of alumina spallation at the edge of the chromosphere at $7.53R_0$.

of magnitude smaller value for the dust parameter, $\Gamma_d = 0.05$; it is to be mentioned that even smaller values may be adopted.

The upper green solid lines in both panels, prior to the silicate condensation region, represent the dust velocity profiles for models with formation of alumina dust in large quantities ($\langle \delta \rangle = 1/2000$). The dust parameter was then given by $\Gamma_d = 0.5$. The purpose being to explore a somewhat extreme case in which alumina forms in large enough amounts to sustain a mild MHD-dust-driven hybrid wind, but is transparent to observations. While such a scenario may well be remote, we explore it for the sake of completeness.

It can clearly be seen in both Scenarios 2 and 3, as expected, that if the dust parameter is larger, then it results in a greater acceleration of the wind closer to the photosphere. Thus, the green lines lie above the red ones. For smaller values of the dust parameter, on the other hand, the effect of this acceleration due to dust, continues to have an effect out to larger distances. As a result, the red long-dashed lines rise above the green long-dashed lines at some distance. Ultimately the terminal velocity of the models with the smaller value of Γ_d are slightly larger due to this effect.

In the upper panel in Figure 4.4, at the silicate dust condensation radius of $30R_0$, we notice a discontinuity, since the silicate dust condenses as well. The red solid line in this region corresponds to a model with parameters $\Gamma_d = \Gamma_d^{\text{alumina}} + \Gamma_d^{\text{silicate}} = 0.05 + 0.5 = 0.55$ with $\langle \delta_{\text{total}} \rangle = 1/2000$. Thus Eq. (4.1) is integrated outwards from $r = r_d$ with these parameters. Similarly the green solid line in this region in the upper panel, represents a model with parameters corresponding to $\Gamma_d = \Gamma_d^{\text{alumina}} + \Gamma_d^{\text{silicate}} = 0.5 + 0.6 = 1.1$, again with $\langle \delta_{\text{total}} \rangle = 1/2000$. Notice that we have kept the dust-to-gas ratio fixed in both cases to the same value. The silicate dust condenses from the gas abruptly at $30R_0$. As a result, the discontinuity in the dust velocity across the silicate dust condensation radius is seen in both models. However, the jump in the velocity is much larger for the green solid line in comparison to the red solid line as this model has a higher value of Γ_d for the same $\langle \delta_{\text{total}} \rangle$.

On the other hand, in the lower panel of Figure 4.4 showing scenarios 3a and 3b, alumina dust is assumed to form close to the photosphere, but is then destroyed at a distance of about $7.53R_0$ due to a chromospheric component. There are some rather subtle differences from Scenarios 2a and 2b and these are detailed below.

In the lower panel of Figure 4.4, once again the lower solid red line shows the dust velocity profile for a model with parameters $\Gamma_d^{\text{alumina}} = 0.05$ and $\langle \delta_{\text{alumina}} \rangle = 1/20000$. The upper green solid line meanwhile, represents

97

the dust velocity profile for a model with parameters $\Gamma_d^{\text{alumina}} = 0.5$ and $\langle \delta_{\text{alumina}} \rangle = 1/2000$. As described earlier, the solutions start off at the base of the wind at the photosphere, subsonic and alumina dust formation occurs at $r = 1.38R_0$. Thus from $r = R_0$ to $r = 1.38R_0$, Eq. (4.1) is integrated as a pure WD wind without the dust parameter. It is to be mentioned that in this region the solutions are not part of the pure WD critical solution. Alumina dust condensation radius is shown at $1.38R_0$ for the two models in this scenario. As can be seen, the model with the larger dust parameter has a greater velocity, evidenced by the green lines lying above the red ones.

In the region $1.38R_0 \leq r \lesssim 7.53R_0$ the winds are hybrid MHD-dust-driven winds and Eq. (4.1) is integrated with the presence of dust parameters for each of the two models. In this region the solutions for the gas velocities are parts of the critical solutions for each of the two hybrid-MHD-dust-driven winds. Alumina dust spallation is assumed to occur at a distance of about $\approx 7.53R_0$ and this produces the sharp discontinuity in both the dust and gas velocity profiles seen in the lower panel of Figure 4.4. In the region $7.53R_0 \lesssim r \leq 30R_0$, Eq. (4.1) is therefore integrated without the dust parameter, i.e. as a pure WD wind, for the two models. However, the gas velocities in this latter region, are no longer part of the respective critical solutions. Hence, these solutions pass through only the radial Alfvén point, but not the fast point. Thus at large distances, these solutions are sub-Alfvénic. Therefore they constitute the so-called failed wind solutions as $r \to \infty$. As a result these models become theoretically non-viable as one of the primary requirements is that the wind should be super-Alfvénic at large distances. Thus with alumina dust spallation in between the sonic point and the radial Alfvén point, at around $7.53R_0$, we see that it is not possible to sustain a physically viable efflux.

For the sake of completeness, we have included silicate dust in Scenario 3. At a distance of $30R_0$ in the wind, silicate dust condensation occurs and beyond $30R_0$, the wind is once more a hybrid MHD-dust-driven wind. The dust velocities are once again calculated after the gas velocity profiles are determined, according to Eq. (4.4). It can be seen that the gas outflow velocity profiles for the two models cross one another at around the radial Alfvén point. As a result the dust and gas velocity profiles in the region $r \geq 30R_0$, for the model with greater amount of alumina (green dashed and solid lines, Scenario 3b) lie slightly below the one with the lesser amount of alumina (red dashed and solid lines, Scenario 3a). In both these models it is assumed that silicate dust forms with a dust-to-gas ratio of $\langle \delta_{\text{silicate}} \rangle =$

1/2000, with $\Gamma_d = 0.5$.

In summary we see in the upper panel of Figure 4.4, that it is possible to obtain a hybrid-MHD-dust-driven wind if alumina forms close to the photosphere and results in a mild wind transporting stellar material to large distances. Silicate dust condenses at a distance of $30R_0$ and adds to the stellar efflux. Inspecting the upper panel of Figure 4.4 reveals that the model with a larger amount of alumina formation close to the star (Scenario 2b), is not viable, since observations do not indicate such a large amount of alumina close to the photosphere. In the second model (Scenario 2a) with a smaller value of Γ_d, while the amount of dust may well be reasonable, current observations do not reveal any dust velocities. The only way we can reconcile this model with observations is by assuming that the alumina dust is transparent.

In the lower panel of Figure 4.4 on the other hand, once again it is seen that it is possible to have alumina formation at close distance, within $1.5R_0$ and subsequent spallation at around $\approx 7.53R_0$ and still achieve a solution with the formation of silicate dust. However, as stated earlier, the gas velocity solutions are not part of the critical solution. As a result, these solutions are sub-Alfvénic as $r \to \infty$. Therefore, they cannot be considered to be viable wind solutions. As a result, alumina spallation at a distance of $7.53R_0$ does not result in a wind, within the framework of the current steady-state hybrid-MHD-dust-driven theory. In addition, the spallation of alumina dust at a distance of around $\approx 7.53R_0$ results in the discontinuity seen in the lower panel of Figure 4.4. Such large discontinuities are a source of concern, particularly because they can lead to fluid flow instabilities and shocks. However, this is not within the realm of investigation of the current theory, a simple steady-state treatment. It may be possible that such instabilities may precipitate in motion of material back towards the photosphere as is seen by Lobel and Dupree [219]. Thus we see that scenarios 3a and 3b are theoretically possible; however, the primary concern is that they predict sub-Alfvénic velocities at large distances. Thus the results of Scenarios 3a and 3b cannot be completely reconciled with observations. This may well point towards the inference that the simplest scenario discussed earlier, Scenario 1a, may well the be the most pertinent.

We now turn our attention to the final scenario before summarising the results obtained in this study.

4.4.3 Scenario 4: Alumina spallation close to the photosphere

Presently, we discuss the cases where alumina dust condensation occurs in both small and large quantities close to the photosphere and subsequent spallation occurs at around $1.5R_0$; Scenarios 4a and 4b respectively. The rationale being, that the reason why alumina dust is not seen between $1.5R_0$ and around $30R_0$ is that it gets destroyed at around $1.5R_0$. This is an alternative to assuming that the alumina grains are transparent until they accumulate silicates on their surfaces. The question then is whether it is possible to achieve a hybrid outflow with alumina dust formation and spallation included in the framework of the hybrid MHD-dust-driven picture. It is to be mentioned at the very outset that the formation of alumina in both small and large quantities was not seen to produce any appreciable influence on the stellar efflux in this scenario. The silicate dust and corresponding gas velocity profiles obtained were seen to be nearly identical to those shown in Figure 5.1. Thus, formation and subsequent spallation of alumina, all within $r = 1.5R_0$ was not seen to be a physically relevant picture for the stellar efflux of Betelgeuse. Nevertheless, a brief description of the calculation and some pertinent points are conveyed below.

For Scenarios 4a and 4b it was assumed that alumina condensation occurs at $r = 1.38R_0$ in small and large quantities. Thus Scenario 4a has parameters $\Gamma_d^{\text{alumina}} = 0.05$ and $\langle \delta_{\text{alumina}} \rangle = 1/20000$, while Scenario 4b has parameters $\Gamma_d^{\text{alumina}} = 0.5$ and $\langle \delta_{\text{alumina}} \rangle = 1/2000$. From $r = R_0$ to $r = 1.38R_0$, Eq. (4.1) is integrated as a pure WD wind without the dust parameter. It is to be mentioned that these parts of the solutions are not part of the WD critical solution. In the region $1.38R_0 \leq r \leq 1.5R_0$, the winds are hybrid MHD-dust-driven winds and Eq. (4.1) is integrated with the presence of dust parameters for the two models. However alumina is dust is then abruptly destroyed at a distance of $1.5R_0$ and therefore in the region $1.5R_0 < r < 30R_0$ the wind is a pure WD type of wind and Eq. (4.1) is integrated without the dust parameter. The portion of the solution in the region $1.5R_0 < r < 30R_0$ corresponds to a pure WD critical solution, one that passes through all three critical points. The critical solution then carries the wind out to a distance of $30R_0$ at which point, silicate condensation occurs and silicate dust grains form. The dust and gas velocities for the two models in Scenario 4a and 4b in the region $r \leq 1.5R_0$ were calculated to be miniscule; $\leq 10^{-10}$ cm/s and as a result immeasurable and not detectable in the form of wind signatures. Thus

in this scenario, for all intents and purposes, alumina dust condensation can be considered to be absent in the wind as it does not produce any appreciable effect, in which case Scenario 4 quite simply reduces to Scenario 1; the most viable picture thus far in the discussion.

This brings us to the end of our discussion of the results obtained in this study. In the following section, the findings are summarised.

4.5 Conclusion

In this study we presented a hybrid-MHD-dust-driven wind model for the red supergiant Betelgeuse ($\alpha-$Orionis). The model is a direct application of our previously derived theory that consists of incorporating a dust-driven wind with a Weber-Davis MHD equatorial wind [see 216].

Overall, the results shown above indicate that MHD effects and radiation pressure on dust grains can have a complementary role to play in the winds of supergiants such as Betelgeuse, alongside the altogether complicated and involved physics of thermal pulsation and convection and other equally complex phenomena such as MHD or acoustic waves.

Within the framework of the model, we investigated four different scenarios for dust formation in the atmosphere of Betelgeuse. It was seen that the simplest hybrid wind scenario; Scenario 1a, was perhaps the most viable one as well. In this picture, a pure WD wind was assumed to begin at the surface of the star, one that would eventually leave the star as a hybrid-MHD-dust-driven wind after the formation of dust grains at the dust condensation radius at around $30R_0$. This provided a mechanism for lifting stellar material from the photosphere of the star up into the atmosphere while maintaining low Mach numbers for the wind in the inner wind region. The dust formation was assumed to occur abruptly at the dust condensation radius where the temperature is low enough for silicate grains to condense. In our model, all the dust grains were assumed to be perfectly spherical with identical size. It was implicitly assumed that radiation pressure was purely in the radial direction without scattering. The opacity of the grains were implicitly assumed to be such that all of the radiation impinging on the grains was absorbed and imparted momentum to the grains. The resulting drag force was assumed to be purely radial as well.

In Scenario 1a, since dust grain condensation occurs outside the fast point, as in our earlier work [see 216], it was seen that adopting a range of values

for the dust parameter Γ_d, resulted in different hybrid winds with different terminal velocities.

It was also seen that by adopting the values for different parameters for Betelgeuse, as given in Table 4.1, the resulting hybrid wind model is able to rationalise several of the observed features of this red supergiant, such as the predicted wind velocities, observed atmospheric temperatures at different distances from the photosphere, observed region of dust formation and temperature inhomogeneities in the circumstellar envelope.

We additionally investigated the possibility of having more than one dust species form in the wind. Scenarios 2-4 dealt with the formation of alumina dust close to the photosphere of Betelgeuse. We also investigated the effect on the efflux, should alumina be destroyed at some distance. In each of these scenarios it was seen that it was possible to form a hybrid-MHD-dust-driven wind, however it was not possible to reconcile the predictions of these models completely with the current observations regarding dust formation and lack of wind signatures interior to the dust shell of Betelgeuse. In addition, we found that for these scenarios to work, within the framework of the hybrid-MHD-dust-driven wind theory, it was required that the surface temperature should be around $T_0 = 2600$ K, to overlap with recent observations for the close circumstellar environment of Betelgeuse [e.g. 205]. Therefore, it is to be concluded that while it may well be possible for alumina to form close to the photosphere of Betelgeuse, it probably does not influence the wind outflow interior to $\sim 30R_0$. However, it is to be remembered that the current model is merely a steady-state treatment of an infinitely more complicated picture. All that can be said at this stage is that the current theory seems to point towards the simplest case; Scenario 1a, as the most likely candidate. It is to be mentioned that the current model may play a complementary role alongside the altogether different and complex mechanisms for stellar outflow involving MHD or acoustic waves.

Future work will extend the modelling towards a more realistic full two- or three-dimensional picture, concomitantly including a poloidal magnetic field and allowing the entire system to be described dynamically with time varying magnetic and velocity fields with convection. The final and indeed ultimate picture would of course, be to then include the stochastic effects of dust formation and dynamics, alongside calculation of the radiative properties of the dust, as is done in some recent work [see 58, 234]. Realisation of this task will ultimately explore the true nature of the outflow from Betelgeuse and other red supergiants, which is now beyond doubt, understood to be more

complicated than at first imagined and yet, presenting a hurdle surmountable in steps. Perhaps the very first of those steps, is the steady-state model described in the current study.

Chapter 5

Is Mira a Magneto-Dusty Rotator? [†]

5.1 Introduction

Mira (omicron-Ceti) is a relatively close evolved star that is in its Asymptotic Giant Branch (AGB) infancy. It is the template upon which the class of stars called *Mira variables* are based, which are characterised most strikingly, by large-amplitude long period variability that is readily discernible. Mira itself varies over a period of about 332 days [e.g. 235]. This variability is linked to its process of mass-loss attributed to the complex interplay of pulsation and convection and the concomitant effect of radiation pressure on dust grains in its envelope [e.g. 59, 137, 145, 214].

This mass-loss is central to stellar evolution of low- and intermediate-mass stars, from the AGB phase to the planetary nebula phase. As such, Mira has been studied quite extensively in the literature at a variety of wavelengths, by employing an array of different instruments. A wealth of understanding has emerged from millimetre and sub-millimetre observations of transitions of the CO molecule in the envelope of Mira, which have been instrumental in probing the physical nature of outflow and the structure of the envelope of Mira. At centimetre wavelengths, for probing the the physical processes at short distances from the photosphere (a few stellar radii), studies of SiO masers have proved to be crucial. These studies have provided an understanding of the dynamics of molecular shells around Mira and other AGB stars. Imaging of Mira in the near infra-red (IR) and optical wavelengths have provided tools for measuring the diameter, while mid-IR low resolution spectra of silicate emission features have facilitated our understanding of the physical conditions and distribution of the dust. This cumulative effort over the past few decades has not only yielded dividends in terms of our under-

---

[†]Based on an article submitted to a journal and currently in review.

standing of the star, but contrastingly and quite importantly, raised more questions than those that have been answered.

Over the years, observations of Mira have revealed much about its intriguing nature. For example, Planesas et al [see for e.g. 236, 237] were among the first to discover asymmetries in the envelope of Mira and they concluded that a mildly collimated outflow may exist in the atmosphere of Mira. The authors speculate that perhaps a mild or even a moderately strong magnetic field, in the equatorial plane at the photosphere, may be responsible for producing density enhancements in the equatorial plane needed for the observed degree of asymmetry in the wind, without producing large effects in the overall structure of the envelope. Shortly thereafter, observations by Bester and co-workers [e.g. 196, 206] found evidence for dust formation in the inner regions of Mira's atmosphere, at around $3R_0$, where R_0 is the photospheric radius. They were also able to estimate the dust temperature at the inner dust radius to be around 1200 K. Around the same time, Young [see 238] did a survey of Mira variables using CO (3-2) and CO (4-3) spectra and was able to estimate outflow velocities. He found a value of about 4.8 km/s for the outflow velocity for Mira's wind, and surmised that the actual outflow velocity was probably larger. He additionally concluded that it is likely that even in Mira variables with small mass-loss rates, radiation pressure on dust grains can support the wind in the inner atmosphere while at a few hundred AU from the star there is no evidence for wind acceleration.

Elsewhere, Lopez et al [see 235] in an involved study found asphericity and temporal variations in the dust shells of Mira using 11 μm visibility observations. They computed both spherically and axially symmetric radiative transfer models for the atmosphere of Mira in order to rationalise the observed visibilities. They were able to model the asphericity of the atmosphere using discrete shells, disks and clumps with a modicum of success. Their findings indicate that while hot spots may modify the spatial power spectrum, resulting in the perceived stellar elongation, it is more likely, they conclude, that a disk in addition to a hot spot may be a more appropriate model. Their CO maps revealed two lobes of gas, that the authors interpret as a slow bipolar outflow, possibly resulting due to partial collimation of high density gas in the equatorial plane, in the inner part of the molecular envelope. In addition to this asymmetry, they also observed asymmetry in the TiO emission in the atmosphere which they attribute to the presence of the hot white dwarf companion star, Mira B, or possibly due to innately inhomogeneous dust distribution in the atmosphere of Mira itself. Overall

105

they modelled the observed visibility of Mira using two shells of dust, at $3R_0$ and at $12R_0$, and they found that the axially symmetric models fared better than the spherically symmetric ones. Moreover, they found that their models with clumps of dust were also reasonably good at rationalising the observed visiblity of Mira. Their models with dust clumps assumed a spot probably exists on the photosphere, in the direction of the clump.

Around the same time Knapp et al [see 239] found evidence for double winds in not only Mira but in numerous other Mira variables, by observing CO(2-1) and CO(3-2) line emission. They speculated that the slower component of the double wind may be due to the resumption of mass-loss after it has been abruptly stopped by some change in the stellar properties. For Mira they found that the fast wind component had a velocity of about 7 km/s while the slow wind had a velocity of about 2.5 km/s. Ryde et al [see 240, 241] in an effort to investigate the physical phenomena in Mira's wind at intermediate distances of $100 - 1000R_0$, carried out observations of photospheric light scattered by vibrational-rotational transitions of the fundamental band of CO. They were able to arrive at an estimate of the mass-loss rate of about $3 \times 10^{-7} M_\odot$ yr^{-1} and an expansion velocity of the envelope of about 2.5 km/s, in agreement with Knapp et al [see 239], however still different from the estimates of Young [see 238]. While it is seen that observations made utilising the line emission spectra from CO transitions, various authors arrive at similar results for the expansion velocity of Mira's envelope at greater distances in the circumstellar environment (CSE) of Mira, there is however not much agreement for the values of the wind velocity in the inner regions of the wind. This situation is further complicated by the fact that in the literature several wind driving mechanisms have been proposed such as jets and acoustic waves etc. Nearly all the mechanisms are able to reproduce the mass-loss and the expansion and turbulent velocities and are even able to reproduce the radio line profiles reasonably well. As a result, as noted by Ryde et al [see 240, 241], there is little consensus regarding the actual expansion velocity of Mira's envelope and even less agreement regarding the wind in the inner wind regions. This may be understandable given the fact that Mira itself may be undergoing non-radial pulsations [242]. In addition to this, there may be present spots on the surface of the star that alter the wind dynamics over the lifetime of the spot [see 127, 216, 242, 243]. Mira B may also be interacting with the wind of the AGB star. And finally, the dust distribution may well be asymmetric and variable over short timescales [59, 196] further complicating observations.

To add to the mysteries surrounding Mira, Soker and Kastner [see 244] developed a model for flaring on AGB stars motivated by the discovery of magnetic fields in AGB stars and X-ray observations of AGB stars [e.g. 245, 246]. They find that the X-ray observation may be attributable to magnetic flares from Mira, but they cannot rule out the possibility that Mira B may be the point of origin of the X-ray luminosity. Moreover, they also make the case from their observation that it is possible that Mira B could be a low-mass main-sequence companion [see 247], although recent evidence seems to support that Mira B is indeed a white dwarf companion [see 248] and the latter authors speculate that this may imply that Mira B can be the launch site for streams, i.e., bipolar outflow. Thus, the nature of the emission and also perhaps the efflux may well be influenced by the white dwarf companion. Indeed the question of such companions and indeed the effect that planets even may have on the asymmetries in the envelopes of AGB stars, has been investigated by Soker [127, 128, 129], Soker and Harpaz [130].

Furthermore, adding to the uncertainties regarding the properties of Mira is that it is essentially a variable star, which is of course linked to the pulsations and convection within the star itself. This, in addition to the fact that the atmosphere is very extended makes the determination of the diameter of the star, essentially a definition of the photosphere, rather difficult. Different researchers arrive at various stellar diameters. For example, Perrin et al [see 249] found that by varying the opacity of the molecular layer just ahead of the photosphere, they are able to account for the apparent changes in the diameter of Mira. In turn, they find that the radius of the star is $346 \pm 46R_0$ when it is at its minimum and $358 \pm 48R_0$ at its maximum. Accordingly, they also find a higher stellar effective temperature (c.f. [e.g. 250, 251], who find $464 \pm 80R_0$ as the radius of Mira).

While transitions of the CO molecule have been the source of a great deal of data for the star Mira, for gaining insight into the physical processes that occur close to the photosphere, at a distance of a few stellar radii or so, as mentioned earlier, SiO maser emission has proven to be the tool of choice. For example, the continuous data obtained for the star TX Cam, by Diamond and Kemball [see 72, 252], provided a detailed picture of the dynamics at the base of the stellar wind, close to the photosphere. Their observations did not reveal large scale contraction of the envelope, as was previously thought, but rather revealed that there is more a predominant expansion, thereby giving hints of the underlying complex phenomena at work, particularly in light of the fact that in TX Cam, there exists a surface magnetic field of about

$5 - 10$ G. Following these observations, Cotton et al [253] find that the SiO emission in Mira occurs in a ring that is only half of the diameter of the inner dust radius. They also find that the AGB star R Aquarii seems to be rotating with a period of about 22 yrs at the distance of the SiO maser emission. Utilising similar data modelling and reduction techniques, Cotton et al [82] detect possible stellar rotation in Mira with a period of $89 \times \sin(i)$ yrs, where 'i', is the unknown angle between the rotation axis and the line of sight to the star. Moreover, they find that the polarization of the SiO maser emission suggests that the magnetic field in Mira is predominantly radial and the jet-like structures in their maser observations suggest that the magnetic field may be elongated in the direction of the masing structure. The authors attribute this to one of two effects; either the dynamical feature observed in the envelope is dragging the magnetic field or, the gas is constrained to flow along the magnetic field. In either case, they conclude that a magnetic field is likely present in the atmosphere of Mira, at the distance of the masing structures. This may suggest that the magnetic field in Mira may well be similar to the magnetic fields observed in other AGB stars, where they find a variety of magnetic field strengths, ranging from a few milli gauss to several tens of gauss [e.g. 73, 77, 78, 254, 255]. Such field strengths suggest that the role of magnetic fields in shaping the outflow as well as properties of the envelope may well be non-trivial and indeed dynamically important. A recent theoretical study by Busso et al [see 256] reveals that buoyant flux tubes may play an important role in transport of stellar material processed in the neighbourhood of the hydrogen burning shells in Red Giant Branch (RGB) and AGB stars. They find that a large magnetic field on the order of 10^6 G is needed at the base of the cold bottom processing region, which from simple arguments of flux conservation translates to a surface field of $\lesssim 20$ G, in agreement with Herpin et al [see 73].

Thus, overall we see that there are several unanswered questions with regard to the nature of the outflow from Mira, its extended atmosphere, and indeed regarding the star itself. From the brief discussion of the literature presented above, it appears that the role that magnetic fields may play in shaping the outflow and influencing certain dynamic features of the envelope cannot be ignored. In the current study we present a rudimentary model integrating the effects of rotation, an equatorial magnetic field and the usual dust-driving picture into one cohesive scenario for delineating certain aspects of Mira's outflow. This theory has already been successfully employed for describing the outflow of the red supergiant star Betelgeuse ($\alpha-$Orionis) [see

243] as well as for intermediate mass AGB stars [see 216]; the work presented here represents an extension of the theory to the low-mass end of AGB stars, by applying it to the star Mira which is about $1.5M_\odot$ [e.g. 257]. The aim of the current work is to raise the question, particularly now that stellar rotation may have detected in Mira [see 82], that *how important is the magnetic field in the stellar outflow and can Mira be a magneto-dusty rotator, given the current observations?*

This chapter is organised as follows. Section 5.2 describes the hybrid-MHD-dust-driven wind model in brief. A listing of the different physical properties of Mira employed in the modelling is also given therein. The numerical methods employed are also discussed in brief. In Section 5.3 we present the results alongside a discussion. Thereafter a summary is provided and implications of the current theory are discussed in Section 5.4, in the conclusion.

5.2 Mira's Hybrid-Wind Model

We confine our attention to an axisymmetric model in the equatorial plane of the star. Therein, the velocity fields of the gas and the dust as well as the magnetic field are assumed to have radial and azimuthal components. However, the azimuthal components are functions of purely the radial distance from the star; this is the central assumption behind the canonical Weber-Davis [see 28, hereafter WD] model for our sun. There are two fluids; the gas which carries the magnetic field and secondly the dust, which moves through the gas, dragging the gas with it. The two fluids are coupled by a drag term in the usual way. The dust-to-gas ratio is kept small around $\sim 1/355$ [e.g. 196] and the individual dust grains are assumed to be spherical in shape. The gas is assumed to have a polytropic equation of state, with a polytropic exponent $\gamma > 1$, where a value of unity represents the isothermal limit. We assume ideal MHD where there is no Lorentz force in the fluid. The input parameters for model of Mira's wind are listed in Table 5.1. A steady-state description of the gas velocity in the hybrid wind in the equatorial plane of Mira can be written as [see 216],

$$\frac{dw}{dx} = \frac{w}{x}\frac{N(w,x)}{D(w,x)} \ , \tag{5.1}$$

where, $w = u/u_A$ is the gas speed normalised using the Alfvén speed and $x = r/r_A$, is the radial distance expressed in units of the Alfvén radius. Hereafter, the subscript 'A' refers to values of the different variables at the Alfvén radius. The quantities $N(w, x)$ and $D(w, x)$ are the numerator and denominator respectively and are given by,

$$N(w, x) = \left(2\gamma S_T(wx^2)^{1-\gamma} - \frac{S_G}{x}(1 - \Gamma_d \cdot \Theta(x - x_d))\right)$$
$$\times(wx^2 - 1)^3 + S_\Omega x^2(w - 1)\left(1 - 3wx^2 + (wx^2 + 1)w\right) \quad (5.2)$$

and

$$D(w, x) = \left(w^2 - \gamma S_T(wx^2)^{1-\gamma}\right)(wx^2 - 1)^3 - S_\Omega x^2 \times$$
$$(wx^2)^2\left(\frac{1}{x^2} - 1\right)^2. \quad (5.3)$$

In the above equations, the parameters $S_T = \frac{2kT_A}{m_p u_A^2}$, $S_G = \frac{GM_*}{r_A u_A^2}$ and $S_\Omega = \frac{\Omega^2 r_A^2}{u_A^2}$ along with γ uniquely determine the locations of the critical points, and hence the morphology of the family of solutions of Eq. (5.1). Here T_A is the gas temperature at the Alfvén radius, k is the Boltzmann constant while m_p is the mass of a proton. The presence of the Heaviside function in Eq. (5.2) represents the formation of dust at the location $x = x_d$. The dust velocity profile is then given by [see 216],

$$v(r) = u(r) + \left(\frac{\sqrt{a_{th}^4 + 4\left(\frac{\Gamma_d GM_*}{\pi a^2 n_d r^2}\right)^2} - a_{th}^2}{2}\right)^{1/2}, \quad (5.4)$$

where a_{th} is the thermal speed given by $a_{th} = \sqrt{2kT/\mu m_u}$ and μm_u is the mean molecular mass of the gas and n_d is the dust grain number density, which is assumed to be given by, $n_d m_d/\rho \approx \langle\delta\rangle$, with $\langle\delta\rangle$, the average dust-to-gas ratio in the wind. Eq. (5.1) is solved numerically on a computer [see 216, 243]. In the following section the results are presented alongside a discussion.

Table 5.1: Various parameters for modelling Mira. The variable parameters are listed as such.

Parameter	Symbol	Value / Comment
Mass	M_*	$\sim 1.5 M_\odot$
Radius	R_0	$\sim 464 R_\odot$
Mass loss rate	$\dot{M}$	$\sim 3 \times 10^{-7} M_\odot/\mathrm{yr}$
Surface magnetic field strength	B_0	variable
Bulk surface gas velocity (radial)	u_0	variable
Surface temperature (effective)	T_0	$\sim 2500\mathrm{K}$
Stellar rotation rate	Ω	$2\pi/[89 \times sin(i)]\ \mathrm{yr}^{-1}$
Rotation axis angle	i	variable
Surface escape velocity	$v_{\mathrm{esc},0}$	3.52×10^6 cm/s
Polytropic exponent	γ	> 1
Alfvén radius	r_A	variable
Alfvén speed	u_A	variable
Dust Parameter	Γ_d	variable
Dust grain radius	a	spherical grains
Dust grain density	ρ_d	2.3 g/cm^3

5.3 Results and Discussion

Along with the basic ingredients of the model listed in Table 5.1, the set of parameters $\{B_0, u_0, u_a, r_a, \gamma, \Gamma_d, i\}$ are varied until a critical solution to Eq. (5.1) is obtained that satisfies the following criteria.

1. The solution passes through all three critical points; the sonic point, the radial Alfvén point and the fast point

2. The solution is continuous through the radial Alfven point.

3. The velocity profile starts at the base of the wind sub-sonic and attains a super-Alfvénic terminal velocity at large distances

4. The temperature range in the dust condensation region (within a few stellar radii from the photosphere) is consistent with observations.

5. The gas terminal velocity is consistent with observations.

This optimisation procedure carried out in tandem with integrating the differential equation in Eq. (5.1) results in a picture of a hybrid MHD-dust-driven wind for Mira as shown in Figure 5.1. The critical wind solution is shown as the solid red line, which comprises of two parts, L_1 and C_2. These two lines intersect at the dust formation radius r_d, which in the current model is located at $3R_0$. In the region $r \geq r_d$ Eq. (5.1) is integrated with the presence of the dust parameter Γ_d, which represents dust grain drag acting on the gas; it is this part of the solution that is labelled C_2. On the other hand, inside $r \leq r_d$ there is no dust and as a result Eq. (5.1) is integrated in this latter region without the dust parameter, as a pure WD solution. This part of the solution is labelled as L_1. Thus in the region $R_0 \leq r \leq r_d$, a pure WD mechanism is responsible for transport of stellar material. Together, $L_1 + C_2$ forms the combined hybrid MHD-dust-driven wind. The radial Alfvén point and the fast point lie nearly coincident upon one another; shown by the black dashed vertical line at $r \approx 43R_0$. Theoretically speaking, if we assume that dust condensation occurs at the photosphere, then we would obtain the combined solution $C_1 + C_2$ by integrating Eq. (5.1) with the dust parameter, over the entire domain $R_0 \leq r \leq 100R_0$. However, in the atmosphere of Mira, dust formation occurs at the dust condensation radius $r = r_d$ and not at the photosphere. Therefore, inside the dust radius, $r \leq r_d$, the wind starts off at the photosphere at some velocity u_0, and proceeds outwards
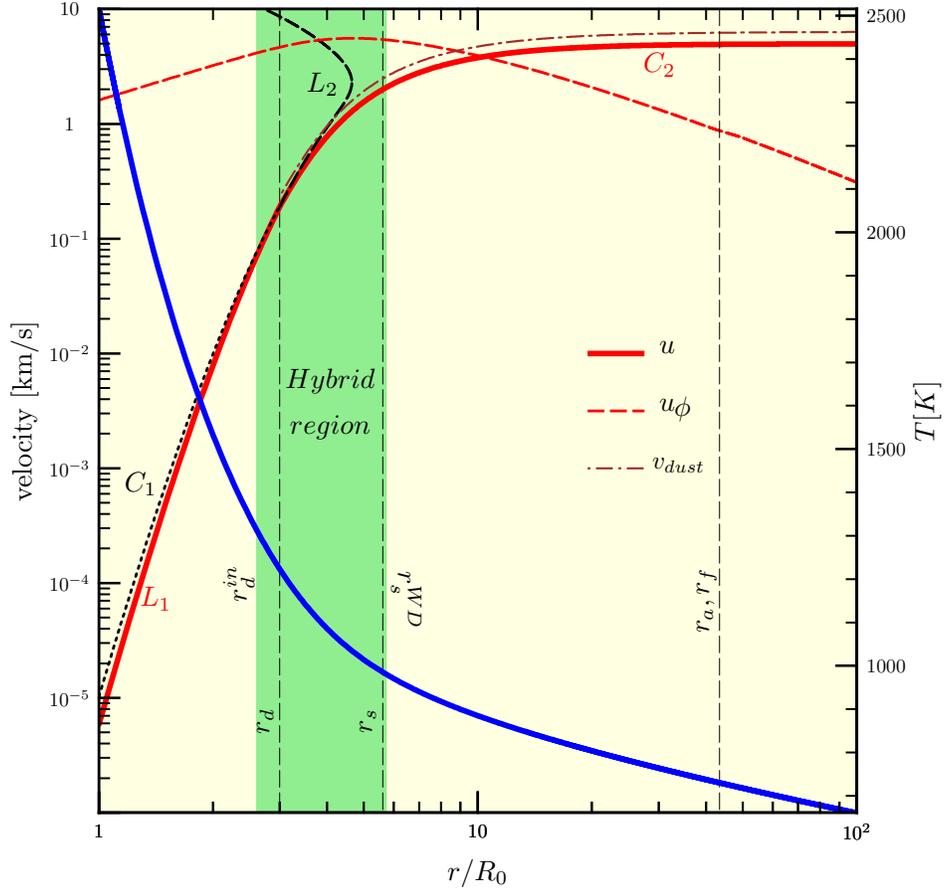
Figure 5.1: Hybrid wind solution is shown for Mira with parameters $u_A \approx 0.14 v_{esc,0}$, $r_A \approx 43.47 R_0$ and for $\Gamma_d \approx 0.06$ and remaining parameters as given in Tables 5.1 and 5.2. The red solid line ($L_1 + C_2$) traces the hybrid MHD-dust-driven wind solution for Mira. The decreasing blue solid line traces the temperature and should be interpreted using the right hand y-axis.

along the trajectory L_1, and after dust condensation at $r = r_d$, the solution then switches to proceed outward along C_2, rather than continue along the unphysical solution L_2.

Thus, it is seen explicitly, that without the onset of dust formation at $r = r_d$, there wouldn't be any efflux from Mira, since there is only one solution (C_2) that passes through all three critical points, and emerges super-Alfvénic at large distances. As can be seen, the gas terminal velocity is about 5km/s in the equatorial plane, which is in reasonably good agreement with estimates of the wind velocity of Mira [e.g. 238, 257].

The dust velocity profile is also shown in Figure 5.1 as the brown dot-dashed line. This is computed according to Eq. (5.4), once the gas velocity profile is known. The dust velocity is slightly larger than the gas velocity, as expected, due to dust-driving. The red dashed line represent the azimuthal velocity profile of the gas. This profile is typical for a magneto-centrifugal wind. The blue solid line shows the temperature profile in the atmosphere of Mira and should be interpreted using the right hand side axis. The photospheric temperature is about 2500 K for the model shown. Finally, the green shaded area shows the so called *hybrid region*. This region is bounded to the left by $r = r_d^{in} \approx 2.6R_0$, this is the lower limit for the inner dust radius as given by [e.g. 196]. To the right, the hybrid region is bounded by the sonic point of the pure WD magneto-centrifugal model. The sonic point of the hybrid model lies at $r \approx 5.61R_0$; just inside the hybrid region. As seen in our earlier study [see 216], one of the ways in which a hybrid wind is possible is if the sonic point of the hybrid model lies within the sonic point of the pure WD model; i.e., $r_s < r_s^{WD}$. Moreover, the dust formation radius must also then lie inside $r \leq r_s$. The temperature in the hybrid region can be inferred from the temperature profile shown, to be about $1000 \lesssim T \lesssim 1300$ K, which is well within the observed range of temperatures at this distance from the star [e.g. 196, 206, 235, 249].

Finally the optimised values for the different variable parameters in the model are given in Table 5.2. Notice that the surface radial magnetic field at the photosphere is obtained to be about 4 G, which is within the range of field strengths estimated by Herpin et al. [73] and Busso et al. [256] for AGB stars.

Presently, we turn our attention to the question of hot spots on the photosphere of Mira, and the related question of the influence of the spot on the stellar wind, ahead of the spot in the atmosphere. Figure 5.2(a) shows a hybid MHD-dust-driven wind model where the photospheric temperature is

increased to about 2700 K. However, in this second model instead of formulating a hybrid wind model as before, with dust formation occurring within the sonic point, we chose a different scenario. Our motivation here was to investigate the possibility regarding dust formation at around $12R_0$, at which distance [e.g. 235] model a second dust shell. Within the framework of the current theory, we found that the only way to have a viable wind scenario with dust formation at this distance, was by collocating the dust formation radius with the radial Alfvén point. However, in this case, as can be seen from Figure 5.2, the solution is not continuous through the radial Alfvén point. In this scenario, the solution need not be continuous at $r = r_A$ as this also happens to be the dust formation radius, hence a discontinuity in the solution is allowed.

In Figure 5.1 it can be seen that the temperature at the left bound of the hybrid region ($r = r_d^{in} = 2.6R_0$) is about 1313 K. This same temperature is calculated to be at a distance of about $2.9R_0$ in Figure 5.2. Thus, ahead of a hot spot in the atmosphere, the viable dust formation region moves further out from the photosphere, as would be expected. In Figure 5.2 the temperature at the sonic point is seen to be about 876 K. Thus the range of temperature in this model is similar to that for the hybrid region in Figure 5.1, therefore it is still possible to formulate a hybrid wind scenario with dust formation occurring within the sonic point, as was shown in Figure 5.1. However, as mentioned earlier, in the current model our goal is to locate a second dust shell outside the sonic point at around $12R_0$ [see 235] and not within it.

In this scenario, with a short-lived hot spot on the photosphere, the temperature in the gas is about 800 K at the radial Alfvén point ($r = r_A$). Thus, the observed temperature for the dust of about 600 K at this distance is quite feasible [e.g. 235]. Overall, for the lifetime of the hot spot, it is possible to sustain a hybrid wind with dust forming at $12R_0$. A pure WD mechanism transports stellar material from the photosphere, through the sonic point and out to the radial Alfvén point. After dust formation at this location, the MHD-dust-driven wind then negotiates its way through the remaining critical point; the fast point and leaves the star super-Alfvénic. Comparing Figure 5.2(a) with Figure 5.1 reveals that hybrid model is quite sensitive to changes in the photospheric temperature and the magnetic field. For the model shown in Figure 5.2, the surface radial magnetic field strength was found to be ≈ 1.15 G. The dust parameter (Γ_d) was found to be about 0.1; a little higher than in the previous model (c.f. Table 5.2). With these pa-
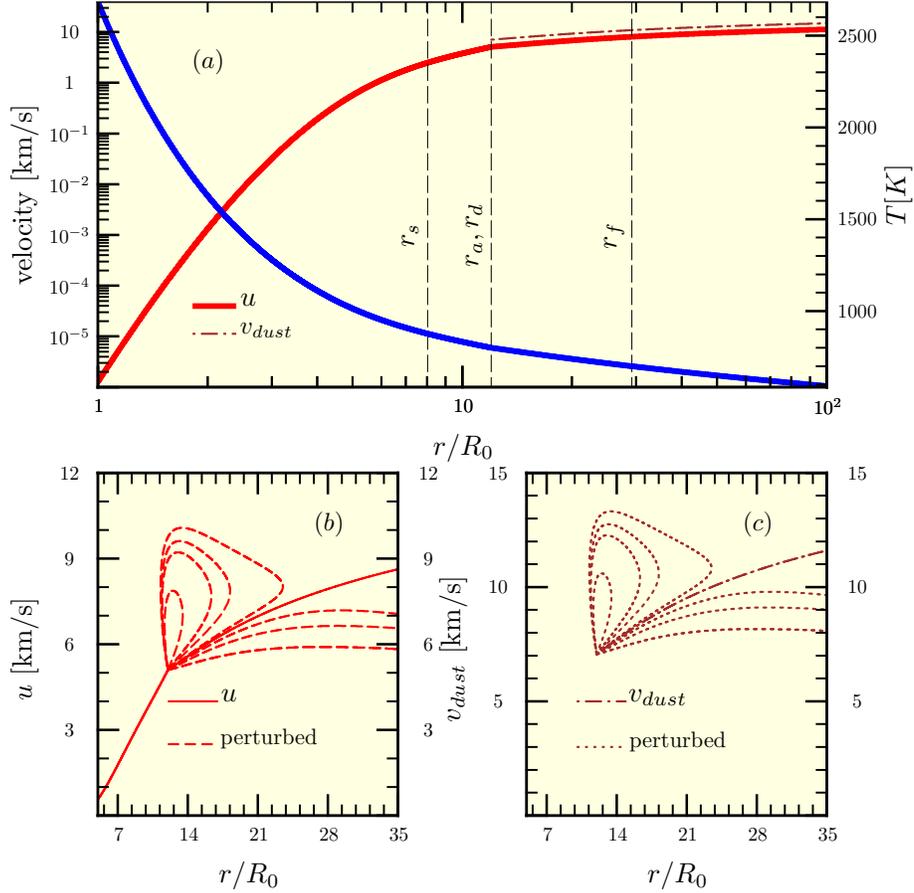
Figure 5.2: (a) Hybrid wind solution is shown for a scenario with a hot spot at the photosphere of Mira. This model has parameters $u_A \approx 0.15 v_{esc,0}$, $r_A \approx 29.21 R_0$ and $\Gamma_d \approx 0.1$ and remaining parameters as given in Table 5.1. The surface magnetic field was found to be $B_0 \approx 1.15$G. The decreasing blue solid line traces the temperature and should be interpreted using the right hand y-axis. (b) Gas velocities obtained by perturbing the solution in the vicinity of r_A and (c) the corresponding dust velocities.

rameters, the terminal wind velocity is also concomitantly higher, at around 11 km/s in the equatorial plane. In comparison to the time for one stellar rotation, since the hot-spot would be short-lived, so too would be the wind ahead of the spot in the atmosphere.

In this regard, there are some concerns that are inherited from collocating the dust formation and radial Alfvén points. In the main, dust formation and growth is a stochastic process that is not completely understood. Particularly, for the wind ahead of a short-lived hot spot in the atmosphere, the physical processes may be quite dynamic over time-scales comparable to the spot lifetime. As a result small changes in the wind velocity in the vicinity of the radial Alfvén point can result in a drastically different wind velocity profile and indeed the wind may not be able to navigate through the fast point. This is shown in Figure 5.2(b) and (c). We have perturbed the gas velocity by a small amount ($\lesssim 0.01\%$) ahead of the radial Alfvén point and then integrated the perturbed solution outwards. Figure 5.2(b) shows the unperturbed solution as the red solid line and the perturbed wind solutions as the dashed lines. We see that this perturbation of the gas velocity results in the wind becoming either a failed wind, where it does not pass through the fast point (the dashed lines below the solid red line) or the wind becomes an unphysical double valued wind (dashed lines above the the red solid line that form loops). In either case, this suggests that minor perturbations of the wind velocity around the radial Alfvén point will drastically change the nature of the outflow. Figure 5.2(c) shows the corresponding dust velocity profile for both the unperturbed and the perturbed solutions. Should the dust follow any of the perturbed trajectories then it will not leave the star and can lead to instabilities in the flow. Therefore, while it is possible that in the atmosphere of Mira, conditions ahead of a mild hot spot may result in a hybrid wind with dust formation at around $12R_0$, these conditions would be limited by the life-time of the spot, and as such cannot be classified as steady-state, even when compared to the stellar rotation time. Such a localised phenomenon ahead of a hot spot may be able to account for clumpiness of the dust distribution and even spatially distinct dust shells around Mira [e.g. 235]. We shall end this discussion by cautioning the reader that fully dynamic 2- or 3-D modelling would be needed for establishing the importance of such dynamic short time-scale phenomena, which cannot be entirely gleaned from the simplistic theory presented here. Presently, the conclusions of the current work are summarised in the following section.

Table 5.2: Optimised values of the variable parameters for the star Mira.

Parameter	Value
B_0	≈ 4.11 G
u_0	$\approx 5.89 \times 10^{-6}$ km/s
u_A	≈ 4.93 km/s
r_A	$\approx 43.47 R_0$
γ	≈ 1.06
Γ_d	≈ 0.06
i	$\approx 26.60° \approx 0.46$ rad

5.4 Conclusion

In this letter we have modelled the stellar wind of Mira as a hybrid MHD-dust-driven wind. The study was motivated largely by hints of the discovery of a magnetic field in the star in addition to a possible detection of stellar rotation.

Since the surface magnetic field strength as well as the rotation rate are not exactly known, these along with a few other physical parameters such as the dust parameter (Γ_d) were treated as variable parameters that were fine-tuned, in order to arrive at a suitable stellar wind model for Mira. We obtained a stellar wind with a terminal velocity of about 5 km/s in the equatorial plane. This value for the wind velocity is in agreement with current estimates. The stellar effective temperature was taken to be about 2500 K and we obtained a surface magnetic field of about ≈ 4 G, in reasonably good agreement with current estimates. We also arrived at an estimate for a *hybrid region* in the inner atmosphere of Mira. This region depicts the range of distances at which dust condensation can occur in order to produce a hybrid wind. The temperature profile obtained for this hybrid region is consistent with models of the atmosphere of Mira.

For the purpose of modelling dust shells around Mira at several stellar radii, we employed a model of a hot-spot that alters the wind dynamics ahead of the spot in the atmosphere. With this we were able to show that it may be possible to facilitate dust formation at around $12R_0$ by collocating the dust formation and radial Alfvén points, resulting in a hybrid wind. However, since such a spot may be short-lived the dust and gas velocities in the vicinity of the radial Alfvén point are likely to change over short time-

scales and can result in failed wind solutions, if not dynamic instabilities, thereby forming localised regions of dusty clumps, or even distinct shells with slightly enhanced dust density.

It is however to be remembered, that the current model is an idealised steady-state description of an infinitely more complicated and dynamic problem. As such, the results obtained here only convey the possibility, that Mira may be a magneto-dusty rotator. However, without doubt, dynamic multi-D modelling of its wind is required for obtaining ultimately, a truer description of the nature of its efflux and of its atmosphere.

Chapter 6

A Two-Dimensional Pseudospectral Hartree-Fock Method for Low-Z Atoms in Intense Magnetic Fields [†]

In the previous chapters we have developed a theory for dust-driven winds with the inclusion of magnetohydrodynamic effects, in the envelopes of cool red giant stars and AGB stars. It was seen that these objects can harbour magnetic fields that can have an influence on the winds. In the current chapter however, we turn our attention to a different but related question. The objects described in the previous chapters at the end of their evolution will form compact objects; likely a neutron star for the red supergiant Betelgeuse and a white dwarf star for the low-mass AGB star Mira, and likewise for the intermediate-mass AGB stars described in Chapter 3. It is possible that these objects can be magnetised like their progenitors, however with much larger fields.

With large magnetic fields, the energy levels of atoms are greatly altered from their field-free configurations. This presents a difficulty when trying to interpret the spectra of such objects. For doing so, we would require accurate estimates of the energy levels of different atoms in strong and intense magnetic fields. In intense magnetic fields the spherical symmetry of the atom is broken and the electrons' interaction with the magnetic field becomes almost or even greater in magnitude, in comparison to their interaction with the nucleus. The loss of spherical symmetry implies that the quantum numbers required to describe the different electronic states in atoms, are now

---

changed as well. Studies of atoms in intense magnetic fields are scarce and only the energy levels of a few of the lowest-lying states are known, and even then, the accuracy of these upper bounds for the energies can be improved. The method of calculation of the energy levels in such a case is a non-perturbative method; the Hartree-Fock technique. Many of the modern methods for solving the problem of atoms in strong and intense magnetic fields are computationally intensive or they resort to several approximations that render the implementation lengthy and often cumbersome.

The work described in the current chapter concerns itself with formulating a straight-forward solution of the above mentioned two-dimensional Hartree-Fock problem. The motivation is to develop a compact atomic structure software capable of computing energy levels of atoms to a high degree of accuracy in a matter of minutes. Such a software can be readily integrated into atmosphere models of magnetised white dwarf stars and neutron stars, as it is does not come with the accompaniment of any great computational overhead. Presently, an introduction to the field of atomic structure in strong magnetic fields is provided and in later sections, the method of solution of the problem is described in detail.

6.1 Introduction

The motivation to study atoms in magnetic fields of strength beyond the perturbative regime is attributable in a large part, due to the discovery of such fields being present in white dwarf stars [e.g. 68, 258, 259] and neutron stars [e.g. 69, 70]. The most commonly observed neutron stars - pulsars, have been observed to have magnetic fields on the order of 10^7 - 10^9T [e.g. 83]. Magnetars [e.g. 260], which are strongly magnetized neutron stars, can have magnetic field strengths well in excess of 10^9T. White dwarf stars on the other hand have somewhat less extreme fields, albeit still high, $\sim 10^2$ - 10^5T [e.g. 83]. Many of the recycled millisecond pulsars can have fields as low as 10^4 T, [see 261], which is still a large field. At such high field strengths, a Zeeman-type perturbative treatment of the field [e.g. 262] is not possible. The structure of atoms is considerably altered from the low field case.

The problem of atoms in magnetic fields has been tackled by various researchers since the 1970's using a variety of different methods. In the literature, there exist numerous studies of hydrogen [e.g. 263–272] and many recent studies of helium [e.g. 89, 273–290] atoms in strong magnetic fields. There

have also been studies conducted for molecules and chains of atoms for both hydrogen and helium atoms in strong to intense magnetic fields [e.g. 291–298]. Moreover, our recent investigation [e.g. 88] using single-configuration Hartree-Fock (HF) theory [e.g. 91] was seen to yield accurate upper bounds for the binding energies of hydrogen and helium in strong magnetic fields. Our later study [see 92], obtained accurate binding energies for helium and lithium atoms in strong magnetic fields. The numerical method employed in the latter study was seen to yield considerable dividends, in terms of reducing the computational time for the solution of the problem. The atomic structure code provided therein is readily portable and could easily be included in existing atmosphere models of neutron stars and white dwarf stars, without much computational expense. Presently, the reader is referred to Ref. [e.g. 88] for a short chronological review of both one- and two-electron systems in strong magnetic fields.

In sharp contrast to these somewhat simpler systems, there is very limited work available in the literature for atoms with more than two electrons. A brief chronological review of the topic is provided herein. One of the first studies to investigate atoms in intense magnetic fields, in particular the iron atom, was by Flowers et al [e.g. 299] in 1977. This variational study extended the work due to the authors in Ref. [300] and obtained binding energies of iron atoms and condensed matter in magnetic fields relevant to neutron stars. Errors in this study were later corrected by Muller [e.g. 301]. Other methods included density functional studies [e.g. 302, 303] and also employed the Thomas-Fermi-Dirac method [e.g. 304, 305] for estimating binding energies of atoms in intense magnetic fields. The first comprehensive HF studies of atoms with more than two electrons were carried out by Neuhauser et al [e.g. 306, 307] for magnetic fields greater than 10^8T, thus being directly relevant to neutron stars. Elsewhere, HF studies of atoms and molecules in intense magnetic fields were conducted by Demuer et al [e.g. 308], with results consistent with previous findings. All of the above treatises, Refs. [299–308], concern themselves with magnetic fields in excess of 10^8T, well into the so-called intense magnetic field regime. At these field strengths, the interaction of the electron with the nucleus of the atom becomes progressively less dominant, in comparison to its interaction with the field itself. One of the first studies to carry out a rigorous HF treatment of atoms with more than two electrons in strong or intermediate field strengths was Ref. [89]. Therein, they obtained estimates of the binding energies of a few low-lying states of lithium and carbon atoms, in low to strong magnetic fields. Elsewhere, Ivanov [e.g. 309] and

Ivanov & Schmelcher [e.g. 288, 289, 310–313], have over recent years, carried out detailed HF and post-HF studies of atoms with more than two electrons using a numerical mesh-method for solving the unrestricted HF equations [e.g. 288]. The special meshes were so constructed as to facilitate finite-difference calculations in a two-dimensional domain using carefully selected mesh node points [e.g. 314]. They were able to ascertain the binding energies of the first few low-lying states of low-Z atoms such as lithium, beryllium and mid-Z atoms such as boron and carbon etc., using this method. Moreover, using a gaussian basis of functions for expressing the wave functions of the electrons [e.g. 281–287], adopting a full configuration-interaction method, Al-Hujaj & Schmelcher [e.g. 90, 315] have been able to estimate the binding energies of lithium and beryllium atoms in strong or intermediate magnetic fields, thereby improving upon previously obtained results. The sodium atom in a strong magnetic field has also been studied by Gonzalez-Ferez & Schmelcher [e.g. 316] with estimates of binding energies for the same. Elsewhere, low lying states of the lithium atom have also been studied in strong magnetic fields using a configuration-interaction method, employing the so-called freezing full-core method both with [e.g. 317] and without [e.g. 318] correlation between electrons. Recently, Medin & Lai [e.g. 294, 295] have also studied atoms and molecules and infinite chains of condensed matter in magnetic fields greater than 10^8T, using density-functional-theory. Mori et al [e.g. 279, 280] have studied mid-Z atoms in strong to intense magnetic fields using perturbation theory as well, obtaining results consistent with previous findings. Finally, as mentioned earlier, recent work on the lithium atom using a single-configuration HF calculation employing spectral methods for solution yielded accurate eigenvalues and eigenvectors of low-lying states in strong or intermediate magnetic field strengths [e.g. 92]. The method was seen to be computationally more economical than conventional HF solution methods using either finite-element techniques [e.g. 88] or finite difference methods [e.g. 83].

In the literature, there are very few studies of atoms with more than two electrons in strong magnetic fields. The methods developed for the determination of binding energies are either very involved such as Quantum Monte-Carlo and configuration-interaction techniques using different basis functions, or they are computationally demanding such as numerical mesh-methods and finite-element techniques. Configuration-interaction (CI) methods rely upon determining the expansion coefficients and assume that the individual electron wave functions are already pre-determined from essentially several

single-configuration calculations, i.e., the orbitals are not optimized during the calculation. A variant of post-HF methods that optimizes the orbitals in addition to the expansion coefficients is the so-called Multi-Configuration Hartree-Fock (MCHF) method [e.g. 319]. Both these post-HF methods yield considerable improvements with regard to the estimates of the upper bounds for the energies of various states. In the intermediate range of magnetic field strengths, where both the nucleus of the atom and the magnetic field have interactions with the electrons that are approximately equal in magnitude, the single configuration approximation then becomes increasingly ineffective with greater number of electrons. However, these methods are computationally more intensive than a single configuration calculation. Thus far, the most accurate CI methods involve decomposing the wave functions into a Gaussian basis set relying upon separation of variables in cylindrical coordinates [e.g. 90, 315]. These methods do however require a large set of basis functions. On the other hand, MCHF methods would require fewer basis functions, as the orbitals get optimized during the computation with the coefficients [e.g. 319]. The separation of variables and/or basis decompositions speed up the computation in these post-HF methods considerably. However, there do not exist hitherto, any fully two-dimensional (2D) post-HF studies of multi-electron atoms in intense magnetic fields. This is partly due to the computational overhead associated with adopting a fully two-dimensional picture. Central to the development of such a method would be the fast and accurate computation of the single-configuration problem in a full 2D framework without any basis expansions and separation of variables. Wave functions so determined could be used directly in 2D configuration-interaction calculations or the problem could be cast into a MCHF framework. In the latter, the orbitals within each configuration could be optimized as the calculation proceeds. Such post-HF studies would yield more accurate data for the structure of atoms in intense magnetic fields. The aim of the current study is to facilitate this larger goal, by providing a fast and accurate solution of the full 2D single configuration problem of atoms in intense magnetic fields.

The method outlined in the current study is an extension of the method developed in our two previous studies Refs. [88, 92]. The framework does not make any assumptions of basis functions and neither is it restricted to the adiabatic approximation. The computations are seen to be readily extendable to arbitrary field strengths and atoms with greater number of electrons. The overall algorithm of solution using pseudospectral methods is also computationally straightforward to implement and has already been seen to yield

considerable dividends in terms of computational time [e.g. 92]. Obtaining accurate estimates of the energy levels of atoms, in particular low-Z atoms, in strong and intense magnetic fields will ultimately facilitate a proper understanding of the spectra of neutron stars and white dwarf stars. Thus the central aim of the current work is to provide accurate estimates of the binding energies of the first few low-lying states of the simplest low-Z atoms; helium and lithium, in strong and intense magnetic fields using an unrestricted two dimensional single-configuration pseudospectral method. Our subsidiary goal is to additionally provide a computationally efficient and economical software that could be directly integrated into atmosphere models of neutron stars.

6.2 The HF Equations

We shall begin with the generalised single-configuration HF equations for an atom with 'n_e' electrons and nuclear charge 'Z', in a magnetic field that is oriented along the z-direction. A derivation of the single-configuration HF equations can be found in our earlier work [see 88], here we shall present only the salient points. We shall be using cylindrical coordinates as the geometry of atoms in strong magnetic fields is more easily described in this basis. We shall employ a single configuration methodology, as a result the wave function of the electrons can be expressed using a single Slater determinant as,

$$\Phi = A_{n_e} \left(\tilde{\psi}_1, \tilde{\psi}_2, \tilde{\psi}_3, ..., \tilde{\psi}_{n_e-1}, \tilde{\psi}_{n_e} \right), \tag{6.1}$$

where A_{n_e} is the anti-symmetrization operator. The individual electronic wave functions $\tilde{\psi}_i$ are given by,

$$\tilde{\psi}_i = \psi_i(\rho_i, z_i) e^{im\phi_i} \chi_i(s_i), \tag{6.2}$$

where i labels each of the n_e electrons. The two-dimensional single particle wave functions $\psi_i(\rho_i, z_i)$ are taken to be real functions. The spin part of the wave function is given by $\chi_i(s_i)$.

The single configuration HF equation can then be written in cylindrical coordinates as shown in Eq. (6.3). Here the length scale is in units of Bohr radii and the energy is scaled in units of Rydberg energy in the Coulomb

potential of charge Ze (see below for definitions).

$$\left[-\nabla^2_{i,(\rho_i,z_i)} + \frac{m_i^2}{\rho_i^2} + 2\beta_Z(m_i - 1) + \beta_Z^2\rho_i^2 - \frac{2}{r_i} \right] \psi_i\left(\rho_i, z_i\right)$$

$$+ \frac{2}{Z} \sum_{j \neq i} \left[\Phi_D \psi_i(\rho_i, z_i) - \alpha_E \psi_j(\rho_i, z_i) \right] = \epsilon_i \psi_i\left(\rho_i, z_i\right), \qquad (6.3)$$

where $i, j = 1, 2, 3, ..., n_e$ and $r_i = \sqrt{\rho_i^2 + z_i^2}$. The differential operator in Eq. (6.3) above is $\nabla^2_{i,(\rho_i,z_i)} \equiv (1/\rho_i)\partial/\partial\rho_i(\rho_i\partial/\partial\rho_i) + \partial^2/\partial z_i^2$. Integration with respect to the azimuthal coordinate, ϕ, has already been carried out, prior to writing the result in Eq. (6.3) above. The contribution due to electron spin has also similarly been averaged out *a priori*. The total Hartree-Fock energy of the state is given by

$$\varepsilon_{total} = \sum_i \epsilon_i - \frac{1}{2}\frac{2}{Z} \sum_{j \neq i} \left[\langle\psi_i(\rho_i, z_i)|\Phi_D|\psi_i(\rho_i, z_i)\rangle - \langle\psi_i(\rho_i, z_i)|\alpha_E|\psi_j(\rho_i, z_i)\rangle \right].$$

$$(6.4)$$

The direct and exchange interactions are determined according to the method outlined in Ref. [88], as the solutions of the elliptic partial differential equations for the potentials given respectively by,

$$\nabla_i^2 \Phi_D = -4\pi|\psi_j(\rho_i, z_i)|^2 \qquad (6.5)$$

and

$$\left[\frac{1}{\rho_i}\frac{\partial}{\partial\rho_i}\left(\rho_i\frac{\partial}{\partial\rho_i} \right) - \frac{(m_i - m_j)^2}{\rho_i^2} + \frac{\partial^2}{\partial z_i^2} \right] \alpha_E(\rho_i, z_i) = -4\pi\psi_j^*(\rho_i, z_i)\psi_i(\rho_i, z_i).$$

$$(6.6)$$

In the current study, we have chosen to work in units of Bohr radii along with the definitions given below. The Bohr radius for an atom of nuclear charge Z is given by a_B/Z, where $a_B = \hbar/\alpha m_e c$ is the Bohr radius of the hydrogen atom. The magnetic field strength parameter β_Z, is given by the expression $\beta_Z = B/(Z^2 B_0)$, where B_0 is the critical field strength at which point the transition to the intense magnetic field regime occurs [see 83]. This is defined as $B_0 = (2\alpha^2 m_e^2 c^2)/(e\hbar) \approx 4.70108 \times 10^5$T. Thus, beyond a value of $\beta_Z \approx 1$, the transition to the intense magnetic field regime occurs and the interaction of the electron with the nucleus becomes progressively less dominant as β_Z increases. The energy parameter of the ith electron is defined as $\epsilon_i = E_i/(Z^2 E_\infty)$, with $E_\infty = \frac{1}{2}\alpha^2 m_e c^2$, the Rydberg energy of

the hydrogen atom. For brevity we shall refer to the units of energy as $E_{Z,\infty}$, which should be remembered as the Rydberg energy in the Coulomb potential of charge Ze. The quantity $\alpha = e^2/(4\pi\epsilon_0 \hbar c) \approx 1/137$ is the fine structure constant. In the current study, all the physical constants were used in SI units. Additionally, the magnetic field B, is taken to be in units of Tesla. The above written Eq. (6.3) represents the N-coupled Hartree-Fock equations in partial differential form for an N-electron system with nuclear charge Z. The system of equations is solved iteratively; see Section 6.4 for the numerical details.

Based upon the above definition of β_Z, it is convenient to classify the field strength [see 320] as low ($\beta_Z \leq 10^{-3}$), intermediate, also called strong ($10^{-3} < \beta_Z \leq 1$) and intense or high ($1 < \beta_Z < \infty$). It is immediately evident upon inspection that Eq. (6.3) is a set of coupled non-linear partial differential equations. The equations are coupled through the exchange interaction term between the electrons. Presently, we shall describe in detail, the numerical methodology developed in the current study.

It is to be mentioned in this regard, that in the current study we shall only be concerned with fully spin-polarised states (FSP), in other words all the electrons of the atom are assumed to be anti-aligned with the magnetic field. Such states have an exchange interaction between the electrons providing an extra coupling term in the HF equations, α_E. Additionally, the FSP states are the seen to be the most bound states in increasing magnetic fields in the intense field regime. The extension to partially spin-polarised configurations is easily achieved by eliminating the exchange term in the HF equations.

6.3 The Pseudospectral Approach

The HF equations collectively given by Eq. (6.3) above, describe a coupled eigenvalue problem. The atomic state function consists of a single Slater determinant that describes the wave function. The numerical solution of the coupled equations in Eq. (6.3) proceeds via the so-called self consistent field (SCF) method due to Hartree [see 91].

First we find a solution to the hydrogenic problem; Eq. (6.3) without the direct and exchange interactions. This allows us to obtain an initial estimate for the wave functions. Second, using these estimates the elliptic partial differential equations for the direct and exchange interaction potentials in Eqs. (6.5) and (6.6) are solved. With these potentials now obtained, the cou-

pled HF problem including the direct and exchange interactions in Eq. (6.3), is solved as a full non-linear eigensystem. The eigenvalues obtained are the individual particle energies ϵ_i and the normalized eigenvectors are the wave functions, $\psi_i(\rho_i, z_i)$. The SCF iterations then proceed with the updated electron wave functions and the steps from the second step described above, are repeated until convergence.

Central to the entire scheme is the method of solution of the partial differential equations. For a numerical solution of the above scheme, we employ a discretization based on a pseudospectral approach as described in an earlier study [see 92]. In contrast to our earlier work, in the current study we employ a cylindrical coordinate system. As a result the methodology for setting up the problem is considerably different from that described in Ref. [92]. This section is arranged as follows. First we describe the methodology employed for solving the hydrogen atom using pseudospectral methods in cylindrical coordinates. Particular emphasis is placed on the implementation of boundary conditions. Thereafter, the treatment is extended to the particular case of the helium atom in a single configuration and a generalization of the scheme is then provided for greater than two electrons.

6.3.1 The Hydrogenic Problem

We begin with the Hamiltonian for the hydrogenic problem (single-electron) in a strong magnetic field,

$$
\left[-\left(\frac{1}{\rho_i} \frac{\partial}{\partial \rho_i} \left(\rho_i \frac{\partial}{\partial \rho_i} \right) + \frac{\partial^2}{\partial z_i^2} \right) + \frac{(m_i)^2}{\rho_i^2} \right.
$$
$$
\left. + \beta_Z^2 \rho_i^2 - \frac{2}{\sqrt{\rho_i^2 + z_i^2}} \right] \psi_i \left(\rho_i, z_i \right) = \epsilon_i \psi_i \left(\rho_i, z_i \right). \tag{6.7}
$$

The solution of the eigenvalue problem in Eq. (6.7) yields the individual electron energies and wave functions in a given configuration. The wave functions thus obtained form the initial guess to begin the Hartree-Fock iterations. The domains of both the radial and the axial coordinates are $0 \leqslant \rho, z < \infty$. The problem maintains azimuthal symmetry and thus, a solution of Eq. (6.7) in this domain, when reflected about the $z = 0$ plane (respecting $z-$parity of course) and revolved about the z-axis through 2π, gives the solution in three-dimensional cylindrical coordinates.

First the semi-infinite domains are compactified using the transformations,

$$x_i = 2 \tanh\left(\rho_i\right) - 1 \tag{6.8}$$

and

$$y_i = 2 \tanh\left(z_i\right) - 1. \tag{6.9}$$

This ensures that the semi-infinite domain is mapped from $[0, \infty) \otimes [0, \infty)$ to $[-1, 1] \otimes [-1, 1]$. There are several mappings that can be carried out to solve the problem of the hydrogen atom without a magnetic field. The interested reader is referred to Ref. [see 321] for a treatise on different choices of mappings for carrying out radial integrals. In the current study however, we are opting to follow a procedure that allows us to formulate a method based on collocation using Chebyshev-Lobatto points. The mapping described above allows us to employ the zeros of the Chebyshev-Lobatto polynomials as the collocation points which lie in the domain $[-1.1]$. With the transformations given in Eqs. (6.8) and (6.9), we can re-write Eq. (6.7) as

$$
\begin{aligned}
\Bigg[-\frac{1}{4}\left(3 - x^2 - 2x\right)^2 \frac{\partial^2}{\partial x^2} &- \frac{1}{2}\left(3 - x^2 - 2x\right) \times \left(\left[\tanh^{-1}\left(\frac{1+x}{2}\right)\right]^{-1} \right. \\
-1 - x\Bigg) \frac{\partial}{\partial x} &- \frac{1}{4}\left(3 - y^2 - 2y\right)^2 \frac{\partial^2}{\partial y^2} + \frac{1}{2}\left(3 - y^2 - 2y\right)\left(1 + y\right)\frac{\partial}{\partial y} \\
&+ \left(m_i\right)^2 \left[\tanh^{-1}\left(\frac{1+x}{2}\right)\right]^{-2} + \beta_Z^2 \left[\tanh^{-1}\left(\frac{1+x}{2}\right)\right]^2 \\
&- \frac{2}{\sqrt{\left[\tanh^{-1}\left(\frac{1+x}{2}\right)\right]^2 + \left[\tanh^{-1}\left(\frac{1+y}{2}\right)\right]^2}} \Bigg] \psi_i\left(x, y\right) = \epsilon_i \psi_i\left(x, y\right),
\end{aligned}
\tag{6.10}
$$

where, we have dropped the subscripts on the coordinate labels. The discretisation points are thereafter taken to be the commonly used Chebyshev-Lobatto points [see 92, 322, 323] given by

$$x_j, y_j = \cos\left(\pi j / N\right), \tag{6.11}$$

where $j = 0, 1, ..., N$. As is customary, we employ monic polynomials of degree N as the cardinal functions to interpolate between these points and

are given by [see 92, 322],

$$p_j(x) = \frac{1}{a_j} \prod_{\substack{k=0 \\ k \neq j}}^{N} (x - x_k), \tag{6.12}$$

with

$$a_j = \prod_{\substack{k=0 \\ k \neq j}}^{N} (x_j - x_k). \tag{6.13}$$

Derivatives of these interpolating polynomials at the discretisation points then yield the so-called Chebyshev differentiation matrix, whose elements are given by,

$$D_{ij} = \frac{1}{a_j} \prod_{\substack{k=0 \\ k \neq i,j}}^{N} (x_i - x_k) = \frac{a_i}{a_j(x_i - x_k)} \quad (i \neq j) \tag{6.14}$$

and

$$D_{jj} = \sum_{\substack{k=0 \\ k \neq j}}^{N} (x_j - x_k)^{-1} \tag{6.15}$$

With the differentiation matrices thus formed, it is possible to write down a differential equation in matrix form as follows. Consider the differential equation,

$$\frac{d^2}{dx^2} u(x) = f(x). \tag{6.16}$$

This can be written using the Chebyshev Differentiation matrix as,

$$\sum_{k'=1}^{N+1} D^2_{j'k'} p(x_{k'}) = f(x_{j'}) \quad j' = 1, ..., N+1, \tag{6.17}$$

where D^2 is the square of the matrix D and $p(x)$ is the polynomial interpolant approximating the solution $u(x)$. In Eq. (6.17) j' and k' refer to rows and columns of the matrices and vectors and hence start from 1 rather than 0 as in Eq. (6.11). Using this matrix formulation, it is then possible to write more complicated differential equations as matrix equations [see 92, 322],

provided the domain has been suitably compactified to $[-1, 1]$. The differential equation in Eq. (6.16) has thus been converted to a discrete equation with an operator (a matrix) acting upon a vector. A simple solution (u) of the above equation can then be obtained by multiplying both sides from the left with the inverse operator, $(D^2)^{-1}$, once appropriate boundary conditions have been imposed.

To illustrate, let us consider the simple case of applying a zero or null-type Dirichlet condition at the end points of the domain ($x = -1, j = N$ and $x = 1, j = 0$). This implies that we are fixing the values at the end points to zero, i.e., $u(x_{k'=1}) = 0$ and $u(x_{k'=N+1}) = 0$ in Eq. (6.17). Therefore the first and the last equation in Eq. (6.17) vanish identically. Thus, the first and last columns of the matrix D^2 can be discarded as they multiply with $u(x_{k'=1}) = 0$ and $u(x_{k'=N+1}) = 0$, respectively. Similarly, the first and last rows of the matrix D^2 can also be discarded as we are ignoring both the first and the last equation in Eq. (6.17) as $f(x_{k'=1,N+1}) = 0$. Therefore the effect of imposing Dirichlet conditions at the end points has the effect of trimming the working matrix by removing appropriate rows and columns. Let us define this trimmed version of the Chebyshev Differentiation matrix as $\tilde{D}_{j'k'}$. The trimmed matrix has indices labelled $j', k' = 2, ..., N$. Thus the solution in the interior of the domain $x_{j'=2,...,N}$ can be found according to

$$p(x_{j'}) = \sum_{k'=2}^{N} (\tilde{D}^2)^{-1}{}_{j'k'} f(x_{k'}) \quad j' = 2, ..., N, \tag{6.18}$$

where $(\tilde{D}^2)^{-1}$ is the inverse of $\tilde{D}^2$, which has a low condition number. The vectors $p(x)$ and $f(x)$ are explicitly given by,

$$\mathbf{p} = \begin{bmatrix} p(x_2) \\ p(x_3) \\ . \\ . \\ . \\ p(x_{N-1}) \\ p(x_N) \end{bmatrix} \qquad \mathbf{f} = \begin{bmatrix} f(x_2) \\ f(x_3) \\ . \\ . \\ . \\ f(x_{N-1}) \\ f(x_N) \end{bmatrix} \tag{6.19}$$

Notice that the vectors $\mathbf{p}$ and $\mathbf{f}$ also have indices running from 2 to N since the first and last rows have been removed due to the imposition of null type Dirichlet boundary conditions. On the other hand, if the Dirichlet conditions

were of the fixed variety with $u(x_{k'=1}) = a$ and $u(x_{k'=N+1}) = b$, then we can write Eq. (6.17) as

$$\sum_{k'=2}^{N} \tilde{D}^2_{j'k'} p(x_{k'}) = f(x_{k'}) - a D^2_{j',1} - b D^2_{j',N+1}$$

$$(j' = 2, ..., N). \tag{6.20}$$

In this case, the solution in the interior of the domain $x_{j'=2,...,N}$ can be written as,

$$p(x_{j'}) = \sum_{k'=2}^{N} (\tilde{D}^2)^{-1}{}_{j'k'} (f(x_{k'}) - a D^2_{j',1} - b D^2_{j',N+1})$$

$$(j' = 2, ..., N). \tag{6.21}$$

It is then immediately evident that if $a = b = 0$, then we recover Eq. (6.18).

Neumann-type boundary conditions are handled in a similiar manner by extending Eq. (6.21) using the differentiation matrix D [see 324]. For example, if we wish to solve Eq. (6.17) subject to the boundary conditions that $u(x_{k'=N+1}) = 0$ and $u'(x_{k'=1}) = 0$, then we can re-write Eq. (6.20) by replacing $b = 0$ and $a = p(x_{k'=1})$, the latter is unknown *a priori*;

$$\sum_{k'=2}^{N} \tilde{D}^2_{j'k'} p(x_{k'}) = f(x_{k'}) - D^2_{j',1} p(x_{k'=1})$$

$$(j' = 2, ..., N). \tag{6.22}$$

Putting $E = \tilde{D}^2_{j'k'}$, with $j', k' = 2, ..., N$ and $E_0 = \left[D^2_{2,1}, D^2_{3,1}, ..., D^2_{N,1} \right]$, we can re-cast Eq. (6.22) in matrix form as,

$$E\mathbf{p} = \mathbf{f} - E_0 p(x_1) \tag{6.23}$$

However, since $u'(x_{k'=1}) = 0$ it implies that the derivative of the solution at the $x = 1$ boundary must vanish. We can write this condition as

$$\sum_{k'=1}^{N} D_{1,k'} p(x_{k'}) = D_{1,1} p(x_1) + \sum_{k'=2}^{N} D_{1,k'} p(x_{k'}) = 0. \tag{6.24}$$

Substituting $B_0 = D_{1,1}$ and $B_1 = [D_{1,2}, D_{1,3}, ..., D_{1,N}]$ we can then immediately re-write Eq. (6.24) as

$$B_0 p(x_1) + B_1 \mathbf{p} = 0. \tag{6.25}$$

This allows us to obtain an expression for the unknown quantity $p(x_1)$ in terms of $\mathbf{p}$ as

$$p(x_1) = -B_0^{-1}B_1\mathbf{p}. \tag{6.26}$$

Substituting Eq. (6.26) in Eq. (6.23) we obtain

$$(E - E_0 B_0^{-1}B_1)\mathbf{p} = \mathbf{f}. \tag{6.27}$$

The solution in the interior can then be obtained as,

$$\mathbf{p} = (E - E_0 B_0^{-1}B_1)^{-1}\mathbf{f}. \tag{6.28}$$

This then yields a straightforward linear algebra problem of solving a system of equations with is readily handled using standard methods. The method outlined above for imposing boundary conditions and formulating the problem, has been extended to the case of two dimensions and is applied to obtain a solution of the problem in Eq. (6.10) which is described below in brief.

At this juncture it is to be mentioned that in writing Eq. (6.10), we have removed the co-ordinate singularity at $x = -1$, by replacing it with $x = -1 + \delta$, where $\delta = 10^{-14}$ in units of Bohr radii. This approximation produced acceptable results within error tolerances. The singularity at the outer boundary of the domain, given by $x = 1$ (corresponding to $\rho = \infty$), is taken care of by imposing a Dirichlet boundary condition since the wave function must vanish at infinity (see below). Similarly, at the other outer boundary; $y = +1$, we impose a Dirichlet condition since here too, the wave function should vanish at infinity. The remaining boundaries at $x, y = -1$ can have either Dirichlet or Neumann boundary conditions, depending upon the behaviour of the wave function. The following discussion delineates the methodology for the 2D problem.

6.3.1.1   An Explicit Example - Domain Discretization

We consider here an explicit example to illustrate the use of pseudospectral methods for solving an eigenvalue problem. In particular, we shall delve into the methodology adopted here for imposing boundary conditions in considerable detail. The method developed here is a non-trivial extension of the one developed by the authors in Ref. [324].

Let us begin with a domain $[-1, 1] \otimes [-1, 1]$ which is discretised using $N+1$ points in each of the two Cartesian directions; x and y, with $N = 3$. This is illustrated in Fig. (6.1) The partial differential equation in Eq. (6.10) is two-
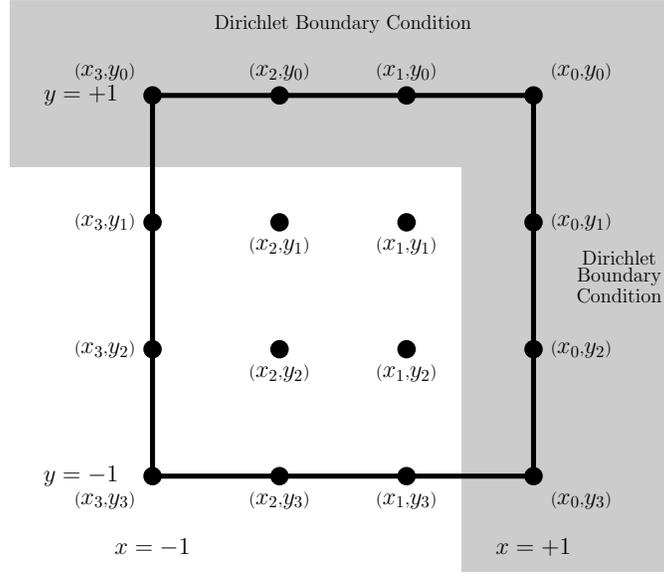
Figure 6.1: Pictorial representation of the domain $[-1,1]\otimes[-1,1]$ discretised using $N+1$ points in each direction, with $N=3$. The outer boundaries have Dirichlet conditions imposed.

dimensional therefore, following the procedure outlined in Refs. [92, 324], we can construct two-dimensional operators by employing Kronecker products of matrices. For example, a differential equation of the form,

$$\frac{\partial^2}{\partial x^2}u + \frac{\partial^2}{\partial y^2}u = f(x,y),$$ (6.29)

can be written in matrix form as,

$$\tilde{D}_x^2\, u(x_i,y_j) + \tilde{D}_y^2\, u(x_i,y_j) = f(x_i,y_j)$$
$$i,j = 1,...,N+1.$$ (6.30)

Note that in the matrices the $\tilde{D}_x$ and $\tilde{D}_y$ the outer boundaries at $x,y = +1$ have already been excised due to Dirichlet boundary conditions and the squares of the respective differentiation matrices have been appropriately trimmed. As a result, the indices i,j are limited to a lower value of $i,j = 1$ rather than $i,j = 0$. The operators $\tilde{D}_x^2$ and $\tilde{D}_y^2$ are then given by kronecker

products with the identity matrices,

$$\tilde{D}_x^2 = [D_x \times D_x] \otimes I_y \tag{6.31}$$

and

$$\tilde{D}_y^2 = I_x \otimes [D_y \times D_y], \tag{6.32}$$

where I_x and I_y are identity matrices of dimension $N_x \times N_x$ and $N_y \times N_y$ respectively. In our example, the number of node points in the x and y-directions are equal, thus $N_x = N_y = N$. Therefore, using the above formalism we can write down Eq. (6.10) in matrix form as,

$$\left[\text{diag}(a) \times \tilde{D}_x^2 + \text{diag}(b) \times \tilde{D}_x + \text{diag}(c) \times \tilde{D}_y^2 \right.$$
$$\left. + \text{diag}(d) \times \tilde{D}_y + \text{diag}(e) \right] \psi_i \equiv L_i \psi_i = \epsilon_i \psi_i, \tag{6.33}$$

where $\tilde{D}_x = D_x \otimes I_y$ and $\tilde{D}_y = I_x \otimes D_y$. Since we are imposing Dirichlet boundary conditions at the two outer boundaries, this implies that we can remove the first row and column from each of the matrices D_x and D_y (see discussion above and Refs. [92, 322]), prior to forming the operators in Eqs. (6.31) and (6.32). The diagonal matrices a, b, c, d and e are the coefficients of the different terms in Eq. (6.10), in the order in which they are written; explicitly,

$$\text{diag}(a) = -\frac{1}{4} \text{diag}((3 - x^2 - 2x)^2), \tag{6.34a}$$

$$\text{diag}(b) = -\frac{1}{2} \text{diag} \left((3 - x^2 - 2x) \times \right.$$
$$\left. \left(\left[\tanh^{-1} \left(\frac{1+x}{2} \right) \right]^{-1} - 1 - x \right) \right), \tag{6.34b}$$

$$\text{diag}(c) = -\frac{1}{4} \text{diag}((3 - y^2 - 2y)^2), \tag{6.34c}$$

$$\text{diag}(d) = \frac{1}{2} \text{diag} \left((3 - y^2 - 2y)(1 + y) \right), \tag{6.34d}$$

$$\text{diag}(e) = \text{diag}\left((m_i)^2 \left[\tanh^{-1}\left(\frac{1+x}{2}\right)\right]^{-2} + \right.$$

$$\left. \beta_Z^2 \left[\tanh^{-1}\left(\frac{1+x}{2}\right)\right]^2 - \frac{2}{\sqrt{\left[\tanh^{-1}\left(\frac{1+x}{2}\right)\right]^2 + \left[\tanh^{-1}\left(\frac{1+y}{2}\right)\right]^2}}\right). \quad (6.34e)$$

Replacing ψ_i with the polynomials in Eq. (6.12), the collocation points of the problem then forms a mesh with the corresponding values $p(x_i, y_j)$ with $i, j = 1, ..., N + 1$. The collocation points are those illustrated in Fig. (6.1). However, instead of writing the polynomial as a matrix of values at the collocation points, we can write the matrix as an extended vector comprising of the different columns, one followed by another. This then forms an $N^2 \times 1$ vector rather than an $N \times N$ matrix. Explicitly, we can reshape the matrix $p(x_i, y_j)$, with values given at the collocation points (see Fig. 6.1), from

$$\mathbf{p} = \begin{bmatrix} p(x_1, y_1) & p(x_2, y_1) & p(x_2, y_1) \\ p(x_1, y_2) & p(x_2, y_2) & p(x_3, y_2) \\ p(x_1, y_3) & p(x_2, y_3) & p(x_3, y_3) \end{bmatrix}, \quad (6.35)$$

to

$$\mathbf{p} = \begin{bmatrix} p(x_1, y_1) \\ p(x_1, y_2) \\ p(x_1, y_3) \\ p(x_2, y_1) \\ p(x_2, y_2) \\ p(x_2, y_3) \\ p(x_3, y_1) \\ p(x_3, y_2) \\ p(x_3, y_3) \end{bmatrix}. \quad (6.36)$$

It is to be remembered that in our explicit example $N = 3$.

6.3.1.2   Boundary Condition Implementation

Presently, Eq. (6.33) can be re-cast into matrix form as,

$$L\mathbf{p} = \lambda\mathbf{p}, \quad (6.37)$$

where the eigenvalues of the spectrum are obtained in λ; the individual single particle energies. At this juncture, let us now suppose that we wish to solve

the eigenvalue problem for the $1s_0$ state of the hydrogen atom. This state in the presence of a field would then be characterized using the notation $\nu^{2S+1}M^{\pi_z}$, where $M = \Sigma_i m_i$ is the total $z-$ component of angular momentum. The summation is over all the electrons in the atom; for the hydrogen atom there is only one electron. Similarly, the total z-parity of the state is the product of the z-parities of each electron, explicitly, $\pi_z = \Pi_{i=1}^{n_e} \pi_{z,i}$. Again for hydrogen there is only one electron. The total $z-$ component of the angular momentum, M, then forms a manifold within which different sub-spaces exist. The quantum number ν counts the excitation level within a given M-manifold and sub-space symmetry. The spin multiplicity is given in the usual way as $2S+1$. Finally, the $z-$parity of the state is indicated using $\pi_z = \pm 1$, indicating positive or negative parity. Therefore, the state $1s_0$ of hydrogen in the presence of a strong field would be written as 1^10^+.

For this state of hydrogen the boundary conditions are as follows. Along both the $x, y = +1$ boundaries the wave function must vanish, therefore we have Dirichlet boundary conditions. Along the $x, y = -1$ boundaries however, we have Neumann conditions. These boundary conditions are to be kept in mind for the following discussion. A pictorial representation of the operator L acting upon the vector $\mathbf{p}$ is given in Fig. (6.2).
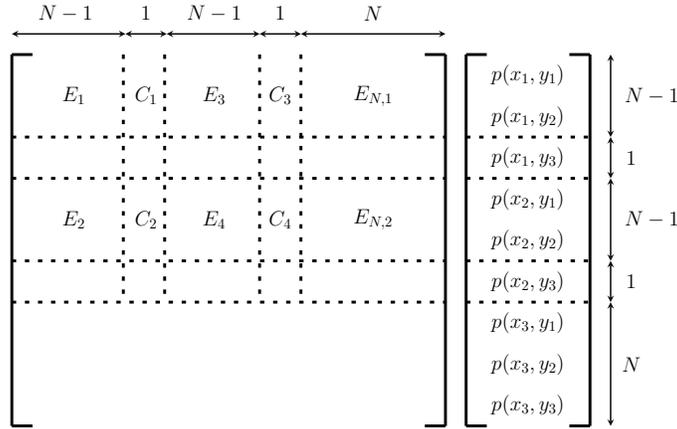
Figure 6.2: Pictorial representation the operator L acting upon the vector $\mathbf{p}$. The number of points in either direction, is $N = 3$ in the current example.

Fig. (6.1) shows the different parts of the matrix operator L. Specifically, the different parts of the matrix that are relevant to the solution in the

interior mesh points of the problem, are labelled. These are the submatrices $E_1, E_2, E_3, E_4,$ $C_1, C_2, C_3, C_4, E_{N,1}$ and $E_{N,2}$. The vector $\mathbf{p}$ can accordingly be split into three components,

$$\mathbf{p}_{\text{int}} = \begin{bmatrix} p(x_1, y_1) \\ p(x_1, y_2) \\ p(x_2, y_1) \\ p(x_2, y_2) \end{bmatrix}, \tag{6.38a}$$

$$\mathbf{p}_{b_y} = \begin{bmatrix} p(x_1, y_3) \\ p(x_2, y_3) \end{bmatrix} \tag{6.38b}$$

and

$$\mathbf{p}_{b_x} = \begin{bmatrix} p(x_3, y_1) \\ p(x_3, y_2) \\ p(x_3, y_3) \end{bmatrix}. \tag{6.38c}$$

In the above, $\mathbf{p}_{\text{int}}$ refers to the function value in the interior points of the mesh given in Fig. (6.1), while the function values at the $x = -1$ boundary are given by $\mathbf{p}_{b_x}$ and correspondingly, the values at the $y = -1$ boundary are given by $\mathbf{p}_{b_y}$. The eigenvalue problem in the interior mesh points is then given by,

$$E\mathbf{p}_{\text{int}} = \lambda \mathbf{p}_{\text{int}} - C\mathbf{p}_{b_y} - E_N \mathbf{p}_{b_x}. \tag{6.39}$$

Compare Eq. (6.39) with Eq. (6.23). Meanwhile, the matrices E, C and E_N are given by (see Fig. (6.2)),

$$E = \begin{bmatrix} E_1 & E_3 \\ E_2 & E_4 \end{bmatrix}_{(N-1)^2 \times (N-1)^2}, \tag{6.40a}$$

$$C = \begin{bmatrix} C_1 & C_3 \\ C_2 & C_4 \end{bmatrix}_{(N-1)^2 \times (N-1)} \tag{6.40b}$$

and

$$E_N = \begin{bmatrix} E_{N,1} \\ E_{N,2} \end{bmatrix}_{(N-1)^2 \times N} \tag{6.40c}$$

The dimensions of the matrices are also quoted for convenience. The objective here is to obtain a solution of the eigenvalue problem in Eq. (6.39). This would be possible if we are able to express the function values at the boundaries, i.e., $\mathbf{p}_{b_x}$ and $\mathbf{p}_{b_y}$ in terms of the solution in the interior $\mathbf{p}_{\text{int}}$. See

discussion above regarding the one-dimensional problem; Eqs. (6.25 - 6.28). However, the values at the boundaries obey Neumann boundary conditions. A Neumann boundary condition imposed on the wave function ψ along a given boundary is given by,

$$\hat{\mathbf{n}} \cdot \nabla \psi = \mathbf{g}, \tag{6.41}$$

where, $\hat{\mathbf{n}}$ is the unit vector normal to the boundary and g is the value to which, the directional derivative of the function along the direction of the normal vector is set. In our case, the boundaries in question are the lines $x, y = -1$. The corresponding normal vectors are then trivial and we obtain the conditions,

$$\left.\frac{\partial}{\partial x}\psi(x, y)\right|_{x=-1} = 0 \tag{6.42}$$

and

$$\left.\frac{\partial}{\partial y}\psi(x, y)\right|_{y=-1} = 0. \tag{6.43}$$

Once again, we can use differentiation matrices to specify these boundary conditions, as,

$$B_x\mathbf{p}|_{x=-1} = 0 \tag{6.44}$$

and

$$B_y\mathbf{p}|_{y=-1} = 0. \tag{6.45}$$

The boundary matrices are defined by $B_x = D_x \otimes I_y$ and $B_y = I_x \otimes D_y$. By virtue of the Kronecker product with the identity matrix, B_x has entries only along the diagonals. The matrix B_y on the other hand, is a block diagonal matrix with each block of dimension $N \times N$. The products $B_x\mathbf{p}$ and $B_y\mathbf{p}$ are required by Eqs. (6.44) and (6.45) to vanish along the specified boundaries, therefore we need only restrict our attention to those parts of the boundary matrices. Fig. (6.3) shows a pictorial representation of the boundary matrix B_x acting on the vector $\mathbf{p}$. Since the derivative is required to vanish along the $x = -1$ boundary, therefore we focus our attention on the part of the boundary matrix B_x, that acts on the vector $\mathbf{p}$ along the boundary in question, i.e., the last N rows. Fig. (6.3) shows the sub-matrices that are needed, these are labelled $B_{0,1}$, $B_{0,2}$, $B_{0,3}$, $B_{0,4}$ and B_N. Thus, we can write Eq. (6.44) as,

$$B_1\mathbf{p}_{\text{int}} + B_2\mathbf{p}_{b_y} + B_N\mathbf{p}_{b_x} = 0. \tag{6.46}$$

The matrices B_1 and B_2 in Eq. (6.46) are given by,

$$B_1 = \begin{bmatrix} B_{0,1} & B_{0,2} \end{bmatrix}_{N \times (N-1)^2} \tag{6.47a}$$
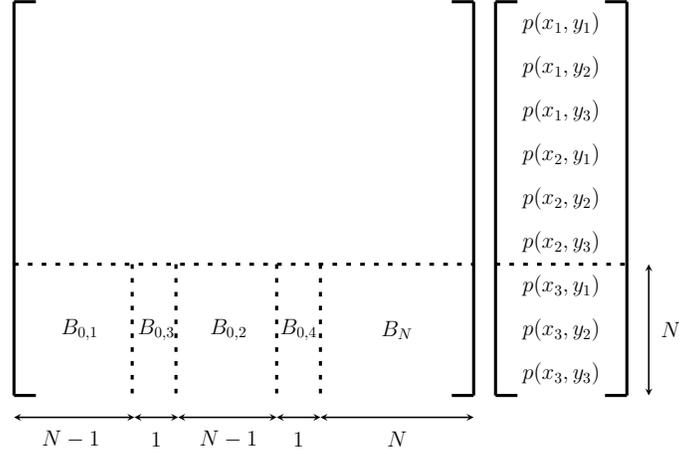
Figure 6.3: Pictorial representation the operator B_x acting upon the vector **p**. The number of points in either direction, is $N = 3$.

and

$$B_2 = \begin{bmatrix} B_{0,3} & B_{0,4} \end{bmatrix}_{N \times (N-1)} \tag{6.47b}$$

The dimensions of the matrices are indicated for convenience. Eq. (6.46) has two unknowns, $\mathbf{p}_{b_x}$ and $\mathbf{p}_{b_y}$ that need to be expressed in terms of $\mathbf{p}_{\text{int}}$. Therefore we need another equation. This is provided by Eq. (6.45). We have shown in Fig. (6.4) a pictorial representation of the boundary matrix B_y acting upon the the vector **p**. The different sub-matrices are also shown in Fig. (6.4). We can then write down an equation for expressing the boundary condition in Eq. (6.45) as,

$$G\mathbf{p}_{\text{int}} + H\mathbf{p}_{b_y} = 0. \tag{6.48}$$

The matrices G and H are given by,

$$G = \begin{bmatrix} G_1 & G_3 \\ G_2 & G_4 \end{bmatrix}_{(N-1) \times (N-1)^2} \tag{6.49a}$$

and

$$H = \begin{bmatrix} H_1 & H_3 \\ H_2 & H_4 \end{bmatrix}_{(N-1) \times (N-1)} \tag{6.49b}$$

It is to be kept in mind that since B_y is a block diagonal matrix, with each block of dimension $N \times N$, only the block diagonal portion of G and

Figure 6.4: Pictorial representation the operator B_y acting upon the vector $\mathbf{p}$. The number of points in either direction, is $N = 3$.

the diagonal of H, are respectively non-zero. In the current explicit example, therefore we have $G_2 = G_3 = [\, 0 \;\; 0 \,]$ and $H_2 = H_3 = 0$. With these definitions in place, we can employ Eqs. (6.46) and (6.48) to obtain expressions for the unknowns $\mathbf{p}_{b_x}$ and $\mathbf{p}_{b_y}$ in terms of the values in the interior $\mathbf{p}_{\text{int}}$ as,

$$\mathbf{p}_{b_y} = -H^{-1}G\mathbf{p}_{\text{int}} \tag{6.50}$$

and

$$\mathbf{p}_{b_x} = -B_N^{-1}(B_1 - B_2 H^{-1}G)\mathbf{p}_{\text{int}}. \tag{6.51}$$

Substituting Eqs. (6.50) and (6.51) in Eq. (6.39) we obtain an eigenvalue problem for the solution in the interior mesh points as,

$$\left(E - E_N B_N^{-1}(B_1 - B_2 H^{-1}G) \; - C H^{-1}G\right)\mathbf{p}_{\text{int}} = \lambda \mathbf{p}_{\text{int}}. \tag{6.52}$$

Eq. (6.52) can then be solved as an eigenvalue problem using standard methods to obtain the eigenvalues λ and the eigenvectors. See Section 6.4 for details regarding the numerical method employed for solving the eigenvalue problem. It is also to be mentioned that in general the master matrices constructed such as in Eq. 6.52 are not in general self-adjoint. As a result, the matrix methods utilised in the solution of these eigenvalue problems, are those employed for general non-symmetric, non-hermitian matrices, such as the non-symmetric algorithms of ARPACK; see § 6.4. For the moment, we turn our attention to extending this methodology to the two-electron problem.

6.3.2 The Two-Electron Problem

The HF problem for the two electron atom can be written, using the matrix formalism detailed above in a compact form as,

$$
\begin{pmatrix} L_1 + \frac{2}{Z}\text{diag}[\Phi_{D,1}] & -\frac{2}{Z}\text{diag}[\alpha_E] \\ -\frac{2}{Z}\text{diag}[\alpha_E] & L_2 + \frac{2}{Z}\text{diag}[\Phi_{D,2}] \end{pmatrix} \begin{pmatrix} \psi_1 \\ \psi_2 \end{pmatrix} = \lambda \begin{pmatrix} \psi_1 \\ \psi_2 \end{pmatrix}.
\tag{6.53}
$$

It is evident upon inspection that Eq. (6.53) is a coupled eigenvalue problem. The operators L_1 and L_2 are the operators defined in Eq. (6.33). The direct and exchange operators, $\text{diag}[\Phi_{D,i}]$ and $\text{diag}[\alpha_E]$ make the problem non-linear, as they depend upon the solutions ψ_i. However, the problem is linearized by estimating the direct and exchange interactions using wave functions from the previous iteration. The exchange interaction still couples the two electrons and as such, we are still required to solve a coupled eigensystem.

Once the hydrogenic problem has been solved to obtain initial estimates for the wave functions, these can then be employed for calculating the direct and exchange potentials. In order to continue with our explicit example, let us suppose that we wish to calculate the energy of the helium atom in the configuration $1^3(-1)^+$, or in terms of field-free notation, $1s_0 2p_{-1}$. Thus the hydrogenic problem would first need to be solved for each of the two electrons in the configuration. Let us label the electrons' wave functions using different letters; $\mathbf{p} \equiv 1s_0$ and $\mathbf{q} \equiv 2p_{-1}$.

The electron in the orbital $2p_{-1}$, in the presence of a magnetic field, has properties rather different from the $1s_0$ electron. The wave function of the former has positive $z-$parity, but goes to zero along the $y-$axis. In other words, $\mathbf{q}_{b_x} = 0$ and it has a Dirichlet condition imposed. There is however still a Neumann condition along the x-direction. This is to be remembered in the following discussion. Presently, we briefly describe the method of solution of the elliptic partial differential equations for obtaining the direct and exchange interactions.

6.3.2.1 The Direct and Exchange Interactions

Let us assume that we have solved the hydrogenic problem and already obtained initial estimates for the wave functions of each of the two electrons, viz., $\mathbf{p}$ and $\mathbf{q}$ for the states $1s_0$ and $2p_{-1}$, using the method described in

Section 6.3.1. Eqs. (6.5) and (6.6) can be re-written after domain compactification as,

$$
\left[\frac{1}{4}\left(3-x^2-2x\right)^2\frac{\partial^2}{\partial x^2}+\frac{1}{2}\left(3-x^2-2x\right)\times\left(\left[\tanh^{-1}\left(\frac{1+x}{2}\right)\right]^{-1}\right.\right.
$$

$$
\left.-1-x\right)\frac{\partial}{\partial x}+\frac{1}{4}\left(3-y^2-2y\right)^2\frac{\partial^2}{\partial y^2}-
$$

$$
\left.\frac{1}{2}\left(3-y^2-2y\right)\left(1+y\right)\frac{\partial}{\partial y}\right]\Phi_{D,i}\left(x,y\right)=-4\pi\left|\psi_j\left(x,y\right)\right|^2,\text{(6.54)}
$$

for the direct interaction and as

$$
\left[\frac{1}{4}\left(3-x^2-2x\right)^2\frac{\partial^2}{\partial x^2}+\frac{1}{2}\left(3-x^2-2x\right)\times\left(\left[\tanh^{-1}\left(\frac{1+x}{2}\right)\right]^{-1}\right.\right.
$$

$$
\left.-1-x\right)\frac{\partial}{\partial x}+\frac{1}{4}\left(3-y^2-2y\right)^2\frac{\partial^2}{\partial y^2}-\frac{1}{2}\left(3-y^2-2y\right)\left(1+y\right)\frac{\partial}{\partial y}
$$

$$
-\left(m_i-m_j\right)^2\left\{\tanh^{-1}\left(\frac{1+x}{2}\right)\right\}^{-2}\right]\alpha_E\left(x,y\right)=-4\pi\psi_j^*\left(x,y\right)\psi_i\left(x,y\right),
$$

$$
\text{(6.55)}
$$

for the exchange interaction. More compactly, Eqs. (6.54) and (6.55) can be written using matrix form as,

$$
L_{\text{dir}}\Phi_{D,i}=-4\pi\begin{cases}\mathbf{q}^2 & \text{for }i=1\\ \mathbf{p}^2 & \text{for }i=2\end{cases}\tag{6.56}
$$

and

$$
L_{\text{exch}}\alpha_E=-4\pi(\mathbf{pq}).\tag{6.57}
$$

In the above, $i=1$ or 2, labels the electrons. We emphasize at this stage that Eqs. (6.56) and (6.57) are written for the two-electron problem. For more than two electrons there would exist summations on right hand sides over the different states (see the direct and exchange terms in Eq. (6.3)). Moreover, $\mathbf{p}^2$, $\mathbf{q}^2$ and $(\mathbf{pq})$ are the element-by-element products of the corresponding vectors that have be suitably normalised. L_{dir} and L_{exch} are the left hand side operators in Eqs. (6.54) and (6.55) respectively, the various terms in which are defined similar to Eqs. (6.34a-e).

In the current explicit example, since $\mathbf{p} \equiv 1s_0$, the boundary conditions for the vector $\mathbf{p}^2$ are identical to that for $\mathbf{p}$, i.e., Neumann conditions along $x, y = -1$. Likewise, since $\mathbf{q} \equiv 2p_{-1}$, the boundary conditions for the vector $\mathbf{q}^2$ are identical to that for $\mathbf{q}$, i.e., Neumann condition along $y = -1$ but Dirichlet condition along $x = -1$; $q_{b_x} = 0$.

The product of the two vectors $(\mathbf{pq})$ on the other hand, vanishes along the line $x = -1$, since $q_{b_x} = 0$; therefore it has a Dirichlet condition given by $(\mathbf{pq})_{b_x} = 0$. However, along the line $y = -1$ a Neumann condition remains, since each individual vector has a Neumann condition.

With these boundary conditions now identified, they can be imposed on the operators L_{dir} and L_{exch} using the methods described in Section 6.3.1.2. The two linear systems of equations at the collocation points, given by Eqs. (6.56) and (6.57), are solved using standard methods, to obtain the direct and exchange potentials as,

$$\Phi_{D,1} = \left\{ E_{\mathrm{dir}} - CH^{-1}G \right\}^{-1} \mathbf{q}_{\mathrm{int}}^2, \tag{6.58a}$$

$$\Phi_{D,2} = \left\{ E_{\mathrm{dir}} - E_{N,\mathrm{dir}} \, B_N^{-1}(B_1 - B_2 H^{-1}G) - CH^{-1}G \right\}^{-1} \mathbf{p}_{\mathrm{int}}^2. \tag{6.58b}$$

and

$$\alpha_E = \left\{ E_{\mathrm{exch}} - CH^{-1}G \right\}^{-1} (\mathbf{pq})_{\mathrm{int}}. \tag{6.58c}$$

In the above, the matrices E_{dir}, $E_{N,dir}$ and E_{exch} are defined similarly to Eqs. (6.40a) and (c), this time however, using the operators L_{dir} and L_{exch} respectively (see Section 6.3.1.2). Once the direct and exchange interactions have been determined, they can be substituted in Eq. (6.53) and the coupled eigensystem can be solved.

We would like to caution at this stage, that the boundary conditions implemented in the explicit example are specifically for the configuration of the helium atom given by $1^3(-1)^+$ or $1s_0 2p_{-1}$. For other configurations, the boundary conditions imposed on $\mathbf{p}$ and $\mathbf{q}$ would be different. In that case, Eqs. (6.58a-c) would change accordingly. With this in mind, we now proceed to the next section which describes the setup of the coupled eigenvalue problem in Eq. (6.53) and the implementation of boundary conditions for its solution.

6.3.2.2   The Coupled Eigenvalue Problem

The direct and exchange potentials are found in Eqs. (6.58a-c) as vectors. These are converted to matrices with entries on the main diagonal before substituting into Eq. (6.53). If we label the operator on the left hand side of Eq. (6.53) as M, then we can re-write Eq. (6.53) as,

$$\begin{pmatrix} M_{11} & M_{12} \\ M_{21} & M_{22} \end{pmatrix} \begin{pmatrix} \mathbf{p} \\ \mathbf{q} \end{pmatrix} = \lambda \begin{pmatrix} \mathbf{p} \\ \mathbf{q} \end{pmatrix}. \tag{6.59}$$

We can depict pictorially, the action of M on the vector $\begin{pmatrix} \psi_1 \\ \psi_2 \end{pmatrix}$ or equivalently $\begin{pmatrix} \mathbf{p} \\ \mathbf{q} \end{pmatrix}$, as shown in Fig. (6.5).
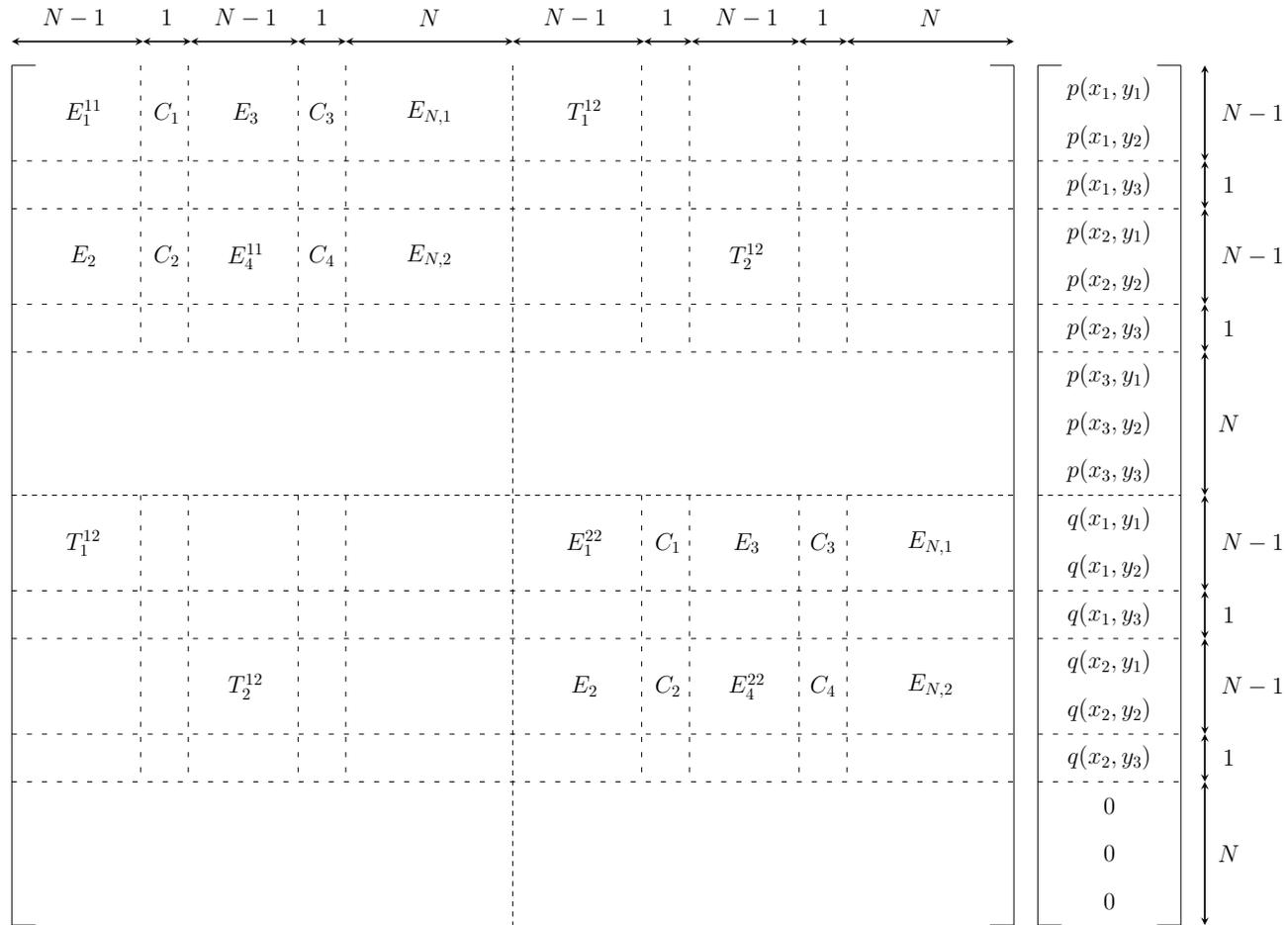
Figure 6.5: Pictorial representation of the action of the operator M in Eq. (6.59).

It can immediately be seen in Fig. (6.5) that in the matrices M_{11} and M_{22}, the off-diagonal sub-matrices are identical to those in Fig. (6.3), see Eqs. (6.40a-c). Also, it can be seen that the matrices M_{12} and M_{21} are diagonal matrices that are identical. These represent the exchange interaction between the two electrons. Only the non-zero parts of these matrices that act on the interior parts of the vectors, $\mathbf{p}_{\text{int}}$ and $\mathbf{q}_{\text{int}}$ are shown in Fig. (6.5). In this explicit example, the vector $\mathbf{p}$ represents the $1s_0$ state, while the vector $\mathbf{q}$ represents the $2p_{-1}$ state. Accordingly, in the vector $\begin{pmatrix} \mathbf{p} \\ \mathbf{q} \end{pmatrix}$, a Dirichlet boundary condition has been imposed explicitly along $x = -1$ for the vector $\mathbf{q}$ by setting $\mathbf{q}_{b_x} = 0$, as shown in Fig. (6.5). The coupled eigensystem can then be written as a system of coupled matrix equations for the interior points as,

$$E^{11}\mathbf{p}_{\text{int}} + T^{12}\mathbf{q}_{\text{int}} = \lambda\mathbf{p}_{\text{int}} - C\mathbf{p}_{b_y} - E_N\mathbf{p}_{b_x} \tag{6.60a}$$

and

$$T^{12}\mathbf{p}_{\text{int}} + E^{22}\mathbf{q}_{\text{int}} = \lambda\mathbf{q}_{\text{int}} - C\mathbf{q}_{b_y}. \tag{6.60b}$$

The sub-matrices C and E_N are defined as given in Eqs. (6.40b & c). However, The sub-matrix E^{11} and E^{22} have slightly different entries on the diagonal and are thus defined as,

$$E^{ii} = \begin{bmatrix} E_1^{ii} & E_3 \\ E_2 & E_4^{ii} \end{bmatrix}_{(N-1)^2 \times (N-1)^2}, \quad i = 1, 2. \tag{6.61}$$

Similar to our discussion regarding the hydrogen atom in Section 6.3.1.2, we are required to express the vectors $\mathbf{p}_{b_x}$, $\mathbf{p}_{b_y}$ and $\mathbf{q}_{b_y}$ in terms of $\mathbf{p}_{\text{int}}$ and $\mathbf{q}_{\text{int}}$ respectively, by implementing Neumann boundary conditions. This would enable us to then cast the coupled eigenvalue problem into its final form, prior to its numerical solution.

Once again we construct the boundary matrices B_x and B_y as described earlier. This time however, we need to implement Neumann boundary conditions for both electrons. Thus, in addition to Eqs. (6.44) and (6.45), we have a Neumann boundary condition along $y = -1$ for the vector $\mathbf{q}$, i.e.,

$$B_y\mathbf{q}|_{y=-1} = 0. \tag{6.62}$$

Expressions for $\mathbf{p}_{b_x}$, $\mathbf{p}_{b_y}$ and $\mathbf{q}_{b_y}$, in terms of $\mathbf{p}_{\text{int}}$ and $\mathbf{q}_{\text{int}}$ respectively, are obtained using the method described earlier in Section 6.3.1.2. These when

substituted into Eqs. (6.60a and b) immediately yield,

$$\left\{ E^{11} - CH^{-1}G - E_N B_N^{-1}(B_1 - B_2 H^{-1}G) \right\} \mathbf{p}_{\text{int}} + T^{12}\mathbf{q}_{\text{int}} = \lambda \mathbf{p}_{\text{int}} \quad (6.63a)$$

and

$$T^{12}\mathbf{p}_{\text{int}} + \left\{ E^{22} - CH^{-1}G \right\} \mathbf{q}_{\text{int}} = \lambda \mathbf{q}_{\text{int}} \quad (6.63b)$$

This can then immediately be recast as a standard coupled eigenvalue problem for the interior mesh points as,

$$\begin{pmatrix} \left[E^{11} - CH^{-1}G - E_N B_N^{-1}(B_1 - B_2 H^{-1}G) \right] & T^{12} \\ T^{12} & \left[E^{22} - CH^{-1}G \right] \end{pmatrix} \times$$

$$\begin{pmatrix} \mathbf{p}_{\text{int}} \\ \mathbf{q}_{\text{int}} \end{pmatrix} = \lambda \begin{pmatrix} \mathbf{p}_{\text{int}} \\ \mathbf{q}_{\text{int}} \end{pmatrix}.$$

$$(6.64)$$

Eq. (6.64) is then solved using standard algorithms to obtain the eigenvectors and eigenvalues. Once the wave functions have been obtained, the direct and exchange interactions are re-evaluated. These updated potentials are then reused to carry out the HF iterations until convergence is achieved. We would like to caution the reader once more that the formulation of the HF problem shown in Eq. (6.64) is for the explicit example of the configuration of helium given by $1^3(-1)^+$ or $1s_0 2p_{-1}$. For other configurations, depending upon the boundary conditions, Eq. (6.64) will take a very different form. The left hand side operator shown in Eq. (6.64) is the pseudospectral representation of the HF operator for a particular configuration of the helium atom.

It is also to be mentioned at this juncture, that we are not finding an approximate effective potential for the exchange interaction as first suggested by Slater [see 325] which greatly simplifies the HF equations. As a result Eq. (6.64) takes the form of a fully coupled eigenvalue problem, *and not*, we emphasize, the usual single-particle form,

$$F_i \psi_i = \epsilon \psi_i, \quad (6.65)$$

where F is the usual Fock operator given explicitly by

$$F_i = H_i + \sum_j (J_j - K_j). \quad (6.66)$$

The direct (J_j) and exchange interactions (K_j) are usually found using an approach similar to Slater's, employing wave functions from the previous iteration. This procedure essentially uncouples the eigenvalue problem [see 325]. It can be seen upon examining Eq. (6.64) that we are not carrying out such an approximation. Therefore we solve the full HF problem as a coupled eigenvalue problem. In our computations for helium we found that the solution of the uncoupled problem following Ref. [325] yielded slightly more bound results, by about $1 - 2\%$. That being said, our goal here is to provide a fast and efficient means of solving the fully coupled problem, therefore the numerical procedure outlined below pertains as such, to the latter and the results presented in Section 6.5 are likewise for a solution of the coupled problem.

The method described above can easily be extended to tackle the case of the multi-electron atom, say lithium. It can be seen that the problem size in Eq. (6.64) will grow not only with the number of mesh points but also with the number of electrons. For a given number of mesh points N in each direction and a certain number of electrons n_e, the size of the HF operator in Eq. (6.64) is $[n_e(N-1)^2) \times (n_e(N-1)^2]$. If one were to express the exchange interactions completely using information from the previous iteration and thus uncouple the eigenvalue problem as in Eq. (6.65), then within each HF iteration, one would be solving n_e eigenvalue problems each of size $[(N-1)^2 \times (N-1)^2]$. Thus, since computer memory requirements are governed by this latter system size, the coupled problem in Eq. (6.64) is readily seen to be far more intensive than the uncoupled problem in Eq (6.65). This important distinction is to be kept in mind when interpreting the results obtained in this study. That being said, we give here presently, the block matrix form that the coupled HF problem will take for the lithium atom,

$$\begin{pmatrix} M_{11} & T^{12} & T^{31} \\ T^{12} & M_{22} & T^{23} \\ T^{31} & T^{23} & M_{33} \end{pmatrix} \begin{pmatrix} \mathbf{p} \\ \mathbf{q} \\ \mathbf{r} \end{pmatrix} = \lambda \begin{pmatrix} \mathbf{p} \\ \mathbf{q} \\ \mathbf{r} \end{pmatrix}. \tag{6.67}$$

The exchange operators are symmetric under permutation, thus $T^{ij} = T^{ji}$, $i, j = 1, 2, 3$. The matrices M_{ii}, $i = 1, 2, 3$, on the other hand, are formulated in a manner similar to that depicted pictorially in Fig. (6.5), modulo implementation of appropriate Dirichlet and Neumann boundary conditions, depending up the state in question.

Thus for a large number of node points and electrons, it becomes imperative that efficient computational methods be used in order to facilitate an economical solution of the fully coupled HF problem in Eq. (6.3), not only in terms of computer memory, but also quite importantly, in terms of computational time. The primary objective, as was stated earlier, is to delineate a method for the expedient solution of the single-configuration HF problem, providing a software that could be easily integrated into atmosphere models for neutron stars. It is to be acknowledged at the very outset, that these results can be improved by using CI or MCHF methods. It is also to be acknowledged that since we are not using the usual approximation for the exchange interaction, the computer memory requirements are quite a lot higher than the uncoupled problem. This fact should be kept in mind should the atomic structure software described herein be considered for integration with atmosphere models.

The following section details the efficient numerical methods employed for this solution and the convergence tests that are carried out.

6.4 Numerical Details

Examination of Fig. (6.5) reveals that the matrix M, is largely a sparse matrix. Thus we can take advantage of this fact and employ sparse matrix methods for the method of solution of the coupled eigenvalue problem.

An atomic structure software package based on the pseudospectral method outlined in Section 6.3 was developed for this study. The code was written in the high level programming language MATLAB$^{\circledR}$ making particular use of its fast matrix manipulation algorithms. The eigenvalue problems described in Eqs. (6.52), (6.64) and (6.67) are solved by discretizing the equations and solving the resultant algebraic eigenvalue problem. The discretization is done using a standard Chebyshev-Lobatto spectral collocation method [see 322]. The coupled eigenvalue problem in Eq. (6.3) is then solved using a sparse matrix generalized eigensystem solver using the implicitly restarted Arnoldi method (IRAM) [see 326–328]. A numerical implementation of this method is readily available in the software package ARPACK [see 328]. The key advantage of employing IRAM is that the memory storage requirements are far less than the original Arnoldi algorithm. Very briefly, it employs a typical Arnoldi factorization to generate an orthogonal basis for forming a Krylov subspace. The implicit restarting is closely related to the well un-

derstood implicitly shifted QR algorithm [see 329, 330], where the idea is to restart the Arnoldi factorization with a vector that is better pre-conditioned so that it can damp unwanted components from the eigenvector expansion. At this stage the reader is referred to Refs. [327, 328, 331] for details on the implementation and other computational aspects of ARPACK. The computational time is remarkably reduced due to implicit restarting, particularly for computing a few eigenvalues in a given part of the spectrum [see 328]. This method was found to yield accurate results for the energy eigenvalues of the first few eigenstates of helium and lithium in intense magnetic fields. In our computations during a typical Arnoldi iteration, it was seen that generating a Krylov subspace with about 50 basis vectors was sufficient for determining around 15 eigenvalues in the vicinity of a given shift (σ), by employing the shift-invert algorithm [see 328]. Runs were carried out for different values of the magnetic field strength parameter β_Z, in the range $5 \times 10^{-1} \leq \beta_Z \leq 10^3$, for the cylindrical pseudospectral code. A typical tolerance of around 10^{-10} was employed for the internal errors of ARPACK. Additionally for testing convergence of the pseudospectral method, we employed up to six different levels of mesh refinement, ranging from coarse to fine mesh i.e., $N = 21, 31, 41, 51, 61$ and 71 mesh points in each direction. The finest mesh calculations for lithium for example, took on the order of $1000 - 1400$ seconds of computing time on an Intel$^{\circledR}$ Xeon$^{\circledR}$ E5620 2.4 GHz processor, for obtaining a fully converged HF solution.

The code takes as its input, the number of electrons in the atom n_e, the nuclear charge Z, and the magnetic field strength parameter β_Z and the configuration for which calculations are to be carried out, such as the state $1s_0 2p_{-1} 3d_{-2}$, etc. It then proceeds to compute systematically the eigenvalues and eigenfunctions of the coupled system of equations in Eq. (6.3), according to the iterative procedure described below in brief.

Eqs. 6.3, 6.5 and 6.6 are solved in a three step process using the iterative self-consistent field (SCF) Hartree-Fock method [see 91]. First, an initial estimate is obtained for the eigenvectors by solving Eq. 6.3 without the contributions due the interaction between the electrons. The second step involves obtaining estimates for the potentials due to the direct and exchange interactions amongst the electrons, using the elliptic partial differential Eqs. 6.5 and 6.6. These are solved using the estimates for the wave functions obtained in the previous step. These potentials are then used to solve for better estimates of the eigenfunctions along with the relevant eigenvalues in Eq. 6.3. The last two steps are iterated in the order described above to obtain progressively

better estimates for the eigenvalues and eigenvectors with each HF iteration. It was observed during our runs that fast convergence was achieved; within about $6-12$ HF iterations. A convergence criterion for the HF iterations was employed wherein the difference between the HF energies for two consecutive iterations was tested. Typically, a tolerance on the order of $10^{-8}E_{Z,\infty}$ was employed for this purpose. Once the HF iterations attained convergence, the total energy of the Hartree-Fock state under consideration is reported according to Eq. 6.4.

Additionally, the current work does not include relativistic corrections to the energies. These corrections have been shown to be small in strong as well as intense magnetic fields for hydrogenic atoms [see 332–334]. Their results for the hydrogen atom reveal that for the states considered in their studies, the fractional change in energy is on the order of 10^{-6} or so. This fractional change in energy was seen to be smaller than the numerical errors arising from convergence of the pseudospectral method, established using different levels of mesh refinements. Thus, while relativistic corrections are important, it was not possible to account for them accurately in the current study.

Moreover, it is to be kept in mind that the current implementation of the pseudospectral method for the solution of the HF problem, is a single configuration calculation. Thus, it does not take into account effects such as electron correlation which can become important for many-electron systems. Post-HF methods, such as configuration-interaction and MCHF methods will no doubt yield more accuracy. However, as mentioned in Section 6.1, the aim of the current study is to facilitate a fast and computationally economical method for the 2D solution of the many-electron single-configuration problem, without resorting to any basis expansion, or separation of variables or even the commonly employed adiabatic approximation. The energies and wave functions obtained from such a calculation, could be directly employed in a 2D-configuration-interaction calculation, or the method described in Section 6.3 could be extended towards a full 2D-MCHF framework. Such an undertaking, while being perhaps the next step in the evolution of the atomic structure code described herein, was considered to be outside the scope of the current study.

Presently, the results are presented alongside a discussion in the following section.

6.5 Results and Discussion

The atomic structure software package developed in the current study extends our earlier computations for atoms in strong magnetic fields [see 88, 92], towards the intense field regime, $\beta_Z \gg 1$. The states that were considered in this study are labelled using both the field-free and strong-field notations for the sake of clarity; these can be found in Table 6.1 which lists these different states of helium and lithium. We have studied the six most tightly bound states of each atom in the intense magnetic field regime ($\beta_Z \gg 1$). Within a given parity sub-space, typically there are crossovers that occur as the magnetic field is reduced and the reader is referred to Ref. [289] for an excellent discussion regarding ground state crossovers which are typically in the regime $\beta_Z < 1$. Within each given parity sub-space, we considered the most tightly bound state in the intense field regime.

Table 6.1: The different states of helium and lithium considered in this study, listed using both intense-field and field-free notation. It is the the field-free configurations that are calculated in the weak- and intermediate-field regimes.

	Intense-field	Field-free
	$1^3(-1)^+$	$1s_0 2p_{-1}$
	$1^3(-1)^-$	$1s_0 3d_{-1}$
Helium	$1^3(-2)^+$	$1s_0 3d_{-2}$
	$1^3(-2)^-$	$1s_0 4f_{-2}$
	$1^3(0)^+$	$1s_0 2s_0$
	$1^3(0)^-$	$1s_0 2p_0$
	$1^4(-3)^+$	$1s_0 2p_{-1} 3d_{-2}$
	$1^4(-3)^-$	$1s_0 2p_{-1} 4f_{-2}$
Lithium	$1^4(-2)^+$	$1s_0 2s_0 3d_{-2}$
	$1^4(-2)^-$	$1s_0 2p_{-1} 3d_{-1}$
	$1^4(-1)^+$	$1s_0 2s_0 2p_{-1}$
	$1^4(-1)^-$	$1s_0 2p_0 2p_{-1}$

6.5.1 The Helium Atom

For the states of helium listed in Table 6.1, eigenvalue computations were carried out and the total HF energies were calculated for six different levels

of mesh refinement. This enables us to extrapolate the convergence of the results to the limit of infinitely fine mesh, as shown in Fig. 6.6. This figure shows the convergence of eigenvalues obtained from a few sample calculations for both helium and lithium. With each level of mesh refinement, the system size grows and the full system size is reported on the $x-$axis of Fig. 6.6. This is the dimension of the coupled eigenvalue problem that is solved. A variety of extrapolation methods were tested and it was seen that using piece-wise continuous cubic Hermite interpolating polynomials [see 335], yielded the most reasonably extrapolated results over the entire range of magnetic field strengths considered here. For extrapolation to infinitely fine mesh, we employed the average area per unit grid size as the abscissa. Thus it was possible to extrapolate to infinitely fine mesh or zero area per unit grid size. It is the extrapolated values that are reported in the tables for the binding energies.

The calculated HF energies for positive parity states of helium are given in Table 6.2, while those for the negative parity states are shown in Table 6.3. The absolute values of the binding energies are given therein. Also shown therein, are the calculated data from other references for comparison. In this study we investigated the three most tightly bound states within each parity sub-space, in the limit of intense magnetic fields. The corresponding weak field orbitals of these states are those listed in Table 6.1. The values given in parentheses are from eigenvalue computations using spherical coordinates. These calculations were carried out using our pseudospectral atomic structure software developed in an earlier study [see 92]. An improved and faster version of the code was employed, again using the same levels of mesh refinement for maintaining consistency. The cylindrical pseudospectral method begins to lose accuracy as the magnetic field decreases, in the weak field region, while in contrast, the spherical pseudospectral method loses accuracy in the intense field limit. Therefore using a combination of the two types of codes, we can explore the entire range in $0 \leq \beta_Z \leq 1000$.

6.5.1.1 The positive $z-$parity sub-space of Helium

It can be seen upon examining the data in Table 6.2 that the results obtained in the current study are in good agreement with values obtained elsewhere and in some instances represent slight to moderate improvements in the upper bound of the binding energy. For the state $1^3(0)^+$ which is comprised of the oribtals $1s_0 2s_0$, we see that the average difference with respect to the most

Table 6.2: Absolute value of the binding energies of the positive parity state $1^3(0)^+$, of helium. Energies are in units of Rydberg energies in the Coulomb potential of nuclear charge $Z = 2$ for helium. Accurate data from other work is also provided for comparison. $(\beta_Z = \gamma/2Z^2)$. The values given in parentheses are obtained from a faster version of our spherical atomic structure code developed earlier [see 92].

β_Z	Here	Refs. [83]/[88]	Ref. [277]	Ref. [see 286]
0	(1.0899)		1.0871 [a]	1.0876
0.01	(1.1256)	1.1213	1.1213	1.1220
0.05	(1.2103)	1.1911	1.2056	1.2064
0.1	(1.2914)	1.2133	1.2860	1.2868
0.125	(1.3301)			1.3253
0.2	(1.4389)		1.4330	1.4338
0.25	(1.5112)			1.4999
0.5	1.7878	1.4670	1.7718	
0.625	1.9064			1.8841
0.7	1.9714	1.6690	1.9447	
1	2.1974	1.9116	2.1601	
1.25	2.3564			2.3137
2	2.7395	2.4793	2.6840	
2.5	2.9461			2.8862
5	3.7022	3.4672	3.6272	
6.25	3.9861			3.9076
7	4.1386			
10	4.6565	4.4362	4.5693	
12.5	5.0117			4.9215
20	5.8449	5.6367	5.7473	
25	6.2837			
50	7.8424	7.6473	7.7334	
62.5	8.4121			
70	8.7150			
100	9.7302	9.5434	9.6143	

[a] Ref. [89]   **continued on next page**

		continued from previous page		
		Refs.	Ref.	Ref.
β_Z	Here	[83]/[88]	[277]	[see 286]
125	10.4152			
200	11.9909	11.8111		
250	12.8052			
500	15.6258	15.4537		
700	17.1629			
1000	18.9191	18.7519		

bound values given therein from other calculations, is about $\Delta \approx 1.25\%$ with the maximum difference being at around $\beta_Z = 6.25$ at around 2%. The results remain accurate to large values of magnetic field strength, i.e., $\beta_Z = 1000$, where little data is available. The results obtained from the cylindrical pseudospectral method are about 0.8% more bound than the results of Ref. [83] at around $\beta_Z = 1000$. Similarly for the state $1^3(-2)^+$, we notice that the average difference from the most tightly bound values obtained elsewhere is about $\Delta \approx 2.5\%$. In particular we see that both the cylindrical and spherical pseudospectral codes are slightly more accurate than our earlier study [see 88] in the intermediate and strong field regime; $10^{-2} \leq \beta_Z \leq 10$, by a maximum of about 5%. The field-free spectroscopic orbital of the second electron in the state $1^3(-2)^+$, is the $3d_{-2}$ orbital, which has a much greater spatial extent than the $1s_0$ orbital, even in strong and intense magnetic fields. The same is true for the $2s_0$ electron in the configuration $1^3(0)^+$. In our earlier study [see 88] we had adopted a finite-element based approach for the solution of the single-configuration HF problem and as a result, had truncated the domain of the problem to about 20 Bohr radii in both the $z-$ and $\rho-$ directions. However, in the current study we are employing a compactification which does not truncate the domain, but rather preserves the information in the entire two-dimensional space. As a result, orbitals such $3d_{-2}$ that have a greater spatial extent, are determined with a little more accuracy in comparison to our previous study [see 88]. Concordantly, we see that the improvement in the strong field regime is on the order of $2-5\%$ with respect to the results obtained in Ref. [88]. We also see that in the limit of intense fields, i.e. $\beta_Z \geq 10$, the accuracy is still preserved and we see an improvement in the estimates with respect to the Quantum Monte Carlo method due to Jones et al. [see

Table 6.3: Absolute value of the binding energies of the positive parity state $1^3(-2)^+$, of helium. Energies are in units of Rydberg energies in the Coulomb potential of nuclear charge $Z = 2$ for helium. Accurate data from other work is also provided for comparison. ($\beta_Z = \gamma/2Z^2$). The values given in parentheses are obtained from a faster version of our spherical atomic structure code developed earlier [see 92].

β_Z	Here	Refs. [83]/[88]	Ref. [277]	Ref. [see 286]
0	(1.0307)	1.0179[a]		1.0278
0.01	(1.0872)	1.0852[a]	1.0830	1.0833
0.05	(1.2212)	1.2175[a]	1.2160	1.2167
0.1	(1.3495)	1.3510[a]	1.3436	1.3450
0.125	(1.4063)			1.4016
0.2	(1.5572)	1.5598[a]		1.5525
0.25	(1.6459)			1.6411
0.5	(2.0035)	2.0009[a]	1.9945	2.1425
0.625	(2.1948)			
0.7	(2.3041)	2.2246[a]	2.2171	
1	2.6328	2.4981[a]	2.4933	
1.25	2.8285			2.6940
2	3.3090	3.1685[a]	3.1634	
2.5	3.5696			3.4274
5	4.5305	4.3740[a]	4.3693	
6.25	4.8938			4.7380
7	5.0894	4.9268[a]	4.9203	
10	5.7563	5.5851[a]	5.5770	
12.5	6.2158			6.0443
20	7.2995	6.9867	7.0938	
25	7.8734			
50	9.9273	9.5806	9.6643	
62.5	10.6835			
70	11.0867		10.7977	
100	12.4434	12.0449	12.1142	

[a] Ref. [88]   **continued on next page**

		continued from previous page		
		Refs.	Ref.	Ref.
β_Z	Here	[83]/[88]	[277]	[see 286]
125	13.3631			
200	15.4914	15.0117		
250	16.5978			
500	20.4605	19.5816		
700	22.5842			
1000	25.0252	24.2004		

89]. While the method developed by the authors in Ref. [89, 277] may be more involved than the simple single-configuration HF treatment given here, nonetheless it is to be remembered that in the current study we are solving a fully coupled eigenvalue problem for the electrons at each HF iteration and are not solving the problem by carrying out an approximation as suggested by Slater [see 325] (see discussion regarding Eqs. (6.65) and (6.66) above). This makes the current solution of the problem computationally more intensive. Thus, overall in the current study, the computational overhead may be slightly more than that of the work in Refs. [89, 277]. With this cautionary note to the reader in place, we see that the pseudospectral code developed in this study produces slightly improved results. The IRAM method that is employed for calculating the eigenvalues (see Section 6.4) however, reduces the computational overhead quite significantly, in comparison to solving for the entire spectrum of the fully coupled problem. On average the computation of the converged values in Tables 6.2 and 6.3 took between about $250-600$ s of computing time for the finest mesh calculations, utilizing about $4-5$GB of computer memory.

The third state that was investigated was the ground state of helium in intense magnetic fields. This is the configuration $1^3(-1)^+$ comprised of the spectroscopic orbitals $1s_0 2p_{-1}$. Here we see that the values obtained from the pseudospectral method produce values that are in general a little more bound than the results obtained in our earlier study Ref. [88]. The maximum improvement in the range $0 \leq \beta_Z \leq 1.25$ is about $\Delta \approx 0.7\%$. However we see that the configuration interaction calculations due to Schmelcher and co-workers, are in general more accurate than the single configuration results, although the results are still in reasonable agreement ($\Delta \approx 1.6\%$ on

Table 6.4: Absolute value of the binding energies of the positive parity state $1^3(-2)^+$, of helium. Energies are in units of Rydberg energies in the Coulomb potential of nuclear charge $Z = 2$ for helium. Accurate data from other work is also provided for comparison. $(\beta_Z = \gamma/2Z^2)$. The values given in parentheses are obtained from a faster version of our spherical atomic structure code developed earlier [see 92].

β_Z	Here	Refs. [83]/[88]	Ref. [277]	Ref. [see 286]
0	(1.0686)	1.0668[a]	1.0657[c]	1.0666
0.01	(1.1223)	1.1183[a]	1.1177	1.1193
0.05	(1.2734)	1.2691[a]	1.2683	1.2704
0.1	(1.4209)	1.4189[a]	1.4151	1.4178
0.125	(1.4859)			1.4828
0.2	(1.6579)	1.6585[a]	1.6508	1.6544
0.25	(1.7583)			1.7545
0.5	(2.1582)	2.1550[a]	2.1490	
0.625	(2.3183)			2.3128
0.7	(2.4060)	2.4029[a]	2.3956	
1	2.7209	2.7026[a]	2.7000	
1.25	2.9254			2.9197
2	3.4213	3.4384[a]	3.4333	
2.5	3.6905			3.7203
5	4.6835	4.7502[a]	4.7441	
6.25	5.0593			5.1421
7	5.2615	5.3474[a]	5.3408	
10	5.9516	6.0543[a]	6.0506	
12.5	6.4271			6.5524
20	7.5490	7.5750	7.6845	
25	8.1432			8.2895[b]
50	10.2704	10.3567	10.4438	
62.5	11.0537			11.2333[b]
70	11.4712		11.6533	
100	12.8764	12.9904	13.0632	

[a] Ref. [88]   **continued on next page**

		Refs.	Ref.	Ref.
β_Z	Here	[83]/[88]	[277]	[see 286]
125	13.8289			14.0161
200	16.0328	16.1516		
250	17.1783			17.3495
500	21.1763	21.2521		
700	23.3733			
1000	25.8978	25.8917		

continued from previous page

average, over the range $2 \leq \beta_Z \leq 12.5$). This shows that taking into account the effects of electron correlation and interactions between different configurations is an important aspect necessary for the accurate solution of the multi-electron problem. The drawback however is that such calculations are computationally more involved than a simple single configuration calculation. We also see that for this state towards the higher end of the intense field regime, i.e., $\beta_Z \approx 1000$, there is a minor loss in accuracy. This is attributed to the fact that the $2p_{-1}$ electron becomes exceedingly bound and concomitantly, greatly reduced in spatial extent and constrained closer to the nucleus while at the same time being elongated along the $z-$direction. Our finest mesh calculation yielded an absolute value for the HF binding energy of about $25.9923 E_{Z,\infty}$, however, the result obtained from extrapolation is what is quoted in Tables $6.2-6.4$. Thus, we see that this result could be made more accurate by increasing the levels of mesh refinement so that better convergence could be achieved for the $2p_{-1}$ orbital in the extreme end of the intense field regime. Our calculations were ultimately limited by computing resources, thus further mesh refinement in excess of $N = 71$ node points in each direction was not possible.

Overall, for the $1^3(-1)^+$ state of helium the agreement with the most bound energy values from different studies, is on average about $\Delta \approx 0.9\%$. Since our primary objective in this study is to delineate a fast and reasonably accurate method for atomic structure calculations in intense magnetic fields, we considered this level of agreement to be sufficient.

Next we discuss the three most tightly bound negative parity states of the helium atom in intense magnetic fields.

6.5.1.2   The negative $z-$parity sub-space of Helium

The three most tightly bound negative parity states of helium in the intense field regime, were investigated in this study. The results for the binding energies are shown in Tables 6.5−6.7. For the state $1^3(0)^-$ we see that the results from the pseudospectral calculations, in both weak and strong fields ($0 \leq \beta_Z \leq 10$), are in general more bound in comparison to the results obtained in our earlier study [see 88]. The average improvement is about $\Delta \approx 3.2\%$. As mentioned earlier, the current study employs a compactification of the entire domain without truncation and as a result the estimation of the orbitals that have a greater spatial extent is slightly more accurate in comparison to Ref. [88]. We also see a moderate improvement in the intense field regime where the average improvement is around $\Delta \approx 4\%$ with respect to the most bound results quoted in the table. At the higher end of the intense field regime ($\beta_Z \geq 50$), the results continue to remain accurate, as the pseudospectral method better estimates the spatial extent and shape of the $2p_0$ electron in the $1^3(0)^-$. Here the improvements with respect to the data from Refs. [83] and [see 277] are about $\Delta \approx 2\%$.

The calculated binding energies of the remaining two tightly bound states $1^3(-1)^-$ and $1^3(-2)^-$ show a similar trend. The average improvements with respect to the most bound results obtained elsewhere are around $\Delta \approx 3.8\%$ in both cases. It can be seen upon examining the data for these states, that the state $1^3(-2)^-$ becomes more bound than the $1^3(-1)^-$ state of helium with increasing magnetic field strength in the intense field regime. However the binding energies are still quite close to each other.

One of the aims of the current study is to provide a fast method for the calculation of the energy landscape of atoms in intense magnetic fields; therefore, we have additionally calculated fits to the data provided in Tables 6.2 through 6.7. The model fits are rational functions whose analytic form is given by,

$$f(x) = \frac{\sum_{i=0}^{n} a_i x^i}{x^m + \sum_{i=0}^{m-1} b_i x^i}, \tag{6.68}$$

where $x = \ln(1 + \beta)$ and $m = n - 2$. The fitting was carried out using a non-linear least squares Levenberg-Marquardt algorithm with line searches [see 336]. The coefficients and the maximal fitting errors over the entire range $\beta_Z = 0$ to $\beta_Z = 10^3$ are given in Table 6.8. As can be seen in Table 6.8, the errors are small enough that these fitting functions could be employed directly in atmosphere models of neutron stars rather than incorporating

Table 6.5: Absolute value of the binding energies of the negative parity state $1^3(0)^-$, of helium. Energies are in units of Rydberg energies in the Coulomb potential of nuclear charge $Z = 2$ for helium. Accurate data from other work is also provided for comparison. $(\beta_Z = \gamma/2Z^2)$. The values given in parentheses are obtained from a faster version of our spherical atomic structure code developed earlier [see 92].

β_Z	Here	Refs. [83]/[88]	Ref. [277]	Ref. [see 286]
0	(1.0686)	1.0641[a]	1.0657[c]	1.0665
0.01	(1.1056)	1.1029[a]	1.1016	1.1026
0.05	(1.2147)	1.2135[a]	1.2099	1.2112
0.1	(1.3229)	1.3231[a]	1.3174	1.3191
0.125	(1.3727)			1.3669
0.2	(1.4982)	1.4988[a]	1.4914	1.4936
0.25	(1.5721)			1.5676
0.5	1.9831	1.8647[a]	1.8593	
0.625	2.1056			1.9796
0.7	2.1722	2.0461[a]	2.0404	
1	2.4025	2.2685[a]	2.2641	
1.25	2.5635			2.4243
2	2.9487	2.8060[a]	2.7989	
2.5	3.1555			3.0057
5	3.9092	3.7522[a]	3.7466	
6.25	4.1916			4.0297
7	4.3431	4.1817[a]	4.1762	
10	4.8579	4.6920[a]	4.6862	
12.5	5.2110			5.0400
20	6.0396	5.7495	5.8585	
25	6.4762			6.2940[b]
50	8.0289	7.7491	7.8346	
62.5	8.5969			
70	8.8990		8.6998	
100	9.9120	9.6370	9.7075	

[a] Ref. [88]   **continued on next page**
[b] Ref. [289]

		continued from previous page		
		Refs.	Ref.	Ref.
β_Z	Here	[83]/[88]	[277]	[see 286]
125	10.5958			
200	12.1694	11.8970		
250	12.9830			
500	15.8018	15.5307		
700	17.3384			
1000	19.0943	18.8230		

a code that calculates the binding energy. Thus, atmosphere models which are computationally intensive to begin with, need not be further complicated with the addition of an atomic structure calculation module, even though the software developed in this study is compact and computationally efficient and economical in terms of computational time as well.

6.5.2   The Lithium Atom

We investigated the six most tightly bound states of the lithium atom in intense magnetic fields. The binding energies obtained from solving the coupled eigenvalue problem in Eq. (6.67) are shown in Tables 6.9 through 6.12. These tables show the results for the positive and negative parity states, respectively. As in the case of the helium atom, the HF binding energies are results that were obtained after extrapolating to the limit of infinitely fine mesh.

6.5.2.1   The positive $z-$parity sub-space of Lithium

In contrast to the helium atom, lithium has been investigated far less often in the literature, and data is scarce for the binding energies of the different states, particularly in the intense field regime. Tables 6.9 through 6.11 show the computed HF binding energies for the three most tightly bound states in the positive parity sub-space of the lithium atom. Once more, the values given in parentheses are those computed using our spherical pseudospectral code. Upon examining the data in Table 6.11, we see that the state $1^4(-3)^+$ of lithium comprised of the orbitals $1s_0 2p_{-1} 3d_{-2}$ is the best investigated

Table 6.6: Absolute value of the binding energies of the positive parity state $1^3(-1)^-$, of helium. Energies are in units of Rydberg energies in the Coulomb potential of nuclear charge $Z = 2$ for helium. Accurate data from other work is also provided for comparison. ($\beta_Z = \gamma/2Z^2$). The values given in parentheses are obtained from a faster version of our spherical atomic structure code developed earlier [see 92].

		Refs.	Ref.	Ref.
β_Z	Here	[83]/[88]	[277]	[see 285]
0	(1.0307)			1.0278
0.01	(1.0745)	1.0693	1.0702	1.0705
0.05	(1.1808)	1.1565	1.1756	1.1761
0.1	(1.2846)	1.2270	1.2764	1.2795
0.125	(1.3308)			1.3255
0.2	(1.4539)	1.3174	1.4469	1.4481
0.25	(1.5262)			1.5202
0.5	1.9260	1.5131	1.8078	
0.625	2.0537			1.9259
0.7	2.1227	1.7202	1.9877	
1	2.3605	1.9678	2.2097	
1.25	2.5264			2.3687
2	2.9224	2.5433	2.7441	
2.5	3.1343			2.9511
5	3.9033	3.5369	3.6950	
6.25	4.1902			3.9795
7	4.3440		4.1264	
10	4.8652	4.5067	4.6387	
12.5	5.2218			4.9947
20	6.0567	5.7056	5.8158	
25	6.4958			
50	8.0536	7.7118	7.7958	
62.5	8.6227			
70	8.9252		8.6651	
100	9.9389	9.6039	9.6748	

continued on next page

		continued from previous page		
		Refs.	Ref.	Ref.
β_Z	Here	[83]/[88]	[277]	[see 285]
125	10.6235			
200	12.1969	11.8675		
250	13.0102			
500	15.8279	15.5050		
700	17.3638			
1000	19.1190	18.7997		

state in the literature thus far. The results obtained from the current study can be seen to be in reasonably good agreement with the estimates obtained elsewhere. The average improvement in the estimate of the binding energy for the state $1^4(-3)^+$, over the entire range $0 \leq \beta_Z \leq 1000$, is about $\Delta \approx 1\%$, with a maximum of around 3% in the strong field regime. The majority of the results for the binding energy of the $1^4(-3)^+$ from other studies in Tables 6.9 through 6.11, are from Ref. [289]. This study was also a single configuration calculation, albeit using a numerical approach employing finite-difference based mesh methods. We see that the current pseudospectral approach preserves accuracy as the magnetic field increases obtaining slightly better estimates than Ref. [289], even at the higher end of the intense field regime. Including effects of electron correlation and relativistic effects will of course improve the results obtained herein.

The second most tightly bound positive parity state of lithium is $1^4(-1)^+$, shown in Table 6.10. This state comprises of the orbitals $1s_0 2s_0 2p_{-1}$. It can be seen that the estimates obtained in the current study are slight improvements with an average of $\Delta \approx 0.8\%$ over the range $0 \leq \beta_Z \lesssim 56$. While this state is not as tightly bound as the $1^4(-3)^+$ state in the intense field regime, examination of the data in weak fields reveals that with decreasing magnetic field strength, this state becomes the most tightly bound of the three states, in the vicinity of $\beta_Z \approx 0.3$.

The third state investigated is $1^4(-2)^+$, which represents the third most tightly bound state of the positive $z-$parity states in intense magnetic fields. Data for this state are shown in Table 6.9. For this state however, there is no data in the intense field regime. The only available data shown is in the weak and strong field regime. We see that in this case the average difference

Table 6.7: Absolute value of the binding energies of the positive parity state $1^3(-2)^-$, of helium. Energies are in units of Rydberg energies in the Coulomb potential of nuclear charge $Z = 2$ for helium. Accurate data from other work is also provided for comparison. $(\beta_Z = \gamma/2Z^2)$. The values given in parentheses are obtained from a faster version of our spherical atomic structure code developed earlier [see 92].

β_Z	Here	Refs. [83]/[88]	Ref. [277]	Ref. [see 284]
0	(1.0189)			1.0156
0.01	(1.0643)	1.0579	1.0601	1.0603
0.05	(1.1684)	1.1364	1.1634	1.1636
0.1	(1.2709)	1.1979	1.2650	1.2655
0.125	(1.3166)			1.3110
0.2	(1.4384)	1.2723	1.4319	1.4326
0.25	(1.5044)			1.5042
0.5	1.8844	1.4937	1.7912	
0.625	2.0174			1.9090
0.7	2.0885	1.7012	1.9709	
1	2.3300	1.9493	2.0500	
1.25	2.4982			2.3522
2	2.8993	2.5269	2.7287	
2.5	3.1136			2.9361
5	3.8898	3.5242	3.6827	
6.25	4.1789			3.9680
7	4.3337		4.1155	
10	4.8581	4.4971	4.6275	
12.5	5.2166			4.9860
20	6.0548	5.6989	5.8091	
25	6.4952			
50	8.0562	7.7080	7.7940	
62.5	8.6260			
70	8.9288		8.6620	
100	9.9434	9.6015	9.6724	

		continued from previous page		
β_Z	Here	Refs. [83]/[88]	Ref. [277]	Ref. [see 284]
125	10.6277			
200	12.2027	11.8661		
250	13.0163			
500	15.8350	15.5043		
700	17.3717			
1000	19.1256	18.7993		

from the results obtained in Ref. [90] is about $\Delta \approx 0.5\%$. And we see that the CI calculations produce a more accurate result at the higher end of the strong field regime, i.e., $\beta_Z \approx 0.5$. To the best of our knowledge, since data is not available in the literature for this state in the range $0.7 \leq \beta_Z \leq 1000$, no comparisons could be made and we state that the results obtained in the current study, represent the first such investigation. The same is true for the state $1^4(-1)^+$ (c.f. Table 6.10) in the range $70 \leq \beta_Z \leq 1000$

6.5.2.2 The negative $z-$parity sub-space of Lithium

Table 6.12 shows the three most tightly bound states of lithium that have negative $z-$parity. It is quite striking to see that the negative parity sub-space has not been tackled much in the literature. To the best of our knowledge, there is data available only for the $1^4(-1)^-$ state of lithium, comprised of the orbitals $1s_0 2p_0 2p_{-1}$. We see that the pseudospectral approach produces estimates that are on average about $\Delta \approx 2.3\%$ more bound than the results from other studies, over the range of magnetic field strengths $0 \leq \beta_Z \lesssim 56$. However, once more there is no data available in the higher end of the intense field regime of $70 \leq \beta_Z \leq 1000$.

The most tightly bound negative parity state of lithium is seen to be the state $1^4(-3)^-$, which is comprised of the orbitals $1s_0 2p_{-1} 4f_{-2}$. It can be seen that this state becomes the most tightly bound negative parity state at around $\beta_Z \approx 20$. Below this field strength, the $1^4(-1)^-$ is the most tightly bound of the three negative parity states of lithium shown in Table 6.12. To the best of our knowledge, this crossover has not been reported elsewhere in the literature. In addition, it can be seen by comparing the binding energies

reported in Tables 6.9 through 6.12, that the state $1^4(-3)^-$, is also the second most tightly bound state of lithium in intense magnetic fields. Moreover, the third state shown therein, the $1^4(-2)^-$ state, comprised of the orbitals $1s_0 2p_{-1} 3d_{-1}$, also has not been investigated in the literature. This latter state represents the third most tightly bound negative parity state of lithium in the intense field regime.

Thus overall we see that for the six most tightly bound states of lithium in intense magnetic fields, two of the states have not been investigated earlier at all ($1^4(-3)^-$ and $1^4(-2)^-$) and a third state ($1^4(-2)^+$) has not been investigated in the intense field regime. Therefore the results presented here appear to be the first of such studies. In addition we see that for the remaining three states that were investigated, the binding energies obtained in the current study show slight improvements relative to the estimates obtained elsewhere.

Furthermore, for the sake of facilitating atmosphere and crustal models of neutron stars, we have also carried out rational function fits to the data. Once again these analytic forms can be implemented directly in such codes, thereby circumventing the need for atomic structure calculations altogether. The rational functions have the same functional form as those described in Eq. (6.68) above. The coefficients of these rational functions are given in Table 6.13 alongside estimates of the fitting errors.

This concludes our discussion of the results obtained in this study. In the following section, we summarize the findings alongside a brief discussion of further avenues for investigation.

6.6 Conclusion

We present below a brief summary of this study and thereafter a short discussion of possible avenues for further work.

6.6.1 Summary

In the current study we have investigated low-Z atoms, helium and lithium in intense magnetic fields. A two-dimensional single-configuration Hartree-Fock method, as described in Ref. [88], was adopted. A key feature of the method is that the potentials for the inter-electronic interactions are obtained as solutions to the elliptic partial differential equations as given in Eqs. (6.5)

and (6.6). The HF equations in Eq. (6.3) are solved using the self consistent field method. In the current study the HF equations are solved as a fully coupled eigenvalue problem, without expressing the exchange interactions as an *effective* single-particle potential [see 325]. Thus it was observed that the system size grew as $n_e(N-1)^2 \times n_e(N-1)^2$, with n_e the number of electrons in the coupled problem and N the number of grid points in each direction.

A pseudospectral approach was adopted for the numerical solution of the problem using cylindrical coordinates so as to facilitate calculations in the intense field regime. The resulting semi-infinite domain of the problem was kept in its entirety and a suitable compactification was carried out. Thereafter, domain discretization was achieved using the commonly employed Chebyshev-Lobatto spectral collocation method. It was seen that the transformed equations had a coordinate singularity along the axis; a remnant of using cylindrical coordinates. The singularity was excised from the domain, by a translation of about $\delta = 10^{-14}$; see Section 6.3.1.

Additionally, we outlined in great detail, the formulation of the pseudospectral problem with a description of the method for imposing boundary conditions. For this purpose we gave explicit examples of the pseudospectral implementation for the ground states of hydrogen and helium in intense magnetic fields. The method developed in the current study is a generalization of the implementation due to the authors in Ref. [324].

The resulting discretized and coupled eigenvalue problem problem was solved using standard sparse matrix methods. The software package ARPACK was employed for computing eigenvalues in the desired part of the spectrum, obtaining a handful of eigenvalues and eigenvectors. A major advantage of the implicitly restarted Arnoldi method is the drastically reduced computational overhead and memory requirements, even for very large system sizes. As a result, we were able to obtain accurate eigenvalues and eigenvectors for helium and lithium in intense magnetic fields.

The key enabling advantage of the psuedospectral approach is the immensely reduced computational time required for obtaining accurate results; on the order of about a thousand seconds. In addition, since we have adopted here an unrestricted two-dimensional approach to the problem [see 88], it has the distinct advantage that we do not require a basis of functions to describe the wave functions. Thus the wave functions obtained in the current unrestricted 2D approach can be thought of in effect, as those arising from the superposition of a large number of basis functions. Simultaneously, we also do not impose a separation of coordinate variables in the functional form

of the individual electron wave functions and adhere instead to the natural symmetries of the problem, i.e., we maintain azimuthal symmetry.

We presented data for the six most tightly bound states of the helium atom in intense magnetic fields, in Tables 6.2 through 6.7. These were seen to be consistent with findings elsewhere. Similarly we investigated the six most tightly bound states of the lithium atom as well. However, we found that the data in the literature to be rather scarce for lithium. As a result we could only compare our results for four of the six states characterized in this study. We also presented, apparently for the first time, calculations for the binding energies for the states $1^4(-2)^-$ and $1^4(-3)^-$ of lithium. We find that the the latter state is also the second most tightly bound state of lithium in intense magnetic fields.

The work described herein was motivated primarily by the need to have accurately determined upper bounds for the binding energies of atoms in intense magnetic fields employing a computationally straight-forward implementation. As the atomic structure software developed here is small and computationally economical, it produces accurate results within a short amount of computing time. As a result, it can be incorporated directly into atmosphere and crustal models for neutron stars. However, while this may be desirable, it may present an additional layer of computational complexity. The user may wish to circumvent this by employing the rational function fits given in Tables 6.8 and 6.13. These analytic forms, model the data in the range $0 \leq \beta_Z \leq 1000$ and thus may simplify atmosphere and crustal models considerably.

6.6.2 Avenues for future work

At this juncture it is prudent to be aware of the limitations of the atomic structure software. First, since the code developed herein is merely a prototype, we have not included effects such as electron correlation, relativistic corrections, finite nuclear mass effects and electron screening. Conceivably, these effects once included, will result in further improvements to the binding energies. These additions would collectively represent one of the directions in which the current software could be improved. Secondly, the cylindrical pseudospectral code begins to lose accuracy in the intermediate range of magnetic field strengths, $\beta_Z \lesssim 0.5$. At this point it becomes necessary to carry out the computations using spherical coordinates. In the current study we are carrying out this switch manually, when we notice a drop in accu-

racy at low fields; this could be automated by keeping track of the change in the eigenvector estimates as the field is lowered gradually, in the weak and intermediate field regimes.

In the current study the memory requirements for the code are quite lean, considering that we are solving a fully coupled eigensystem. As a result the current study can be extended to tackle the case of mid-Z atoms such as beryllium, boron, carbon, oxygen etc., for which binding energy data is even more scarce than that for lithium. This would be the obvious next step in the utilization of the current version of the software for determining atomic structure in intense magnetic fields. In this regard it may possible to enhance computational efficiency by rendering certain parts of the code to execute on a parallel architecture. In particular, the determination of the eigenvalues within each HF iteration could be computed on a distributed system employing PARPACK; a parallel implementation of the implicitly restarted Arnoldi method. This would have a considerable impact on the usage of memory as well, since array storage requirements would be distributed over numerous nodes. In addition, at present in the serial version of the code, the interactions between each pair of electrons are calculated one after the next. As a result the computational time for determining the interaction matrices depends cumulatively on the number of pair-wise interactions. Clearly this becomes an issue with increasing number of electrons in the atom. This computation would directly benefit from calculating each pair-wise interaction on a different node in parallel, thereby reducing computational time and the rate would then be limited by the slowest pair-wise computation rather than the cumulative time for all the pair-wise computations. Concordantly, with parallelization it would be possible to increase mesh refinement particularly for atoms with $n_e \geq 3$. In the current prototype of the software, we were restricted to $N = 61$ node points for lithium, due to an upper limit on the available computer memory.

Moreover, the current version of the code is only accurate for the low-lying states. For example it was not possible to obtain accurate estimates of excited states within a given symmetry sub-space, such as say the $2^4(-3)^+$ state of lithium etc. This is to be acknowledged as a drawback although it can be related directly to computing resources. The binding energy of these excited states are significantly lower than the ground state configurations within a given M-manifold. With further excitations the binding energy reduces still more. Thus, from a theoretical point of view, these states are of interest, however in the astrophysical context, which this work focuses

on, these excited states are not of as much importance as the ground state configurations within various M-manifolds. The oscillator strengths between these excited states and the tightly bound ground state configurations are small. That being said, the software developed in this study can be extended to calculate binding energies of these excited states. In this study we are generating a reasonably sized Krylov subspace for determining a handful of eigenvectors of the fully coupled HF problem. Our primary concern was with regard to memory usage, which can grow rapidly with system size. An obvious step would be to decouple the electrons in the HF iterations by calculating an effective single particle exchange potential [see 325] and solve the effective single particle HF equations as shown in Eq. (6.65). This would reduce the computational memory requirements as the number of electrons in the problem are increased. By doing so, it would be possible to determine further excited states in the spectrum, than what can be resolved in the coupled HF problem, for a given Krylov sub-space size and computer memory. Second, the mesh refinement can be increased further to resolve a greater part of the spectrum better. Once more this is limited quite obviously by computer memory. Although, it may be possible to have non-uniform grids in the $x-$ and $y-$ directions. At the moment, the number of points in each direction is the same. This makes the formulation of the pseudospectral method somewhat simpler. However, with increasing magnetic field strength the electron orbitals become not only greatly reduced in spatial extent but also elongated along the direction of the magnetic field. Thus, by introducing greater number of points in the $y-$direction than in the $x-$ direction it may be possible to re-formulate the problem in a more computationally efficient manner.

Furthermore, the software described in the current study could be extended towards a full 2D configuration interaction or even a 2D-MCHF framework. These post-HF methods would lead to an immediate improvement in the estimates of the binding energies obtained herein. The inclusion of different configurations and incorporating concomitantly, correlation effects between configurations, would produce better results. This would particularly be the case, in the weak and intermediate field regimes where correlation effects can contribute to the binding energy reasonably significantly. In either case, the method developed herein would be central to such enhancements and as such, the current study represents the very first implementation of a cylindrical pseudospectral method for atomic structure calculations in intense magnetic fields.

Finally, there is the question of the explaining the accuracy of the collocation methods used in this study. The pseudospectral methods employed here fall under the broad category of the Discrete Variable Representation (DVR) methods. Numerous authors have investigated and commented upon the accuracy of such methods. In general there is agreement that these methods owe their accuracy to the fact that the inter-electronic potentials and the Coulomb potentials are merely computed at a handful of discrete points rather than computing the matrix elements of these interactions numerically or analytically over large domains. Furthermore, as was noted by Baye and co-workers [see 271], these methods are very useful for obtaining fast and accurate results for four or five decimal places. It is also seen that the accuracy of the estimates decreases rapidly with increasing magnetic field strength. In the current study, it is exactly this sort of behaviour that is observed. To investigate the issue of whether the collocation method is consistent with the variational principle, different collocation methods can be implemented and then checked for internal consistency. This was considered to be outside the scope of the current study and is therefore left as a matter to be explored in future work.
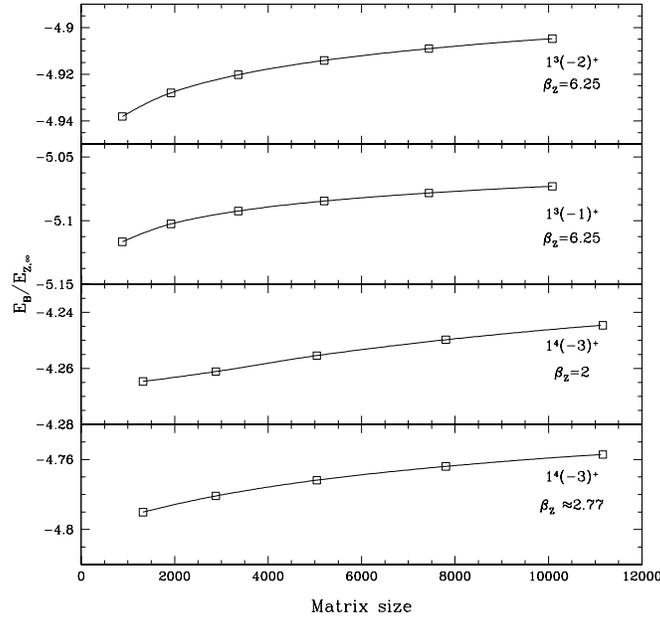
Figure 6.6: Convergence of the binding energy with mesh refinement is shown. The plot shows results from eigenvalue computations for two states of helium (top two panels) and lithium (bottom two panels) each, at different magnetic field strengths. The levels of mesh refinement employed correspond to $N = 21, 31, 41, 51, 61$ and 71 points in each of the $x-$ and $y-$ directions for helium and up to $N = 61$ for lithium. The lines drawn through the data are interpolating piece-wise cubic hermite polynomials that are also employed for extrapolation.

Table 6.8: Coefficients of the different rational functions for fitting the six states of helium discussed. The absolute maximum fractional error of the eigenvalue relative to the fit from $\beta_Z = 0$ to $\beta_Z = 10^3$ is reported in the variable ϵ

State	Coefficients		State	Coefficients	
				$a_0 =$	0.045473505
	$a_0 =$	-1.7217123		$a_1 =$	1.3416631
	$a_1 =$	-17.814316		$a_2 =$	-1.9945187
	$a_2 =$	-19.974289		$a_3 =$	-9.5055929
$1^3(-1)^+$	$a_3 =$	0.70874301	$1^3(-2)^-$	$a_4 =$	0.56822486
$1s_02p_{-1}$	$a_4 =$	-0.94000973	$1s_04f_{-2}$	$a_5 =$	-0.48530257
	$b_0 =$	1.6042624		$b_0 =$	-0.044558692
	$b_1 =$	9.5985466		$b_1 =$	-1.1134528
	$\epsilon =$	6×10^{-3}		$b_2 =$	3.776243
				$\epsilon =$	5×10^{-3}
	$a_0 =$	-0.26130228		$a_0 =$	-0.058636537
	$a_1 =$	-3.9622156		$a_1 =$	-7.202045
	$a_2 =$	7.69114		$a_2 =$	2.1397541
	$a_3 =$	7.1549007		$a_3 =$	75.211465
	$a_4 =$	-24.249904		$a_4 =$	6.6163959
$1^3(-2)^+$	$a_5 =$	2.1137011	$1^3(-1)^-$	$a_5 =$	3.6429931
$1s_03d_{-2}$	$a_6 =$	-0.99080421	$1s_03d_{-1}$	$a_6 =$	-0.044520254
	$b_0 =$	0.2528006		$b_0 =$	0.05689405
	$b_1 =$	2.5631582		$b_1 =$	6.6097765
	$b_2 =$	-9.7214586		$b_2 =$	-17.233698
	$b_3 =$	9.8712035		$b_3 =$	-19.204331
	$\epsilon =$	5×10^{-3}		$\epsilon =$	3×10^{-3}
	$a_0 =$	-0.21346351		$a_0 =$	0.69370335
	$a_1 =$	-7.0538773		$a_1 =$	0.0079933198
	$a_2 =$	-10.924921		$a_2 =$	-5.9113942
$1^3(0)^+$	$a_3 =$	0.35137528	$1^3(0)^-$	$a_3 =$	0.31958673
$1s_02s_0$	$a_4 =$	-0.5304386	$1s_02p_0$	$a_4 =$	-0.39964524
	$b_0 =$	0.1956651		$b_0 =$	-0.64093914
	$b_1 =$	5.8292412		$b_1 =$	1.5039961
	$\epsilon =$	4×10^{-3}		$\epsilon =$	1×10^{-2}

Table 6.9: Absolute value of the binding energies of the positive parity state of lithium, $1^4(-2)^+$. Energies are in units of Rydberg energies in the Coulomb potential of nuclear charge $Z = 3$ for lithium. Accurate data from other work is also provided for comparison. $(\beta_Z = \gamma/2Z^2)$. The values given in parentheses are obtained from a faster version of our spherical atomic structure code developed earlier [see 92].

β_Z	Here	Ref. [90]
0	(1.1492)	1.1491
0.00056	(1.1541)	1.1544
0.0028	(1.1780)	1.1720
0.0056	(1.1961)	1.1901
0.0111	(1.2267)	1.2203
0.0278	(1.2964)	1.2886
0.0556	(1.3912)	1.3930
0.5	2.2993	
0.5556	2.3759	2.4145
0.7	2.5557	
1	2.8657	
1.1111	2.9664	
2	3.6114	
2.7778	4.0396	
5	4.9451	
5.5556	5.1282	
7	5.5536	
10	6.2788	
11.1111	6.5099	
20	7.9535	
27.7778	18.8840	
50	10.7991	
55.5556	11.1787	
70	12.0662	
100	13.5238	
111.1111		
200	16.8116	

continued from previous page

β_Z	Here	Ref. [90]
277.7778	18.5917	
500	22.1657	
555.5556	22.8620	
700	24.4514	
1000	27.0771	

Table 6.10: Absolute value of the binding energies of the positive parity state of lithium, $1^4(-1)^+$. Energies are in units of Rydberg energies in the Coulomb potential of nuclear charge $Z = 3$ for lithium. Accurate data from other work is also provided for comparison. ($\beta_Z = \gamma/2Z^2$). The values given in parentheses are obtained from a faster version of our spherical atomic structure code developed earlier [see 92].

β_Z	Here	Elsewhere
0	(1.1968)	1.1926[a]
0.00056	(1.2024)	1.1969[a]
0.0028	(1.2194)	1.2121[c]
0.0056	(1.2390)	1.2334[a]
0.0111	(1.2735)	1.2674[a]
0.0278	(1.3530)	1.3463[a]
0.0556	(1.4529)	1.4432[a]
0.5	2.4094	
0.5556	2.4885	2.4246[a]
0.7	2.6749	
1	3.0006	
1.1111	3.1063	3.0432[b]
2	3.7837	
2.7778	4.2333	4.1781[b]
5	5.1836	
5.5556	5.3756	5.3304[c]
7	5.8219	
10	6.5822	
11.1111	6.8244	6.7909[c]
20	8.3368	
27.7778	9.3109	9.2936[c]
50	11.3187	
55.5556	11.7205	11.7000[c]

[a] Ref. [90]
[b] Ref. [289]
[c] Ref. [309]

continued from previous page

β_Z	Here	Elsewhere
70	12.6336	
100	14.1628	
111.1111		
200	17.5969	
277.7778	19.4541	
500	23.1796	
555.5556	23.9049	
700	25.5599	
1000	28.2923	

Table 6.11: Absolute value of the binding energies of the positive parity state of lithium, $1^4(-3)^+$. Energies are in units of Rydberg energies in the Coulomb potential of nuclear charge $Z = 3$ for lithium. Accurate data from other work is also provided for comparison. $(\beta_Z = \gamma/2Z^2)$. The values given in parentheses are obtained from a faster version of our spherical atomic structure code developed earlier [see 92].

β_Z	Here	Elsewhere
0	(1.1357)	1.1427[a] [1.1299][d]
0.00056	(1.1425)	1.1487
0.0028	(1.1652)	1.1663
0.0056	(1.1897)	1.1869
0.0111	(1.2324)	1.2278
0.0278	(1.3354)	1.3294
0.0556	(1.4699)	1.4627
0.5	2.6782	
0.5556	2.7697	2.6572[a]
0.7	2.9822	
1	3.3547	
1.1111	3.4721	3.3695[b]
2	4.2352	
2.7778	4.7438	4.6779[b]
5	5.8237	
5.5556	6.0426	6.0043[b]
7	6.5525	
10	7.4242	
11.1111	7.7027	7.6856[c]
20	9.4492	
27.7778	10.5810	10.5685[b]
50	12.9213	
55.5556	13.3871	13.3464[b]

[a] Ref. [90]
[b] Ref. [289]
[c] Ref. [309]
[d] Ref. [337]

continued from previous page

β_Z	Here	Elsewhere
70	14.4618	
100	16.2704	
111.1111	16.8412	16.7294
200	20.3551	
277.7778	22.5789	22.2774
500	27.0683	
555.5556	27.9464	27.4029
700	29.9557	
1000	33.2904	

Table 6.12: Absolute value of the binding energies of the negative parity states of lithium. Energies are in units of Rydberg energies in the Coulomb potential of nuclear charge $Z = 3$ for lithium. Accurate data from other work is also provided for comparison. $(\beta_Z = \gamma/2Z^2)$. The values given in parentheses are obtained from a faster version of our spherical atomic structure code developed earlier [see 92].

	$1^4(-2)^-$	$1^4(-1)^-$		$1^4(-3)^-$
β_Z	Here	Here	Elsewhere	Here
0	(1.1400)	(1.1687)	1.1652[c]	(1.1306)
0.00056	(1.1457)	(1.1735)	1.1695[c]	(1.1361)
0.0028	(1.1644)	(1.1909)	1.1865[c]	(1.1556)
0.0056	(1.1827)	(1.2110)	1.2065[c]	(1.1755)
0.0111	(1.2183)	(1.2469)	1.2417[c]	(1.2104)
0.0278	(1.3073)	(1.3354)	1.3297[c]	(1.2964)
0.0556	(1.4248)	(1.4500)	1.4463[c]	(1.4113)
0.5	2.5144	2.5901		2.4866
0.5556	2.5985	2.6712	2.4842[a]	2.5718
0.7	2.7941	2.8611		2.7752
1	3.1302	3.1899		3.1167
1.1111	3.2387	3.2961	3.1035[a]	3.2265
2	3.9287	3.9735		3.9241
2.7778	4.3831	4.4211	4.2319[a]	4.3826
5	5.3384	5.3651		5.3445
5.5556	5.5309	5.5577	5.3767[b]	5.5379
7	5.9775	6.0017		5.9885
10	6.7403	6.7636		6.7562
11.1111	6.9858	7.0095	6.8298[b]	7.0060
20	8.5011	8.5128		8.5180
27.7778	9.4756	9.4858	9.3242[a]	9.4947
50	11.4806	11.4889		11.5022
55.5556	11.8781	11.8861	11.7269[a]	11.8999

[a] Ref. [309]   **continued on next page**
[b] Ref. [289]
[c] Ref. [90]

	$1^4(-2)^-$	$1^4(-1)^-$	$1^4(-3)^-$
	continued from previous page		
β_Z	Here	Here	Here
70	12.7929	12.8008	12.8156
100	14.3263	14.3347	14.3504
200	17.7625	17.7758	17.7921
277.7778	19.6188	19.6369	19.6531
500	23.3394	23.3705	23.3862
555.5556	24.0634	24.0974	24.1130
700	25.7156	25.7561	25.7715
1000	28.4424	28.4943	28.5116

Note: There is no data available in the literature for comparison for $\beta_Z \geq 70$.

Table 6.13: Coefficients of the different rational functions for fitting the six states of lithium discussed. The absolute maximum fractional error of the eigenvalue relative to the fit from $\beta_Z = 0$ to $\beta_Z = 10^3$ is reported in the variable ϵ

State	Coefficients	
$1^4(-3)^+$ $1s_02p_{-1}3d_{-2}$	$a_0 =$	-535.72875
	$a_1 =$	-5798.3255
	$a_2 =$	-3697.7541
	$a_3 =$	-75.172313
	$a_4 =$	-110.3002
	$b_0 =$	468.35702
	$b_1 =$	2070.8459
	$\epsilon =$	9×10^{-3}
$1^4(-1)^+$ $1s_02s_02p_{-1}$	$a_0 =$	-3.9323519
	$a_1 =$	-42.850795
	$a_2 =$	-39.165039
	$a_3 =$	0.42649409
	$a_4 =$	-1.4493673
	$b_0 =$	3.2679311
	$b_1 =$	19.93254
	$\epsilon =$	7×10^{-3}
$1^4(-2)^+$ $1s_02s_03d_{-2}$	$a_0 =$	-3.5455821
	$a_1 =$	-37.85524
	$a_2 =$	-35.186156
	$a_3 =$	0.52456655
	$a_4 =$	-1.3412409
	$b_0 =$	3.0591966
	$b_1 =$	18.498756
	$\epsilon =$	9×10^{-3}

continued on next page

continued from previous page	
State	Coefficients
$1^4(-3)^-$ $1s_0 2p_{-1} 4f_{-2}$	$a_0 =$ -9.3555515
	$a_1 =$ -88.389164
	$a_2 =$ -62.302697
	$a_3 =$ -0.17161294
	$a_4 =$ -2.0600694
	$b_0 =$ 8.2232868
	$b_1 =$ 34.29776
	$\epsilon =$ 7×10^{-3}
$1^4(-1)^-$ $1s_0 2p_0 2p_{-1}$	$a_0 =$ 1.0841938
	$a_1 =$ -1.9251408
	$a_2 =$ -148.33918
	$a_3 =$ -101.67185
	$a_4 =$ -1.2270097
	$a_5 =$ -3.1352421
	$b_0 =$ -0.92575833
	$b_1 =$ 7.0913811
	$b_2 =$ 60.317953
	$\epsilon =$ 3×10^{-3}
$1^4(-2)^-$ $1s_0 2p_{-1} 3d_{-1}$	$a_0 =$ -17.90019903
	$a_1 =$ -25.29627281
	$a_2 =$ -661.06955428
	$a_3 =$ -1219.55537379
	$a_4 =$ -139.85464269
	$b_0 =$ 429.60387534
	$b_1 =$ 121.92364211
	$\epsilon =$ 6×10^{-3}

Chapter 7

Conclusion

7.1 Final Remarks

In this thesis we investigated the implications of a magnetic field on the late stages of stellar evolution. The first part of the study involved examining the influence of a dynamically important magnetic field on the stellar wind in evolved giants, in particular AGB stars. The primary goal was to determine whether it was possible to include self-consistently, magneto-rotational effects with the effects of radiation pressure on dust grains in the envelope of an AGB star.

We formulated a theory that combines a classical Weber-Davis type MHD wind with a momentum equation for the dust grains. This picture requires a dual-fluid description. The gas forms the first fluid that carries the magnetic field while the dust forms the second fluid that moves through it. The two fluids are coupled to each other through drag. We saw in Chapter 3 that the solution of such a hybrid model resulted in an interesting stellar wind, with traits of both types of winds being preserved. The presence of magnetosonic points puts a limit on the viable locations for the dust formation radii. On the other hand, the presence of dust formation was seen to be crucial for escape of stellar material from the star. Thus is in this picture, a WD mechanism plays a secondary role, providing support to the wind by transporting material from the photosphere out to the dust formation radius.

In this regard we saw that two possible types of hybrid models emerged. In the first type, the dust formation radius was required to lie within the sonic point of the pure WD model. This also implied that the sonic point of the hybrid model was also within the sonic point of the pure WD model. Thus after dust condensation, the wind could get accelerated to supersonic velocities after passing through the sonic point. Further out, this wind solution being the critical solution, would pass through the two Alfvén point and emerge super-Alfvënic at large distances. This type of hybrid wind solution resulted in dust formation typically within a few stellar radii, consistent with

observations, and the wind velocity attained at large distances was around $\sim 15 - 20$ km/s, in agreement with current observations. It was seen that for such hybrid winds the dust parameter was required to be less than unity in order to achieve an outflow from the star.

We additionally formulated a second type of hybrid wind model in which the dust formation occurs outside the fast point. This typically places the location of dust formation many stellar radii away from the photosphere. It was seen that such a combination was theoretically possible and it was concluded that while such a large distance for dust formation though not reasonable for AGB stars, was probably suitable for other types of stars such as eruptive variable R-Coronae Borealis (RCB) stars. In this type of model, the WD mechanism was responsible for transport of stellar material all the way from the photosphere out to the dust formation radius, many stellar radii away. It was seen that for such a scenario, the dust parameter was merely required to be greater than zero.

Overall, at the end of Chapter 3 it was ascertained that it is indeed possible to have the effects of a magnetic field coupled with the usual dust formation picture, resulting in the very first dual-fluid hybrid MHD-dust-driven wind model.

We adapted this hybrid stellar wind theory to tackle the case of the red supergiant star Betelgeuse (Chapter 4). The primary motivations for this study were first the discovery of a magnetic field in the star at the distance of the SiO masers, of about 1 G. Secondly, the reason why Betelgeuse is so interesting is that there appears to be very little dust inside $r \lesssim 30R_0$, as a result one of the outstanding questions regarding its mass-loss is, *how is the stellar wind supported if dust forms at such a large distance from the star?*

In an attempt to answer this question, we adapted our hybrid MHD-dust-driven wind theory for a red supergiant. We investigated several dust formation (and spallation) scenarios in the atmosphere of Betelgeuse and concluded that while it is possible that the more complicated scenarios may result in stellar wind velocities consistent with observations, the simplest of such scenarios was perhaps the most viable one. In this scenario, a WD mechanism transports stellar material out to about $30R_0$ at which location the temperature of the gas is conducive for dust condensation. Thereafter a hybrid MHD-dust-driven wind then results in a mild efflux with a terminal wind speed of about 14 km/s, in agreement with recent estimates. It was also seen in Chapter 4 that the temperature profile of the gas and the estimated dust temperatures were consistent with studies elsewhere.

Thus, it was concluded at the end of Chapter 4 that a hybrid MHD-dust-driven wind can support transport of stellar material from the photosphere, out to distances in the extended atmosphere where dust formation occurs resulting in a combined efflux of dust and gas. This mechanism was proposed as an *additional* mechanism that can play a role alongside stellar pulsation and convection, as well as MHD and acoustic waves.

In Chapter 5, we adapted the same hybrid MHD-dust-driven wind theory to model the wind from the prototype of long period variables, the star Mira itself. This study was motivated once more by hints of not only detection of a magnetic field in the atmosphere of Mira, but also a possible detection of rotation. In Mira's atmosphere observations suggest an inner radius for the dust shell at around $3R_0$. Thus we modelled the wind using a model of the first kind, where dust forms inside the sonic point. With such a model we were able to obtain a wind terminal velocity of ~ 5 km/s, inside $100R_0$, in agreement with current estimates. The temperature profile obtained was also consistent with inferred dust temperatures at different distances from the photosphere. In order to obtain a wind solution to this model, we treated the surface magnetic field as a variable parameter, among others. We obtained, within the framework of the simple hybrid MHD-dust-driven wind theory, that a surface magnetic field strength of about 4 G would be required, given the other parameters of the star, for obtaining a wind expansion velocity of about 5 km/s. This magnetic field strength was seen to lie well within theoretical and observational estimates for AGB stars.

Thus it is seen that the hybrid MHD-dust-driven wind model can be adapted successfully for modelling the winds of low- and intermediate-mass AGB stars as well as red supergiants, establishing the need for developing further, more realistic models.

The latter part of the thesis focussed on the end products of stellar evolution, viz., magnetised neutron stars and white dwarf stars. This study was motivated by the need to have accurate data for atomic structure of low-Z elements in strong and intense magnetic fields. The overall aim was to facilitate a correct interpretation of the spectra of these objects. We implemented a pseudospectral method of solution for the generalised 2D single-configuration HF equations of few-electron systems. It was seen that this method was many orders of magnitude faster than contemporary finite-element based methods. The algorithm developed is also computationally straight-forward to implement in comparison to full configuration interaction or quantum Monte-Carlo methods. This study represents the first cylindrical pseudospectral imple-

mentation of atoms in strong magnetic fields and as such represents the first step in the realisation of full 2-D pseudospectral multi-configuration HF methods, without relying upon any explicit basis functions or the adiabatic approximation. We also obtained data for the binding energies of two low-lying states of the lithium atom that had not been studied thus far in the literature.

The atomic structure package developed for this study (see Appendix B), is compact and is developed so that other configurations can be easily added with minimal effort.

7.2 Future Work

At this stage there are various directions in which the current thesis can be extended. First, the hybrid MHD-dust-driven wind can be improved in two directions. Broadly speaking, within the framework of a steady-state description, it can be assumed as noted earlier that there also exists drag in the azimuthal direction. This would result in the inclusion of an azimuthal drag term. Concomitantly, by allowing the dust-to-gas ratio to change with distance rather than use an average value, the momentum equations would get accordingly modified to result in four coupled ODE's (one each for the radial and azimuthal momenta of both the gas and the dust) that can be solved simultaneously to yield the dust and gas velocity profiles in both the radial and azimuthal directions. This would also change the dust parameter with distance from the star and it will change the topology of the solutions. Moreover, the dust grain sizes can be assumed to have a distribution, rendering the determination of the drag force more tedious, but definitely closer to reality. There can even be assumed to exist a certain degree of scattering, which will effectively change the radiation pressure term in the momentum equations.

Finally, modelling can be made far more realistic by adopting a fully dynamic time-dependent form for the velocity and magnetic fields. A 2-D axisymmetric model with magneto-rotational effects coupled with dust formation in the envelope would ultimately enable capturing the onset of MHD instabilities. The dust-grain physics can also be handled in a more realistic way by allowing for stochastic in-situ dust grain formation. The results of the current study could be used as a check for the steady-state solution of such a model. Such an endeavour, as noted earlier would answer

the question of whether such instabilities can lead to appreciably asymmetric mass loss and momentum transfer and perhaps even result in white-dwarf kicks. These improvements would then ultimately enable the formulation of a model of the stellar winds of evolved stars that would present a picture that is more accurate than the simple treatment provided in Chapters 3, 4 and 5.

With regard to atomic structure in strong magnetic fields there are also several avenues in which the current study can be advanced. At the very outset, the code can be cast into a parallel form so that taking advantage of distributed computing, a great speed up can be achieved. This would also imply that the memory usage can be reduced as well. These two developments would ensure that first not only atoms with greater number of electrons can be tackled, but also secondly, it would make it possible to extend the treatment towards a 2D-configuration interaction or a full multi-configuration framework. This would ultimately make it possible to take into account the important effects of electron-correlation and would improve the current estimates for the binding energies give in Chapter 6.

Finally, since the atomic structure package developed for this study is merely a prototype, effects due to finite nuclear mass, relativistic corrections, electron screening and correlation can be included, making the determination of the wave functions more accurate. These collective improvements would ultimately enable a better interpretation of the spectra of the magnetised end products of stellar evolution.

Bibliography

[1] H. J. Habing and H. Olofsson, editors. *Asymptotic giant branch stars.* Springer, 2003.

[2] E. Hertzsprung. Ueber die Verwendung photographischer effektiver Wellenlaengen zur Bestimmung von Farbenaequivalenten. *Publikationen des Astrophysikalischen Observatoriums zu Potsdam*, 63, 1911.

[3] H. N. Russell. Relations Between the Spectra and Other Characteristics of the Stars. *Popular Astronomy*, 22:275–294, May 1914.

[4] M. W. Feast. The long period variables. *MNRAS*, 125:367, 1963.

[5] I. S. Glass and T. L. Evans. A period-luminosity relation for Mira variables in the Large Magellanic Cloud. *Nature*, 291:303, June 1981. doi: 10.1038/291303a0.

[6] M. F. McCarthy. Angelo Secchi and the Discovery of Carbon Stars. In C. J. Corbally, R. O. Gray, and R. F. Garrison, editors, *The MK Process at 50 Years: A Powerful Tool for Astrophysical Insight*, volume 60 of *Astronomical Society of the Pacific Conference Series*, page 224, 1994.

[7] H. N. Russell. Molecules in the Sun and Stars. *ApJ*, 79:317, April 1934. doi: 10.1086/143539.

[8] I. Iben, Jr. Thermal pulses; p-capture, alpha-capture, s-process nucleosynthesis; and convective mixing in a star of intermediate mass. *ApJ*, 196:525–547, March 1975. doi: 10.1086/153433.

[9] D. Sugimoto and K. Nomoto. Thermal instability of helium-burning shell in stars evolving toward carbon-detonation supernovae. *Journal of the Pacific Astronomical Society of Japan*, 27:197–213, 1975.

[10] S. J. Little, I. R. Little-Marenin, and W. H. Bauer. Additional late-type stars with technetium. *AJ*, 94:981–995, October 1987. doi: 10.1086/114532.

[11] I. R. Little-Marenin and S. J. Little. Technetium in late-type stars. I - Observations. *AJ*, 84:1374–1383, September 1979. doi: 10.1086/112554.

[12] S. P. W. Merrill. Spectroscopic Observations of Stars of Class. *ApJ*, 116:21, July 1952. doi: 10.1086/145589.

[13] H. A. Bethe. Energy Production in Stars. *Physical Review*, 55:434–456, March 1939. doi: 10.1103/PhysRev.55.434.

[14] C. F. von Weizsäcker. Über Elementumwandlungen in Innern der Sterne. II. *Physikalische Zeitschrift*, 39:633, 1938.

[15] I. Iben, Jr. Stellar Evolution. I. The Approach to the Main Sequence. *ApJ*, 141:993, April 1965. doi: 10.1086/148193.

[16] H. C. Arp, W. A. Baum, and A. R. Sandage. The color-magnitude diagram of the globular cluster M 92. *AJ*, 58:4, February 1953. doi: 10.1086/106800.

[17] A. R. Sandage and M. Schwarzschild. Inhomogeneous Stellar Models. II. Models with Exhausted Cores in Gravitational Contraction. *ApJ*, 116:463, November 1952. doi: 10.1086/145638.

[18] F. Hoyle and M. Schwarzschild. On the Evolution of Type II Stars. *ApJ*, 2:1, June 1955. doi: 10.1086/190015.

[19] M. Schwarzschild and R. Härm. Therma Instability in Non-Degenerate Stars. *ApJ*, 142:855, October 1965. doi: 10.1086/148358.

[20] A. Weigert. Sternentwicklung VI: Entwicklung mit Neutrinoverlusten und thermische Pulse der Helium-Schalenquelle bei einem Stern von 5 Sonnenmassen. *Zeitschrift für Astrophysik*, 64:395, 1966.

[21] M. Schwarzschild and R. Härm. Hydrogen Mixing by Helium-Shell Flashes. *ApJ*, 150:961, December 1967. doi: 10.1086/149396.

[22] R. H. Sanders. S-Process Nucleosynthesis in Thermal Relaxation Cycles. *ApJ*, 150:971, December 1967. doi: 10.1086/149397.

[23] E. M. Burbidge, G. R. Burbidge, W. A. Fowler, and F. Hoyle. Synthesis of the Elements in Stars. *Reviews of Modern Physics*, 29:547–650, 1957. doi: 10.1103/RevModPhys.29.547.

[24] G. Neugebauer and R. B. Leighton. Two-micron sky survey; a preliminary catalog. *NASA Special Publication*, 3047, 1969.

[25] W. J. Wilson and A. H. Barrett. Discovery of OH Radio Emission from the Infrared Star NML Cygni. *Astronomical Journal, Vol. 73, p. 209*, 73:209, 1968.

[26] P. Solomon, K. B. Jefferts, A. A. Penzias, and R. W. Wilson. Observation of CO Emission at 2.6 Millimeters from IRC+10216. *ApJ, Letters*, 163:L53, January 1971. doi: 10.1086/180665.

[27] L. Biermann. Kometenschweife und solare Korpuskularstrahlung. *Zeitschrift für Astrophysik*, 29:274, 1951.

[28] E. J. Weber and L. Davis, Jr. The Angular Momentum of the Solar Wind. *ApJ*, 148, April 1967. doi: 10.1086/149138.

[29] L. Mestel. Star Formation in Rotating Magnetic Clouds. *Memoires of the Societe Royale des Sciences de Liege*, 15, 1967.

[30] A. J. Deutsch. The Circumstellar Envelope of Alpha Herculis. *ApJ*, 123:210, March 1956. doi: 10.1086/146152.

[31] L. H. Auer and N. J. Woolf. Mass Loss and the Formation of White-Dwarf Stars. *ApJ*, 142:182, July 1965. doi: 10.1086/148275.

[32] F. C. Gillett, F. J. Low, and W. A. Stein. Stellar Spectra from 2.8 to 14 Microns. *ApJ*, 154:677, November 1968. doi: 10.1086/149789.

[33] N. J. Woolf and E. P. Ney. Circumstellar Infrared Emission from Cool Stars. *ApJ, Letters*, 155:L181, March 1969. doi: 10.1086/180331.

[34] D. Reimers. Circumstellar absorption lines and mass loss from red giants. *Memoires of the Societe Royale des Sciences de Liege*, 8:369–382, 1975.

[35] N. C. Wickramasinghe, B. D. Donn, and T. P. Stecher. A Mechanism for Mass Ejection in Red Giants. *ApJ*, 146:590, November 1966. doi: 10.1086/148926.

[36] P. Goldreich and N. Scoville. OH-IR stars. I - Physical properties of circumstellar envelopes. *ApJ*, 205:144–154, April 1976. doi: 10.1086/154257.

[37] M. Elitzur, P. Goldreich, and N. Scoville. OH-IR stars. II. A model for the 1612 MHz masers. *ApJ*, 205:384–396, April 1976. doi: 10.1086/154289.

[38] A. Renzini and M. Voli. Advanced evolutionary stages of intermediate-mass stars. I - Evolution of surface compositions. *Astron. & Astroph.*, 94:175–193, January 1981.

[39] D. Engels, E. Kreysa, G. V. Schultz, and W. A. Sherwood. The nature of OH/IR stars. I - Infrared Mira variables. *Astron. & Astroph.*, 124:123–138, July 1983.

[40] B. Baud and H. J. Habing. The maser strength of OH/IR stars, evolution of mass loss and the creation of a superwind. *Astron. & Astroph.*, 127:73–83, October 1983.

[41] I. Iben, Jr. and A. Renzini. Asymptotic giant branch evolution and beyond. *ARA&A*, 21:271–342, 1983. doi: 10.1146/annurev.aa.21.090183.001415.

[42] F. Herwig. Evolution of Asymptotic Giant Branch Stars. *ARA&A*, 43:435–479, September 2005. doi: 10.1146/annurev.astro.43.072103.150600.

[43] S. E. Woosley, A. Heger, and T. A. Weaver. The evolution and explosion of massive stars. *Reviews of Modern Physics*, 74:1015–1071, November 2002. doi: 10.1103/RevModPhys.74.1015.

[44] L. A. Willson. Mass Loss From Cool Stars: Impact on the Evolution of Stars and Stellar Populations. *ARA&A*, 38:573–611, 2000. doi: 10.1146/annurev.astro.38.1.573.

[45] H. van Winckel. Post-Agb Stars. *ARA&A*, 41:391–427, 2003. doi: 10.1146/annurev.astro.41.071601.170018.

[46] R. Keppens and J. P. Goedbloed. Numerical simulations of stellar winds: polytropic models. *Astron. & Astroph.*, 343:251–260, March 1999.

[47] R. Keppens and J. P. Goedbloed. Stellar Winds, Dead Zones, and Coronal Mass Ejections. *ApJ*, 530:1036–1048, February 2000. doi: 10.1086/308395.

[48] Y. Zaliznyak, R. Keppens, and J. P. Goedbloed. Three-dimensional magnetohydrodynamic simulations of in situ shock formation in the coronal streamer belt. *Physics of Plasmas*, 10:4478–4488, November 2003. doi: 10.1063/1.1618235.

[49] Paul A. Crowther. Physical properties of wolf-rayet stars. *Annual Review of Astronomy and Astrophysics*, 45(1):177–219, 2007. doi: 10.1146/annurev.astro.45.051806.110615.

[50] Rolf-Peter Kudritzki and Joachim Puls. Winds from hot stars. *Annual Review of Astronomy and Astrophysics*, 38(1):613–666, 2000. doi: 10.1146/annurev.astro.38.1.613.

[51] K. Tsinganos and E. Trussoni. Nonlinear mhd models of astrophysical winds. *Annals of the New York Academy of Sciences*, 617(1):118–125, 1990. ISSN 1749-6632. doi: 10.1111/j.1749-6632.1990.tb37800.x.

[52] B. T. Draine, W. G. Roberge, and A. Dalgarno. Magnetohydrodynamic shock waves in molecular clouds. *ApJ*, 264:485–507, January 1983. doi: 10.1086/160617.

[53] B. T. Draine. *Physics of the Interstellar and Intergalactic Medium*. Princeton University Press, 2011.

[54] J. A. Nuth, F. J. M. Rietmeijer, S. L. Hallenbeck, P. A. Withey, and F. Ferguson. Nucleation, Growth, Annealing and Coagulation of Refractory Oxides and Metals: Recent Experimental Progress and Applications to Astrophysical Systems. *Thermal Emission Spectroscopy and Analysis of Dust, Disks, and Regoliths*, 196:313–332, March 2000.

[55] A. C. Andersen. Grain Nucleation Experiments and Other Laboratory Data. In F. Kerschbaum, T. Lebzelter, and R. F. Wing, editors, *Why Galaxies Care about AGB Stars II: Shining Examples and Common Inhabitants*, volume 445 of *Astronomical Society of the Pacific Conference Series*, page 215, September 2011.

[56] J. Gürtler, T. H. Henning, and J. Dorschner. Properties of circumstellar silicate dust (review). *Astronomische Nachrichten*, 310(4):319–327, 1989. ISSN 1521-3994. doi: 10.1002/asna.2113100419. URL http://dx.doi.org/10.1002/asna.2113100419.

[57] B. Zuckerman. Dusty circumstellar disks. *Annual Review of Astronomy and Astrophysics*, 39(1):549–580, 2001. doi: 10.1146/annurev.astro.39.1.549.

[58] P. Woitke and G. Niccolini. Dust cloud formation in stellar environments. II. Two-dimensional models for structure formation around AGB stars. *Astron. & Astroph.*, 433:1101–1115, April 2005. doi: 10.1051/0004-6361:20040227.

[59] P. Woitke. 2D models for dust-driven AGB star winds. *Astron. & Astroph.*, 452:537–549, June 2006. doi: 10.1051/0004-6361:20054202.

[60] E. A. Dorfi and S. Hoefner. Non-spherical dust driven winds of slowly rotating AGB stars. *Astron. & Astroph.*, 313:605–610, September 1996.

[61] L Mestel. *Stellar Magnetism*. Oxford University Press, 2003.

[62] R. D. Robinson, S. P. Worden, and J. W. Harvey. Observations of magnetic fields on two late-type dwarf stars. *ApJ, Letters*, 236:L155–L158, March 1980. doi: 10.1086/183217.

[63] M. S. Giampapa and S. P. Worden. Methods and results for detecting magnetic fields on late-type stars. In J. O. Stenflo, editor, *Solar and Stellar Magnetic Fields: Origins and Coronal Effects*, volume 102 of *IAU Symposium*, pages 29–33, 1983.

[64] G. Basri, G. W. Marcy, and J. A. Valenti. Limits on the magnetic flux of pre-main-sequence stars. *ApJ*, 390:622–633, May 1992. doi: 10.1086/171312.

[65] D. W. Richards and J. M. Comella. The Period of Pulsar NP 0532. *Nature*, 222:551–552, May 1969. doi: 10.1038/222551a0.

[66] T. Gold. Rotating Neutron Stars and the Nature of Pulsars. *Nature*, 221:25–27, January 1969. doi: 10.1038/221025a0.

[67] F. Pacini. Magnetic Field Decay in a Neutron Star and the Distribution of Pulsar Periods. *Nature*, 224:160, October 1969. doi: 10.1038/224160a0.

[68] J. C. Kemp, J. B. Swedlund, J. D. Landstreet, and J. R. P. Angel. Discovery of Circularly Polarized Light from a White Dwarf. *ApJ, Letters*, 161:L77, August 1970.

[69] J. Trümper, W. Pietsch, C. Reppin, and B. Sacco. Evidence for Strong Cyclotron Emission in the Hard X-Ray Spectrum of Her X-1. In M. D. Papagiannis, editor, *Eighth Texas Symposium on Relativistic Astrophysics*, volume 302 of *New York Academy Sciences Annals*, page 538, 1977.

[70] J. Truemper, W. Pietsch, C. Reppin, W. Voges, R. Staubert, and E. Kendziorra. Evidence for strong cyclotron line emission in the hard X-ray spectrum of Hercules X-1. *ApJ, Letters*, 219:L105–L110, February 1978. doi: 10.1086/182617.

[71] D. R. Johnson and F. O. Clark. Observations of circular polarization of the J = 2-1, V = 1 transition of the SiO maser. *ApJ, Letters*, 197: L69–L72, April 1975. doi: 10.1086/181780.

[72] A. J. Kemball and P. J. Diamond. Imaging the Magnetic Field in the Atmosphere of TX Cam. *ApJ, Letters*, 481:L111, June 1997. doi: 10.1086/310664.

[73] F. Herpin, A. Baudry, C. Thum, D. Morris, and H. Wiesemeyer. Full polarization study of SiO masers at 86 GHz. *Astron. & Astroph.*, 450: 667–680, May 2006. doi: 10.1051/0004-6361:20054255.

[74] W. H. T. Vlemmings, P. J. Diamond, and H. J. van Langevelde. Magnetic fields in the envelopes of late-type stars - circular polarization

of H2O masers. In Y. Nakada, M. Honma, & M. Seki, editor, *Mass-Losing Pulsating Stars and their Circumstellar Matter*, volume 283 of *Astrophysics and Space Science Library*, pages 291–294, April 2003.

[75] W. H. T. Vlemmings, P. J. Diamond, and H. J. van Langevelde. Circular polarization of water masers in the circumstellar envelopes of late type stars. *Astron. & Astroph.*, 394:589–602, November 2002. doi: 10.1051/0004-6361:20021166.

[76] S. Etoka and P. Diamond. First polarimetric images of NML Cyg at 1612 and 1665 MHz. *MNRAS*, 348:34–45, February 2004. doi: 10.1111/j.1365-2966.2004.07370.x.

[77] W. H. T. Vlemmings, H. J. van Langevelde, and P. J. Diamond. The magnetic field around late-type stars revealed by the circumstellar H_2O masers. *Astron. & Astroph.*, 434:1029–1038, May 2005. doi: 10.1051/0004-6361:20042488.

[78] W. H. T. Vlemmings, P. J. Diamond, and H. Imai. A magnetically collimated jet from an evolved star. *Nature*, 440:58–60, March 2006. doi: 10.1038/nature04466.

[79] W. H. T. Vlemmings and P. J. Diamond. Intrinsic Properties of the Magnetically Collimated H_2O Maser Jet of W43A. *ApJ, Letters*, 648: L59–L62, September 2006. doi: 10.1086/507679.

[80] M. Aurière, J.-F. Donati, R. Konstantinova-Antova, G. Perrin, P. Petit, and T. Roudier. The magnetic field of Betelgeuse: a local dynamo from giant convection cells? *Astron. & Astroph.*, 516:L2+, June 2010. doi: 10.1051/0004-6361/201014925.

[81] P. Petit, M. Aurière, R. Konstantinova-Antova, A. Morgenthaler, G. Perrin, T. Roudier, and J. . Donati. Magnetic field and convection in Betelgeuse. *ArXiv e-prints*, September 2011.

[82] W. D. Cotton, W. Vlemmings, B. Mennesson, G. Perrin, V. Coudé du Foresto, G. Chagnon, P. J. Diamond, H. J. van Langevelde, E. Bakker, S. Ridgway, H. McAllister, W. Traub, and S. Ragland. Further VLBA observations of SiO masers toward Mira variable stars. *Astron. & Astroph.*, 456:339–350, September 2006. doi: 10.1051/0004-6361: 20065134.

[83] H. Ruder, G. Wunner, H. Herold, and F. Geyer. *Atoms in Strong Magnetic Fields: Quantum Mechanical Treatment and Applications in Astrophysics and Quantum Chaos.* Astronomy and Astrophysics Library. Springer-Verlag, New York, 1994.

[84] L. B. Zhao and P. C. Stancil. Hydrogen Photoionization Cross Sections for Strong-Field Magnetic White Dwarfs. *ApJ*, 667:1119–1125, October 2007. doi: 10.1086/520948.

[85] G. D. Schmidt, S. C. West, J. Liebert, R. F. Green, and H. S. Stockman. The new magnetic white dwarf PG 1031 + 234 - Polarization and field structure at more than 500 milion Gauss. *ApJ*, 309:218–229, October 1986. doi: 10.1086/164593.

[86] B. Külebi, S. Jordan, F. Euchner, B. T. Gänsicke, and H. Hirsch. Analysis of hydrogen-rich magnetic white dwarfs detected in the Sloan Digital Sky Survey. *Astron. & Astroph.*, 506:1341–1350, November 2009. doi: 10.1051/0004-6361/200912570.

[87] F. Euchner, S. Jordan, K. Beuermann, K. Reinsch, and B. T. Gänsicke. Zeeman tomography of magnetic white dwarfs. III. The 70-80 Megagauss magnetic field of PG 1015+014. *Astron. & Astroph.*, 451:671–681, May 2006. doi: 10.1051/0004-6361:20064840.

[88] A. Thirumalai and J. S. Heyl. Hydrogen and helium atoms in strong magnetic fields. *Phys. Rev. A*, 79(1):012514, January 2009. doi: 10. 1103/PhysRevA.79.012514.

[89] M. D. Jones, G. Ortiz, and D. M. Ceperley. Hartree-Fock studies of atoms in strong magnetic fields. *Phys. Rev. A*, 54:219–231, July 1996.

[90] Omar-Alexander Al-Hujaj and Peter Schmelcher. Lithium in strong magnetic fields. *Phys. Rev. A*, 70(3):033411, Sep 2004. doi: 10.1103/ PhysRevA.70.033411.

[91] Douglas R. Hartree. *The Calculation of Atomic Structures.* J. Wiley, New York, 1957.

[92] J. S. Heyl and A. Thirumalai. Pseudo-spectral methods for atoms in strong magnetic fields. *Monthly Notices of the Royal Astronomical*

Society, 407:590–598, September 2010. doi: 10.1111/j.1365-2966.2010. 16937.x.

[93] Henny J. G. L. M. Lamers and Joseph P. Cassinelli. *Introduction to Stellar Winds*, chapter 7, pages 145–186. Cambridge University Press, 1999.

[94] N. Amiri, W. Vlemmings, and H. J. van Langevelde. The magnetic field of the evolved star W43A. *Astron. & Astroph.*, 509:A26+, January 2010. doi: 10.1051/0004-6361/200913194.

[95] S. Jordan, K. Werner, and S. J. O'Toole. Discovery of magnetic fields in central stars of planetary nebulae. *Astron. & Astroph.*, 432:273–279, March 2005. doi: 10.1051/0004-6361:20041993.

[96] L. Sabin, A. A. Zijlstra, and J. S. Greaves. Magnetic fields in planetary nebulae and post-AGB nebulae. *MNRAS*, 376:378–386, March 2007. doi: 10.1111/j.1365-2966.2007.11445.x.

[97] L. Sabin, A. A. Zijlstra, and J. S. Greaves. Magnetic Fields in Post-AGB Stars. In F. Kerschbaum, C. Charbonnel, & R. F. Wing, editor, *Why Galaxies Care About AGB Stars: Their Importance as Actors and Probes*, volume 378 of *Astronomical Society of the Pacific Conference Series*, November 2007.

[98] L. F. Miranda, Y. Gómez, G. Anglada, and J. M. Torrelles. Water-maser emission from a planetary nebula with a magnetized torus. *Nature*, 414:284–286, November 2001.

[99] Y.-H. Chu, G. H. Jacoby, and R. Arendt. Multiple-shell planetary nebulae. I - Morphologies and frequency of occurrence. *ApJ*, 64:529–544, July 1987. doi: 10.1086/191207.

[100] L. Stanghellini, R. L. M. Corradi, and H. E. Schwarz. The correlations between planetary nebula morphology and central star evolution. *Astron. & Astroph.*, 279:521–528, November 1993.

[101] A. Frank. Bipolar outflows and the evolution of stars. *New Astronomy Review*, 43:31–65, May 1999. doi: 10.1016/S1387-6473(99)00005-6.

[102] J. Franco, G. García-Segura, S. E. Kurtz, and J. A. López. Photoionized gaseous nebulae and magnetized stellar winds: The evolution and shaping of H II regions and planetary nebulae. *Physics of Plasmas*, 8: 2432–2438, May 2001. doi: 10.1063/1.1351825.

[103] T. A. Gardiner and A. Frank. Magnetic Collimation in Planetary Nebulae. *ApJ*, 557:250–255, August 2001. doi: 10.1086/321494.

[104] G. Pascoli. On a magnetohydrodynamical process of mass loss in AGB stars. *ApSS*, 219:249–256, September 1994. doi: 10.1007/BF00628241.

[105] G. Pascoli. Axisymmetrical Models for the Origin and Shaping of Proto-Planetary Nebulae. *ApSS*, 234:281–301, December 1995. doi: 10.1007/BF00627673.

[106] G. Pascoli. On Circumstellar Envelope Formation. *ApJ*, 489, November 1997. doi: 10.1086/304794.

[107] G. Pascoli and L. Lahoche. Shaping of Planetary Nebulae by Magnetic Fields. *Pubs. Astron. Soc. Pac.*, 120:1267–1270, December 2008. doi: 10.1086/594377.

[108] R. A. Chevalier and D. Luo. Magnetic shaping of planetary nebulae and other stellar wind bubbles. *ApJ*, 421:225–235, January 1994. doi: 10.1086/173640.

[109] V. V. Dwarkadas, R. A. Chevalier, and J. M. Blondin. The Shaping of Planetary Nebulae: Asymmetry in the External Wind. *ApJ*, 457, February 1996. doi: 10.1086/176772.

[110] R. A. Chevalier. Expansion of a Photoionized Stellar Wind. *ApJ*, 488, October 1997. doi: 10.1086/304705.

[111] G. García-Segura, J. A. López, and J. Franco. Winds, Bubbles, ...but Magnetized: Solutions for High Speed Post-AGB Winds and Their Extreme Collimation. In J. Arthur & W. J. Henney, editor, *Revista Mexicana de Astronomia y Astrofisica Conference Series*, volume 15 of *Revista Mexicana de Astronomia y Astrofisica Conference Series*, pages 12–16, January 2003.

[112] M. T. García-Díaz, J. A. López, G. García-Segura, M. G. Richer, and W. Steffen. The Planetary Nebula NGC 1360: A Test Case of Magnetic Collimation and Evolution after the Fast Wind. *ApJ*, 676:402–407, March 2008. doi: 10.1086/527468.

[113] G. García-Segura, J. A. López, and J. Franco. Magnetically Driven Winds from Post-Asymptotic Giant Branch Stars: Solutions for High-Speed Winds and Extreme Collimation. *ApJ*, 618:919–925, January 2005. doi: 10.1086/426110.

[114] G. García-Segura, J. A. López, and J. Franco. MHD Solutions for Proto-Planetary Nebulae. In M. Meixner, J. H. Kastner, B. Balick, & N. Soker, editor, *Asymmetrical Planetary Nebulae III: Winds, Structure and the Thunderbird*, volume 313 of *Astronomical Society of the Pacific Conference Series*, July 2004.

[115] J. Franco, G. García-Segura, S. E. Kurtz, and J. A. López. Photoionized gaseous nebulae and magnetized stellar winds: The evolution and shaping of H II regions and planetary nebulae. *Physics of Plasmas*, 8: 2432–2438, May 2001. doi: 10.1063/1.1351825.

[116] G. García-Segura and J. A. López. Three-dimensional Magneto-hydrodynamic Modeling of Planetary Nebulae. II. The Formation of Bipolar and Elliptical Nebulae with Point-symmetric Structures and Collimated Outflows. *ApJ*, 544:336–346, November 2000. doi: 10.1086/317186.

[117] G. García-Segura, N. Langer, M. Różyczka, and J. Franco. Shaping Bipolar and Elliptical Planetary Nebulae: Effects of Stellar Rotation, Photoionization Heating, and Magnetic Fields. *ApJ*, 517:767–781, June 1999. doi: 10.1086/307205.

[118] G. Garcia-Segura, J. A. Lopez, and J. Franco. Late AGB Magnetic Cycles: MHD Solutions for the HST PN Rings. *ArXiv Astrophysics e-prints*, April 2001.

[119] B. J. Hrivnak, S. Kwok, and K. Y. L. Su. The Discovery of Circumstellar Arcs around Two Bipolar Proto-planetary Nebulae. *AJ*, 121: 2775–2780, May 2001. doi: 10.1086/320400.

[120] S. Matt, B. Balick, R. Winglee, and A. Goodson. Disk Formation by Asymptotic Giant Branch Winds in Dipole Magnetic Fields. *ApJ*, 545: 965–973, December 2000. doi: 10.1086/317843.

[121] N. Soker and J. H. Kastner. Magnetic Flares on Asymptotic Giant Branch Stars. *ApJ*, 592:498–503, July 2003. doi: 10.1086/375686.

[122] N. Soker and E. Zoabi. Turbulent dynamo in asymptotic giant branch stars. *MNRAS*, 329:204–208, January 2002. doi: 10.1046/j.1365-8711. 2002.05021.x.

[123] N. Soker. Local circumstellar magnetic fields around evolved stars. *MNRAS*, 336:826–830, November 2002. doi: 10.1046/j.1365-8711.2002. 05817.x.

[124] N. Soker and G. C. Clayton. Dust formation above cool magnetic spots in evolved stars. *MNRAS*, 307:993–1000, August 1999. doi: 10.1046/j. 1365-8711.1999.02686.x.

[125] N. Soker and A. Harpaz. Stellar structure and mass loss on the upper asymptotic giant branch. *MNRAS*, 310:1158–1164, December 1999. doi: 10.1046/j.1365-8711.1999.03062.x.

[126] N. Soker. Magnetic field, dust and axisymmetrical mass loss on the asymptotic giant branch. *MNRAS*, 299:1242–1248, October 1998. doi: 10.1046/j.1365-8711.1998.01884.x.

[127] N. Soker. Why Magnetic Fields Cannot Be the Main Agent Shaping Planetary Nebulae. *Pubs. Astron. Soc. Pac.*, 118:260–269, February 2006. doi: 10.1086/498829.

[128] N. Soker. Formation of Bipolar Lobes by Jets. *ApJ*, 568:726–732, April 2002. doi: 10.1086/339065.

[129] N. Soker. Collimated Fast Winds in Wide Binary Progenitors of Planetary Nebulae. *ApJ*, 558:157–164, September 2001. doi: 10.1086/322458.

[130] N. Soker and A. Harpaz. Can a single AGB star form an axially symmetric planetary nebula? *Pubs. Astron. Soc. Pac.*, 104:923–930, October 1992. doi: 10.1086/133076.

[131] N. Mastrodemos and M. Morris. Bipolar Preplanetary Nebulae: Hydro-dynamics of Dusty Winds in Binary Systems. I. Formation of Accretion Disks. *ApJ*, 497, April 1998. doi: 10.1086/305465.

[132] N. Mastrodemos and M. Morris. Bipolar Pre-Planetary Nebulae: Hydrodynamics of Dusty Winds in Binary Systems. II. Morphology of the Circumstellar Envelopes. *ApJ*, 523:357–380, September 1999. doi: 10.1086/307717.

[133] N. Soker. Extrasolar planets and the rotation and axisymmetric mass-loss of evolved stars. *MNRAS*, 324:699–704, June 2001. doi: 10.1046/j.1365-8711.2001.04353.x.

[134] N. Soker. A Solar-like Cycle in Asymptotic Giant Branch Stars. *ApJ*, 540:436–441, September 2000. doi: 10.1086/309326.

[135] N. Soker. On the Formation of Multiple Arcs around Asymptotic Giant Branch Stars. *ApJ*, 570:369–372, May 2002. doi: 10.1086/339573.

[136] N. Soker. Asymmetry and inhomogeneity in proto- and young planetary nebulae. *MNRAS*, 318:1017–1022, November 2000. doi: 10.1046/j.1365-8711.2000.03676.x.

[137] M. Elitzur, Ž. Ivezić, and D. Vinković. The structure of winds in AGB stars. In Y. Nakada, M. Honma, & M. Seki, editor, *Mass-Losing Pulsating Stars and their Circumstellar Matter*, volume 283 of *Astrophysics and Space Science Library*, pages 265–273, April 2003.

[138] G. H. Bowen. Dynamical modeling of long-period variable star atmospheres. *ApJ*, 329:299–317, June 1988. doi: 10.1086/166378.

[139] G. H. Bowen and L. A. Willson. From wind to superwind - The evolution of mass-loss rates for Mira models. *ApJ, Letters*, 375:L53–L56, July 1991. doi: 10.1086/186086.

[140] A. J. Fleischer, A. Gauger, and E. Sedlmayr. Circumstellar dust shells around long-period variables. I - Dynamical models of C-stars including dust formation, growth and evaporation. *Astron. & Astroph.*, 266:321–339, December 1992.

[141] P. R. Wood. Pulsation and mass loss in Mira variables. *ApJ*, 227: 220–231, January 1979. doi: 10.1086/156721.

[142] P. J. Bedijn. Pulsation, mass loss, and evolution of upper asymptotic giant branch stars. *Astron. & Astroph.*, 205:105–124, October 1988.

[143] K. Tsinganos. Theory of MHD Jets and Outflows. In J. Ferreira, C. Dougados, & E. Whelan, editor, *Lecture Notes in Physics, Berlin Springer Verlag*, volume 723 of *Lecture Notes in Physics, Berlin Springer Verlag*, 2007.

[144] J. Dorschner. From Dust Astrophysics Towards Dust Mineralogy - A Historical Review. In T. K. Henning, editor, *Astromineralogy*, volume 609 of *Lecture Notes in Physics, Berlin Springer Verlag*, pages 1–54, 2003.

[145] H.J. Habing and H Olofsson. *Asymptotic Giant Branch Stars*. Springer, 2004.

[146] L. Mestel. Magnetic braking by a stellar wind-I. *MNRAS*, 138, 1968.

[147] I. Okamoto. Magnetic braking by a stellar wind-IV. The effect of different poloidal field structures. *MNRAS*, 166:683–702, March 1974.

[148] I. Okamoto. Magnetic braking by a stellar wind. V - Approximate determination of the poloidal field. *MNRAS*, 173:357–379, November 1975.

[149] P. Goldreich and W. H. Julian. Stellar Winds. *ApJ*, 160, June 1970. doi: 10.1086/150486.

[150] F. C. Michel. Relativistic Stellar-Wind Torques. *ApJ*, 158, November 1969. doi: 10.1086/150233.

[151] G. W. Pneuman and R. A. Kopp. Gas-Magnetic Field Interactions in the Solar Corona. *Sol. Phys.*, 18:258–270, June 1971. doi: 10.1007/BF00145940.

[152] T. Yeh. Mass and angular momentum effluxes of stellar winds. *ApJ*, 206:768–776, June 1976. doi: 10.1086/154437.

[153] J. W. Belcher and K. B. MacGregor. Magnetic acceleration of winds from solar-type stars. *ApJ*, 210:498–507, December 1976. doi: 10.1086/154853.

[154] P. K. Barker and J. M. Marlborough. Weber and Davis revisited - Mass losing rotating magnetic winds. *ApJ*, 254:297–300, March 1982. doi: 10.1086/159733.

[155] S. K. Chakrabarti. Weber / Davis Model Revisited - Standing Magnetohydrodynamic Shocks in Accretion and Winds. *MNRAS*, 246, September 1990.

[156] T. Sakurai. Magnetic stellar winds - A 2-D generalization of the Weber-Davis model. *Astron. & Astroph.*, 152:121–129, November 1985.

[157] R. Keppens, G. Tóth, R. H. J. Westermann, and J. P. Goedbloed. Growth and saturation of the Kelvin-Helmholtz instability with parallel and antiparallel magnetic fields. *Journal of Plasma Physics*, 61:1–19, January 1999. doi: 10.1017/S0022377898007223.

[158] R. Keppens, K. B. MacGregor, and P. Charbonneau. On the evolution of rotational velocity distributions for solar-type stars. *Astron. & Astroph.*, 294:469–487, February 1995.

[159] H.-P. Gail and E. Sedlmayr. Dust formation in stellar winds. IV - Heteromolecular carbon grain formation and growth. *Astron. & Astroph.*, 206:153–168, November 1988.

[160] A. Gauger, E. Sedlmayr, and H.-P. Gail. Dust formation, growth and evaporation in a cool pulsating circumstellar shell. *Astron. & Astroph.*, 235:345–361, August 1990.

[161] A. J. Fleischer, A. Gauger, and E. Sedlmayr. Generation of shocks by radiation pressure on newly formed circumstellar dust. *Astron. & Astroph.*, 242:L1–L4, February 1991.

[162] A. J. Fleischer, A. Gauger, and E. Sedlmayr. Circumstellar dust shells around long-period variables. III. Instability due to an exterior κ-mechanism caused by dust formation. *Astron. & Astroph.*, 297, May 1995.

[163] S. Hoefner, M. U. Feuchtinger, and E. A. Dorfi. Dust formation in winds of long-period variables. III. Dynamical models and confirmation of a dust-induced κ-mechanism. *Astron. & Astroph.*, 297, May 1995.

[164] C. Sandin and S. Höfner. Three-component modeling of C-rich AGB star winds. III. Micro-physics of drift-dependent dust formation. *Astron. & Astroph.*, 413:789–798, January 2004. doi: 10.1051/0004-6361: 20031530.

[165] S. Höfner, R. Gautschy-Loidl, B. Aringer, and U. G. Jørgensen. Dynamic model atmospheres of AGB stars. III. Effects of frequency-dependent radiative transfer. *Astron. & Astroph.*, 399:589–601, February 2003. doi: 10.1051/0004-6361:20021757.

[166] A. C. Andersen, S. Höfner, and R. Gautschy-Loidl. Dust formation in winds of long-period variables. V. The influence of micro-physical dust properties in carbon stars. *Astron. & Astroph.*, 400:981–992, March 2003. doi: 10.1051/0004-6361:20030036.

[167] S. Höfner. Winds of AGB stars: does size matter? *Physica Scripta Volume T*, 133(1), December 2008. doi: 10.1088/0031-8949/2008/T133/014007.

[168] J. E. J. Woodrow and J. R. Auman. Time-dependent models of grain-forming stellar atmospheres. *ApJ*, 257:247–263, June 1982. doi: 10.1086/159983.

[169] P. Woitke. 2D models for the winds of AGB stars. In A. Wilson, editor, *ESA Special Publication*, volume 577 of *ESA Special Publication*, pages 461–462, January 2005.

[170] P. Woitke and A. Quirrenbach. The Chaotic Winds of AGB Stars: Observation Meets Theory. In A. Richichi, F. Delplancke, F. Paresce, & A. Chelli, editor, *The Power of Optical/IR Interferometry: Recent Scientific Results and 2nd Generation*, 2008.

[171] P. Woitke. Dust-driven Winds Beyond Spherical Symmetry. In L. Deng & K. L. Chan, editor, *IAU Symposium*, volume 252 of *IAU Symposium*, pages 229–234, October 2008. doi: 10.1017/S1743921308022849.

[172] C. Reimers, E. A. Dorfi, and S. Höfner. Shaping of elliptical planetary nebulae. The influence of dust-driven winds of AGB stars. *Astron. & Astroph.*, 354:573–578, February 2000.

[173] E. Lagadec and A. A. Zijlstra. The trigger of the asymptotic giant branch superwind: the importance of carbon. *MNRAS*, 390:L59–L63, October 2008. doi: 10.1111/j.1745-3933.2008.00535.x.

[174] U. Dirks, V. Schirrmacher, and E. Sedlmayr. Astrophysical dust formation under the influence of temperature fluctuations. A general stochastic approach and its application to AGB winds. *Astron. & Astroph.*, 491:643–662, December 2008. doi: 10.1051/0004-6361:20079243.

[175] H. C. Spruit. Origin of the rotation rates of single white dwarfs. *Astron. & Astroph.*, 333:603–612, May 1998.

[176] D. S. Davis, H. B. Richer, I. R. King, J. Anderson, J. Coffey, G. G. Fahlman, J. Hurley, and J. S. Kalirai. On the radial distribution of white dwarfs in the globular cluster NGC 6397. *MNRAS*, 383:L20–L24, January 2008. doi: 10.1111/j.1745-3933.2007.00402.x.

[177] J. Heyl. Constraining white dwarf kicks in globular clusters. *MNRAS*, 381:L70–L73, October 2007. doi: 10.1111/j.1745-3933.2007.00369.x.

[178] J. Heyl. Orbital evolution with white-dwarf kicks. *MNRAS*, 382:915–920, December 2007. doi: 10.1111/j.1365-2966.2007.12441.x.

[179] J. Heyl. Constraining white-dwarf kicks in globular clusters - III. Cluster heating. *MNRAS*, 390:622–624, October 2008. doi: 10.1111/j.1365-2966.2008.13724.x.

[180] J. S. Heyl. Constraining white dwarf kicks in globular clusters - II. Observational significance. *MNRAS*, 385:231–235, March 2008. doi: 10.1111/j.1365-2966.2007.12719.x.

[181] J. Heyl and M. Penrice. Constraining white dwarf kicks in globular clusters - IV. Retarding core collapse. *MNRAS*, 397:L79–L81, July 2009. doi: 10.1111/j.1745-3933.2009.00688.x.

[182] K. B. MacGregor, D. B. Friend, and R. L. Gilliland. Winds from rotating, magnetic, hot stars - Consequences for the rotational evolution of O and B stars. *Astron. & Astroph.*, 256:141–147, March 1992.

[183] K. B. MacGregor and D. B. Friend. Winds from rotating, magnetic, hot stars. II - The azimuthal velocity and magnetic force. *ApJ*, 312: 659–665, January 1987. doi: 10.1086/164911.

[184] D. B. Friend and K. B. MacGregor. Winds from rotating, magnetic, hot stars. I - General model results. *ApJ*, 282:591–602, July 1984. doi: 10.1086/162238.

[185] C. H. Poe, D. B. Friend, and J. P. Cassinelli. A rotating, magnetic, radiation-driven wind model for Wolf-Rayet stars. *ApJ*, 337:888–902, February 1989. doi: 10.1086/167159.

[186] C. H. Poe and D. B. Friend. A rotating, magnetic, radiation-driven wind model applied to Be stars. *ApJ*, 311:317–325, December 1986. doi: 10.1086/164773.

[187] E. G. Blackman, A. Frank, and C. Welch. Magnetohydrodynamic Stellar and Disk Winds: Application to Planetary Nebulae. *ApJ*, 546: 288–298, January 2001. doi: 10.1086/318253.

[188] D. Falceta-Gonçalves and V. Jatenco-Pereira. The Effects of Alfvén Waves and Radiation Pressure in Dust Winds of Late-Type Stars. *ApJ*, 576:976–981, September 2002. doi: 10.1086/341794.

[189] D. Falceta-Gonçalves, A. A. Vidotto, and V. Jatenco-Pereira. On the magnetic structure and wind parameter profiles of Alfvén wave driven winds in late-type supergiant stars. *MNRAS*, 368:1145–1150, May 2006. doi: 10.1111/j.1365-2966.2006.10190.x.

[190] L. C. Dos Santos, V. Jatenco-Pereira, and R. Opher. Mass loss from Wolf-Rayet stars due to radiation pressure and Alfven waves. *ApJ*, 410: 732–739, June 1993. doi: 10.1086/172790.

[191] J.J. More. *Numerical Analysis*, volume 630, chapter "The Levenberg-Marquardt Algorithm: Implementation and Theory", pages 105–116. Springer-Verlag, 1978.

[192] A.C. Hindmarsh. *Scientific Computing, Applications of Mathematics and Computing to the Physical Sciences*, volume 1 of *IMACS Transactions on Scientific Computation*, chapter "ODEPACK, A Systematized Collection of ODE Solvers", pages 55–64. Elsevier, 1983.

[193] P. N. Brown and A. C. Hindmarsh. Reduced storage matrix methods in stiff ode systems. *Journal of Applied Mathematics and Computing*, 31:40–91, 1989.

[194] T. E. Holzer and K. B. MacGregor. Mass loss mechanisms for cool, low-gravity stars. In M. Morris & B. Zuckerman, editor, *Mass Loss from Red Giants*, volume 117 of *Astrophysics and Space Science Library*, pages 229–255, 1985.

[195] P. David and R. Papoular. The circumstellar silicate dust as seen by IRAS. I - Opacity and temperature. *Astron. & Astroph.*, 237:425–435, October 1990.

[196] W. C. Danchi, M. Bester, C. G. Degiacomi, L. J. Greenhill, and C. H. Townes. Characteristics of dust shells around 13 late-type stars. *AJ*, 107:1469–1513, April 1994. doi: 10.1086/116960.

[197] N. Smith, K. H. Hinkle, and N. Ryde. Red Supergiants as Potential Type IIn Supernova Progenitors: Spatially Resolved 4.6 μm CO Emission Around VY CMa and Betelgeuse. *AJ*, 137:3558–3573, March 2009. doi: 10.1088/0004-6256/137/3/3558.

[198] G. M. Harper and A. Brown. Electron Density and Turbulence Gradients within the Extended Atmosphere of the M Supergiant Betelgeuse (α Orionis). *ApJ*, 646:1179–1202, August 2006. doi: 10.1086/505073.

[199] G. M. Harper, A. Brown, and E. F. Guinan. A New VLA-Hipparcos Distance to Betelgeuse and its Implications. *AJ*, 135:1430–1440, April 2008. doi: 10.1088/0004-6256/135/4/1430.

[200] B. Plez and D. L. Lambert. The outer atmosphere of the M-type supergiant alpha Orionis: K I 7699 Åemission. *Astron. & Astroph.*, 386:1009–1018, May 2002. doi: 10.1051/0004-6361:20020363.

[201] A. P. Bernat, D. N. B. Hall, K. H. Hinkle, and S. T. Ridgway. Observations of CO circumstellar absorption in the 4.6 micron spectrum of Alpha Orionis. *ApJ, Letters*, 233:L135–L139, November 1979. doi: 10.1086/183092.

[202] A. Noriega-Crespo, D. van Buren, Y. Cao, and R. Dgani. A Parsec-Size Bow Shock around Betelgeuse. *AJ*, 114:837–840, August 1997. doi: 10.1086/118517.

[203] T. Ueta, M. Meixner, D. E. Moser, L. A. Pyzowski, and J. S. Davis. Near-Infrared Photometric Survey of Proto-planetary Nebula Candidates. *AJ*, 125:2227–2238, April 2003. doi: 10.1086/373928.

[204] G. M. Harper, M. J. Richter, N. Ryde, A. Brown, J. Brown, T. K. Greathouse, and S. Strong. Texes Observations of M Supergiants: Dynamics and Thermodynamics of Wind Acceleration. *ApJ*, 701:1464–1483, August 2009. doi: 10.1088/0004-637X/701/2/1464.

[205] G. Perrin, T. Verhoelst, S. T. Ridgway, J. Cami, Q. N. Nguyen, O. Chesneau, B. Lopez, C. Leinert, and A. Richichi. The molecular and dusty composition of Betelgeuse's inner circumstellar environment. *Astron. & Astroph.*, 474:599–608, November 2007. doi: 10.1051/0004-6361:20077863.

[206] M. Bester, W. C. Danchi, C. G. Degiacomi, C. H. Townes, and T. R. Geballe. Distribution of dust about Omicron Ceti and Alpha Orionis based on 11 micron spatial interferometry. *ApJ, Letters*, 367:L27–L31, January 1991. doi: 10.1086/185924.

[207] M. Bester, W. C. Danchi, D. Hale, C. H. Townes, C. G. Degiacomi, D. Mekarnia, and T. R. Geballe. Measurement at 11 Micron Wavelengths of the Diameters of alpha Orionis and alpha Scorpii: Changes in Effective Temperature of alpha Orionis and Very Recent Dust Emission. *ApJ*, 463, May 1996. doi: 10.1086/177246.

[208] C. J. Skinner, S. M. Dougherty, M. Meixner, M. F. Bode, R. J. Davis, S. A. Drake, J. F. Arens, and J. G. Jernigan. Circumstellar environments - V. The asymmetric chromosphere and dust shell of alpha Orionis. *MNRAS*, 288:295–306, June 1997.

[209] T. Verhoelst, L. Decin, R. van Malderen, S. Hony, J. Cami, K. Eriksson, G. Perrin, P. Deroo, B. Vandenbussche, and L. B. F. M. Waters. Amorphous alumina in the extended atmosphere of α Orionis. *Astron. & Astroph.*, 447:311–324, February 2006. doi: 10.1051/0004-6361:20053359.

[210] R. Guandalini, M. Busso, S. Ciprini, G. Silvestro, and P. Persi. Infrared photometry and evolution of mass-losing AGB stars. I. Carbon stars revisited. *Astron. & Astroph.*, 445:1069–1080, January 2006. doi: 10. 1051/0004-6361:20053208.

[211] M. Jura. Multiple circumstellar shells and radiation pressure on grains in the outflows from late-type giants. *ApJ*, 282:200–205, July 1984. doi: 10.1086/162192.

[212] L. Hartmann and K. B. MacGregor. Momentum and energy deposition in late-type stellar atmospheres and winds. *ApJ*, 242:260–282, November 1980. doi: 10.1086/158461.

[213] L. Hartmann and E. H. Avrett. On the extended chromosphere of Alpha Orionis. *ApJ*, 284:238–249, September 1984. doi: 10.1086/ 162402.

[214] M. Elitzur and Ž. Ivezić. Dusty winds - I. Self-similar solutions. *MNRAS*, 327:403–421, October 2001. doi: 10.1046/j.1365-8711.2001. 04706.x.

[215] S. Liberatore, J.-P. J. Lafon, and N. Berruyer. Self-consistent coupling of radiative transfer and dynamics in dust-driven winds. *Astron. & Astroph.*, 377:522–537, October 2001. doi: 10.1051/0004-6361:20011115.

[216] A. Thirumalai and J. S. Heyl. A hybrid steady-state magnetohydrodynamic dust-driven stellar wind model for AGB stars. *MNRAS*, 409: 1669–1681, December 2010. doi: 10.1111/j.1365-2966.2010.17414.x.

[217] K.-P. Schröder and M. Cuntz. A critical test of empirical mass loss formulas applied to individual giants and supergiants. *Astron. & Astroph.*, 465:593–601, April 2007. doi: 10.1051/0004-6361:20066633.

[218] J. Lim, C. L. Carilli, S. M. White, A. J. Beasley, and R. G. Marson. Large convection cells as the source of Betelgeuse's extended atmosphere. *Nature*, 392:575–577, April 1998. doi: 10.1038/33352.

[219] A. Lobel and A. K. Dupree. Spatially Resolved STIS Spectroscopy of α Orionis: Evidence for Nonradial Chromospheric Oscillation from Detailed Modeling. *ApJ*, 558:815–829, September 2001. doi: 10.1086/ 322284.

[220] H. Uitenbroek, A. K. Dupree, and R. L. Gilliland. Spatially Resolved Hubble Space Telescope Spectra of the Chromosphere of alpha Orionis. *AJ*, 116:2501–2512, November 1998. doi: 10.1086/300596.

[221] E. E. Bloemhof, C. H. Townes, and A. H. B. Vanderwyck. Diffraction-limited spatial resolution of circumstellar dust shells at 10 microns. *ApJ, Letters*, 276:L21–L24, January 1984. doi: 10.1086/184180.

[222] G. M. Harper, A. Brown, and J. Lim. A Spatially Resolved, Semiempirical Model for the Extended Atmosphere of α Orionis (M2 Iab). *ApJ*, 551:1073–1098, April 2001. doi: 10.1086/320215.

[223] T. Onaka, T. de Jong, and F. J. Willems. A study of M Mira variables based on IRAS LRS observations. I - Dust formation in the circumstellar shell. *Astron. & Astroph.*, 218:169–179, July 1989.

[224] B. Rodgers and A. E. Glassgold. The temperature of the circumstellar envelope of Alpha Orionis. *ApJ*, 382:606–616, December 1991. doi: 10.1086/170748.

[225] S. B. F. Dorch. Magnetic activity in late-type giant stars: Numerical MHD simulations of non-linear dynamo action in Betelgeuse. *Astron. & Astroph.*, 423:1101–1107, September 2004. doi: 10.1051/0004-6361: 20040435.

[226] X.-N. Bai. Magnetorotational-instability-driven Accretion in Protoplanetary Disks. *ApJ*, 739:50, September 2011. doi: 10.1088/ 0004-637X/739/1/50.

[227] E. T. Vishniac, A. Lazarian, and J. Cho. Problems and Progress in Astrophysical Dynamos. In E. Falgarone & T. Passot, editor, *Turbulence and Magnetic Fields in Astrophysics*, volume 614 of *Lecture Notes in Physics, Berlin Springer Verlag*, pages 376–401. Springer, 2003.

[228] P. A. Davidson. *An Introduction to Magnetohydrodynamics*, chapter 3. Cambridge University Press, 2001.

[229] R. W. Wilson, J. E. Baldwin, D. F. Buscher, and P. J. Warner. High-resolution imaging of Betelgeuse and Mira. *MNRAS*, 257:369–376, August 1992.

[230] R. W. Wilson, V. S. Dhillon, and C. A. Haniff. The changing face of Betelgeuse. *MNRAS*, 291, November 1997.

[231] D. F. Buscher, J. E. Baldwin, P. J. Warner, and C. A. Haniff. Detection of a bright feature on the surface of Betelgeuse. *MNRAS*, 245:7P–11P, July 1990.

[232] X. Haubois, G. Perrin, S. Lacour, T. Verhoelst, S. Meimon, L. Mugnier, E. Thiébaut, J. P. Berger, S. T. Ridgway, J. D. Monnier, R. Millan-Gabet, and W. Traub. Imaging the spotty surface of ¡AS-TROBJ¿Betelgeuse¡/ASTROBJ¿ in the H band. *Astron. & Astroph.*, 508:923–932, December 2009. doi: 10.1051/0004-6361/200912927.

[233] M. Schwarzschild. On the scale of photospheric convection in red giants and supergiants. *ApJ*, 195:137–144, January 1975. doi: 10.1086/153313.

[234] A. Lobel and R. Blomme. Modeling Ultraviolet Wind Line Variability in Massive Hot Stars. *ApJ*, 678:408–430, May 2008. doi: 10.1086/529129.

[235] B. Lopez, W. C. Danchi, M. Bester, D. D. S. Hale, E. A. Lipman, J. D. Monnier, P. G. Tuthill, C. H. Townes, C. G. Degiacomi, T. R. Geballe, L. J. Greenhill, P. Cruzalebes, J. Lefevre, D. Mekarina, J. A. Mattei, D. Nishimoto, and P. W. Kervin. Nonspherical Structures and Temporal Variations in the Dust Shell of O Ceti Observed with a Long Baseline Interferometer at 11 Microns. *ApJ*, 488:807, October 1997. doi: 10.1086/304719.

[236] P. Planesas, R. Bachiller, J. Martin-Pintado, and V. Bujarrabal. The molecular envelope of Mira. *ApJ*, 351:263–270, March 1990. doi: 10.1086/168461.

[237] P. Planesas, J. D. P. Kenney, and R. Bachiller. Asymmetric outflow in the molecular envelope of Mira. *ApJ, Letters*, 364:L9–L12, November 1990. doi: 10.1086/185862.

[238] K. Young. A CO(3-2) survey of nearby Mira variables. *ApJ*, 445:872–888, June 1995. doi: 10.1086/175747.

[239] G. R. Knapp, K. Young, E. Lee, and A. Jorissen. Multiple Molecular Winds in Evolved Stars. I. A Survey of CO (2-1) and CO (3-2) Emission from 45 Nearby AGB Stars. *ApJ*, 117:209, July 1998. doi: 10.1086/ 313111.

[240] N. Ryde, B. Gustafsson, K. Eriksson, and K. H. Hinkle. Mira's Wind Explored in Scattering Infrared CO Lines. *ApJ*, 545:945–956, December 2000. doi: 10.1086/317832.

[241] N. Ryde and F. L. Schöier. Modeling CO Emission from Mira's Wind. *ApJ*, 547:384–392, January 2001. doi: 10.1086/318341.

[242] M. Karovska, W. Hack, J. Raymond, and E. Guinan. First Hubble Space Telescope Observations of Mira AB Wind-accreting Binary Systems. *The Astrophysical Journal, Letters*, 482:L175, June 1997. doi: 10.1086/310704.

[243] A. Thirumalai and J. S. Heyl. The magnetized bellows of Betelgeuse. *Monthly Notices of the Royal Astronomical Society*, 422(2):1272–282, May 2012. doi: 10.1111/j.1365-2966.2012.20703.x.

[244] N. Soker and J. H. Kastner. Magnetic Flares on Asymptotic Giant Branch Stars. *ApJ*, 592:498–503, July 2003. doi: 10.1086/375686.

[245] M. Hünsch. X-ray Emission from M-type Giants - Activity in Advanced Evolutionary Stages? In E. R. Schielicke, editor, *Astronomische Gesellschaft Meeting Abstracts*, volume 18 of *Astronomische Gesellschaft Meeting Abstracts*, page 710, 2001.

[246] M. Jura and D. J. Helfand. X-rays from accretion of red giant winds. *ApJ*, 287:785–792, dec 1984. doi: 10.1086/162737.

[247] J. H. Kastner and N. Soker. X-Rays from the Mira AB Binary System. *ApJ*, 616:1188–1192, December 2004. doi: 10.1086/424921.

[248] J. L. Sokoloski and L. Bildsten. Evidence for the White Dwarf Nature of Mira B. *ApJ*, 723:1188–1194, November 2010. doi: 10.1088/ 0004-637X/723/2/1188.

[249] G. Perrin, S. T. Ridgway, B. Mennesson, W. D. Cotton, J. Woillez, T. Verhoelst, P. Schuller, V. Coudé du Foresto, W. A. Traub, R. Millan-Gabet, and M. G. Lacasse. Unveiling Mira stars behind the molecules. Confirmation of the molecular layer model with narrow band near-infrared interferometry. *Astron. & Astroph.*, 426:279–296, October 2004. doi: 10.1051/0004-6361:20041098.

[250] C. A. Haniff, M. Scholz, and P. G. Tuthill. New Diameter Measurements of 10 Mira Variables - Implications for Effective Temperatures Atmospheric Structure and Pulsation Modes. *MNRAS*, 276: 640, September 1995.

[251] F. van Leeuwen, M. W. Feast, P. A. Whitelock, and B. Yudin. First results from HIPPARCOS trigonometrical parallaxes of Mira-type variables. *MNRAS*, 287:955–960, June 1997.

[252] P. J. Diamond and A. J. Kemball. A Movie of a Star: Multiepoch Very Long Baseline Array Imaging of the SiO Masers toward the Mira Variable TX Cam. *ApJ*, 599:1372–1382, December 2003. doi: 10.1086/379347.

[253] W. D. Cotton, B. Mennesson, P. J. Diamond, G. Perrin, V. Coudé du Foresto, G. Chagnon, H. J. van Langevelde, S. Ridgway, R. Waters, W. Vlemmings, S. Morel, W. Traub, N. Carleton, and M. Lacasse. VLBA observations of SiO masers towards Mira variable stars. *Astron. & Astroph.*, 414:275–288, January 2004. doi: 10.1051/0004-6361:20031597.

[254] N. Amiri, W. H. T. Vlemmings, A. J. Kemball, and H. J. van Langevelde. VLBA SiO maser observations of the OH/IR star OH 44.8-2.3: magnetic field and morphology. *Astron. & Astroph.*, 538: A136, February 2012. doi: 10.1051/0004-6361/201117452.

[255] W. H. T. Vlemmings, E. M. L. Humphreys, and R. Franco-Hernández. Magnetic Fields in Evolved Stars: Imaging the Polarized Emission of High-frequency SiO Masers. *ApJ*, 728:149, February 2011. doi: 10. 1088/0004-637X/728/2/149.

[256] M. Busso, G. J. Wasserburg, K. M. Nollett, and A. Calandra. Can Extra Mixing in RGB and AGB Stars Be Attributed to Magnetic Mechanisms? *ApJ*, 671:802–810, December 2007. doi: 10.1086/522616.

[257] D. C. Martin, M. Seibert, J. D. Neill, D. Schiminovich, K. Forster, R. M. Rich, B. Y. Welsh, B. F. Madore, J. M. Wheatley, P. Morrissey, and T. A. Barlow. A turbulent wake as a tracer of 30,000years of Mira's mass loss history. *Nature*, 448:780–783, August 2007. doi: 10.1038/ nature06003.

[258] J. R. P. Angel. Magnetic white dwarfs. *ARA&A*, 16:487–519, 1978. doi: 10.1146/annurev.aa.16.090178.002415.

[259] J. R. P. Angel, E. F. Borra, and J. D. Landstreet. The magnetic fields of white dwarfs. *ApJ*, 45:457–474, March 1981. doi: 10.1086/190720.

[260] R. C. Duncan and C. Thompson. Formation of very strongly magnetized neutron stars - Implications for gamma-ray bursts. *ApJ, Letters*, 392:L9–L13, June 1992. doi: 10.1086/186413.

[261] D. R. Lorimer. Binary and Millisecond Pulsars. *Living Reviews in Relativity*, 11:8, November 2008.

[262] L.D. Landau and E.M. Lifshitz. *Quantum Mechanics (Non-relativistic Theory), Third Edition*. Butterworth Heinemann, MA, 2003.

[263] V. Canuto and D. C. Kelly. Hydrogen Atom in Intense Magnetic Field. *ApSS*, 17:277, 1972.

[264] H. C. Praddaude. Energy Levels of Hydrogenlike Atoms in a Magnetic Field. *Phys. Rev. A*, 6:1321–1324, October 1972. doi: 10.1103/ PhysRevA.6.1321.

[265] J. Simola and J. Virtamo. Energy levels of hydrogen atoms in a strong magnetic field . *Journal of Physics B Atomic Molecular Physics*, 11: 3309–3322, October 1978.

[266] H. Friedrich. Bound-state spectrum of the hydrogen atom in strong magnetic fields. *Phys. Rev. A*, 26:1827–1838, October 1982.

[267] G. Wunner and H. Ruder. Lyman- and Balmer-like transitions for the hydrogen atom in strong magnetic fields. *Astron. & Astroph.*, 89: 241–245, September 1980.

[268] W. Roesner, H. Herold, H. Ruder, and G. Wunner. Approximate solution of the strongly magnetized hydrogenic problem with the use of an asymptotic property. *Phys. Rev. A*, 28:2071–2077, October 1983.

[269] W. Roesner, G. Wunner, H. Herold, and H. Ruder. Hydrogen atoms in arbitrary magnetic fields. I - Energy levels and wavefunctions. *Journal of Physics B Atomic Molecular Physics*, 17:29–52, January 1984.

[270] M. V. Ivanov. The hydrogen atom in a magnetic field of intermediate strength . *Journal of Physics B Atomic Molecular Physics*, 21:447–462, February 1988.

[271] D. Baye, M. Vincke, and M. Hesse. Simple and accurate calculations on a Lagrange mesh of the hydrogen atom in a magnetic field. *Journal of Physics B Atomic Molecular Physics*, 41(5):055005, March 2008. doi: 10.1088/0953-4075/41/5/055005.

[272] D. Baye, M. Hesse, and M. Vincke. The unexplained accuracy of the Lagrange-mesh method. *Phys. Rev. E*, 65(2):026701, February 2002. doi: 10.1103/PhysRevE.65.026701.

[273] P. Proeschel, W. Roesner, G. Wunner, H. Ruder, and H. Herold. Hartree-Fock calculations for atoms in strong magnetic fields. I - Energy levels of two-electron systems. *Journal of Physics B Atomic Molecular Physics*, 15:1959–1976, July 1982.

[274] G. Thurner, H. Korbel, M. Braun, H. Herold, H. Ruder, and G. Wunner. Hartree-Fock calculations for excited states of two-electron systems in strong magnetic fields . *Journal of Physics B Atomic Molecular Physics*, 26:4719–4750, December 1993.

[275] M. V. Ivanov. Hartree-Fock mesh calculations of the energy levels of the helium atom in magnetic fields . *Journal of Physics B Atomic Molecular Physics*, 27:4513–4521, October 1994.

[276] M. D. Jones, G. Ortiz, and D. M. Ceperley. Released-phase quantum Monte Carlo method. *Phys. Rev. E*, 55:6202–6210, May 1997. doi: 10.1103/PhysRevE.55.6202.

[277] M. D. Jones, G. Ortiz, and D. M. Ceperley. Spectrum of neutral helium in strong magnetic fields. *Phys. Rev. A*, 59:2875–2885, April 1999.

[278] J. S. Heyl and L. Hernquist. Hydrogen and helium atoms and molecules in an intense magnetic field. *Phys. Rev. A*, 58:3567–3577, November 1998.

[279] K. Mori and C. J. Hailey. Atomic Calculation for the Atmospheres of Strongly Magnetized Neutron Stars. *ApJ*, 564:914–929, January 2002. doi: 10.1086/323985.

[280] K. Mori and W. C. G. Ho. Modelling mid-Z element atmospheres for strongly magnetized neutron stars. *MNRAS*, 377:905–919, May 2007. doi: 10.1111/j.1365-2966.2007.11663.x.

[281] O.-A. Al-Hujaj and P. Schmelcher. Helium in superstrong magnetic fields. *Phys. Rev. A*, 67(2):023403, February 2003. doi: 10.1103/ PhysRevA.67.023403.

[282] Omar-Alexander Al-Hujaj and Peter Schmelcher. Electromagnetic transitions of the helium atom in superstrong magnetic fields. *Phys. Rev. A*, 68(5):053403, Nov 2003. doi: 10.1103/PhysRevA.68.053403.

[283] W. Becken and P. Schmelcher. Electromagnetic transitions of the helium atom in a strong magnetic field. *Phys. Rev. A*, 65(3):033416, Feb 2002. doi: 10.1103/PhysRevA.65.033416.

[284] W. Becken and P. Schmelcher. Higher-angular-momentum states of the helium atom in a strong magnetic field. *Phys. Rev. A*, 63(5):053412, May 2001. doi: 10.1103/PhysRevA.63.053412.

[285] W. Becken and P. Schmelcher. Non-zero angular momentum states of the helium atom in a strong magnetic field . *Journal of Physics B Atomic Molecular Physics*, 33:545–568, February 2000.

[286] W. Becken, P. Schmelcher, and F. K. Diakonos. The helium atom in a strong magnetic field. *Journal of Physics B Atomic Molecular Physics*, 32:1557–1584, March 1999.

[287] Armin Luhr, Omar-Alexander Al-Hujaj, and Peter Schmelcher. Resonances of the helium atom in a strong magnetic field. *Physical Review A (Atomic, Molecular, and Optical Physics)*, 75(1):013403, 2007. doi: 10.1103/PhysRevA.75.013403.

[288] M. V. Ivanov and P. Schmelcher. Ground state of the lithium atom in strong magnetic fields. *Phys. Rev. A*, 57:3793–3800, May 1998. doi: 10.1103/PhysRevA.57.3793.

[289] M. V. Ivanov and P. Schmelcher. Ground states of H, He,..., Ne, and their singly positive ions in strong magnetic fields: The high-field regime. *Phys. Rev. A*, 61(2):022505, February 2000. doi: 10.1103/PhysRevA.61.022505.

[290] Xiaofeng Wang and Haoxue Qiao. Configuration-interaction method with hylleraas-gaussian-type basis functions in cylindrical coordinates: Helium atom in a strong magnetic field. *Physical Review A (Atomic, Molecular, and Optical Physics)*, 77(4):043414, 2008. doi: 10.1103/PhysRevA.77.043414.

[291] D. Lai, E. E. Salpeter, and S. L. Shapiro. Hydrogen molecules and chains in a superstrong magnetic field. *Phys. Rev. A*, 45:4832–4847, April 1992.

[292] D. Lai, E. E. Salpeter, and S. L. Shapiro. Hydrogen Molecules and Chains in a Magnetic Neutron Star Atmosphere. In K. A. van Riper, R. I. Epstein, and C. Ho, editors, *Isolated Pulsars*, page 160, 1993.

[293] D. Lai and E. E. Salpeter. Hydrogen molecules in a superstrong magnetic field: Excitation levels. *Phys. Rev. A*, 53:152–167, January 1996.

[294] Zach Medin and Dong Lai. Density-functional-theory calculations of matter in strong magnetic fields. i. atoms and molecules. *Physical Review A (Atomic, Molecular, and Optical Physics)*, 74(6):062507, 2006. doi: 10.1103/PhysRevA.74.062507.

[295] Zach Medin and Dong Lai. Density-functional-theory calculations of matter in strong magnetic fields. ii. infinite chains and condensed matter. *Physical Review A (Atomic, Molecular, and Optical Physics)*, 74 (6):062508, 2006. doi: 10.1103/PhysRevA.74.062508.

[296] T. Detmer, P. Schmelcher, and L. S. Cederbaum. Hydrogen molecule in a magnetic field: The lowest states of the π manifold and the global ground state of the parallel configuration. *Phys. Rev. A*, 57(3):1767–1777, Mar 1998. doi: 10.1103/PhysRevA.57.1767.

[297] P. Schmelcher, T. Detmer, and L. S. Cederbaum. Excited states of the hydrogen molecule in magnetic fields: The singlet σ states of the parallel configuration. *Phys. Rev. A*, 61(4):043411, Mar 2000. doi: 10.1103/PhysRevA.61.043411.

[298] P. Schmelcher, T. Detmer, and L. S. Cederbaum. Excited states of the hydrogen molecule in magnetic fields: The triplet σ states of the parallel configuration. *Phys. Rev. A*, 64(2):023410, Jul 2001. doi: 10. 1103/PhysRevA.64.023410.

[299] E. G. Flowers, M. A. Ruderman, J.-F. Lee, P. G. Sutherland, W. Hillebrandt, and E. Mueller. Variational calculation of ground-state energy of iron atoms and condensed matter in strong magnetic fields. *ApJ*, 215:291–301, July 1977. doi: 10.1086/155358.

[300] M. L. Glasser and J. I. Kaplan. The Surface of a Neutron Star in Superstrong Magnetic Fields. *ApJ*, 199:208–219, July 1975. doi: 10. 1086/153683.

[301] E. Mueller. Variational calculation of iron and helium atoms and molecular chains in superstrong magnetic fields. *Astron. & Astroph.*, 130: 415–418, January 1984.

[302] P. B. Jones. Density-functional calculations of the cohesive energy of condensed matter in very strong magnetic fields. *Phys. Rev. Lett.*, 55 (12):1338–1340, Sep 1985. doi: 10.1103/PhysRevLett.55.1338.

[303] P. B. Jones. Properties of condensed matter in very strong magnetic fields. *MNRAS*, 218:477–485, February 1986.

[304] R. O. Mueller, A. R. P. Rau, and Larry Spruch. Statistical model of atoms in intense magnetic fields. *Phys. Rev. Lett.*, 26(18):1136–1139, May 1971. doi: 10.1103/PhysRevLett.26.1136.

[305] J. E. Skjervold and E. Ostgaard. Heavy atoms in superstrong magnetic fields. *Physica Scripta*, 29:543–550, June 1984. doi: 10.1088/ 0031-8949/29/6/008.

[306] D. Neuhauser, K. Langanke, and S. E. Koonin. Hartree-Fock calculations of atoms and molecular chains in strong magnetic fields. *Phys. Rev. A*, 33:2084–2086, March 1986. doi: 10.1103/PhysRevA.33.2084.

[307] D. Neuhauser, S. E. Koonin, and K. Langanke. Structure of matter in strong magnetic fields. *Phys. Rev. A*, 36:4163–4175, November 1987. doi: 10.1103/PhysRevA.36.4163.

[308] M. Demeur, P.-H. Heenen, and M. Godefroid. Hartree-fock study of molecules in very intense magnetic fields. *Phys. Rev. A*, 49(1):176–183, Jan 1994. doi: 10.1103/PhysRevA.49.176.

[309] M. V. Ivanov. Hartree-Fock calculation of the $1s^2 2s^2$ state of the Be atom in external magnetic fields from γ=0 up to γ=1000. *Physics Letters A*, 239:72–80, February 1998.

[310] P. Schmelcher, M. V. Ivanov, and W. Becken. Exchange and correlation energies of ground states of atoms and molecules in strong magnetic fields. *Phys. Rev. A*, 59(5):3424–3431, May 1999. doi: 10.1103/PhysRevA.59.3424.

[311] M. V. Ivanov and P. Schmelcher. Ground state of the carbon atom in strong magnetic fields. *Phys. Rev. A*, 60:3558–3568, November 1999. doi: 10.1103/PhysRevA.60.3558.

[312] M. V. Ivanov and P. Schmelcher. The beryllium atom and beryllium positive ion in strong magnetic fields. *European Physical Journal D*, 14:279–288, June 2001. doi: 10.1007/s100530170194.

[313] M. V. Ivanov and P. Schmelcher. The boron atom and boron positive ion in strong magnetic fields. *Journal of Physics B Atomic Molecular Physics*, 34:2031–2044, May 2001.

[314] M. V. Ivanov and P Schmelcher. Finite-Difference Calculations for Atoms and Molecules in Strong Magnetic and Static Electric Fields. In J. Sabin, E. Brandas, P-O. Lowden, and M. Zerner, editors, *Advances in Quantum Chemistry, Volume 40, part 2*, pages 361–379, 2001.

[315] Omar-Alexander Al-Hujaj and Peter Schmelcher. Beryllium in strong magnetic fields. *Phys. Rev. A*, 70(2):023411, Aug 2004. doi: 10.1103/PhysRevA.70.023411.

[316] R. González-Férez and P. Schmelcher. Sodium in a strong magnetic field. *European Physical Journal D*, 23:189–199, May 2003. doi: 10.1140/epjd/e2003-00031-y.

222

[317] Haoxue Qiao and Baiwen Li. Calculations of lithium in magnetic fields with a modified freezing full-core method. *Phys. Rev. A*, 62(3):033401, Aug 2000. doi: 10.1103/PhysRevA.62.033401.

[318] Xiaoxu Guan and Baiwen Li. Energies and oscillator strengths of lithium in a strong magnetic field. *Phys. Rev. A*, 63(4):043413, Mar 2001. doi: 10.1103/PhysRevA.63.043413.

[319] Charlotte Froese Fischer. *Computational Atomic Structure, An MCHF Approach.* Institute of Physics Publishing, Bristol, UK, 1997.

[320] M. D. Jones, G. Ortiz, and D. M. Ceperley. Hartree-Fock studies of atoms in strong magnetic fields. *Phys. Rev. A*, 54:219–231, July 1996.

[321] Peter M. W. Gill and Siu-Hung Chien. Radial quadrature for multi-exponential integrands. *Journal of Computational Chemistry*, 24(6): 732–740, 2003.

[322] Lloyd N. Trefethen. *Spectral Methods in MATLAB.* Society for Industrial and Applied Mathematics, Philadelphia, Pennsylvania, 2000.

[323] John P. Boyd. *Chebyshev and Fourier Spectral Methods.* Dover Publications, Mineola, New York, second (revised) edition, 2001.

[324] C. Talbot and A. Crampton. Application of the pseudo-spectral method to 2d eigenvalue problems in elasticity. *Numerical Algorithms*, 38:95–110, 2005.

[325] J. C. Slater. A Simplification of the Hartree-Fock Method. *Physical Review*, 81:385–390, February 1951. doi: 10.1103/PhysRev.81.385.

[326] W. E. Arnoldi. The principle of minimized iteration in the solution of the matrix eigenvalue problem. *Quart. J. Applied Mathematics, 9:17-29*, 1951.

[327] D. C. Sorensen. Implicit application of polynomial filters in a k-step arnoldi method. *SIAM Journal of Matrix Analysis and Applications*, 13:357–385, 1992.

[328] R. B. Lehoucq, D. C. Sorensen, and C Yang. *ARPACK User's Guide.* SIAM, Philadelphia, 1998.

[329] J. G. F. Francis. The qr transformation a unitary analogue to the lr transformation, part 1. *The Computer Journal*, 4(3):265–271, 1961. doi: 10.1093/comjnl/4.3.265.

[330] J. G. F. Francis. The qr transformationpart 2. *The Computer Journal*, 4(4):332–345, 1962.

[331] Youcef Saad. Chebyshev acceleration techniques for solving non-symmetric eigenvalue problems. *Mathematics of Computation*, 42 (166):567–588, 1984. ISSN 0025-5718. doi: 10.2307/2007602. URL `http://dx.doi.org/10.2307/2007602`.

[332] A. Poszwa and A Rutkowski. Hyrogen atom in a strong magnetic field. II. Relativistic corrections for low-lying states. *Phys. Rev. A*, 69: 023403, February 2004.

[333] A. Poszwa and A. Rutkowski. Highly accurate calculations for hydrogenic atoms in a magnetic field of arbitrary strength. *Phys. Rev. A*, 63:043418, Mar 2001. doi: 10.1103/PhysRevA.63.043418. URL `http://link.aps.org/doi/10.1103/PhysRevA.63.043418`.

[334] Zonghua Chen and S. P. Goldman. Relativistic and nonrelativistic finite-basis-set calculations of low-lying levels of hydrogenic atoms in intense magnetic fields. *Phys. Rev. A*, 45: 1722–1731, Feb 1992. doi: 10.1103/PhysRevA.45.1722. URL `http://link.aps.org/doi/10.1103/PhysRevA.45.1722`.

[335] F. N. Fritsch and R. E. Carlson. Monotone piecewise cubic interpolation. *SIAM Journal on Numerical Analysis*, 17(2):238–246, 1980. doi: 10.1137/0717021.

[336] W. H. Press, S. A. Teukolsky, W. T. Vetterling, and B. P. Flannery. *Numerical Recipes in C*. Cambridge University Press, New York, 1992.

[337] Y. Ralchenko, A.E. Kramida, J. Reader, and N.A. Team. *Technical Report, National Institute of Standards and Technology*, 2008. available:http://physics.nist.gov/asd3.

Appendix A

Hybrid Wind Model - Source Code

The central driver routine for the hybrid wind model, written in Fortran 77, is provided here. A suitable bash, Perl or Ruby wrapper can run the driver for various initial conditions. It needs to be directly compiled alongside ODEPACK [192, 193]. The latter is available at

https://computation.llnl.gov/casc/odepack/odepack_home.html.

```
C       The following is a driver program for solving the Weber-
     Davis solar wind model
C       on a uni-dimensional grid of points.
C       The problem to be solved is an ordinary differential
     equation
C
C       dy/dt= (y/t) * ((2 g ST (yt^2)^(1-g) -Sg/t)(yt^2-1)^3 + SW
     t^2 (y-1)
C                *[ (yt^2+1)y - 3 yt^2 +1 ] /
C                ( (y^2 - g ST (yt^2)^(1-g))(yt^2-1)^3 - SW y^2 t^2
     (1-t^2)^2 )
C
C       on the interval from t = t0 to t = tmax, with initial
     conditions
C       y0 supplied at t0. The problem is stiff.
C
C       The following coding solves this problem with DLSODE,
     using
C       MF = 21. It uses
C       ITOL = 1 and ATOL about 1.D-12.
C       At the end of the run, statistical quantities of interest
     are printed.
C
C       NOTE: A shell script wrapper runs this driver program
C              running various initial conditions.

          external   fex, jex
```

```
      integer   iopt , iout , istate , itask , itol , iwork(21) , liw
          , lrw
      integer   mf, neq , counter , iflag , nyh , k, ten
      integer  derivchk , iwrite , thousand , divnum
      integer   write_counter , hundred , icont , itcount , itask0 ,
          iopt0
      integer*8 numsteps
      double precision   atol , rtol , rwork(32) , t, tout , tstep ,
          y(1)
      double precision y0 , t0 , tout0 , rtol0 , atol0 , tcrit0
      double precision st_param , sg_param , sw_param ,
          gamma_param
      double precision st_param0 , sg_param0 , sw_param0 ,
          gamma_param0
      double precision nu_tsing , s_tsing , omega_tsing ,
          gamma_tsing
      double precision xc , vc , xf , vf , tprev , yprev , tend ,
          yend
      double precision dky , g_dusty , xa , va , xa0p99 , dlast ,
          tento4
      double precision va0p9 , va1p01 , xa0p98 , xa1p01 , xa1p02
      double precision xa0p975 , last_y_good , last_t_good ,
          dky_prev
      double precision flux , ff , st , sg , sw , g, xd , xmin , xmax
      common /wd_params/ st_param , sg_param , sw_param ,
          gamma_param
      common / flags / icont , itcount , dlast


c      open various output files , main output file if "output .
   dat"

      open (1 , file='output.dat' , status='new' , access='
          sequential ' ,
   #form='formatted' , action='write')

      open (2 , file='deriv.dat' , status='new' , access='sequential
          ' ,
   #form='formatted' , action='write')

      open (3 , file='last_deriv.dat' , status='new' , access='
          sequential ' ,
   #form='formatted' , action='write')

      open (9 , file='istate.dat' , status='new' , access='
```

```fortran
              sequential',
     #form='formatted',action='write')

          open (10,file='deldky.dat',status='replace',
     #access='sequential',form='formatted',action='write')

          open (11,file='last_integration.dat',status='replace',
     #access='sequential',form='formatted',action='write')

c      counter is for carring out multiple integrations in the u-
     r phase space
c      in the current version it is set to zero. Otherwise the
     wrapper script
c      will introduce it and increment it.
          counter = 0

c      input variables
c      y0 <-- initial condition for the dependent variable
c      t0 <-- starting point for integration
c      tout0 <-- the next time/space step. tout0-t0=step size
c      rtol0 <-- relative tolerance, see dlsode docs
c      atol0 <-- absolute tolerance, see dlsode docs
c      itask0 <-- task type, see dlsode docs
c      iopt <-- extra options, see dlsode docs
c      istate0 <-- initial state for integration, see dlsode docs
c      tcrit0 <-- location of any critical point, see dlsode docs
c      st_param0 <-- ST parameter
c      sg_param0 <-- SG parameter
c      sw_param0 <-- SW parameter
c      gamma_param0 <-- polytropic exponent
c      numsteps <-- number of steps wanted. deprecated
c      icont <-- (1 or 0) whether to continue after parameter;
     adjusted mid-way.
c                 deprecated
c      g_dusty <-- dust parameter
c      xa <-- =1 location of Alfven point.
c      va <-- =1 Alfven velocity
c      dlast <-- last location of integration. deprecated
c      xd <-- location of the dust formation radius.


      write(*,*) 'please provide the following in that order'
      write(*,*) 'y0, t0, tout0, rtol0, atol0, itask0, iopt0,
     #istate0, tcrit0,st_param0, sg_param0, sw_param0,
     #gamma_param0, numsteps, icont,g_dusty, xa, va, dlast, xd'
```

```
       read(*,*) y0, t0, tout0, rtol0, atol0, itask0, iopt0,
           istate0,
      #tcrit0 , st_param0 , sg_param0 , sw_param0 , gamma_param0 ,
           numsteps ,
      #icont , g_dusty , xa, va, dlast , xd

c        optional read statement, not required in current version
c          read (2 ,*) xc
c          read (2 ,*) vc
c          read (3 ,*) xf
c          read (3 ,*) vf

c        initialise options needed by dlsode. see docs.
          neq = 1
          y(1) = y0
          t    = t0
          tout = tout0
          itol = 1
          itask = itask0
          istate = 1
          iopt=iopt0
          if (iopt .eq. 1) then
              rwork(5)=0.0D0
              rwork(6)=0.0D0
              rwork(7)=0.0D0
              rwork(8)=0.0D0
              rwork(9)=0.0D0
              rwork(10)=0.0D0
              iwork(5)=0
              iwork(6)=1000
              iwork(7)=0
              iwork(8)=0
              iwork(9)=0
              iwork(10)=0
          endif
C          iopt = 0
          lrw = 32
          liw = 21
          mf = 21
          nyh = 1
          tstep = tout-t
          k=1
          hundred=100
          thousand=1000
```

228

```fortran
         ten=10
         if (itask .eq. 4 ) then
             rwork(1)=tcrit0
             tend=xa
             yend=va
         endif

c       locate the minimum and maximum integration limits.
c       xmin is R0/ra
c       xmas is arbitrary
         xmin=0.067D0
         xmax=5.0D0

             gamma_param=gamma_param0
             st_param=st_param0
             sg_param=sg_param0
             sw_param=sw_param0

             g=gamma_param0
             st=st_param0
             sg=sg_param0
             sw=sw_param0

 10         if (counter .gt. 0) write(*,*) "reducing tols and trying
     again"

         if (counter .gt. 0) then
             rtol = rtol*10.d0
             atol = atol*10.d0
             istate = 1
         else
             atol=atol0
             rtol=rtol0
         endif

c       you typically want rtol no less than ~ 1d-8
c       you typically want atol no less than ~ 1d-8
c        first we shall try to perform calculation with rtol=atol=1
     d-12
c       if it does not suceed and produces istate=-1
c       then and only then do we try to reduce rtol and atol by
     factors
c       of 10 and try again. we do this until rtol=atol<=1d-8
c        if we obtain an output with istate .ne. -1 then all is
     good
```

```fortran
c       %——————————%
c       % Central Driver %
c       %——————————%

          write (1,20) t, y(1)
          write_counter = 0

 14       if (tout .lt. xmax ) then
                  yprev = y(1)
              call dlsode (fex, neq, y, t, tout, itol, rtol, atol,
                 itask,
     #               istate, iopt, rwork, lrw, iwork, liw, jex, mf)
                  tprev = t
                  if (istate .eq. 2 ) then
                      last_y_good=y(1)
                      last_t_good=tout
                  endif

          if (tout .gt. xmin .and. .not. ( (y(1)+1.0) .eq. y(1))
                 .and.
     # (mod(write_counter,10000) .eq. 0)) then
c          the second logical relationship prevents us from
     writing nan's


                  write(1,20) t, y(1)
 20               format(f18.14,6x,f18.14)

              endif


              if (istate .lt. −1 .and. istate .gt. −5 .or. counter
     #.gt.2 .or.tout .lt.0.d0 .or. istate .lt. −5 ) then
                  go to 80
              elseif (istate .eq. −1 .and. counter .le. 2) then
                  counter = counter + 1
                  go to 10
              elseif (istate .eq. −5 ) then
                  istate = 1
                  tstep=10*tstep
                  tout=tout+2*tstep
                  y(1)=yprev
                  t=tprev
```

```fortran
                goto 40
             endif

             write_counter=write_counter + 1
 40          tout = tout+tstep

             go to 14

         endif


         write(6,60)  iwork(11), iwork(12), iwork(13)
 60      format(/' no. steps =',i4,',   no. f-s =',i4,',   no. j-s
     =',i4)

 65      write(11,68) last_t_good, last_y_good
 68      format(f18.14,6x,f18.14)

         stop

 80      write(6,90)  istate
 90      format(///' error halt.. istate =',i3)
 95      format(i3)


c 130       write(*,*) 'Integreation reached dust formation radius
     ; xd'
 140        write(*,*) 'Integration reached outer limit xmax'



         write (*,*) 'this is the end, my only friend, the end'

         close(1)
         close(2)
         close(3)
         close(9)
         close(10)
         close(11)

        stop
        end

c       %———%
c       % END %
```

```fortran
c       %——%

c       ————————————————————

c       %————————————————————————%
c       % optional function for derivative %
c       % to be calculated outside dlsode   %
c       % for the sake of comparison        %
c       %————————————————————————%

        subroutine   fex (neq, t, y, ydot)
        integer    neq
        double precision   t, y(1), ydot(1), t_deriv, y_deriv
        double precision st_param, sg_param, sw_param,
            gamma_param
        double precision st,sg,sw,g
        double precision numer, denom
        common /wd_params/ st_param, sg_param, sw_param,
            gamma_param
        common /flags/ icont, itcount, dlast

        st = st_param
        sg = sg_param
        sw = sw_param
        g  = gamma_param

        numer = (2 * g * st * ( y(1) * t*t )**(1-g) - sg/t )*(y
            (1) * t*
    #t - 1 )**3 + sw * t*t *( y(1) - 1 )*( (y(1)*t*t +1)*y(1)
        -3*y(1)
    #*t*t + 1 )

        denom = ( y(1)*y(1) - g * st * ( y(1) * t*t )**(1-g) )*
            (y(1)*t*
    #t - 1 )**3 - sw * y(1) * y(1) * t*t *(1-t*t)*(1-t*t)

        if (icont .eq. 1 ) then
        open (7,file='prev_deriv.dat',status='old',access='
            sequential',
    #form='formatted',action='read')

        read (7,150) t_deriv, y_deriv
 150        format(f25.14,6x,f25.14)
        ydot(1)=y_deriv
C         ydot(1)=dlast
```

```fortran
            icont=0
            close(7)
         elseif (icont .eq. 2 ) then
            ydot(1)=dlast
            icont=0
         else
            ydot(1) = (y(1) / t) * numer/denom
         endif


         return
         end

c        _____
c        %—————————————————%
c        % Jacobian of the problem %
c        %—————————————————%



         subroutine   jex (neq, t, y, ml, mu, pd, nrpd)
         integer   neq, ml, mu, nrpd
         double precision   t, y(1), pd(1,1)
         double precision st_param, sg_param, sw_param,
             gamma_param
         double precision st,sg,sw,g

         common /wd_params/ st_param, sg_param, sw_param,
             gamma_param
         common /flags/ icont, itcount, dlast

         st = st_param
         sg = sg_param
         sw = sw_param
         g  = gamma_param


         pd(1,1) = 1 / t * ((2 * g * st * (y(1) * t ** 2) ** (1 -
             g) - sg
 #/ t) *(y(1) * t ** 2 - 1) ** 3 + sw * t ** 2 * (y(1) - 1)
        * ((y(1)
 #*t ** 2 + 1)* y(1) - 3 * y(1) * t ** 2 + 1)) / ((y(1) ** 2
        - g * s
 #t * (y(1) * t ** 2) ** (1 - g)) * (y(1) * t ** 2 - 1) ** 3
        - sw *
 #y(1) ** 2 * t ** 2 * (1 - t **2) ** 2) + y(1) / t * (2 * g
```

```
                * st *
#(y(1) * t ** 2) ** (1 - g) * (1 - g) / y(1) * (y(1) * t **
    2 - 1)
#** 3 + 3 * (2 * g * st * (y(1) * t ** 2) **(1 - g) - sg /
    t) * (y(
#1) * t ** 2 - 1) ** 2 * t ** 2 + sw * t ** 2 *((y(1) * t
    ** 2 + 1)
#* y(1) - 3 * y(1) * t ** 2 + 1) + sw * t ** 2 * (y(1) - 1)
    * (2 *
#y(1) * t ** 2 + 1 - 3 * t ** 2)) / ((y(1) ** 2 - g * st *
    (y(1) *t
#** 2) ** (1 - g)) * (y(1) * t ** 2 - 1) ** 3 - sw * y(1)
    ** 2 * t
#**2 * (1 - t ** 2) ** 2) - y(1) / t * ((2 * g * st * (y(1)
    * t **
#2) ** (1- g) - sg / t) * (y(1) * t ** 2 - 1) ** 3 + sw * t
    ** 2 *
#(y(1) - 1) *((y(1) * t ** 2 + 1) * y(1) - 3 * y(1) * t **
    2 + 1))
#/ ((y(1) ** 2 - g * st *(y(1) * t ** 2) ** (1 - g)) * (y
    (1) * t **
#2 - 1) ** 3 - sw * y(1) ** 2 * t ** 2 * (1 - t ** 2) ** 2)
    ** 2 *
#((2 * y(1) - g * st * (y(1) * t ** 2)** (1 - g) * (1 - g)
    / y(1))
#* (y(1) * t ** 2 - 1) ** 3 + 3 * (y(1) ** 2 -g * st * (y
    (1) * t **
#2) ** (1 - g)) * (y(1) * t ** 2 - 1) ** 2 * t **2 - 2 * sw
    * y(1)
#* t ** 2 * (1 - t ** 2) ** 2)

    return
    end
```

c _____

Appendix B

Pseudospectral Method for Atoms - Source Code

The cylindrical pseudospectral atomic structure code described in Chapter 6 is provided below. The software is written in the high-level programming language Matlab. The code depends up a routine "cheb.m" which is available with the suite of programs developed by Lloyd N. Trefethen.

```
% This is a spectral code for solving the helium atom in strong
% magnetic fields

% The PDE that we are trying to solve is of the following form:
%
% a1u_xx + b1u_x + c1u_yy + d1u_y + e1u + fv = \lambda u
% a2v_xx + b2v_x + c2v_yy + d2v_y + e2v + fu = \lambda v
%
% where,
% a1,a2=-0.25*(3-x^2-2*x)^2;
% b1,b2=-0.5*(3-x^2-2*x)*(1./atanh(0.5*(1+x))-1-x);
% c1,c2=-0.25*(3-y^2-2*y)^2;
% d1,d2=0.5*(3-y^2-2*y)*(1+y);
%
% e1=m_1^2*rho2inv + betaZ_Z2*rho2 -2*Znucl./sqrt(rho2+z2) + ...
%            2*betaZ_Z*(m1-1) + 2/Z*Phi_D_1;
%
% e2=m_2^2*rho2inv + betaZ_Z2*rho2 -2*Znucl./sqrt(rho2+z2) + ...
%            2*betaZ_Z*(m2-1) + 2/Z*Phi_D_2;
%
% f=2/Z*alpha_E;
%
% \rho is the radial cylindrical coordinate and is related to x
%    via the
% transformation:
%
% x = 2tanh(rho)-1 ; rho = atanh(0.5*(1+x)) ; with -1 <= x <= +1
%
% z is the axial cylindrical coordinate and is related to y via
```

```
     the
% transformation:
%
% y = 2tanh(z)−1 ; z = atanh(0.5*(1+y)) ; with −1 <= y <= +1
%
% The radial coordinate (\rho) is semi−infinite [0,inf] and the
     axial
% coordinate (z) is semi−infinite.
% The compactification puts them both in the interval [−1,1]
% Thus we can use Chebyshev points for both these directions


% ====================== IMPORTANT NOTE ======
% If the problem is a generalised eigenvalue problem
% (A u = \lambda B u) then use a QZ algorithm by invoking eig(A,
     B)
% in matlab.
% ON the other hand should the problem become too large, many
     node
% points or if the problem becomes sparse, then use Krylov
     Subspace
% method such as the iterative Arnoldi algorithm or Lanczos
% iterations (should the matrix be symmetric). Use 'eigs'
     routine for
% the above cases.
% =================================================


% % The boundary conditions are as shown below pictorially
% %
% %       Dirichlet
% %     ———————— D
% % N |             |i
% % e |             |r     Example:
% % u |             |i     This is for the m=0 electron
% % m |             |c     of Hydrogen
% % a |             |h
% % n |             |l
% % n |             |e
% %     ———————— t
% %       Neumann


% %
% %       Dirichlet
% % D ———————— D
% % i |             |i
% % r |             |r     Example:
```

```
% % i |              | i    This is for the m=−1 electron
% % c |              | c    of Hydrogen
% % h |              | h
% % l |              | l
% % e |              | e
% % t    ——————————— t
% %        Neumann


clear all
clear global

% shift the singularity by tiny amount
tiny=1e−14;

tic ,

% % ——————————————————————————————
% % ——————————————————————————————

% Defining the problem —— user need only input the following :
%——————————————————————————————

Znucl=3; % Nuclear charge assume: nelectrons=Znucl

config_term=['1s0  ';'2p−1';'3d−2'] % the configuration of the
    atom
% each string in term must be the same length , so pad with
    blanks
% for this , see the string 1s0 above for example and compare
    with
% 2p−1
config_term_cell=cellstr(config_term); % convert to cell array
betaZar =[0.2 5/18 0.5 10/18 ...
          0.7 1 20/18 2 ...
          50/18 5 100/18 7 ...
          10 200/18 20 500/18 ...
          50 1000/18 70 100 ...
          1000/18 200 5000/18 500 ...
          10000/18 700 1000];
for betaZcount=1:length(betaZar) ,

  betaZ=betaZar(betaZcount)
  sigma_guess_ar=[−1 −1 −1 −1.5 ...
                  −2 −2 −2 −2.5 ...
```

```
                     −3  −3  −3.5  −3.5  ...
                     −4  −4  −4.5  −5   ...
                     −5.5  −6.5  −7.5  −8  ...
                     −10  −12  −13  −14  ...
                     −14  −15  −16]; % guess for arnoldi method.
sigma_guess=sigma_guess_ar(betaZcount)
for N=21:10:41, % number of node points in the rho and z
    directions

  %——————————————————————

  %——————————————————————
  % begin calculations
  % first define the 'electron' data structure
  % more states can be added to the statements below
  %——————————————————————

  for i=1:Znucl,
    if (strcmp(config_term_cell(i),'1s0'))
      electron(i).m=0;                    % azimuthal quantum
          number
      electron(i).parity=1;              % z−parity for betaZ
          −−> infinity
      electron(i).Neumann=[1,1];         % Neumann conditions on
           inner boundaries
      electron(i).excitation=0;          % excitation level of
          the state
      electron(i).term=config_term(i,:); % the term of the
          electron
    elseif (strcmp(config_term_cell(i),'2s0'))
      electron(i).m=0;
      electron(i).parity=1;
      electron(i).Neumann=[1,1];
      electron(i).excitation=1;
      electron(i).term=config_term(i,:);
    elseif (strcmp(config_term_cell(i),'2p−1'))
      electron(i).m=−1;
      electron(i).parity=1;
      electron(i).Neumann=[0,1];
      electron(i).excitation=0;
      electron(i).term=config_term(i,:);
    elseif (strcmp(config_term_cell(i),'3p−1'))
      electron(i).m=−1;
      electron(i).parity=1;
      electron(i).Neumann=[0,1];
```

```matlab
      electron(i).excitation=1;
      electron(i).term=config_term(i,:);
  elseif (strcmp(config_term_cell(i),'3d-2'))
      electron(i).m=-2;
      electron(i).parity=1;
      electron(i).Neumann=[0,1];
      electron(i).excitation=0;
      electron(i).term=config_term(i,:);
  elseif (strcmp(config_term_cell(i),'3d-2'))
      electron(i).m=-2;
      electron(i).parity=1;
      electron(i).Neumann=[0,1];
      electron(i).excitation=1;
      electron(i).term=config_term(i,:);
  elseif (strcmp(config_term_cell(i),'2p0'))
      electron(i).m=0;
      electron(i).parity=-1;
      electron(i).Neumann=[1,0];
      electron(i).excitation=0;
      electron(i).term=config_term(i,:);
  elseif (strcmp(config_term_cell(i),'3p0'))
      electron(i).m=0;
      electron(i).parity=-1;
      electron(i).Neumann=[1,0];
      electron(i).excitation=1;
      electron(i).term=config_term(i,:);
  elseif (strcmp(config_term_cell(i),'3d-1'))
      electron(i).m=-1;
      electron(i).parity=-1;
      electron(i).Neumann=[1,0];
      electron(i).excitation=0;
      electron(i).term=config_term(i,:);
  elseif (strcmp(config_term_cell(i),'4d-1'))
      electron(i).m=-1;
      electron(i).parity=-1;
      electron(i).Neumann=[1,0];
      electron(i).excitation=1;
      electron(i).term=config_term(i,:);
  elseif (strcmp(config_term_cell(i),'4f-2'))
      electron(i).m=-2;
      electron(i).parity=-1;
      electron(i).Neumann=[1,0];
      electron(i).excitation=0;
      electron(i).term=config_term(i,:);
  elseif (strcmp(config_term_cell(i),'5f-2'))
```

```matlab
            electron(i).m=−2;
            electron(i).parity=−1;
            electron(i).Neumann=[1,0];
            electron(i).excitation=1;
            electron(i).term=config_term(i,:);
        end
    end

    betaZ2=betaZ^2;
    msq=zeros(Znucl,1);
    delta_m_sq=zeros(Znucl,Znucl);
    for i=1:Znucl,
        msq(i)=electron(i).m^2;
    end
    for i=1:Znucl,
        for j=1:Znucl,
            if (j~=i)
                delta_m_sq(i,j)=(electron(i).m−electron(j).m)^2;
            end
        end
    end

    % Differentiation matrices for Chebyshev grid on [−1,1]
    [D,x]=cheb(N);
    D2=D^2;

    % There are Dirichlet conditions at the zeroth end of x and
        y
    % So remove first rows of Dx,Dy,Dx2,Dy2.
    D=D(2:N+1,2:N+1);
    D2=D2(2:N+1,2:N+1);

    % resize the grid and excise infinity at x=−1
    x(end)=x(end)+tiny;
    x=x(2:N+1);
    y=x;

    % mesh the grid
    [xx,yy]=meshgrid(x,y);
    xx=xx(:);
    yy=yy(:);

    % use x = 2tanh(rho)−1 ; rho = atanh(0.5*(1+x)) ; with −1 <=
        x <= +1
    rho=atanh(0.5*(1+xx));
```

```
rhoinv =1./rho;
rho2=rho.^2;
rho2inv =1./rho2;
z=atanh(0.5*(1+yy));
z2=z.^2;

% Constructing the operator coefficients
a=-0.25*(3-xx.^2-2*xx).^2;
b=-0.5*(3-xx.^2-2*xx).*(rhoinv-1-xx);
c=-0.25*(3-yy.^2-2*yy).^2;
d=0.5*(3-yy.^2-2*yy).*(1+yy);

ecoeff=zeros(N^2,Znucl);
for i=1:Znucl,
   ecoeff(:,i)=msq(i)*rho2inv + betaZ2*rho2 -2./sqrt(rho2+z2)
       ;
end

e_exch=zeros(N^2,Znucl,Znucl);
for i=1:Znucl,
   for j=1:Znucl,
     if (j~=i)
        e_exch(:,i,j)=delta_m_sq(i,j)*rho2inv;
     end
   end
end

% Next form the LHS operator.
I=eye(N);

Dx2kr=kron(D2,I);
Dxkr=kron(D,I);
Dy2kr=kron(I,D2);
Dykr=kron(I,D);

aDx2=diag(a)*Dx2kr;
bDx=diag(b)*Dxkr;
cDy2=diag(c)*Dy2kr;
dDy=diag(d)*Dykr;

Lmtrx=zeros(N^2,N^2,Znucl);
Lpmtrx=zeros(N^2,N^2,Znucl);

for i=1:Znucl,
   Lmtrx(:,:,i)=aDx2+bDx+cDy2+dDy+diag(ecoeff(:,i)) ; % one
```

241

```matlab
        for each electron
    Lpmtrx(:,:,i)=aDx2+bDx+cDy2+dDy+diag(ecoeff(:,i))+ ...
        2*betaZ*(electron(i).m - 1)*eye(N^2); % one for each
            electron
end

Ldirect= -aDx2-bDx-cDy2-dDy;            % Notice the minus
    signs
Lexchng=zeros(N^2,N^2,Znucl,Znucl);
for i=1:Znucl,
  for j=1:Znucl,
    if (j~=i)
      Lexchng(:,:,i,j)= -aDx2-bDx-cDy2-dDy-diag(e_exch(:,i,j
          )); % Notice the minus signs
    end
  end
end

% Next remove every Nth row in the first N*(N-1) rows,
    included.
Lmtrx(N:N:N*(N-1),:,:) =[];
Lexchng(N:N:N*(N-1),:,:,:) =[];
Lpmtrx(N:N:N*(N-1),:,:) =[];
Ldirect(N:N:N*(N-1),:) =[];

% Define the C matrix
Cmtrx=zeros((N-1)^2,N-1); % note that Cdirect and/or
    Cexchng = - Cmtrx
for i=N:N:N*(N-1),
  Cmtrx(:,i/N)=Lmtrx(1:(N-1)^2,i,1);
end

% Next remove every Nth column in the first N*(N-1) columns,
    included.
Lmtrx(:,N:N:N*(N-1),:) =[];
Ldirect(:,N:N:N*(N-1)) =[];
Lexchng(:,N:N:N*(N-1),:,:) =[];
Lpmtrx(:,N:N:N*(N-1),:) =[];

% Define the matrix E
Emtrx=zeros((N-1)^2,(N-1)^2,Znucl);
Eexchng=zeros((N-1)^2,(N-1)^2,Znucl,Znucl);
Epmtrx=zeros((N-1)^2,(N-1)^2,Znucl);
Emtrx(1:(N-1)^2,1:(N-1)^2,:)=Lmtrx(1:(N-1)^2,1:(N-1)^2,:);
Edirect=Ldirect(1:(N-1)^2,1:(N-1)^2);
```

```
Eexchng(1:(N−1)^2,1:(N−1)^2,:,:)=Lexchng(1:(N−1)^2,1:(N−1)
    ^2,:,:);
Epmtrx(1:(N−1)^2,1:(N−1)^2,:)=Lpmtrx(1:(N−1)^2,1:(N−1)^2,:);

% Define the matrxix En
ENmtrx=zeros((N−1)^2,N);      % Note: ENp=ENmtrx
ENtilde=zeros((N−1)^2,N−1); % Note: ENp_tilde = ENtilde
ENmtrx(1:(N−1)^2,1:N,:)=Lmtrx(1:(N−1)^2,(N−1)^2+1:end,1);
ENtilde(1:(N−1)^2,1:N−1)=ENmtrx(1:(N−1)^2,1:N−1);
ENdirect=Ldirect(1:(N−1)^2,(N−1)^2+1:end); % Note: ENexchng=
    ENdirect
ENdirect_tilde=ENdirect(:,1:N−1);              % Note:
    ENdirect_tilde=ENexchng_tilde

% free up some memory
clear Lexchng Ldirect

% % Next set up the boundary condition matrices
B=kron(D,I); % boundary matrix for the derivative in the x−
    direction.

B0=B(N*(N−1)+1:end,1:N*(N−1));
B2=zeros(N,N−1);
for i=N:N:N*(N−1),
  B2(:,i/N)=B0(:,i);
end
B0(:,N:N:N*(N−1)) =[];
BN=B(N*(N−1)+1:end,N*(N−1)+1:end);
BN_tilde=BN(1:N−1,1:N−1);
B1=B0;
B1_tilde=B1(1:N−1,:);

% % Next we set up the bounday condition matrix in the y−
    direction
By=kron(I,D);
Bycopy=By; % setup a copy for defining further arrays

% % Define the H matrix
H=zeros(N−1,N−1);
for i=N:N:N*(N−1),
  for j=N:N:N*(N−1),
    H(i/N,j/N)=By(i,j);
  end
end
```

```matlab
% % Remove every Nth columns in the first N*(N−1) columns
Bycopy(:,N:N:N*(N−1))=[];

% % Define the J matrices
Jfull=Bycopy(1:N*(N−1),N*(N−1)−N+1+1:end);
J=zeros(N−1,N);
for i=N:N:N*(N−1),
  J(i/N,:)=Jfull(i,:);
end

% % Prune Bycopy array −− get rid of the Jfull part
Bycopy=Bycopy(1:N*(N−1),1:N*(N−1)−N+1);

% % Define the G matrix
G=zeros(N−1,N*(N−1)−N+1);
for i=N:N:N*(N−1),
  G(i/N,:)=Bycopy(i,:);
end

% % Define inverse matrices to be used
BNinv=inv(BN);
BN_tildeinv=inv(BN_tilde);
Hinv=inv(H);
HJBinv=inv(H−J*BNinv*B2);
GJB=G−J*BNinv*B1;
CHG=Cmtrx*Hinv*G;
EBHG=ENmtrx*(BNinv*(B1−B2*Hinv*G));
EBHGdir=ENdirect*(BNinv*(B1−B2*Hinv*G));
EBBtilde=ENtilde*BN_tildeinv*B1_tilde;
EBBtildedir=ENdirect_tilde*BN_tildeinv*B1_tilde;

% % clear variables to free up memory
clear D D2 By Bycopy x xx y yy rho rhoinv rho2 rho2inv z ...
    z2 a b c d ecoeff e_exch I Dx2kr Dxkr Dy2kr Dykr aDx2
        bDx ...
    cDy2 dDy Lmtrx Lpmtrx Ldirect Lexchng Cmtrx ...
    ENmtrx ENtilde ENdirect ENdirect_tilde B B0 B2 BN ...
    BN_tilde B1 B1_tilde H Jfull J G BNinv BN_tildeinv Hinv
        ...
    HJBinv GJB


% we setup and solve the eigenvalue problem

Mmtrx=zeros((N−1)^2,(N−1)^2,Znucl);
```

```matlab
Mdirect=zeros((N-1)^2,(N-1)^2,Znucl);
Mexchng=zeros((N-1)^2,(N-1)^2,Znucl,Znucl);

for i=1:Znucl,

  if (electron(i).parity==1)

    Mmtrx(:,:,i)=Emtrx(:,:,i)-electron(i).Neumann(1)*EBHG -
        ...
         electron(i).Neumann(2)*CHG;

    Mdirect(:,:,i)=Edirect-electron(i).Neumann(1)*EBHGdir
        ...
        - electron(i).Neumann(2)*(-CHG);
    % note the minus sign on CHG: see definition of Cmtrx
        above

  else

    Mmtrx(:,:,i)=Emtrx(:,:,i)-electron(i).Neumann(1)*
        EBBtilde ;

    Mdirect(:,:,i)=Edirect-electron(i).Neumann(1)*
        EBBtildedir;

  end

end


for i=1:Znucl,
  for j=1:Znucl,
    if (j~=i)
      if (electron(i).parity==1 && electron(j).parity==1)
        Mexchng(:,:,i,j)=Eexchng(:,:,i,j)-electron(i).
            Neumann(1)*  ...
            electron(j).Neumann(1)*EBHGdir ...
            - electron(i).Neumann(2)*electron(j).Neumann(2)
                *(-CHG);
      % note minus sign in CHG; see definition of
      % Cmtrx above
      else
        Mexchng(:,:,i,j)=Eexchng(:,:,i,j)-electron(i).
            Neumann(1)*  ...
            electron(j).Neumann(1)*EBBtildedir ...
```

```matlab
                    - electron(i).Neumann(2)*electron(j).Neumann(2)
                        *(-CHG);
                % note minus sign in CHG; see definition of
                % Cmtrx above
            end
        end
    end
end

% free up some more memory
clear EBHGdir EBBtildedir Edirect Eexchng Emtrx

Mdinv=zeros((N-1)^2,(N-1)^2,Znucl);
Mexinv=zeros((N-1)^2,(N-1)^2,Znucl,Znucl);

for i=1:Znucl,
    Mdinv(:,:,i)=inv(Mdirect(:,:,i));
    for j=1:Znucl,
        if (j~=i)
            Mexinv(:,:,i,j)=inv(Mexchng(:,:,i,j));
        end
    end
end

% free up some memory
clear Mdirect Mexchng

% convert the full matrix to a sparse matrix
% by squeezing out the zeros and find eigenvalues

% options for arpack
opts.disp=0;
opts.p=50;
opts.tol=1e-10;

V=zeros((N-1)^2,15,Znucl);
Lam=zeros(15,15,Znucl);
for i=1:Znucl,
    [V(:,:,i),Lam(:,:,i)]=eigs(sparse(Mmtrx(:,:,i)),15,'sm',
        opts);
end
Lamsort=zeros(15*Znucl,1);
for i=1:Znucl,
    [Lamsort,ii]=sort(diag(Lam(:,:,i)));
    llam=Lamsort+2*betaZ*(electron(i).m - 1);
```

```matlab
    electron(i).eigval=llam(electron(i).excitation+1);
    electron(i).eigvec=V(:,1+electron(i).excitation,i);
end

disp('hydrogenic problem solved')

% % Free up memory
clear V Lam Lamsort llam Mmtrx ii

% % Now that we have eigenvectors, normalise them
f=zeros(N^2,Znucl);

for j=1:Znucl,
    for i=1:N-1,
        f(i*N+2:(i+1)*N,j)=electron(j).eigvec((i-1)*(N-1)+1:i*N-
            i);
    end
end

% Differentiation matrices for Chebyshev grid on [-1,1]
[DD,xn]=cheb(N);
xn=xn(1:N);
xn(1)=xn(1)-tiny;
yn=xn;
wx=inv(DD(1:N,1:N));wx=wx(1,:); % Matlab

%  wx=inv(DD(1:N,1:N))(1,:);
wy=wx;
wx=(8*pi*atanh(0.5*(1+xn')))./(3-xn'.^2-2*xn').*wx);
wy=2./(3-yn'.^2-2*yn').*wy;
we=kron(wx,wy);

norm=zeros(Znucl,1);
for i=1:Znucl,
    norm(i)=we*f(:,i).^2;
end

% % v's are normalised and defined only on interior points
for i=1:Znucl,
    electron(i).eigvec=electron(i).eigvec/sqrt(norm(i));
end

% % clear unneeded variables
clear DD xn yn wx wy f
```

```matlab
for i=1:Znucl,
  electron(i).eigvec_prev_iter=electron(i).eigvec;
  electron(i).eigval_prev_iter=electron(i).eigval;
end



%————————————————————————————————
%————————————————————————————————

% % Start Hartree Fock iterations

% % First we determine the direct and exchange interactions
% % We are trying to solve the following PDE's for the
%     direct and
% % exchange interactions.
% %
% % ——————— Direct Interactions ————————————
% % au_xx + bu_x + cu_yy + du_y = fii_inter

% % ——————— Exchange Interaction ————————————
% % au_xx + bu_x + cu_yy + du_y + eu = fij_inter

% % The boundary conditions are as shown below pictorially
% %
% %        Dirichlet
% %     ————————————— D
% % N |               | i
% % e |               | r     Example:
% % u |               | i     Direct Interaction
% % m |               | c     for 1s0 electron
% % a |               | h
% % n |               | l
% % n |               | e
% %     ————————————— t
% %        Neumann

% %
% %        Dirichlet
% % D ————————————— D
% % i |               | i
% % r |               | r     Example:
% % i |               | i     Exchange Interaction
% % c |               | c     b/w 1s0 and 2p−1
% % h |               | h
% % l |               | l
```

```matlab
% % e  |                |e
% % t   ───────────── t
% %          Neumann

% % First we determine the RHS for the interactions on
    interior
% % grid points; boundary conditions are imposed on the
    boundaries
% % inter suffix stands for 'interior'.

% begin HF iterations
eigvalold(1:Znucl)=0;
del_eigval(1:Znucl)=10;
%del_eigval1=10;
%del_eigval2=10;
del_E_HF=10;
E_HFold=0;

iter=0;
maxiter=25;

% eigvalold1=0;
% eigvalold2=0;

% initialise the interaction matrix
% This is constructed as follows:
% ─────────────────────────────
%    __          __
% |  I11  I12  I13  |
% |  I21  I22  I23  |
% |  I31  I32  I33  |
%    __          __
% ─────────────────────────────
% where Iij is the interaction of electron 'i' with electron
     'j'
% and Iij is an (N-1)^2 by (N-1)^2 matrix


while (abs(del_E_HF) >= 1e-8)

  if (iter==maxiter), break; end

  iter=iter+1;

  finter=zeros((N-1)^2,Znucl,Znucl);
```

```matlab
for i=1:Znucl,
  for j=1:Znucl,
    if (i==j)
      finter(:,i,i)=-4*pi*(electron(i).eigvec.^2);
    else
      finter(:,i,j)=-4*pi*(electron(i).eigvec.* ...
                                electron(j).eigvec);
    end
  end
end

interact=zeros((N-1)^2,Znucl,Znucl);
for i=1:Znucl,
  for j=1:Znucl,
    if (i==j)
      interact(:,i,i)=Mdinv(:,:,i)*finter(:,i,i);
    else
      interact(:,i,j)=Mexinv(:,:,i,j)*finter(:,i,j);
    end
  end
end

% initialise and setup master matrix with bc's
Master=zeros(Znucl*(N-1)^2,Znucl*(N-1)^2);

% add bc's with nuemann conditions
for i=1:Znucl,
  for j=1:Znucl,
    if (i==j)
      if (electron(i).parity==1)
        Master((i-1)*(N-1)^2+1:i*(N-1)^2,(i-1)*(N-1)^2+1:i
            *(N-1)^2) ...
            = Epmtrx(:,:,i) - electron(i).Neumann(1)*EBHG
                - ...
              electron(i).Neumann(2)*CHG;
      else
        Master((i-1)*(N-1)^2+1:i*(N-1)^2,(i-1)*(N-1)^2+1:i
            *(N-1)^2) ...
            = Epmtrx(:,:,i) - electron(i).Neumann(1)*
                EBBtilde;
      end
    end
  end
end
```

```matlab
for i=1:Znucl,
  electron(i).PhiD=zeros((N-1)^2,(N-1)^2);
  for j=1:Znucl,
    if (j~=i)
      electron(i).PhiD=electron(i).PhiD + 2/Znucl*diag(
          interact(: ...
                                            ,j,j));
    end
  end
end

% find the direct and exchange interactions
ffdir=zeros((N-1)^2,Znucl);
ffex=zeros((N-1)^2,Znucl);
for i=1:Znucl,
  for j=1:Znucl,
    if (i==j)
      for k=1:Znucl,
        if (k~=i)
          ffdir(:,i)=ffdir(:,i)+(electron(i).eigvec.^2).*
              ...
                interact(:,k,k);
        end
      end
    else
      ffex(:,i)=ffex(:,i)+(electron(i).eigvec.*electron(j)
          .eigvec).* ...
                interact(:,i,j);
    end
  end
end

fdirect=zeros(N^2,Znucl);
fexchng=zeros(N^2,Znucl);
for j=1:Znucl,
  for i=1:N-1,
    fdirect(i*N+2:(i+1)*N,j)=ffdir((i-1)*(N-1)+1:i*N-i,j);
    fexchng(i*N+2:(i+1)*N,j)=ffex((i-1)*(N-1)+1:i*N-i,j);
  end
end

for i=1:Znucl,
  electron(i).direct_energy=we*fdirect(:,i);
  electron(i).exchange_energy=we*fexchng(:,i);
end
```

```matlab
% clear memory
clear ffdir ffex fdirect fexchng

% complete setup of the master matrix
for i=1:Znucl,
  for j=1:Znucl,
    if (i==j)
      Master((i-1)*(N-1)^2+1:i*(N-1)^2,(i-1)*(N-1)^2+1:i*(
        N-1)^2) ...
          = Master((i-1)*(N-1)^2+1:i*(N-1)^2,(i-1)*(N-1)
            ^2+1:i*(N-1)^2) ...
          + electron(i).PhiD;
    else
      Master((i-1)*(N-1)^2+1:i*(N-1)^2,(j-1)*(N-1)^2+1:j*(
        N-1)^2) ...
          = -2/Znucl*diag(interact(:,i,j));
    end
  end
end

% clear some memory
clear finter interact

% convert master matrix to a sparse one
MS=sparse(Master);

% clear some more memory
clear Master
rmfield(electron,'PhiD');

% % Find eigenvalues of sparse matrix MS
[V,Lam]=eigs(MS,15,sigma_guess,opts);
Lam=diag(Lam);
bimag=find(imag(Lam)~=0);
V(:,bimag)=[];
Lam(bimag)=[];
[Lamsort,ii]=sort(Lam);
b=find(Lamsort<0);
Lamgood=Lamsort(b);


for i=1:Znucl,
  temp=0;
  for j=1:length(b),
```

```matlab
            testvec=V((i-1)*(N-1)^2+1:i*(N-1)^2,ii(j));
          % find overlap
          overlap=abs(testvec'*electron(i).eigvec_prev_iter);
          if (overlap >= temp)
            temp=overlap;
            jval=j;
            electron(i).eigvec=testvec;
            electron(i).eigval=Lamgood(jval);
          end
      end
  end

% % First, normalise them
f=zeros(N^2,Znucl);

for j=1:Znucl,
  for i=1:N-1,
    f(i*N+2:(i+1)*N,j)=electron(j).eigvec((i-1)*(N-1)+1:i*
        N-i);
  end
end

norm=zeros(Znucl,1);
for i=1:Znucl,
  norm(i)=we*(f(:,i).^2);
end

% % v's are normalised and defined only on interior points
for i=1:Znucl,
  electron(i).eigvec=electron(i).eigvec/sqrt(norm(i));
end

% clear memory
clear f norm

% clear memory
clear f norm

for i=1:Znucl,
  del_eigval(i)=electron(i).eigval-electron(i).
      eigval_prev_iter;
  electron(i).eigval_prev_iter=electron(i).eigval;
  electron(i).eigvec_prev_iter=electron(i).eigvec;
end
```

```matlab
    % clear variables to free memory
    clear f norm V Lam bimag MS Lamgood b testvec

    E_HF=0;
    for i=1:Znucl,
      E_HF=E_HF + electron(i).eigval - (1/Znucl)* ...
            (electron(i).direct_energy - electron(i).
                exchange_energy);
    end
    E_HF
    del_E_HF=E_HF-E_HFold;
    E_HFold=E_HF;

end

% clear some memory
rmfield(electron,'PhiD');

E_HFname=strcat('E_HF_betaZ_',num2str(betaZ),'_N_',num2str(N
    ),'_.dat');
fid_e=fopen(E_HFname,'w+');
fprintf(fid_e,'%48s\n','
        _____');
fprintf(fid_e,'%-24s %24.18f\n',  'E_HF             :',E_HF)
    ;
fprintf(fid_e,'%-24s %24.18f\n',  'betaZ            :',betaZ
    );
fprintf(fid_e,'%48s\n','
        _____');
for i=1:Znucl,
  fprintf(fid_e,'%-24s %24s\n',    'term             :',
      electron(i).term);
  fprintf(fid_e,'%-24s %24.18f\n','electron number   :',i);
  fprintf(fid_e,'%-24s %24.18f\n','m                :',
      electron(i).m);
  fprintf(fid_e,'%-24s %24.18f\n','parity            :',
      electron(i).parity);
  fprintf(fid_e,'%-24s %24.18f %24.18f\n','Neumann
      :', ...
          electron(i).Neumann(1),electron(i).Neumann(2));
  fprintf(fid_e,'%-24s %24.18f\n','excitation  level:',
      electron(i).excitation);
  fprintf(fid_e,'%-24s %24.18f\n','energy eigenvalue:',
      electron(i).eigval);
  fprintf(fid_e,'%-24s %24.18f\n','direct energy    :',
```

```matlab
            electron(i).direct_energy);
        fprintf(fid_e,'%-24s %24.18f\n','exchange energy   :', ...
                electron(i).exchange_energy);
        fprintf(fid_e,'%48s\n','
            _____');
    end

    vecs=zeros((N-1)^2,Znucl);
    for i=1:Znucl,
        vecs(:,i)=electron(i).eigvec;
    end

    save(strcat('eigenvectors','_betaZ_',num2str(betaZ), ...
                '_N_',num2str(N),'_.dat'),'-ascii','-double','-
                    tabs' ...
            ,'vecs');

    % free memory
    clear vecs;

  end

end

toc

}
```